

ABSTRACT

Title of Dissertation: MECHANICAL CHARACTERIZATION OF
PRESSURE-SENSITIVE ADHESIVE (PSA)
BONDED ASSEMBLY

Hao Huang, Doctor of Philosophy, 2019

Dissertation directed by: Professor Abhijit Dasgupta, Department of
Mechanical Engineering

This study focuses on comprehensive empirical and mechanistic understanding of the mechanical behavior of adhesive bonded assemblies bonded with pressure sensitive adhesives (PSAs). PSAs are capable of very large deformation. The stress-strain and creep behavior of such bonded assemblies are complex due to constant competition between cavitation dynamics in the bulk and at interfaces; and fibrillation and nonlinear visco-plastic behavior of the PSA material. The behavior is further altered by the presence of flexible or semi-rigid carrier layers because they alter the stress field within the bonded assembly and also provide additional interfaces for sequential cavity nucleation and growth. These mechanisms are known to result in multiple phases and transitions in their stress-strain and creep curves. The number of transitions depends on the presence (or absence) of carrier layers and the severity of the secondary transitions depends on the flexural compliance of the carrier layers). The effective mechanical response of the PSA bonded assembly is therefore affected by this complex set of

events during slow deformation process, including the final stage when the PSA starts to debond from the substrate and/or carrier layer. This morphological evolution of the PSA depends on the adhesive material properties, bonded assembly configuration (bonded assembly aspect ratio and presence/absence of carrier layers), bonding substrate surface properties (surface energy, roughness and presence of contaminants), carrier layer properties (surface energy, surface roughness and flexural rigidity) and loading conditions (loading rate, stress level and temperature). This study consists of experimentation and mechanistic modeling.

In the experimental study, bonded PSA test specimens were fabricated for selected PSA/substrate combinations, after detailed parametric study to gain insights into the influences of the lamination conditions (bonding pressure, bonding time, bonding pressure, post-cure and aging protocols). The bonded assembly performance parameters of interest for this parametric study include: (i) tensile strength, ductility and creep resistance; (ii) peak stress and peak strain; and (iii) number of transitions and severity of transitions. These specimens were subjected to mechanical tests on a dynamic mechanical analyzer (DMA) to measure stress-strain response and creep response for different loading conditions.

In the modeling phase, mechanistic models are developed to provide fundamental insights about the dominant deformation mechanisms in PSA bonded assemblies. This has the added advantage of reducing the enormous amount of physical testing that engineers would need to conduct to empirically characterize every PSA-substrate combination of interest over all the loading conditions of interest. The predictive mechanistic model is based on enhancement of a simple 'block' model that has been

proposed in the literature for simulating the stress-strain and creep behavior of the PSA/substrate at different loading conditions. This model acts as a virtual test, predicting the mechanical response of a PSA bonded assembly by explicitly accounting for the PSAs' nonlinear visco-plastic material properties, cavity dynamics in the bulk and at the interfaces, fibrillation dynamics, and other system configurations such as bonding substrate surface properties and carrier layer properties. This model is shown to be able to predict the stress-strain and creep behavior of PSA bonded assemblies under a broad range of operating conditions, after proper calibration by a few corner cases of physical tests. The predictive model can become a virtual testing method that for real-time prognostic health management (PHM) for PSA bonded assemblies.

Test equipment includes a commercially available Dynamic Mechanical Analysis (DMA), to conduct the constant speed stress-strain test and constant force uniaxial creep test on the sample of selected PSA bonded assemblies at selected loading conditions. An observation fixture is also designed for studying the morphological evolution of PSA layer by video recording the cavitation and debonding at the PSA-substrate interface during tensile deformation of a PSA bonded assembly.

Complexity in the study includes: (i) structural change of PSA system due to cavitation and fibrillation; (ii) sequential cavitation and fibrillation due to additional interface introduced by carrier layer; (iii) bonded assembly parameter (material, configuration, surface roughness any surface energy); (iv) nonlinear rate-dependent plastic material properties of bulk PSA; and (v) implementation of new material model into commercial FEA tools.

MECHANICAL CHARACTERIZATION OF PRESSURE-SENSITIVE ADHESIVE
(PSA) BONDED ASSEMBLY

by

Hao Huang

Dissertation submitted to the Faculty of the Graduate School of the
University of Maryland, College Park, in partial fulfillment
of the requirements for the degree of
Doctor of Philosophy
2019

Advisory Committee:

Professor Abhijit Dasguta, Chair

Professor Hugh Bruck

Professor Patrick McCluskey

Professor Teng Li

Professor Robert Briber (Dean's Representative)

© Copyright by
Hao Huang
2019

Acknowledgements

I would like to thank my advisor, Professor Abhijit Dasgupta for guiding and supporting me over years. Abhijit is someone you will instantly love and never forget once you meet him. He has set an example of excellence as a researcher, instructor, mentor and role model.

I am grateful to all the committee members of my dissertation, Professor Hugh Bruck, Professor Teng Li, Professor Robert Briber, and Professor Patrick McCluskey for their support and valuable suggestions to improve the quality of my work. Also, I would like to thank the Microsoft reliability team for their assistance in characterize mechanical properties of pressure-sensitive adhesive bonded assembly in my research.

Additionally, I'd like to thank all the former and current A-Team members, CALCE sponsors and employees, and my friends in the engineering school, not only for their assistance and inspirations, but also for making my graduate school experience a fulfilled one: countless telecons, CALCE meetings, finals, reports, presentations, conferences ... and the list goes on.

Finally, I owe all the thanks to my beloved wife and my parents, with all their support, love and encouragements that I always need.

Table of Contents

Acknowledgements	ii
Table of Contents	iii
List of Tables	vi
List of Figures	vii
Chapter 1. Introduction	1
1.1 Background and motivation	3
1.2 Problem statement	4
1.3 Literature review	7
1.3.1 Debonding mechanisms of PSA bonded assembly:	7
1.3.2 Effects of bonding conditions on mechanical performance of PSA bonded assembly:	13
1.3.3 Effects of loading conditions on PSA bonded assemblies' mechanical performance:	14
1.3.4 Effects of configuration on mechanical behavior of PSA bonded assemblies:	18
1.3.5 Effects of substrate surface properties on PSA bonded assemblies' mechanical performance:	21
1.3.6 Modeling mechanical response of the PSA bonded assemblies:	23
1.4 Research gaps and Objectivities	25
Chapter 2. Approaches of Dissertation	29
2.1 Mechanical testing on PSA bonded assemblies	30
2.1.1 Design of test setup:	31
2.1.2 Stress-strain behavior of single-layered PSA:	33
2.1.3 Creep response of single-layered PSA:	34
2.1.4 Stress-strain and creep response of double-layered PSA:	34
2.1.5 Optical <i>In-situ</i> observation of the bonding interface during debonding process:	34
2.1.6 Failure analysis in PSA bonding interface after debonding process:	35
2.2 Modeling the debonding process of PSA bonded assemblies	35
2.2.1 Stress-strain mechanistic model:	42
2.2.2 Creep behavior of single-layered PSA bonded assembly:	43
2.2.3 Stress-strain and creep behaviors of double-layered PSA bonded assembly:	46
Chapter 3. Stress-Strain Response of Assemblies Bonded with Single-Layered PSA ...	48
3.1 Abstract	48
3.2 Introduction	49
3.3 Uniaxial tensile experiment	51
3.3.1 Cavitation and fibrillation:	53
3.3.2 Effects of loading rate:	55
3.3.3 Effect of bonding conditions:	56
3.3.4 Effect of surface roughness:	59
3.3.5 Effect of substrate surface free energy:	64

3.4	Predictive mechanistic model	65
3.4.1	Constitutive equation for bulk PSA:	69
3.4.2	Cavitation criterion:	71
3.4.3	Interfacial cavity growth criterion:	73
3.4.4	Total debonding force:	77
3.4.5	Simulation results:	78
3.5	Conclusion	81
Chapter 4.	Creep Response of Assemblies Bonded with Single-Layered PSA.....	83
4.1	Abstract	83
4.2	Introduction.....	84
4.3	Uniaxial creep experiment	87
4.3.1	Unique creep response:	87
4.3.2	Effect of loading stress level:.....	91
4.3.3	Effect of bonded assembly geometry:.....	93
4.3.4	Effect of substrate surface condition:	94
4.4	Creep predictive mechanistic model.....	96
4.4.1	PSA material constitutive model for creep:	99
4.4.2	Creep response of single-layered PSA bonded assembly:	103
4.4.3	Deformation and history of stress component:	105
4.4.4	Effects of loading stress level:	106
4.4.5	Effect of adhesive modulus and viscosity:.....	107
4.4.6	Effect of substrate surface roughness:	109
4.4.7	Effect of substrate surface free energy:	110
4.5	Conclusion	111
Chapter 5.	Stress-Strain and Creep Response of Assemblies Bonded with Double-Layered PSA.....	113
5.1	Abstract	113
5.2	Introduction.....	114
5.3	Experiment.....	117
5.3.1	Stress-strain behavior of double-layered PSA:	119
5.3.2	Creep of double-layered PSA:	125
5.3.3	Delamination of PSA bonded assembly:	128
5.4	Mechanistic model	130
5.4.1	Stress-strain response of double-layered PSA bonded assembly:	131
5.4.2	Creep response of double-layered PSA bonded assembly:.....	140
5.5	Conclusion	144
Chapter 6.	Discussion and Summary	145
6.1	Conclusions.....	146
6.2	Contributions.....	150
6.3	Limitations & future work	153
Appendices	156
A1:	Identification of Preferred Bonding Conditions	156
A2:	Finite Element Modeling the Effect of Carrier Layer Thickness on Deformation of Double-Layered PSA Bonded Assemblies	163
A3:	Statistical Significance.....	168

A4: Effects of Macro-Void (Air Trapped) on the Mechanical Response of PSA Bonded assembly..... 169
A5: MATLAB Code: Stress-Strain Response of Single-Layered PSA 175
A6: MATLAB Code: Creep Model of Single-Layered PSA..... 181
A7: MATLAB code: Stress-Strain and Creep Model of Double-Layered PSA..... 189
A8: Phenomenological Series Model for Creep Deformation of PSA Bonded with PSA Systems 199
Bibliography 206

List of Tables

Table 1: Simulation parameters for single-layered PSA model.....	79
Table 2: Simulation parameters	104
Table 3: Simulation parameters for simplified double-layered model	133
Table 4: Test matrix for desired fabrication conditions identification	158
Table 5: Sample model constant of double-stage model	202

List of Figures

Fig. 1. Stress-strain curves of selected single and double-layered PSA	5
Fig. 2. Creep curves of selected single and double-layered PSA	5
Fig. 3. Different stages of adhesive layer during debonding process (Lakrou al et., 1999)	11
Fig. 4. Cavities grow from defects to hemisphere local and the macroscopic stress field becomes much flatter promoting the nucleation of cavities randomly distributed along the surface (Deplace et al., 2009b)	13
Fig. 5. Schematic of five different types of stress-strain curves (Lakrou al et., 1999)....	16
Fig. 6. Image of bonding interface of late bonding stage: (A) Type I curve; (B) Type III curve; (C) Type II and Type IV curves; (D) Type V curve (Lakrou al et., 1999).....	17
Fig. 7. (a) Typical force-displacement curve of PSA system with thin carrier layer. (b) Snapshots for displacement values corresponding to the letter in (a). The carrier layer is at the boundary between two colors (Yamaguchi et al., 2008).....	20
Fig. 8. Force displacement curves at two separation speed (a) $v_1 = 10 \mu\text{m/s}$ and (b) $v_2 =$ $100 \mu\text{m/s}$ for various double-layered PSA systems with different carrier layer thickness (Yamaguchi et al., 2010).....	20
Fig. 9. Approaches for mechanical characterization of PSA bonded assembly	29
Fig. 10. Schematic of selected PSA systems	30
Fig. 11. Specimen configuration for uniaxial stress-strain and creep testing	31
Fig. 12. Specimen architecture for in-situ observation	32
Fig. 13. Test setup for stress-strain tensile and creep test.....	32
Fig. 14. Optical setup for real time in-situ real-time observation.....	33
Fig. 15. Deformation of adhesive layer during the debonding process (top); schematic of 2D block model (bottom).....	36
Fig. 16. Block numbering and model components. P_i is the pressure in the region between the block $i-1$ and i . $P_{\text{cav},i}$ is the internal pressure of the cavity. R_i is the character size of the cavity.	37
Fig. 17. Realistic schematic of cavity in the ‘block’ model.....	37
Fig. 18. Material and spatial coordinate system to describe the block motion and deformation. A point at the internal coordinate (ξ, η) is transformed in the point (x, z) in the block. λ is the elongation ratio, (X, Z) are the coordinates of the center of gravity, and X_s is the coordinate of the central position of the surface. C is the parameter characterizing the parabola (Yamaguchi et al., 2006).	38
Fig. 19. Force balance acting on the block i . X_i is the mass center of the block and X_{si} is the x-coordinate of the center point of the interface of PSA and bonding substrate	40
Fig. 20. Numerical algorithm of classic ‘block’ model (Yamaguchi et al., 2006)	41
Fig. 21. Approaches of enhanced the classic single-layered ‘block’ model.....	42
Fig. 22. 2D schematic of PSA fibril during debonding. σ_{vert} is the deviatoric stress along vertical (loading) direction in the fibril, σ is the converted stress along the fibril foot in horizontal direction (Glassmaker et al., 2007).....	43
Fig. 23. Approaches of develop a predictive model for creep response of single-layered PSA bonded assembly.....	44
Fig. 24. Approaches of develop a predictive model for stress-strain and creep response of double-layered PSA bonded assembly.....	46

Fig. 25. Schematic of double-layered model configuration.....	47
Fig. 26. Schematic of test sample: single-layered PSA bonded between two rigid substrates.....	52
Fig. 27. Surface of new PSA.....	54
Fig. 28. Surface of PSA delaminated from bonding substrate.....	54
Fig. 29. highly cavitated and fibrillated adhesive layer during uniaxial deformation process.....	55
Fig. 30. Loading rate dependent stress-strain behavior of PSA bonded assemblys (missing part of yellow plot is due to the limitation of tester frame).	56
Fig. 31. Effects of bonding pressure and post bonding aging time on the bond strength of PSA bonded assemblys.	57
Fig. 32. Effects of bonding time (10s and 30s) on the bond-strength of PSA bonded assemblys (30 psi bonding pressure and 24hrs post bonding age).	58
Fig. 33. Effects of bonding temperature (RT and 50°C) on the bond strength of PSA bonded assemblys (30 psi bonding pressure and 24 hrs post bonding age).....	58
Fig. 34. Stress-strain response of smooth glass (blue, $R_a=20\text{\AA}$), matt glass (red, $R_a=310\text{\AA}$), and rough glass (orange, $R_a=3300\text{\AA}$).....	60
Fig. 35 Surface topography of (a) smooth glass ($R_a=20\text{\AA}$); (b) matt glass ($R_a=400\text{\AA}$);...	61
Fig. 36. schematic idealization of interfacial bonding condition between PSA and substrate.	61
Fig. 37. Effect of roughness on stress-strain behavior of aluminum substrate with three different roughness (blue line, $R_a=270\text{\AA}$; red line, $R_a=715\text{\AA}$; orange line, $R_a=3100\text{\AA}$)...	62
Fig. 38. Delamination interface of PSA bonded (a) with median rough substrate (large mean free path), (b) with rough substrate (small mean free path).....	63
Fig. 39. schematic of effects of wavelength on the size of initial defect.....	64
Fig. 40. Effect of bonding substrate material.....	65
Fig. 41. Coordinate description of block motion and deformation. Coordinate (ξ, ζ) is the material coordinate and coordinate (x, z) is the spatial coordinate.....	66
Fig. 42. Force balance of i-th block. P_i is the pressure in the cavity region between block i-1 and i.	68
Fig. 43. Schematic of standard linear model.....	70
Fig. 44. Schematic idealization of interfacial bonding condition between PSA and substrate.	72
Fig. 45. Effects of interfacial friction coefficient μ on the stress-strain prediction of Yamaguchi's 'block' model.....	74
Fig. 46. Footprint of PSA fibril on glass substrate	75
Fig. 47. 2D schematic of PSA fibril during debonding. σ_{vert} is the deviatoric stress along vertical (loading) direction in the fibril, σ is the converted stress along the fibril foot in horizontal direction.....	76
Fig. 48. Simulation result of total debonding stress and its deviatoric (loading direction) and hydrostatic stress component.	78
Fig. 49. Effect of substrate surface roughness, red line is the reference modeling prediction, R_z of blue line is $0.5R_z^*$; R_z of blue line is R_z ; R_z of orange line is $2R_z^*$	80
Fig. 50. Effects surface free energy (SFE) on the stress strain curve. SFE of red line is $2\gamma^*$; SFE of blue line is $2\gamma^*$; SFE of orange line is $0.5\gamma^*$	81
Fig. 51. Schematic of single-layered PSA and loading direction	87

Fig. 52. Creep test result of single-layered PSA under 50 kPa and 70 °C.....	88
Fig. 53. Top view of the PSA/glass substrate bonding interface (from the real time observation of stress-strain test). Filaments in the fibril foot area are highlighted by circle.	90
Fig. 54. highly fibrillated adhesive layer during debonding process (from the real time observation of stress-strain test).....	90
Fig. 55. Schematic of change in hydrostatic σ_H and deviatoric σ' stress due to the mechanism of cavitation, cavity growth and fibrillation. Cavity initiation and growth decreases the geometric confinement of the adhesive layer, thus decreasing σ_H and increasing σ'	91
Fig. 56. Effects of stress-level on creep response of single-layered PSA bonded assembly at 70 °C	92
Fig. 57. Creep test result of single-layered PSA under 70 KPa and 70 °C.....	93
Fig. 58. Creep response of Thin PSA (50 μm) vs. Thick PSA (130 μm) PSA under loading conditions of 50 KPa and 70 °C.....	94
Fig. 59. Effect of surface roughness on the creep responses of PSA bonded with Aluminum substrate with different roughness (blue line, $R_a=715\text{\AA}$; red line, $R_a=3100\text{\AA}$)	95
Fig. 60. Marco-voids (air trapped) at the bonding interface during the bonding process when PSA bonded with glass substrates. The dark region is the good bonding region, where adhesive wets well to the substrate; the grey region is the poor bonding region, where the adhesive does not wet the substrate, potentially due to trapped air.	96
Fig. 61. Material coordinate and spatial coordination to describe the block motion and deformation	97
Fig. 62. Force balance of i-th block. P_i is the pressure in the region between block i-1 and i. b is the parameter to identify the actual contact length between the fibril foot and bonding substrate	99
Fig. 63. Initial stress ramp-up in creep test under different preset loading stress level. Targeted stress level is expected to apply on the test coupon within the first 3 seconds of the test.	101
Fig. 64. Modeling algorithm of single-layered creep model	101
Fig. 65. Model prediction of creep response of PSA bonded assembly based on the parameter on Table 2	105
Fig. 66. History plot of z-component of the deviatoric stress tensor and hydrostatic stress in the foot area of PSA fibril.....	106
Fig. 67. Effects of loading stress level on creep model prediction	107
Fig. 68. Effects of adhesive modulus on creep model prediction	108
Fig. 69. Effects of PSA stress relaxation time on creep model prediction	109
Fig. 70. Effect of substrate surface roughness on creep model prediction	110
Fig. 71. Effect of substrate surface free energy on creep model prediction	111
Fig. 72. Schematic of double-layered PSA system and interested loading direction	116
Fig. 73. Double-layered PSA system bonded with aluminum tabs	118
Fig. 74. Effect of carrier layer thicknesses on the stress-strain performance of PSA bonded assembly (carrier thickness: 30 vs.130 μm).....	120
Fig. 75. Different response of secondary transition when PSA on thick carrier layer ...	121

Fig. 76. Initial macro void at the bonding interface between PSA and glass substrate: (a) at the corner region; (b) at the center region.....	122
Fig. 77. Flat of thick carrier layer due to force balance by high flexible rigidity of thick carrier layer	124
Fig. 78. Global tilted of thick carrier layer due to asymmetric stress distribution	124
Fig. 79. Wrinkling of thin carrier layered due to transverse Poisson contraction	125
Fig. 80 Creep response of double-layered PSA bonded assembly	126
Fig. 81. Creep response of single-layered PSA bonded assembly.....	127
Fig. 82. Effects of carrier layer thickness on creep response of double-layered PSA bonded assembly.....	128
Fig. 83. Different failure modes of double-layered PSA bonded with aluminum substrate due to the variation of adhesion strength: (a) adhesive failure at PSA/carrier interface; (b) adhesive failure at PSA/substrate interface; (c) mixed mode failure; (d) cohesive failure	130
Fig. 84. Schematic of model configuration for double-layered PSA showing segmented carrier layer	132
Fig. 85. Modeling algorithm of double-layered stress-strain model.....	136
Fig. 86. Sample of model prediction of the simplified double-layered stress-strain model	137
Fig. 87. Stress-strain response of ‘compliant’ region (amber line) and ‘stiff’ region (red line) during the debonding process of double-layered PSA systems.....	138
Fig. 88. Schematic of simulation result of five deformation stages of double-layered PSA bonded assembly (for stress-strain deformation the dark blue represents the ‘compliant’ region and the light blue represents the ‘stiff’ region; for creep deformation dark blue represents the ‘stiff’ region and the light blue represents the ‘compliant’ region) at (a) small deformation $\epsilon=0.2$ (Region I in Fig. 80); (b) during primary transition $\epsilon=2$ (cavitation in ‘compliant’ region); (c) spring reaches maximum deformation; (d) during secondary transition (cavitation in ‘stiff’ region and fibrillation in ‘compliant’ region); (e) $\epsilon=8$ (fibrillation in both regions).....	139
Fig. 89. Modeling algorithm of double-layered creep model	141
Fig. 90. Predictive model prediction of double-layered PSA bonded assembly creep response.....	142
Fig. 91. History of zz-component deviatoric stress (true stress) in bulk adhesive of ‘stiff’ and ‘compliant’ regions during debonding process.	143
Fig. 92 Schematic of PSA bonded assembly in tester	158
Fig. 93 Effect of bonding pressure and post aging time on PSA bonded assemblies:....	160
Fig. 94 Effects of bonding temperature on the PSA bonded assembly strength and ductility	161
Fig. 95 Effects of contact time on the PSA bonded assembly strength and ductility	162
Fig. 96 Wavy carrier layer during debonding process (thin carrier).....	163
Fig. 97 Flat carrier layer during debonding (thick carrier)	164
Fig. 98 Tilted carrier layer during debonding (thick carrier).....	165
Fig. 99 Schematic of carrier layer pattern: (A) tilted (flat) carrier layer; (B) wavy carrier layer.....	165
Fig. 100 FEA result of PSA system with (a) pressure status of adhesive on thin carrier layer; (b) pressure status of adhesive on thick carrier layer.....	166

Fig. 101 FEA result of tilted carrier layer.....	167
Fig. 102 Hydrostatic stress history of elements on two side of carrier layer (thin and thick carrier).....	168
Fig. 103 Bonding interface of PSA and glass substrate.....	171
Fig. 104. non-wetted and good wetted area of PSA-substrate interface.....	172
Fig. 105. Schematic of macro-voids at the bonding interface	174
Fig. 106. (a) Perfect bonding model; (b) Bonding interface with macro-voids.....	174
Fig. 107. FEA results with 0, 5, 10, 15, and 20 % non-wetted region and the theoretical prediction	175
Fig. 108 segmental model for creep deformation	200
Fig. 109 Multi-stage creep curves at different stress level	200
Fig. 110 (a) Schematic of symmetric half of test coupon; (b) FEA model and mesh	201
Fig. 111 FEA model fit to creep curves at (a) different stress levels; (b) different loading temperature	204

Chapter 1. Introduction

PSAs are widely used in industry as bonding media because of their ease of design, affordability, low processing temperature (room temperature), environmentally friendly bonding and re-work procedures, and uniform thickness and gap filling properties, but the debonding process of a PSA bonded assembly is an intractable issue in soft material with highly confined geometry. First, PSAs are highly deformable. Under some loading conditions, ductility of some PSAs that are able to cavitate and fibrillate during the debonding process can be more than 15 times their initial adhesive thickness. Second, stress-strain and creep response of highly ductile PSA bonded assemblies contain prominent transition behavior under suitable loading conditions. This unique behavior is due to the competition between the mechanism of cavitation, fibrillation, and interfacial slippage which can cause sudden changes in the apparent stiffness of the PSA layer during the debonding process (Chun et al., 2007; Ozel et al., 2005). Third, the mechanical responses of a PSA bonded assembly are highly dependent on the surface conditions, such as surface free energy and surface roughness, of the bonding substrate which it bonds to. Accordingly, a proper constitutive model for a PSA bonded assembly should always include the effects of substrate surface conditions.

One example of the PSAs application is bonding the liquid crystal display (LCD) panel and polarizing film in the monitor assembly (Shon et al., 2003; Chun et al., 2007; Lin et al., 2015). The deformation and degradation of the PSA layer can cause the edge of the polarizing film to shrink and misalign with the edge of LCD cell, then resulting in light leakage (backlight bleed). Light leakage causes uneven brightness of the screen

and is considered as a major failure mode of LCD module. Another application of PSA is to bond a heat sink to a power component for heat dissipation. Deformation and degradation of the PSA layer also leads to a decrement in the heat dissipation rate from the power component to the heat sink, reducing the performance of the cooling system (Eveloy et al., 2004). Understanding the mechanical behavior, failure modes and mechanisms of PSA bonded assembly are the keys to comprehend the lifetime and the reliability of PSA bonded assembly in a product under complex loading conditions during their life cycle.

The mechanical performances of PSA bonded assemblies are mainly characterized by the industry standard test, such as peel, shear and tack (Sun et al., 2013), but these widely recognized test methods are not able to fully describe mechanical performance of the PSA bonded assembly in field applications. This can be the case of probe tack test; such test describes the stress-strain performance of a PSA bonded assembly with short-term bonding process (short contact time and no post-bonding aging). Despite, in most of applications, the PSA bonded assemblies have been stored for a certain period before they are use in the field. Therefore, the tackiness metric is enough to describe the performance of the PSA bonded assembly with short-term bonding process, such as the quick note and medical tape, but not the best metric for evaluating the assembly strength of the PSA bonded assemblies with long-term bonding and storage, i.e. product with self-storage in warehouse. The uniaxial test method presented in this dissertation study provides an opportunity to comprehend the mechanical performance of PSA are bonded assemblies from another perspective.

1.1 Background and motivation

With the increase of PSA popularity and application in the electronics industry, the concerns in mechanical performance and reliability of PSA bonded assemblies increased. PSAs normally show superior performance in the shear direction. However, they are more vulnerable to loading in the tensile direction. Many studies have focused on the tack, shear and peel performance of PSAs, but limited attention has been paid to the evaluation and prediction of uniaxial stress-strain and long-term creep performance of PSA bonded assemblies. Due to the complexity of debonding mechanisms of PSA bonded assembly, three major factors are required for mechanical characterization of PSA bonded assembly. First, identifying loading conditions based on the operating conditions that a product is expected to experience throughout their lifecycle. Second, the PSA configurations. PSAs are available in various configurations; some systems have sandwich structure with adhesive layer on both sides of a carrier layer; while some are available as a single-layered adhesive without a carrier film. Third, the surface properties of the bonding substrate. Substrates with different surface free energy and surface roughness can significantly influence the mechanical performance of PSA bonded assemblies. The mechanical performance of a PSA bonded assembly will also be influenced by the bonding conditions (Nakamura et al., 2012; Sun et al. 2013), that are bonding pressure, bonding temperature, bonding time and post-bonding aging time.

The primary motivation of this dissertation is to facilitate a durability of assessment of PSA bonded assemblies that experience out-of-plane loadings due to the degradation and warpage of the bonding substrate during field application. In a broader sense, a thorough understanding of the stress-strain and creep behavior of PSA bonded

assemblies. Then based on the empirical finding to develop a mechanistic model for stress-strain and creep response of PSA bonded assembly. Such understanding and mechanistic model is useful to: i) guide product design for choosing suitable combination of PSA and substrates and minimizing the premature delamination of PSA bonded assemblies; ii) become a virtual testing method to supplement physical testing; and (iii) become a virtual tool for real-time prognostic health management (PHM). By continuously re-calibrating this model by using real-time in-situ data, such as strain, loading stress and temperature, the tune ‘digital twin’ can provide updated residual life of such adhesive assembly in real time.

1.2 Problem statement

Preliminary studies indicate that the mechanical responses of PSA bonded assemblies are complex and unique with multiple phases. Interaction of cavitation, fibrillation and interfacial slippage mechanisms during the debonding process can result in multi-transition and multi-phase uniaxial stress-strain and creep response, as shown in Fig. 1 and Fig. 2. The unique multiphase mechanical response is only observed in the assemblies bonded with highly ductile PSA systems. Assemblies bonded with less ductile PSAs delaminates soon after it reaches maximum stress in the stress-strain test, as shown in green line in Fig. 1.

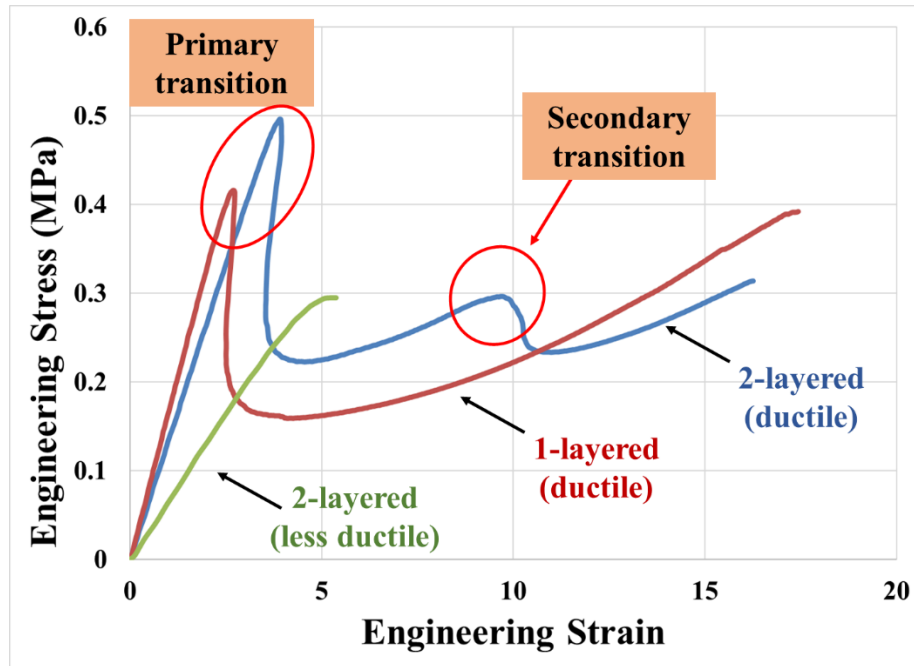


Fig. 1. Stress-strain curves of selected single and double-layered PSA

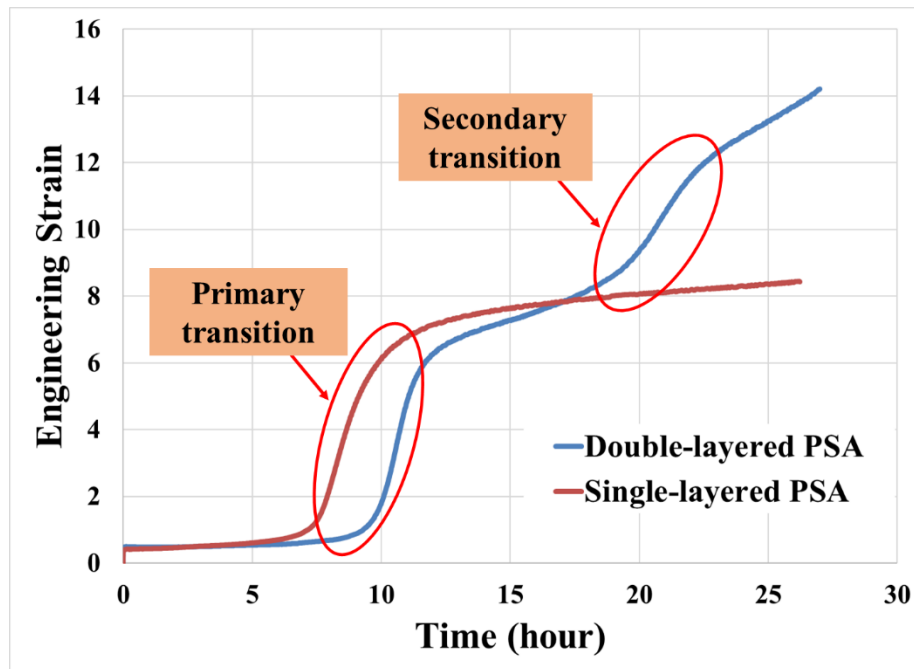


Fig. 2. Creep curves of selected single and double-layered PSA

Additional phases and transitions in the stress-strain and creep curves of the selected double-layered PSA system are caused by sequential cavitation and fibrillation in the different layer of PSA in the multilayered PSA system when there is carrier layer

presented (Yamaguchi et al., 2012). For different combinations of PSA systems and bonding substrates, these transitions can cause an overall softening in its tensile strength or significant decrement in its creep resistance. The stress relaxation and transition of PSAs' material properties during their deformation are rarely included by the conventional constitutive models that are used to describe the mechanical behaviors of polymeric materials. Debonding mechanisms mentioned above are also highly dependent on the bonding substrate surface conditions (surface roughness and surface free energy). Every time, a new combination of PSA and substrate is used, the mechanical response of the assembly can change dramatically. Therefore, when characterizing the mechanical behavior of PSA bonded assemblies, the PSA/substrate combination should always be treated as a single entity. A proper constitutive model for PSA bonded assemblies must include the effects of substrate surface properties. Consequently, the complexity of the mechanical behaviors of PSA bonded assemblies and the lack of modeling techniques on the corresponding mechanical response motivate the study of developing a predictive mechanics model. This model aims to predict the unique behaviors of the stress-strain and creep responses of the PSA bonded assemblies. The model prediction can be used as constitutive models to describe the mechanical behavior of different PSA and substrate combinations under various loading conditions.

An insightful investigation is needed to understand the mechanical response of bonded assemblies with different PSA and substrate combinations. The following aspects of the mechanical characterization need further investigation

- The influence of bonding conditions (bonding pressure, temperature, contact time and post-bonding aging time) on mechanical performance of PSA bonded assemblies
- Effects of loading and environmental conditions on the stress-strain and creep response and potential failure modes of PSA bonded assemblies
- Effects of PSAs' configuration and substrate surface properties on the stress-strain and creep response and potential failure modes of PSA bonded assemblies
- Effects of PSAs' configuration and substrate surface properties on the failure modes of PSA bonded assemblies
- Effects of carrier layer (double-layered PSA only) on the stress-strain and creep response of PSA bonded assemblies
- Effects of carrier layer (double-layered PSA only) on the failure modes of PSA bonded assemblies

1.3 Literature review

Investigation on the PSA systems (single-layered PSA and PSA on either side of a carrier layer) are getting more focus as their popularity is fast-growing in electronics manufacturing. Based on the focuses on the bonding performance of PSA bonded assembly, these studies are classified into the following categories:

1.3.1 Debonding mechanisms of PSA bonded assembly:

Zosel (Zosel, 1985) first studied the morphological change of PSA during the debonding process of the probe-tack test. The real time observation on the bonding interface clearly shows formation of cavities and fibrillary structure due to the

excessive deformation in the adhesive layer. Formation and evolution of those structural are highly dependent on the PSA entanglement network. Change of the PSA structure shows significant effects on their mechanical performance (Zosel, 1989; Zosel, 1991). When PSA contact against an imperfect surface (as most bonding surface) leaves small air pockets where the adhesive not at contact with substrate. These pockets can be the seed of a localized deformation when a tensile stress is applied to the adhesive layer, leading to either the propagation of interfacial cracks or to the growth of cavities in the bulk that eventually evolve to a complex fibrillar structure (Zosel, 1998; Chikina and Gay, 2000; Gay 2002)

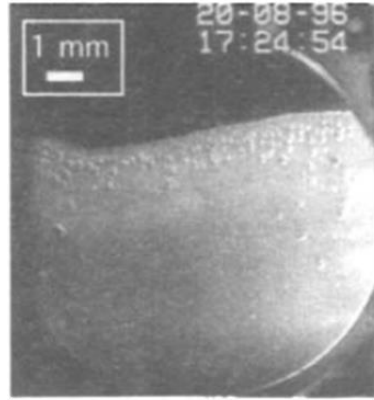
Lakroun and Creton study the morphological evolution of adhesive layer by directly observing the bonding interface through a probe tack apparatus. Their investigations indicated that formation of cavity first appeared at the interface between the adhesive and the probe after the initial homogeneous. Formation of cavities is due to the growth of hydrostatic stress in a highly geometric confined adhesive layer. Expansion of cavities release the hydrostatic stress in the adhesive, which results in reduction in the tension during the probe tack test. As the nominal strain increases, the ‘wall’ (bulk PSA) between cavities were being stretched in the direction normal to the bonding interface. Their experiments were conducted with a custom-design optical setup, which allows simultaneous acquisition of nominal stress-strain curve and deformation of the adhesive film from underneath the transparent substrate, on the MTS hydraulic testing machine. The tests results show that the stress-strain behavior in the probe tack test was directly related to cavitation. The debonding process of PSA in the probe tack test

abides by the following manner (corresponding pictures of different stages of debonding process are shown in Fig. 3) (Lakrouf et al., 1999; Creton et al., 2000):

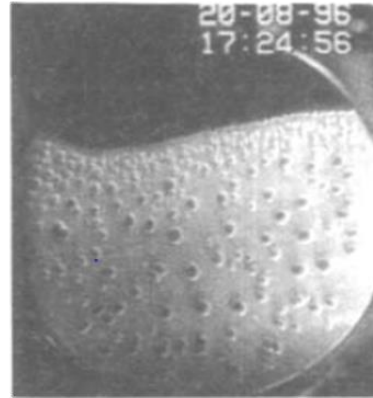
- i. Homogeneous deformation of the adhesive layer. In this phase, the force increases rapidly with displacement and no visible cavities.
- ii. Nucleation and rapidly growth of cavity at the interface between adhesive and the probe. The cavitation first happens in the region which was last brought into contact with the probe during the bonding stage and then relatively homogeneous over the whole bonding interface;
- iii. Cavities grow slowly and occupy most of the interfacial area. The length of this phase is highly sensitive to the PSA material and the conditions of bonding substrate. In Creton's study, slowly growing process takes half of the total debonding time. But for some other materials, which will be discussed later, it lasts shorter;
- iv. Growth of the cavities normal to the film and formation of a fibrillary structure. There is not obviously structural change of the PSA layer during this phase (similar to Phase iii). But the thickness of adhesive wall of the cellular structure becomes thinner.
- v. Air penetrates the voids and the walls between the cells are broken forming isolated fibrils which eventually debond from the probe (adhesive failure) or break (cohesive failure). During this stage, nominal stress decreases slowly to zero.

In the rest of the paper, Phase i is simply called as homogeneous deformation, Phase ii is called as cavitation, Phase iv is called fibrillation and Phase v is called interfacial delamination (interfacial slippage). Cavitation and expansion of cavities occurs in the

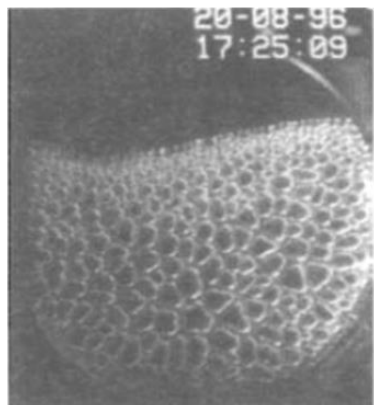
early stage of the debonding process and accompanied by material softening; fibrillation dominates the late stage of the debonding process and accompanied by strain hardening (Creton et al., 2011); interfacial delamination (interfacial slippage) determines the effective bonding area through the entire debonding process.



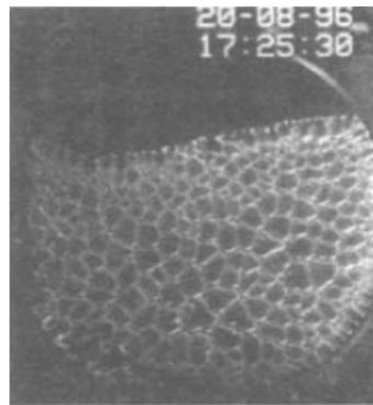
(i) Uniform deformation of the film



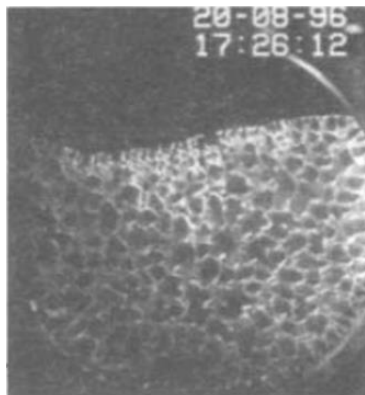
(ii) Nucleation of cavities in the bonding interface



(iii) Lateral expansion of cavities (parallel to the film)



(iv) Growth of the cavities (normal to the film) and formation of fibrillary structure



(v) Fracture of fibrils by creep or debonding of the foot of the fibril from the probe

Fig. 3. Different stages of adhesive layer during debonding process (Lakrouf et al., 1999)

According to the equilibrium of bubble dynamics (Brennen, 1995), the rapid initial expansion of cavities (right after cavitation process) induces additional hydrostatic stress in the bulk of adhesive layer (medium around the cavities). As the size of cavities increases, the rate of cavity increment decreases, the induced hydrostatic stress will reach its maximum value and then start to release due to the loss of geometric confinement. Compared to the total debonding procedure, the change of hydrostatic stress of the PSA around the cavities lasts for a relatively short period of debonding time and lead to the corresponding fluctuation in the total separation stress during debonding process. Therefore, there are multiple phases in the stress-strain curve. Two kinds of cavity shown in Fig. 4: i) a more interfacial mechanism where cavities grow as cracks, mainly along the interface; ii) a bulk mechanism where cavities grow mainly in the direction parallel to the tensile direction, and form cigars (Deplace et al., 2009b)

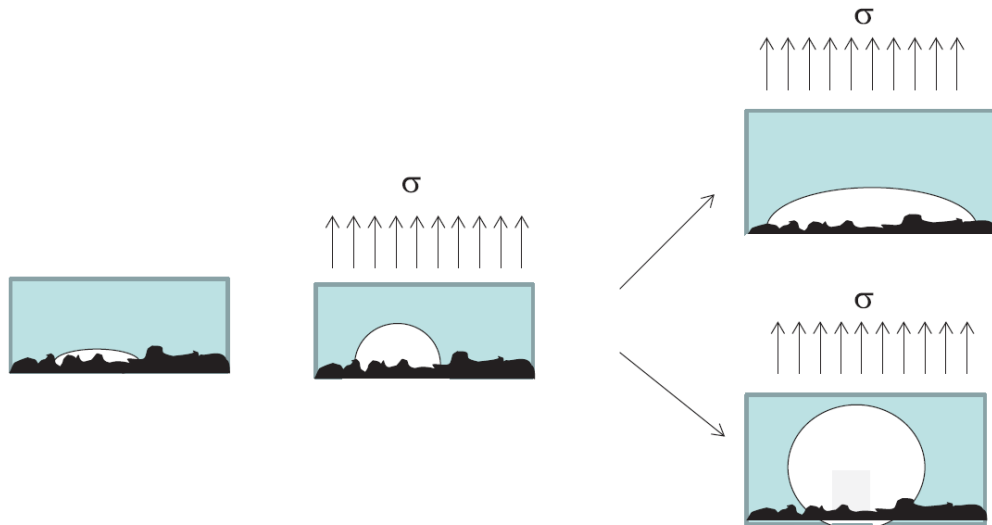


Fig. 4. Cavities grow from defects to hemisphere local and the macroscopic stress field becomes much flatter promoting the nucleation of cavities randomly distributed along the surface (Deplace et al., 2009b)

1.3.2 Effects of bonding conditions on mechanical performance of PSA bonded assembly:

A proper bonding temperature is necessary to ensure the PSA has enough flow capacity. Thus, the adhesive can make it easier to create a bond with the substrate when it is first brought into intimate contact with the adherent on a molecular scale (Vakula and Pritykin, 1991). Zosel studied the relationship between the fracture energy and the contact time through a probe tack test. The value of the adhesive fracture energy increased by an order of magnitude as the contact time increased from 0.02 to 100 s. His study also concluded that the fibrillation is incompletely developed within a short contact time (Zosel, 1992). Typically, PSA mechanical performance, such as strength, ductility and fracture energy increase proportionally to the applied stress and contact time, when the values of bonding conditions are at a relatively low level. However, assembly strength, ductility and fracture energy are saturated as the applied stress and contact time reach a critical level in the probe tack test (Creton and Leibler, 1996). Nakamura studied the effects of contact time and temperature on mechanical performance of three model adhesives by probe tack test. At room temperature, the tackiness increased as the contact time increased for most of model adhesives. The temperature dependence of tackiness shows peak tack value above room temperature and dependent of different model adhesive on temperature are various (Nakamura et al., 2011).

1.3.3 Effects of loading conditions on PSA bonded assemblies' mechanical performance:

In a peel test of PSA, the adherend energy increases with the peel angle and this dependence is separable from the peeling velocity dependence (Villey et al., 2015). Lakrouf et al. studied the effects of temperature and separation rate on the maximum stress and adhesion energy along with the probe tack tests. Their experimental results demonstrate that the physics of rate dependent mechanical behavior of PSA is believed to be the viscoelastic loss occurring in the adhesive layer (Lakrouf et al., 1999). Moreover, they also concluded that the effects of temperature on the adhesive layer is more complicated, which includes the effects on the kinetics of bonding and debonding process. According to their investigations, the nominal stress-strain curve can be classified into five different categories based on the trends seen in Fig. 5. These stress strain curves are related to the different combinations of separation rate and loading temperature. The Type I curve occurs at high temperature and low debonding rate condition; the Type II curve occurs at intermediate temperature and low debonding rate; the Type III curve occurs at low to intermediate debonding rates and high temperatures; the Type IV curve occurs at high debonding rate (except at very low temperature); and the Type V curves are observed at low temperature and high debonding rates. The corresponding shape of cavities at the bonding interface of five types curve are shown in Fig. 6. To ensure the bonding stress relaxes in the adhesive and better conforms to the topographic irregularities of the substrate surface, bonding is designed to be a very low strain rate process at small deformation while debonding by peeling is typically a high rate process. The other part of Lakrouf's investigation studies the failure

mechanisms of PSA bonded assembly and the failure locus is believed to be related to the separation rate and loading temperature (Lakrouf et al., 1999). The same phenomenon was found by Fujita et al. (Fujita et al. 1998) on their study of how the miscibility affects the peel strength of natural rubber-based PSA by 180° peel test. As the pulling rate increased, the failure mode of all tested PSA samples with different tackifier content changed from cohesive failure to interfacial, slip-stick and glassy failure. Poh and Khan carried out a systematic investigation on the effect of test rate on the loop tack, peel strength, and shear strength of natural rubber (ENR-25 and ENR50) based PSA. They found that at low testing rates, the rubber-based adhesives response is predominantly viscous and cohesive failure occurs. The cohesive failure is mainly due to the weaker internal strength rather than the bonded strength between adhesive and adherent at low separation speed, and the adhesive fails within its bulk. However, under higher testing loading, the response becomes predominantly elastic because its elastic components become significant and results in adhesion failure. Their study also showed that PSA sample strengths increased as the mechanical response changed from more viscous to more elastic (Poh and Khan, 2011).

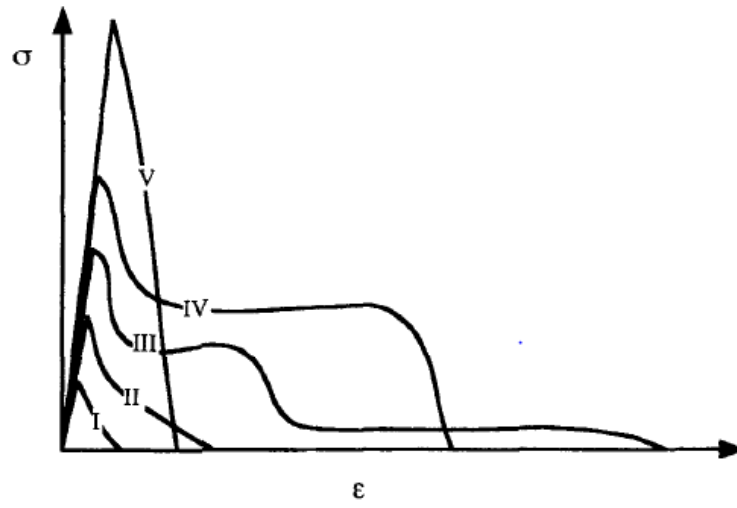


Fig. 5. Schematic of five different types of stress-strain curves (Lakrouf et al., 1999)

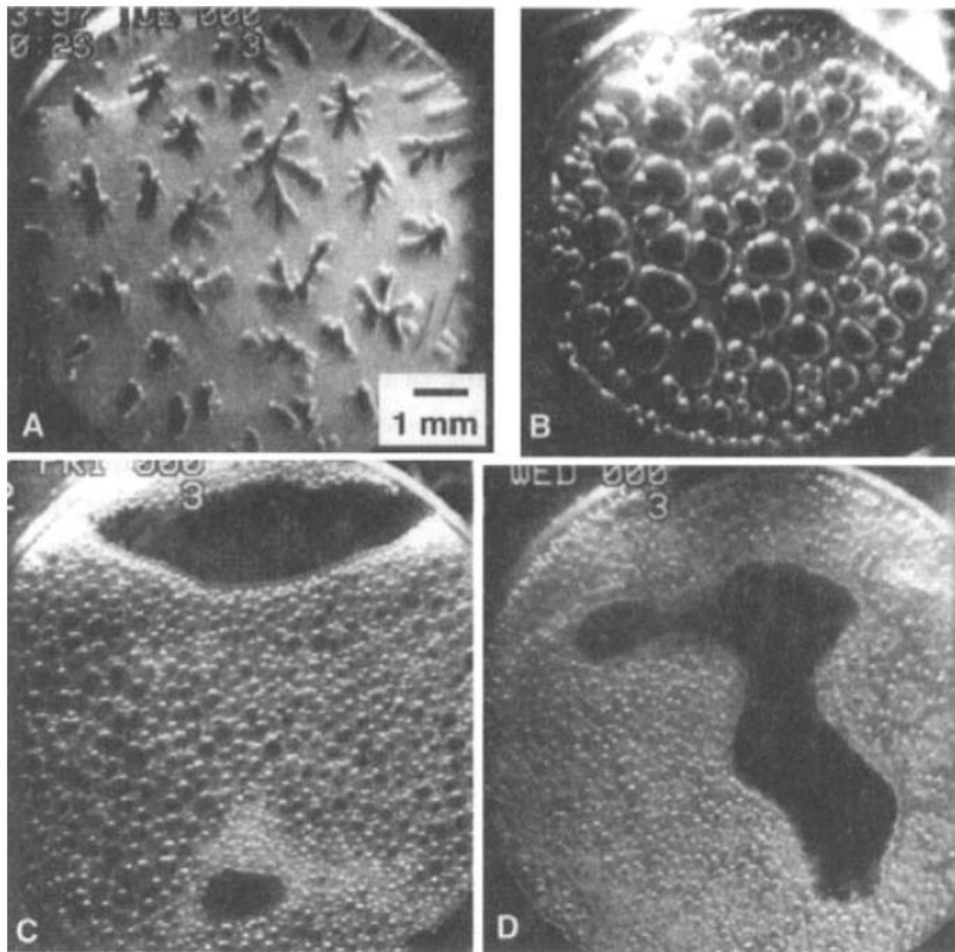


Fig. 6. Image of bonding interface of late bonding stage: (A) Type I curve; (B) Type III curve; (C) Type II and Type IV curves; (D) Type V curve (Lakrouf et al., 1999)

The temperature of PSAs field applications is usually above their glass transition region, in where, the PSAs can exhibit the maximum adhesion energy. In this temperature range, the intermolecular interactions determine the mechanical behavior of PSA (Lamanna and Basile, 2013). Creton and Leibler studied the temperature dependent of PSA tackiness. As temperature increases from T_g (glass transition temperature) to 60 °C, the adhesion energy of PSA with short-term contact time is first increases, then decreases. Meanwhile, the adhesion energy of PSA with long-term contact time decreases monotonically (Creton and Leibler, 1996). Lai et al. investigated the effect of humidity and temperature on the adhesive strength of the PSA (Flexbond 150) with Mylar film. Their study shows that the adhesive strength decreases significantly with an increase in the temperature in general. However, the sample preparation conditions, e.g., bonding pressure and contact time, are important in determining the humidity effects (Lai et al., 1985). A PSA durability study conducted by Sohn also indicates that the life time of PSA bonded assemblies decreased by one order of magnitude, after the samples were exposed to a high humidity field (Shon, 2003). Investigations on the effects of environmental conditions on PSA bonded assembly also indicates that the swelling process of moisture into the adhesive makes the failure site transition from the adhesive layer to the adhesive/adherent interface. Temiz et al. evaluated the durability of structural adhesives at very harsh environmental conditions. They exposed the samples to 100% RH conditions and 3.5% NaCl solution for 90 days (marine application). All specimens lost their bonding strength significantly

after the long-term exposure test and the SEM images of the fracture surface indicated the failure mode changed from cohesive failure to adhesive failure (Temiz et al., 2004).

1.3.4 Effects of configuration on mechanical behavior of PSA bonded assemblies:

In order to accommodate different applications and designs, PSA systems have their own configurations, including different area geometries and laminated structures. The differences for each kind of PSA system affects their mechanical performance in various ways. For example, for single-layered PSA system, under the same interfacial bonding quality, increases the PSA film aspect ratio (ratio of shortest edge to edge distance to thickness of adhesive layer) leads to significantly increase the PSA bonded assembly performance, such as peel strength, and tackiness (Kaelble, 1992). The reason behind that is as the thickness of the adhesive decreases, the in-plane deformation increases dramatically due to its thin film geometry and Poisson's effects. Therefore, enhances the accumulation of hydrostatic stress in the bulk of the adhesive layer. Thus, increasing the resistance of adhesive layer to the mechanical loads. However, as the PSA system's configuration becomes more complex, such as double-layered PSA system, the mechanical behaviors of PSA bonded assemblies are also affected by the interaction between each lamina in the system, such as flex of carrier layer and the interaction between the carrier layer and adhesive layer.

Yamaguchi investigated the debonding process of double-layered adhesive tape with an inner film as its carrier layer. In their investigation, the PSA tape is bonded with two glass substrates and the deformation of each adhesive layer is video recorded during separation (Yamaguchi et al., 2012). Unlike the single-layered PSA, which shows only one peak in its force-displacement curve, the force-displacement curve of

the PSA with a carrier layer presents a secondary peak, shown in Fig. 7(a). By comparing the force-displacement curve and the video of debonding process of PSA system, the secondary peak of this force-displacement curve is caused by the progressive cavitation and fibrillation in both adhesives layer due to the additional interface introduced by the carrier layer as shown in Fig. 7(b). Fig. 8 shows the effects of loading rate and carrier film thickness on the force-displacement curve, at the lower test rate, an increase in the thickness of the carrier layer leads to a decrease in the degree of the second transition; at the higher loading rate, this trend becomes less obviously, but the secondary transition is noticeable in all the force-displacement curves presented in Fig. 8.

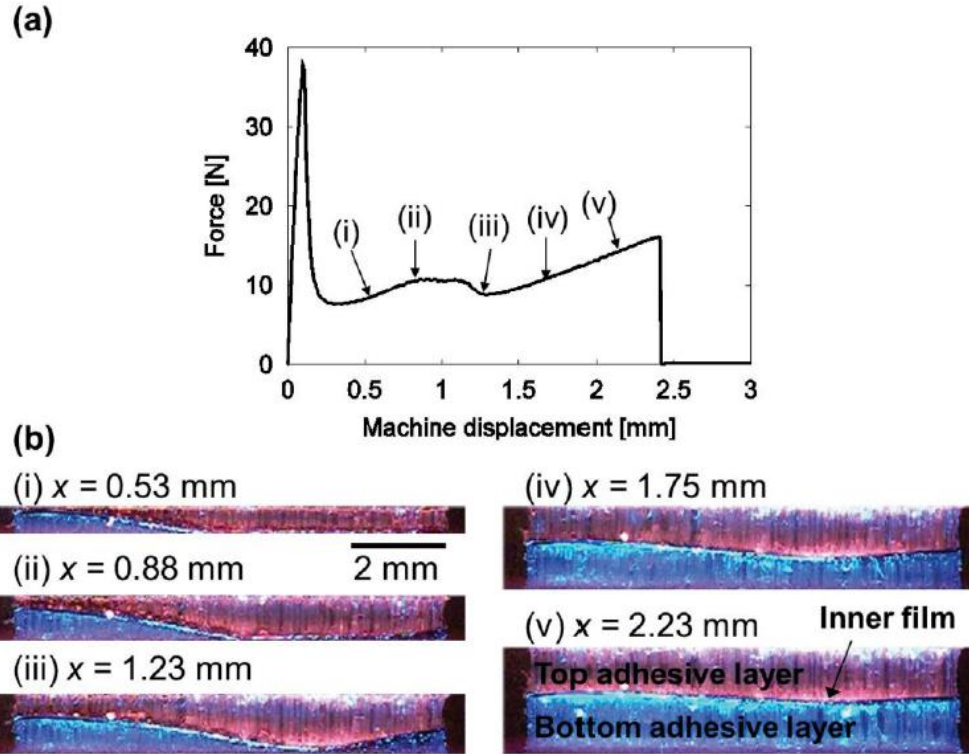


Fig. 7. (a) Typical force-displacement curve of PSA system with thin carrier layer. (b) Snapshots for displacement values corresponding to the letter in (a). The carrier layer is at the boundary between two colors (Yamaguchi et al., 2008)

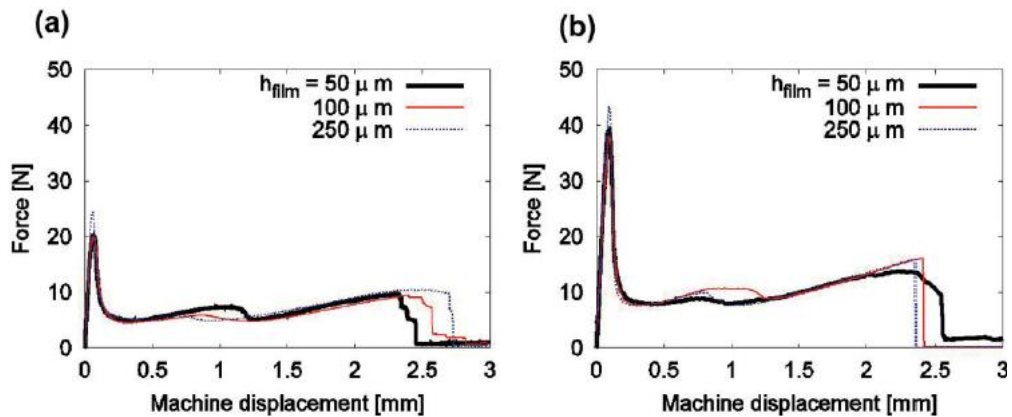


Fig. 8. Force displacement curves at two separation speed (a) $v_1 = 10 \mu\text{m/s}$ and (b) $v_2 = 100 \mu\text{m/s}$ for various double-layered PSA systems with different carrier layer thickness (Yamaguchi et al., 2010)

1.3.5 Effects of substrate surface properties on PSA bonded assemblies' mechanical performance:

The wettability of PSA on the bonding substrate is affected both by the rheology properties of the PSA itself and the surface properties of the bonding substrate. Creton and Leibler studied the relation between the roughness of the substrate surface and tackiness of the PSA. Since the substrate surface is never perfect smooth, for a specific PSA under same bonding conditions, the actual surface area of substrate is proportional to the number of asperities, and the actual contact area is inversely proportional to the applied pressure (Creton and Leibler, 1998). However, considering the flow characteristic of the PSA, the longer contact time, the more relaxed the adhesive (time dependent elastic modulus decreases, then reach a plateau region as the stress applied time increases). This manner is also reflected in the effects of after bonding aging time. Normally, longer past bonding aging time (storage conditions) lets PSA relaxed more and creates a better contact with the adherent. Therefore, they believed the bonding energy or force, measured from tack test, was directly proportional to the actual area of contact when the other debonding conditions are kept constant and the variation in contact area does not affect the debonding mechanism. Investigations on the effects of substrate properties are also focusing on how the surface energy affects the wettability. Chiche et al. studied how to control the adhesion of soft PSA on a stainless-steel surface by controlling the surface roughness. To compare the effects of the roughness, five probes with different roughness have been used. Their test results indicated that the surface roughness has dual effects on the performance of PSA. Large surface roughness can (1) decrease the stress level at the beginning of the debonding process, due to the

earlier cavitation process (Chiche et al., 2000). Steven-Fountain et al. compared the fracture toughness of PSA bonded with two different thickness Melinex backing tape through a numerical method. Their study showed that the fracture toughness of 90° peeling test increased by around 10% as the thickness of the backing tape increased from 0.34 to 0.76 mm (Steven-Fountain et al., 2002). Toyama et al. investigated the relationship between the surface energy of adherends and PSA adhesion. The difference between surface energy of PSA and adherend has significant effect on the adhesion. Optimal bonding strength achieves when the surface energy of adherend is slightly higher (20% to 30%) than the PSA surface energy (Toyama et al., 1973). Sohn and Yang studied the adhesion and peel strength between PSA and seven different polymeric films, whose surface energy varies from 35 to 72 mJ/m² (Sohn and Yang, 2003). For creating different value surface energies to fill the band gap some surface treatment methods, such as Corona treatment (Sun et al., 1999), were introduced to modify the surface energy of some polymeric film. The test results in Sun's studies showing that the peel strength is proportional to the film surface energy under different peel rates. Besides that, the peel performance of the samples with higher surface energy are found to be more dependent on the peel rate. Kowalski et al. conducted similar study on understanding the role of surface energy on bonding performance. Their investigation found that increased the surface energy from 20.5 to 42.9 mJ/m² increased the tackiness by about 300–700%, but a higher surface energy, 65 mJ/m², reduces the adhesion (Kowalski and Czech, 2013). One of the latest studies by Kowalski indicates that increasing the surface roughness of bonding substrate could either enhance or decrease the tack performance depending on the thickness and the crosslinker

concentration of the PSA (Kowalski and Czech, 2015). They concluded that the tack of PSA decreases as the substrate surface roughness and PSA crosslinker degree both increases. Chiche et al., investigated the tack performance of PSA bonded with stainless probe with five surface roughness. Their study indicated that the rougher surface results in deeper groove that can i) increase the size of air trapped during the contact stage; ii) alter the stress distribution near the surface in such a way that more spots are under residual tension stress. The amplitude of roughness plays an important role in the interfacial cavitation between PSA and substrate (Chiche et. al., 2000).

1.3.6 Modeling mechanical response of the PSA bonded assemblies:

The complicated mechanical behavior of PSAs motivates researchers to extend the investigations from the experimental perspective to the modeling perspective for systematic studying of the debonding dynamics of the PSA systems. Mohammed et al. (Mohammed et al., 2014) used the cohesive zone in finite element model (FEM) for studying the interfacial peeling of PSA. In their study the adhesive has been defined as a viscoelastic material and its interfacial properties was represented by a cohesive zone. The material and interfacial properties for the FEM were measured directly from the probe tack test and calculated analytically from the peel and relaxation experiments. Crosby et al. estimates the adhesive performance of PSA by using a linear elastic fracture mechanics approach (Crosby et al., 1999). In their model, the evolution of radius of contact area of viscoelastic materials is defined by Hui et al. (Hui et al. 1998) with a modified Johnson, Kendall and Roberts (JKR) model (Johnson et al. 1971).

Debonding mechanism of PSA bonded assembly includes cavitation, fibrillation, and interfacial slippage. Instead of studying the debonding mechanism bonded

assemblyly, some scholar chose to understand effects of each mechanism on the performance of PSA bonded assembly separately. For example, in order to understand the effects of dense cavities on PSA, scholars started with understanding the dynamics of a single bubble in a different medium, such as a viscous medium (Brennen, 1995), elastic medium (Gent al et., 1958; Williams al et., 1965; Lin and Hui, 2004), or viscoelastic medium (Street, 1968; Everitt, 2003). The fundamental knowledge from the bubble dynamics has been applied to interpret the growth kinetic of cavities in PSA. Katerina et al., investigated the inception and deformation of single bubble placed in the filament through a finite element calculation. Both Newtonian and viscoelastic fluid were applied as material property for the filament (Katerina et al., 2004). Creton et al., correlated the occurrence of cavitation to the deformation of adhesive based on the degree of hydrostatic stress in the adhesive layer (Creton et al., 2000). Their study demonstrated that if the tensile test is under displacement control, cavitation occurs when the hydrostatic stress reaches a critical value. Yamaguchi et al., combined the different mechanism that affect the mechanical response of the PSA bonded assemblies and developed a ‘block’ model for simulating the stress-strain response of a PSA bonded assemblies (Yamaguchi et al. 2006). In order to distinguish the ‘block’ model proposed by Yamaguchi and the enhanced ‘block’ model in this dissertation, the Yamaguchi’s model is named as classic ‘block’ model thereafter. In the classic model, the adhesive layer has been divided into several smaller blocks. Each block represents a small portion of the bulk PSA. The gap between two neighboring blocks represents a cavity. During the debonding process, each block experiences the tensile stress caused by uniaxial load and transverse stress caused by the Poisson’s effect. To simplify the

modeling process, Yamaguchi assumed that each block has the geometric freedom to deform individually. The shape of each block is discriminated by a parabolic parameter, which is related to the stretch ratios and the spatial coordinate of each block. Their simulation results show that the classic ‘block’ model can effectively capture the transitions followed by the plateau region and also able to see the effects of aspect ratio of adhesive, substrate surface properties, adhesive material properties and loading conditions on the stress-strain behavior, but the limits of these models are also obvious, such as lack of cavitation criterion, oversimplified model configuration, insufficient control over the interfacial friction and improper constitutive model for bulk adhesive. Moreover, In the classic ‘block’ model, the cavities are assumed to pre-exist in the model, so cavitation initiation mechanics is not included. As a result, there is inadequate control over the threshold stress value for cavitation to occur. Thus, the primary transition in the classic ‘block’ model occurs prematurely and independent to the substrate surface properties and loading rate. Lately, Yamaguchi et al., proposed another simple model that can describe the debonding process of soft adhesive in probe-tack test. The theoretical results, such as cavity diameter, peak stress, strain at peak stress, maximum strain and adhesive energy are in quantitative agreement with the experiments, but the full stress-strain curves generated by the model only agreed with limited empirical results (Yamaguchi et al., 2018)

1.4 Research gaps and Objectivities

Past studies focused more on the mechanical performance of single-layered PSA systems. However, resources on the configuration of double-layered PSA system and the uniaxial creep behavior are limited. Additionally, the complex stress-strain and

creep response of single and double-layered PSA bonded assemblies cannot be adequately described by the conventional constitutive models. Therefore, the research gaps for this topic are summarized as:

Research gaps in experimental investigations:

- i) Stress strain behavior: lack of empirical investigations on the uniaxial tensile performance of PSA bonded assembly with long-term post-bonding aging;
- ii) Creep behavior: lack of literatures on the uniaxial tensile creep performance of PSA systems;
- iii) Effects of macro-void (air trapped) at the bonding interface on the stress-strain and creep performance of PSA bonded assemblies are not fully understood;
- iv) Effects of carrier layer in the double-layered PSA system on the stress-strain and creep behavior are not fully understood.

Research gaps in mechanistic modeling of PSA bonded assembly:

- i) The classic stress-strain ‘block’ model has no control over the nucleation of bulk and interfacial cavities.
- ii) The classic stress-strain ‘block’ model has insufficient control over the interfacial interaction, e.g. interfacial cavity growth and interfacial slippage between the adhesive and substrate.
- iii) There is no mechanistic model for uniaxial creep behavior of single-layered PSA bonded assembly.
- iv) There is no mechanistic model available for uniaxial stress-strain and creep behavior of double-layered PSA bonded assembly.

The objective of this dissertation study consists of two parts and listed as below:

Experimental investigations to understand influence of key fabrication and loading conditions on the unique response of rigid to rigid substrate bonded by PSA:

- i) tensile stress-strain test on single and double-layered PSA bonded assemblies with extended post bonding aging time
- ii) creep test on single and double-layered PSA bonded assemblies with extended post-bonding aging time
- iii) effect of substrate surface properties (surface free energy and surface roughness) on stress-strain and creep behavior of PSA bonded assemblies
- iv) effects of carrier layer (double-layered PSA) on the stress-strain and creep response of PSA bonded assemblies
- v) relationship between the size of initial interfacial macro-voids (due to air trapped) and bond strength
- vi) relationship between the size of micro (due to surface roughness) defects and the bond strength

Predictive mechanistic model for virtual testing and prognostic health management of PSA bonded assemblies:

- i) proper constitutive model for bulk PSA
- ii) cavitation criterion of bulk and interfacial cavity
- iii) cavity growth criterion of interfacial cavity
- iv) non-monotonic dependent on the bonding substrate surface properties
- v) develop mechanistic model to capture the uniaxial creep deformation of single-layered PSA bonded assemblies

- vi) develop new model configuration for capturing the additional transition and phases in the stress-strain and creep responses of double-layered PSA bonded assemblies
- vii) develop new model algorithm for capturing the effects of carrier layer on the stress-strain and creep response of double-layered PSA bonded assembly

Chapter 2. Approaches of Dissertation

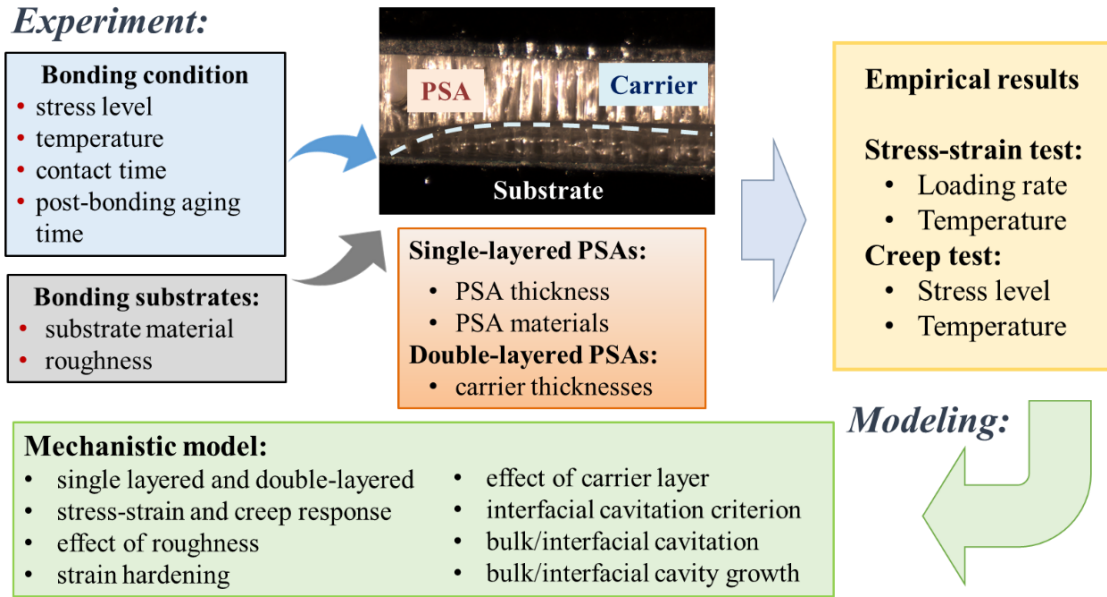


Fig. 9. Approaches for mechanical characterization of PSA bonded assembly

Fig. 9 shows the approaches for this dissertation study that consist of two phases. Phase I focuses on the empirical investigation on different kinds of PSA systems. Study focuses include effect of loading conditions (loading stress, strain and temperature), effects of PSA material, effects of substrate surface properties (surface free energy and surface roughness), and effects of PSA configuration (aspect ratio of adhesive layer and flexural rigidity of carrier layer) Phase II focuses on developing a predictive mechanistic model to evaluate the mechanical behavior of PSAs/substrate at different operating conditions. This model can perform virtual tests on the PSA, which can generate stress-strain and creep constitutive model for single and double-layered PSA systems. The empirical results generated from Phase I are used as fundamental basics for developing and calibrating the mechanistic model in Phase II.

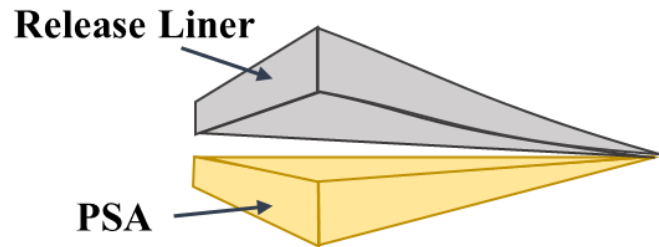
Three kinds of PSA systems with different configurations and three kinds of bonding substrates will be investigated in this dissertation study:

PSA configuration 1: single-layered PSA with adhesive layer only (two adhesive thickness), Fig. 10 (a).

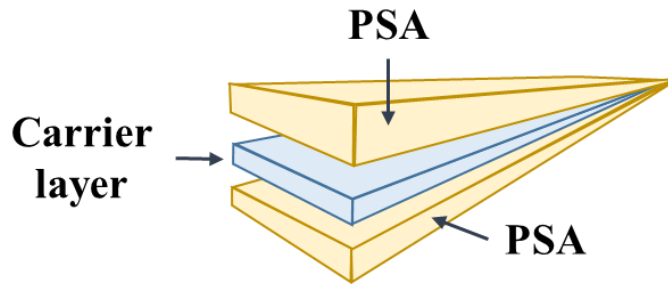
PSA configuration 2: double-layered PSA (three carrier layer thickness), Fig. 10 (b).

Carrier materials: polyolefin foam and PET film.

Bonding substrates: Aluminum, glass and glass coated with black mask.



(a) Schematic of single-layered PSA (with release liner)



(b) Schematic of double-layered PSA (without release liner)

Fig. 10. Schematic of selected PSA systems

2.1 Mechanical testing on PSA bonded assemblies

The task in this phase includes: tensile stress-strain and creep tests with different selected loading conditions, real time *in-situ* observation of the bonding interface

during the debonding process, post-test analysis of the failure modes, and statistically significant analysis of the tests' data.

2.1.1 Design of test setup:

The configuration of the test coupon is shown as Fig. 11. It is PSA bonded with two rigid flat substrates (simply called as PSA bonded assembly in the rest of this dissertation). T-shape tabs are designed for fitting the DMA grip. Also, the bonding substrates are changed based on the purpose of study in different phase. For example, in order to obtain the optical access onto bonding interface, the T-tab aluminum substrate will be replaced by a flat transparent substrate for the optical observation, as shown in Fig. 12. All test coupon prepared by following the protocol developed earlier in this dissertation study (detailed bonding parameters selection and bonding processes are discussed in Appendix I). Different substrate materials and surface preparation are used to investigate the effects of surface energy and surface roughness on the mechanical behaviors of PSA bonded assemblies.

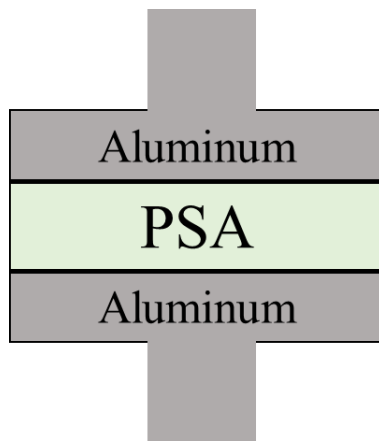


Fig. 11. Specimen configuration for uniaxial stress-strain and creep testing

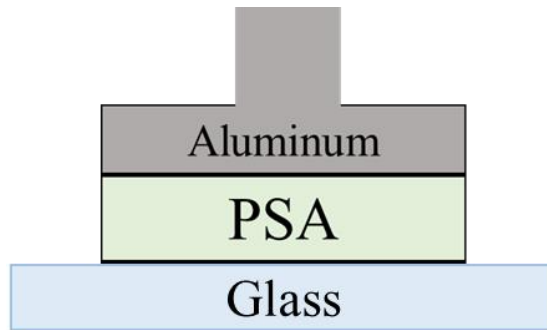


Fig. 12. Specimen architecture for in-situ observation

As shown in Fig. 13 and Fig. 14, there are two different test setups for this study. The one shown in Fig. 13 is for uniaxial stress-strain and creep tests; the other one is for the optical real time *in-situ* observation. The test setup for tensile stress-strain and creep test is very straight forward. Test coupon mentioned above is directly mounted on the DMA by gripping its two ends. The deformation process of the PSA system is also recorded by a video camera from the side.

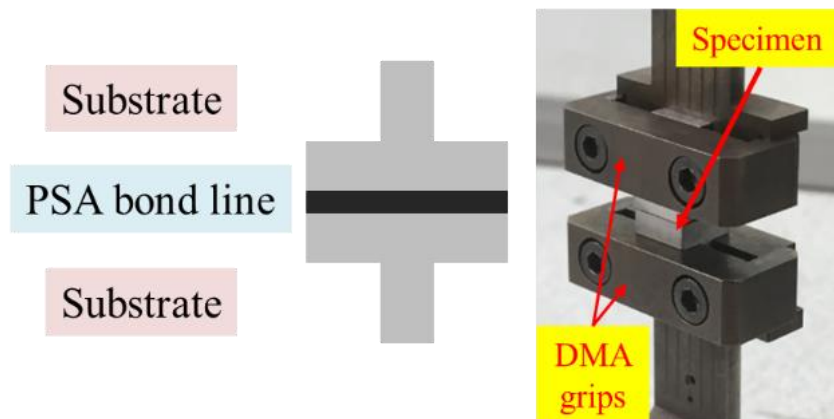


Fig. 13. Test setup for stress-strain tensile and creep test

Fig. 14 is the test setup for optical observation; the white block with open square window on the top and extended arm on the bottom is designed to work as an observation station. Similar to T-tab aluminum substrate, when testing, the extended arm of the block setup is gripped by the DMA lower arm. The configuration of test

coupon for real time observation is different from those for uniaxial tensile tests. In order to obtain the optical access to the bonding interface, one side of the PSA is bonded with a thin flat transparent glass substrate, as shown in Fig. 12. Area of the glass substrate is larger than the area of open window on the top of the block setup. Therefore, when the sample being pulled from the side bonded with the aluminum T-tab, the transparent glass substrate on the other side is mechanically locked by the open window due to the difference in area. During the real time observation, a 45-degree mirror system is secured inside the block setup for providing a horizontal view of the bonding interface. To better compare the real time morphological evolution of the bonding interface and the stress-strain behavior, a microscopic video camera system is used for recording the debonding process through the 45-degree mirror system.

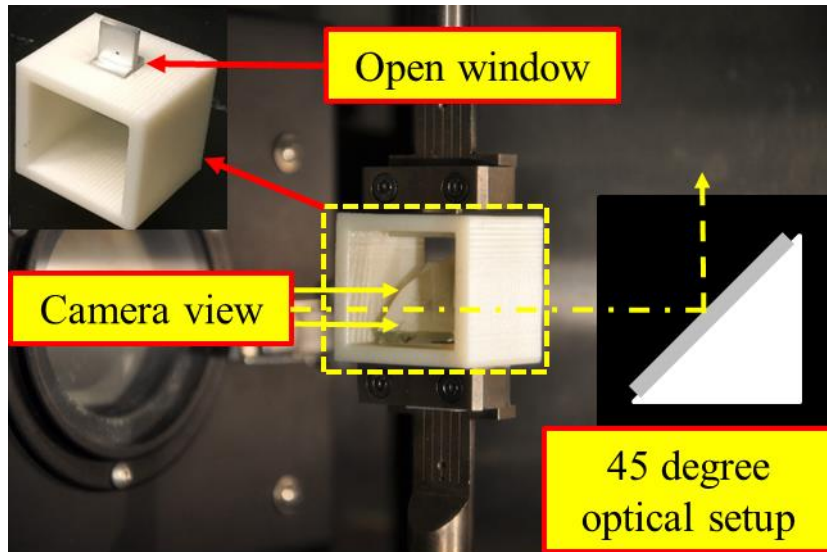


Fig. 14. Optical setup for real time *in-situ* real-time observation

2.1.2 Stress-strain behavior of single-layered PSA:

In this part, the stress-strain behaviors of single-layered PSA systems are investigated. PSA bonded assembly parameters include the thickness of adhesive layer,

substrate surface roughness and substrate surface free energy (substrate material). Tensile testing parameters including the separation rate and loading temperature. Supplementary tests are required to measure the surface free energy of selected substrates.

2.1.3 Creep response of single-layered PSA:

In this part, the uniaxial creep performances of single-layered PSA systems are investigated. The PSA bonded assembly parameters including the thickness of adhesive layer, substrate surface roughness and surface free energy. The testing parameters including the loading stress and loading temperature.

2.1.4 Stress-strain and creep response of double-layered PSA:

In this part, the stress-strain and creep performances of double-layered PSA system are evaluated. The double-layered PSA bonded assembly parameters including the thickness of carrier layer, surface free energy, and surface substrate roughness. The testing parameters including the loading stress level, rate and temperature.

2.1.5 Optical *In-situ* observation of the bonding interface during debonding process:

For single-layered PSA system, a real time *In-situ* optical observation on the bonding interface during the debonding process is conducted for understanding the deformation in the bulk of the adhesive layer and at the interface between the adhesive and substrate.

For double-layered PSA system, a real time *In-situ* optical observation on the side of the PSA bonded assemblies during the debonding process is conducted for understanding the deformation of the adhesive layer and flex of the carrier layer.

2.1.6 Failure analysis in PSA bonding interface after debonding process:

In this part, the bonding interface of the delamination (fail) sample is investigated to understand the effects of combinations of PSA/substrate, substrate surface properties, and loading conditions on the failure mode of PSA bonded assemblies. Therefore, to correlate the bonding performance to the failure mode.

2.2 Modeling the debonding process of PSA bonded assemblies

Predictive mechanical model for the stress-strain and creep behaviors of PSA bonding assemblies are carried out in this part of study. The model based on the classic ‘block’ model. Modeling approach is a simplified 2D approximation, as shown in Fig. 15. In the classic ‘block’ model, each block represents the bulk adhesive and the gap between two neighboring blocks represent the cavity (Yamaguchi et al. (2006)). The substrate is treated as rigid body, since its modulus is much larger than the PSA’s modulus. In the model representation, the blocks are visually separated by dummy cavity (gap between two neighboring blocks). However, they initially connect closely with each other by the internal pressure terms. The discrete ‘block’ model configuration provides the geometric freedom for the cavitation and fibrillation during the debonding process of PSA bonded assembly. The predictive mechanistic model is based on the mechanisms of cavitation, fibrillation and interfacial slippage. The classic ‘block’ model has some intrinsic limitations that are discussed in this paper and improvements are proposed to overcome these limitations.

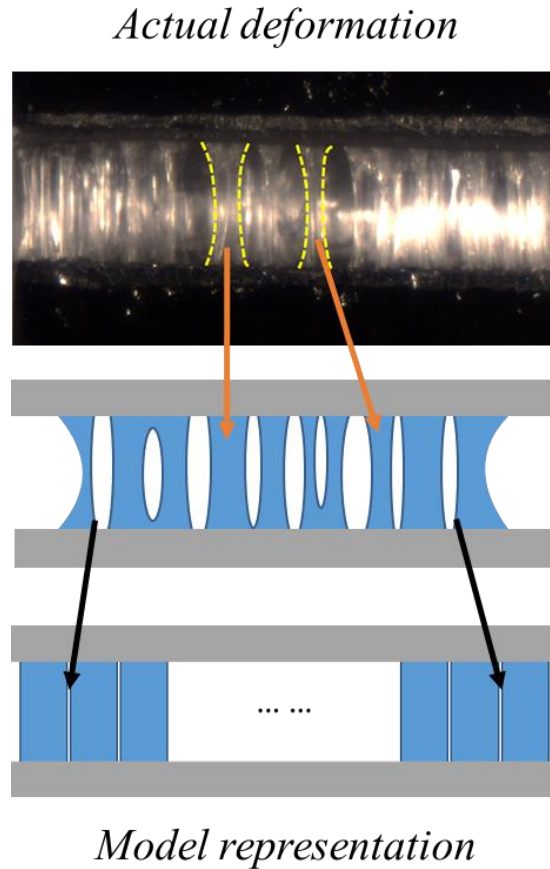


Fig. 15. Deformation of adhesive layer during the debonding process (top); schematic of 2D block model (bottom)

Fig. 16 shows the numbering of each adhesive block and the cavity. Number of blocks and cavities are pre-set in the classic ‘block’ model. P_i represents the pressure in the region between block i and $i-1$, $P_{cav,i}$ is the pressure of cavity between block i and $i-1$, R_i is the characteristic size of cavity between block i and $i-1$. It is important to note that in the model representation, two neighboring blocks are always separated by a cavity. However, this is just the simplified schematic to represent the actual initial debonding status shown in Fig. 17. The discrete model configuration can provide geometric freedom for modeling the debonding process.

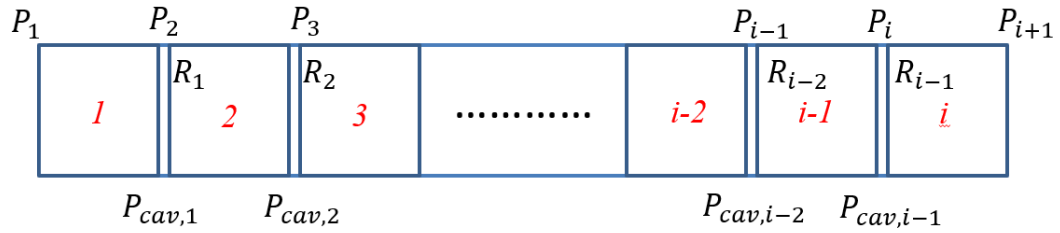


Fig. 16 Block numbering and model components. P_i is the pressure in the region between the block $i-1$ and i . $P_{cav,i}$ is the internal pressure of the cavity. R_i is the character size of the cavity.

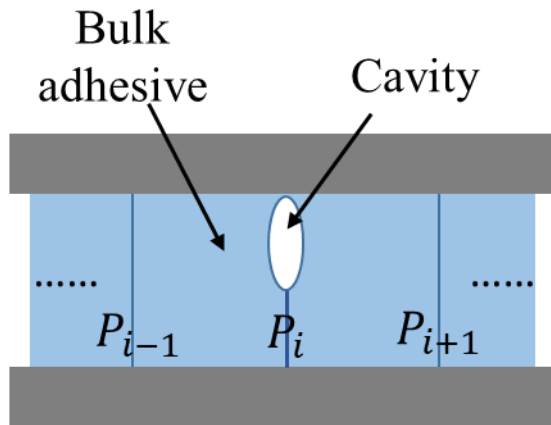


Fig. 17. Realistic schematic of cavity in the ‘block’ model

The coordinate system to describe the block motion and deformation is shown in Fig. 18 and the relation between material coordinate and spatial coordinate is describing in Equations (1) and (2).

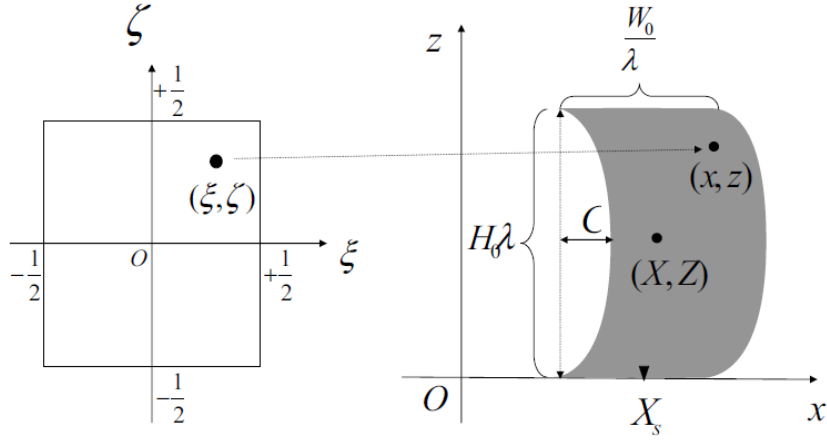


Fig. 18. Material and spatial coordinate system to describe the block motion and deformation. A point at the internal coordinate (ξ, ζ) is transformed in the point (x, z) in the block. λ is the elongation ratio, (X, Z) are the coordinates of the center of gravity, and X_s is the coordinate of the central position of the surface. C is the parameter characterizing the parabola (Yamaguchi et al., 2006).

$$x = X_i + \frac{W_0\xi}{\lambda} + \frac{C_i}{3}(1 - 12\zeta^2) \quad (1)$$

$$z = H_0\lambda\left(\zeta + \frac{1}{2}\right) \quad (2)$$

where C_i is the parameter characterizing the parabola.

Based on Eqs. (1) and (2) and by expressing (ξ, ζ) with (x, y) the velocity at the material point is given by

$$v_x = \dot{X}_i - \frac{\dot{\lambda}}{\lambda^2}(x - X_i) + \frac{\dot{C}_i}{3}\left(\frac{\dot{\lambda}}{\lambda} - \frac{\dot{C}_i}{C_i}\right)\left[1 - 12\left(\frac{z}{\lambda H_0} - \frac{1}{2}\right)\right] \quad (3)$$

$$v_z = \frac{\dot{\lambda}}{\lambda}z \quad (4)$$

The velocity gradient tensor for the thin film adhesive is calculated as:

$$\frac{\partial v_x}{\partial x} = -\frac{2\dot{\lambda}}{\lambda}$$

$$\begin{aligned}\frac{\partial v_x}{\partial z} &= -\frac{8\xi\dot{C}}{\lambda(t)} \\ \frac{\partial v_z}{\partial x} &= -\frac{8\xi\dot{C}}{\lambda(t)} \\ \frac{\partial v_z}{\partial z} &= \frac{2\dot{\lambda}}{\lambda}\end{aligned}\tag{5}$$

where $\dot{C}_i/C_i \approx (\dot{\lambda}/\lambda)(L/H) \gg \dot{\lambda}/\lambda$

Given the velocity gradient, for Newton fluids, the stress is given by

$$\sigma_{tot} = \eta D - pI \tag{6}$$

where η is the viscosity, $D = \nabla v + (\nabla v)^T$

In the current problem (tensile model), the relevant stress components are σ_{xz} and σ_{zz}

that are defined in the following equations

$$\sigma_{zz} + \tau\dot{\sigma}_{zz} - \tau\sigma_{zz}\left(\frac{2\dot{\lambda}}{\lambda}\right) = G\tau\left(\frac{2\dot{\lambda}}{\lambda}\right) \tag{7}$$

$$\sigma_{si} + \tau\dot{\sigma}_{si} - \tau\sigma_{zz}\left(\frac{4\dot{C}}{H_0\lambda}\right) = G\tau\left(\frac{4\dot{C}}{H_0\lambda}\right) \tag{8}$$

Fig. 19 shows the force balance of block i and the corresponding equation is written as

$$(P_{i+1} - P_i)H_0\lambda = -2\sigma_{si}\frac{W_0}{\lambda} \tag{9}$$

The block slips at the interface if the shear force σ_{si} is large enough. Let X_{si} be the x -coordinate of the middle point of the interface between i^{th} block and of the adherend.

$$X_{si} = X_i - \frac{2}{3}C_i \tag{10}$$

The slip velocity is proportional to the stress at the inter face

$$\mu \dot{X}_{si} = \sigma_{si} \quad (11)$$

where μ is the friction coefficient at the bonding interface.

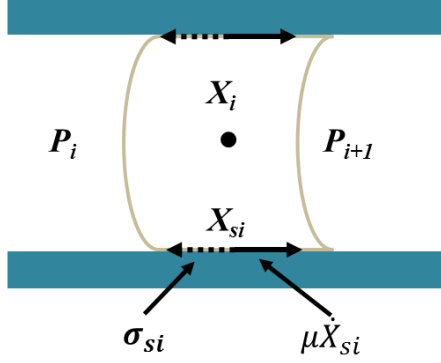


Fig. 19. Force balance acting on the block i . X_i is the mass center of the block and X_{si} is the x-coordinate of the center point of the interface of PSA and bonding substrate

In the classic ‘block’ model, the size of the cavity is defined by the difference between the distance of material point X_i and X_{i-1} and the current width of the block.

$$\pi R_i^2 = H_0 \lambda \left(X_i - X_{i-1} - \frac{W_0}{\lambda} \right) \quad (12)$$

Considering the effect of surface tension, hyper-elasticity, and viscosity the cavity expansion is written as

$$\dot{R} = \frac{R}{4\eta} \left(-P_i - \frac{2\gamma}{R_i} - \frac{G}{2} \left\{ 5 - \left(\frac{R_{0i}}{R_i} \right)^4 - 4 \frac{R_{0i}}{R_i} \right\} \right) \quad (13)$$

where η is the viscosity of adhesive, γ is the surface tension, R_0^i is the initial size for the i^{th} cavity and G is the modulus of the bulk adhesive.

Therefore, the time evolution of the system can be determined by the equation given above. The z-component deviatoric stress is determined by

$$\sigma_{zz} + \tau \dot{\sigma}_{zz} - \tau \sigma_{zz} \left(\frac{2\dot{\lambda}}{\lambda} \right) = G \tau \left(\frac{2\dot{\lambda}}{\lambda} \right) \quad (14)$$

Given σ_{zz} , the interfacial shear stress σ_{si} can be obtained by the following set of equations:

- (1) The force balance equation Eq. (9)
- (2) The cavity expansion equation Eq. (13)
- (3) The rheological constitutive equation Eq. (8)
- (4) The interfacial slippage equation Eq. (11)

The numerical algorithms for the classic ‘block’ model as shown blow:

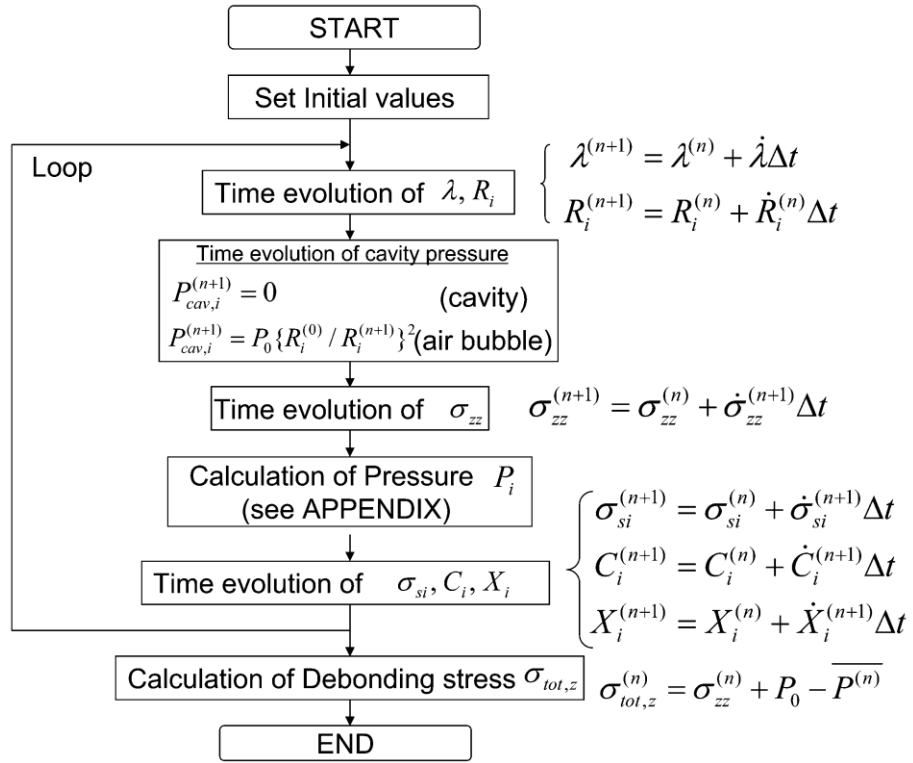


Fig. 20. Numerical algorithm of classic ‘block’ model (Yamaguchi et al., 2006)

Considering the atmosphere pressure, z -component of deviatoric stress and the hydrostatic stress inside each block, the total debonding stress is calculated by

$$\sigma_{tot,z} = \sigma_{zz} + (P_0 - \bar{P}) \quad (15)$$

where $\bar{\dots}$ stands for the average over all blocks.

It is important to note that the ‘classic’ model does differentiate the effective loading surface area between block stress component and the atmosphere pressure.

2.2.1 Stress-strain mechanistic model:

The classic ‘block’ model (as discussed before) is improved in this part of study by adding cavitation criterion (for bulk and interfacial cavity), adding interfacial cavity growth criterion, and applying proper material constitutive for bulk adhesive.

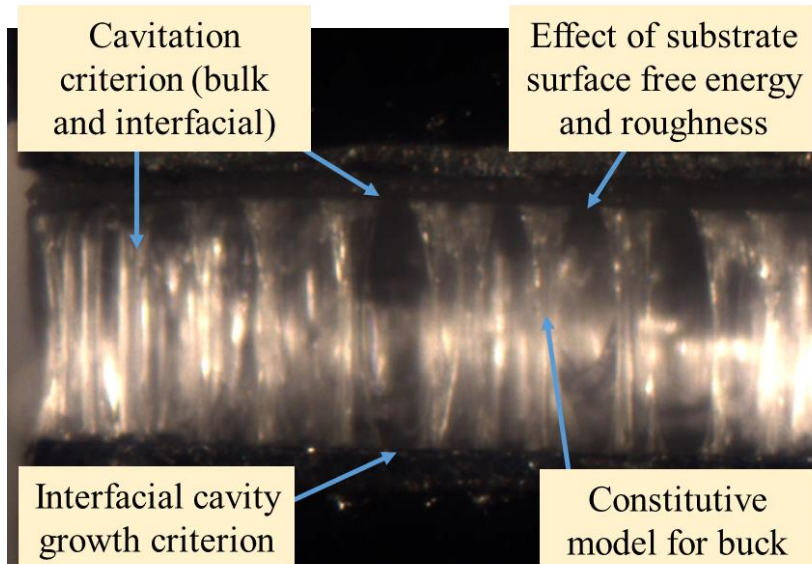


Fig. 21. Approaches of enhanced the classic single-layered ‘block’ model

Constitutive model for bulk PSA

Stress-strain behaviors of PSA systems are highly nonlinearly dependent (strain level does not linearly increase as the strain rate increases). Proper constitutive model needs to be selected for the bulk adhesive of the mechanistic model.

Cavitation criterion

In this part, a criterion of onset of the cavitation is chosen and applied to control the initiation of cavitation in the classic ‘block’ model. Cavities are still pre-seeded in the

adhesive layer. However, a critical stress value is used to control when these cavities start to deform.

Interfacial cavity growth criterion

The growth of interfacial cavity consists by lateral and vertical growth in the bulk adhesive and lateral growth at the bonding interface. Growth in the bulk is simply governed by Eq. (13). In here, the shape of the cavity is ignored. The lateral expansion at the bonding interface will expose new surface, both for adhesive and substrate. The receding of contact front is controlled by the fibril detachment criterion proposed by Glassmaker (Glassmaker et al., 2007). As shown in Fig. 22, the horizontal force to shorten the fibril foot can be related to the vertical force in the fibril body by the conservation of energy in the debonding system.

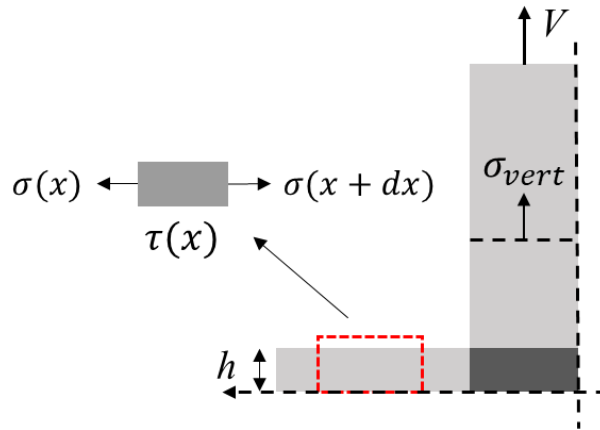


Fig. 22. 2D schematic of PSA fibril during debonding. σ_{vert} is the deviatoric stress along vertical (loading) direction in the fibril, σ is the converted stress along the fibril foot in horizontal direction (Glassmaker et al., 2007)

2.2.2 Creep behavior of single-layered PSA bonded assembly:

A creep model is developed by modified the enhanced ‘block’ model. The debonding mechanisms of the creep model are that same as the mechanisms of the

stress-strain model that are cavitation, fibrillation, and interfacial slippage. However, some modifications, as listed in Fig. 21, need to be addressed.

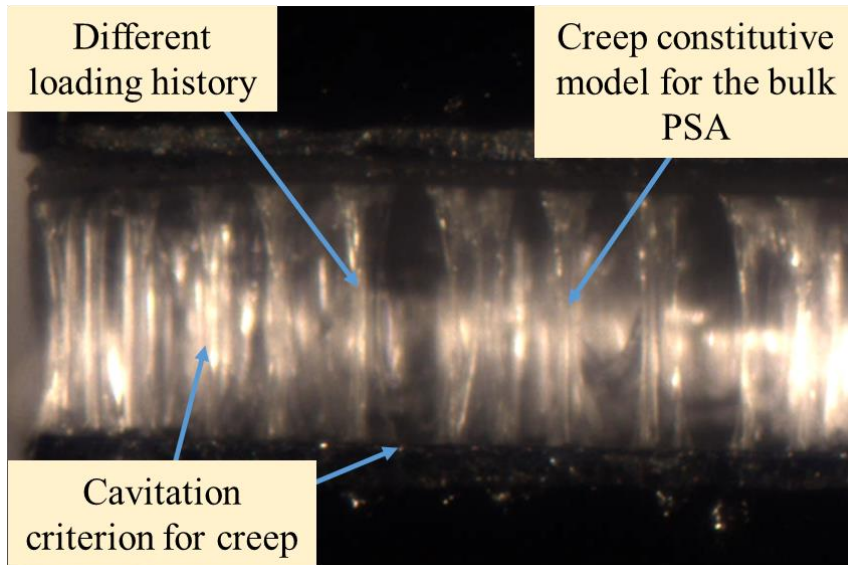


Fig. 23. Approaches of develop a predictive model for creep response of single-layered PSA bonded assembly

Stress component in creep model

During the creep test, the total applied force is controlled. But the deviatoric and volumetric stress change over time. Creep deformation is mainly driven by the deviatoric stress. Hence, as the stress change over time due to the competition of cavitation and fibrillation, the creep rate also changed.

Constitutive model for bulk PSA

In order to extend the model capacity for capturing the creep response of PSA bonded assemblies, some modifications need to be implemented due to the different loading histories of stress-strain and creep tests. The evolution of a creep model is highly dependent on the history of the stress components. Therefore, to obtain the full history of the deformation process, the initial stress ramp-up process must be included

in the creep model. Based on the different loading history, the algorithm of the creep model is also different to the stress-strain model. The algorithm of the creep model consists of displacement-controlled part (stress ramp-up) and force-controlled part (creep).

Cavitation criterion

The stress level in creep deformation is lower than in stress-strain testing under specific range of strain rate. However, plenty of cavities are still observed during the long-term creep deformation process. Therefore, in the creep model, the critical stress criterion is no longer suitable for cavity initiation. In the current stage, a strain criterion is assigned for the creep model to control when the cavity starts initiate or when the initial defects start growth. The value of the strain for creep cavitation criterion is observed from the experimental results.

Cavity growth criterion

In creep deformation, due to the huge differences in the deformation rate of the adhesive, there are two deformation regions. One is the slow deformation region, which in the bulk adhesive in the far-field from of cavities, and the other is the quick deformation region, which in the near-field of the cavities, especially when the cavity is in the early growth stage. When the cavity size is large enough, the deformation rate is similar for these two fields. Therefore, rate dependent material properties are required to assign for the adhesive in the different fields. In the current study, different relaxation times are assigned for the close field and the far field adhesive.

2.2.3 Stress-strain and creep behaviors of double-layered PSA bonded assembly:

The mechanistic models for stress-strain and creep response of double-layered PSA bonded assembly are developed by modified single-layered stress-strain and creep model. The debonding mechanisms of the creep model are that same as the mechanisms of the stress-strain model that are cavitation, fibrillation, and interfacial slippage. However, some modifications listed in Fig. 24 need to be addressed.

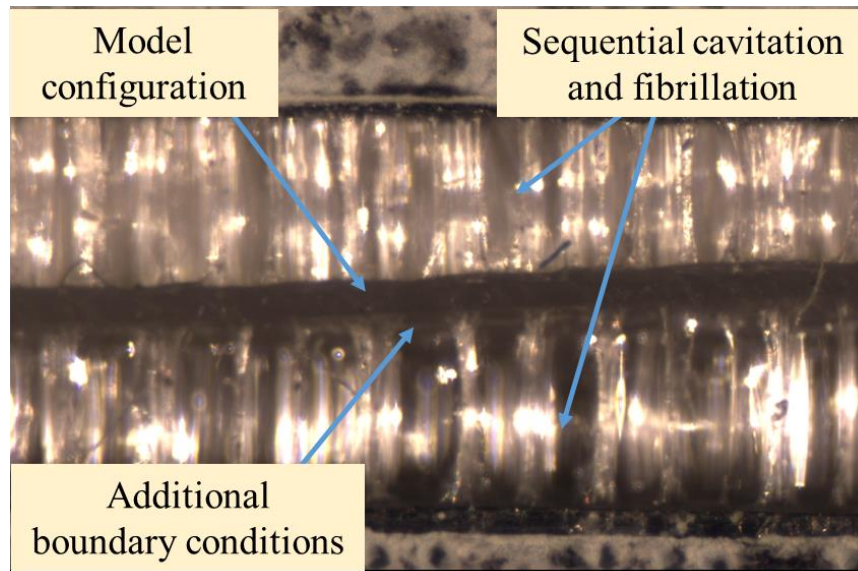


Fig. 24. Approaches of develop a predictive model for stress-strain and creep response of double-layered PSA bonded assembly

Model configuration

In order to modeling the double-layered PSA system. Two ‘block’ models are stack together, each ‘block’ model represent one layer of the adhesive. This allows independent cavitation and fibrillation in each of block system. For simplification, the carrier layer is treated as a flexural rigid element. The geometric constraints provided by the carrier layer are presented by some simple structural connector such as spring system. Schematic of double-layered model configuration is shown in Fig. 25.

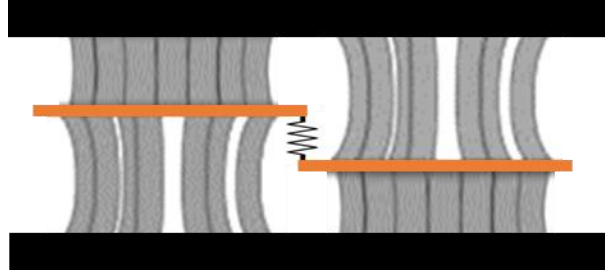


Fig. 25. Schematic of double-layered model configuration

Sequential cavitation and fibrillation

In order to obtain sequential cavitation process, two different defect density are assigned for each ‘block’ layer. Therefore, under the same loading condition, one region can cavitate faster than the other region and the spring connector, as shown in Fig. 25 allows different degree of deformation of local adhesive. So, the model enables to capture the additional transition in the stress-strain and creep curve.

Additional boundary conditions

Presence of carrier layer introduce additional boundary conditions to the adhesive layers. Since the carrier layer can flex during the deformation process, the deformation of the adhesive layer on both sides of the carrier layer must follow the local flex of the carrier layer.

Chapter 3. Stress-Strain Response of Assemblies Bonded with Single-Layered PSA

3.1 Abstract

The challenges of modeling the deformation of structures containing pressure sensitive adhesive (PSA) bonded assemblies includes the dependence of the PSA deformation mechanism on (a) PSA adhesive properties and (b) the bonding substrate's surface properties, such as surface energy and surface roughness. These parameters have significant and unique effects on the mechanical response of the bonded assembly.

This chapter is part I of two-part series on the mechanical response of single-layered pressure sensitive adhesive (PSA) bonded assemblies, where a mechanism-based predictive model, supported by empirical observation, is presented for modeling the uniaxial tensile stress-strain behavior of a single-layered PSA bonded assembly. The underlying model is based on multiple mechanisms: (i) cavity nucleation and growth in bulk adhesive material of the PSA system, as well as at the interfaces between the PSA and the substrate; (ii) fibrillation of the adhesive layer and (iii) interfacial slippage between the adhesive and the bonding substrate. This study is motivated by the fact that the resulting nonlinear stress-strain response is quite complex and unlike the conventional polymer constitutive models currently available in commercial FEA tools. Additionally, the current mechanistic models in the literature are insufficient to make reasonable predictions of the stress-strain responses of PSA bonded assemblies because: (i) they fail to correctly model the combinations of bulk and interfacial cavitation; and (ii) fail to correctly model the nonlinear viscoelastic strain hardening due to fibrillation. The proposed model is an improvement over the classic 'block'

model that has been proposed by Yamaguchi and co-workers for single-layered PSA (Yamaguchi et al., 2006). This proposed model can be used as a virtual testing tool to generate stress-strain curves for constitutive models of PSA bonded assemblies when using commercial Finite Element Analysis (FEA) tools, such as ABAQUS or ANSYS, for assessing the deformation of structures containing single-layered PSA bonded assemblies under different loading conditions.

3.2 Introduction

Single-layered PSA system has the simplest configuration among all PSA systems. They only have one layer of adhesive, no carrier layer, and no additional interfaces. The adhesive layer only interacts with the bonding substrates during the debonding process. Gay and Leibler investigated the uniaxial debonding of single-layered PSA and proposed that the stress maximum of elastic PSA depends on its elasticity and size of initial defects between adhesive and bonding substrate (Gay and Leibler, 1999). Creton investigated the individual contributions from bulk and bonding interface to the debonding stress (Creton et al., 2001). The critical energy release rate has significant effects on whether the adhesive properties are controlled by bulk or by the interface between PSA and substrate. Sosson investigated the shear failure mechanism of PSA and found that interfacial slippage can play a significant role in viscoelastic adhesion under both tensile and shear loading (Sosson et al., 2005). Mohammed used a FEA model to numerically predict peel force and the result showed good agreement with the experimentally measured peel force over the range of the peel angles considered (Mohammed et al., 2016). Kowalski and Czech measured the peel performance of PSA bonded with different materials and reported that the tack performance increases as the

surface energy of polymeric substrates increase from 20.5 to 42.9 mJ/m² (Kowalski and Czech, 2015). Glassmaker investigated the elongation of soft viscoelastic fibril and proposed a mechanical model that can estimate the actual contacting footprint of the viscoelastic fibril on the bonding substrate. Evolution of the footprint is sensitive to the interfacial shear stress and fails via a sliding mechanism (Glassmaker et al., 2008). Yamaguchi and his coworkers used a 3D imaging process to investigate the cavity expansion in the bulk and bonding interface of a PSA bonded assembly and proposed a block model that can capture some characteristic features in the stress-strain curve of single-layered PSA bonded assembly based on the mechanisms of cavity initiation, cavity growth, fibrillation, and interfacial slippage. The ‘block’ model is a simple mechanical model that can capture the primary transition followed by a plateau region in the force-displacement curve of tack test. However, due to the simplification of the geometric representation of bulk cavities and interfacial cavities in the modeling methodology, this model has insufficient control over transition initiation, delamination, and shows almost no strain hardening past the transition in its stress-strain prediction, which are not consistent with experimental results. The limitations of the model prediction are due to: (i) no proper cavitation criterion in the model – pre-existing cavities start evolving at the first step of iteration; (ii) inaccurate material model for bulk PSA – strain hardening cannot be captured properly; and (iii) insufficient control over the interfacial interaction and interfacial cavitation between bulk PSA and substrate.

The common adhesion experiments such as peel, shear, and tack have been widely studied on PSA film. However, the literature regarding the stress-strain performance of

PSA bonded assemblies after shelf storage is limited. Moderate post bonding aging at room temperature can improve the adhesion between the adhesive and bonding substrate (better wetting). And therefore, can change the stress-strain behavior, such as strain hardening before delamination, which is not common in the results from tack tests.

This chapter consists of empirical and modeling sections. In the experimental section, the effects of bonding and loading conditions on the mechanical behavior of PSA bonded assemblies are studied. Then parametric experiments are conducted, to understand the effects of substrate surface condition (roughness and material) on the stress-strain response of such adhesive bonded sample. The purpose of the empirical study is to explore the importance of different material and geometric properties on the mechanical response. This helps identify which parameters need to be included in the mechanistic model. In the modeling part, a generalized predictive mechanistic model is presented for a single-layered PSA. This model predicts the characteristic features of the stress strain curves due to effects of PSA and substrate properties. Subsequently, parametric model predictions are presented, describing the effects of surface conditions on the stress-strain response. The creep response of single-layered PSA bonded assemblies is presented in the Chapter 2.

3.3 Uniaxial tensile experiment

Tensile stress-strain test is performed at room temperature on a commercial PSA. The test sample is shown in Fig. 26. The adhesive tape (7mm x 7 mm) is placed in between two T-shaped tabs as a bonding media. The surface condition of the tab (material and roughness) and the thickness of PSA tape are varied, to examine the

effects of each parameter. The PSA bonded assembly is loaded in tension using the Dynamic Mechanical Analyzer (DMA). The displacement rate for tensile test is $2\mu\text{m/s}$. This analyzer gives access to the relationship between pulling force F (g) and displacement D (m), from which we can estimate the average stress, σ , and the engineering strain, ε , associated with the deformation of the adhesive. For simplification, engineering stress and engineering strain are used in this dissertation. The true stress and true strain are significantly different, since excessive cavitation and fibrillation results in large changes in the true cross-section and large nonlinear axial deformation. Each result presented in this study is the average value of five replicates.

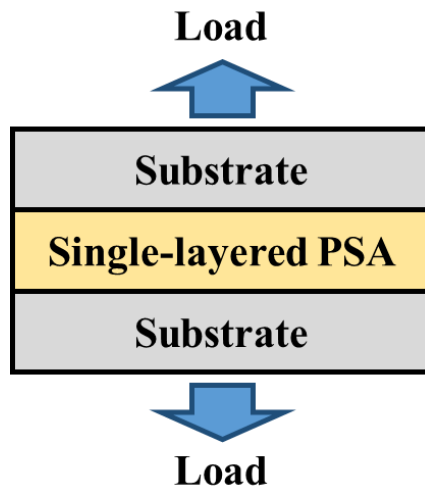


Fig. 26. Schematic of test sample: single-layered PSA bonded between two rigid substrates.

In order to verify the occurrence of cavitation and fibrillation in this selected PSA, a real time in-situ observation is conducted on the interface of PSA bonded with glass substrate by the use of a customized 45° mirror setup, as shown early in Fig. 12. When using the mirror setup, one side of the bonded assembly is replaced by a transparent glass slide.

3.3.1 Cavitation and fibrillation:

Cavitation and growth of cavities has been observed during the test and is believed to occur due to excessive stresses near the bonding surface. This is crucial to the mechanical performance of the PSA. In-situ observation of the debonding process, reveals some differences in the PSA surface before and after debonding, and provides some evidence for those processes in this PSA. Fig. 27 is the bonding surface of a new sample. In order to ensure there is not any damage on the bonding surface, this picture is taken right after the protective cover has been removed. Fig. 28 is the bonding surface of the sample after delamination. By comparing these two pictures, the delamination process can be seen to increase the roughness of the bonding surface and result in pit-like defects, which is suspected cause by the expansion of cavities, on the bonding surface. During the tensile test, the volume of the PSA layer is preserved. Therefore, there is excessive elongation of the adhesive layer, with more than 1500% strain to failure, resulting in large permanent deformation inside the bulk of the adhesive. Although the adhesive is stress free after delamination, the permanent deformation cannot be fully recovered and is manifested as pit-like defects.

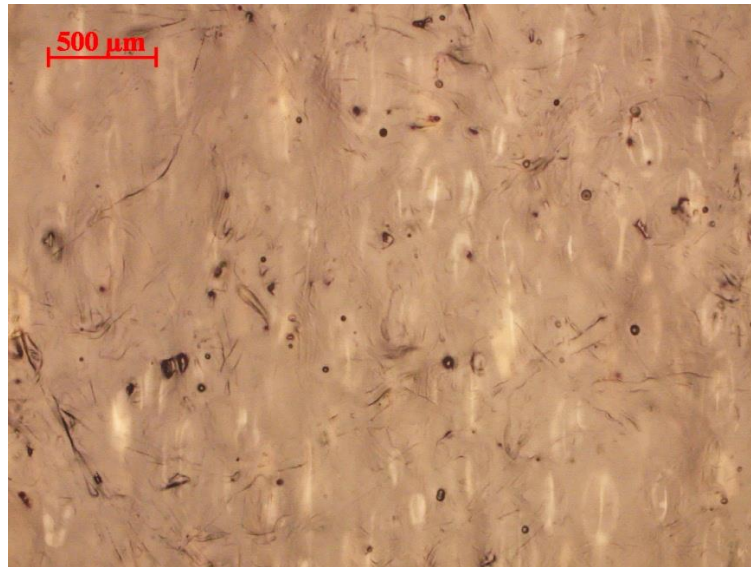


Fig. 27. Surface of new PSA

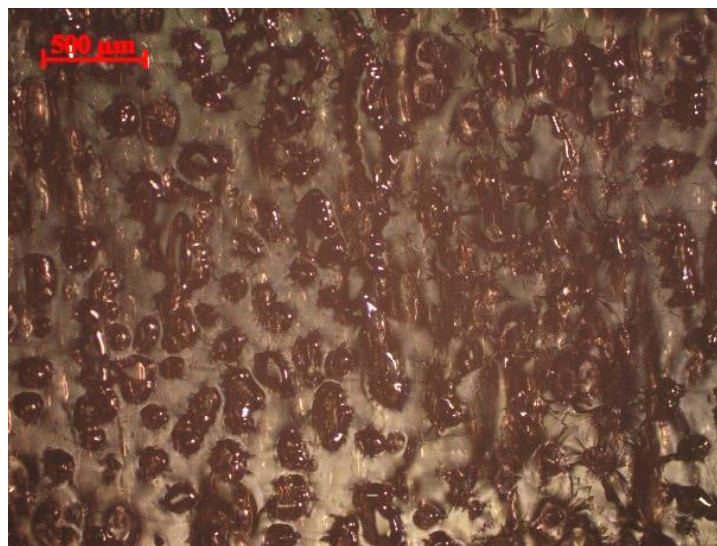


Fig. 28. Surface of PSA delaminated from bonding substrate

Noticeable change in instantaneous stiffness of the adhesive material system is detected under suitable loading rate. This phenomenon is attributed to the microstructural change in the adhesive layer during the debonding process. As shown in a side view in Fig. 29, a fibrillar structure, consisting of fibrils separated by prolate spheroidal cavities, is typically found during excessive deformation in the adhesive

layer. The material has lost its stability soon after the initiation of cavitation and therefore lost its ability to sustain such level of force. The dropping in the stress value means that the stress is relaxing, and it relaxes faster than the stress accumulated from the loading process. This results in non-convex relaxation behavior, evidenced as a drop in the stress strain curve. This drop in the engineering stress implies that the softening relaxation mechanism (cavitation) is outpacing the combined effects of the loading rate and the hardening rate (fibrillation).

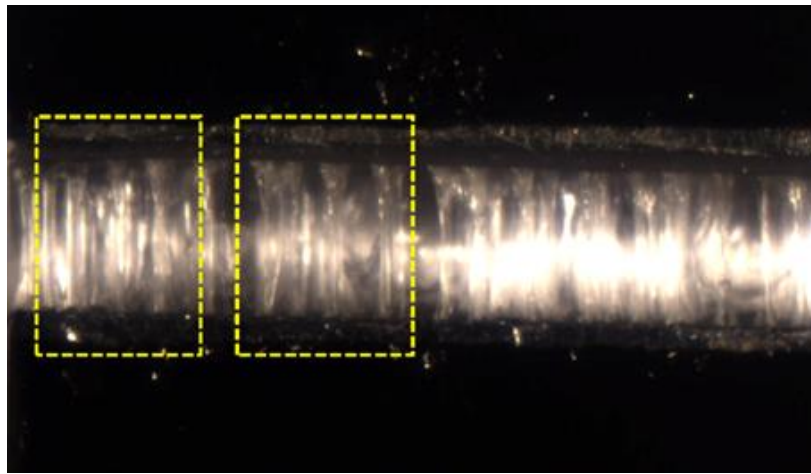


Fig. 29. highly cavitated and fibrillated adhesive layer during uniaxial deformation process.

3.3.2 Effects of loading rate:

The stress-strain curve is found to be strongly non-monotonic at the loading rate (displacement rate) used in this study. As shown in Fig. 30, the strength of the non-monotonicity is loading rate dependent. The underlying cause for this non-monotonic rate-dependent deformation behavior of the PSA bonded assembly is a constant interplay between softening due to cavitation and hardening due to fibrillation. At a certain point the stress level resumes its rise, implying that the combination of the

loading rate and the hardening rate due to increasing rates of fibrillation is now outpacing the continuing softening (cavitation) rate. This hardening during fibrillation occurs because polymer chains in the PSA fibrils reorient and stretch along the loading direction. When the backbone of the polymer chain becomes parallel to the loading direction, the polymer molecule is pulled taut, thus resulting in strain hardening. Such distinct behavior is only for adhesives that are capable of cavitation and fibrillation when proper loading conditions are applied.

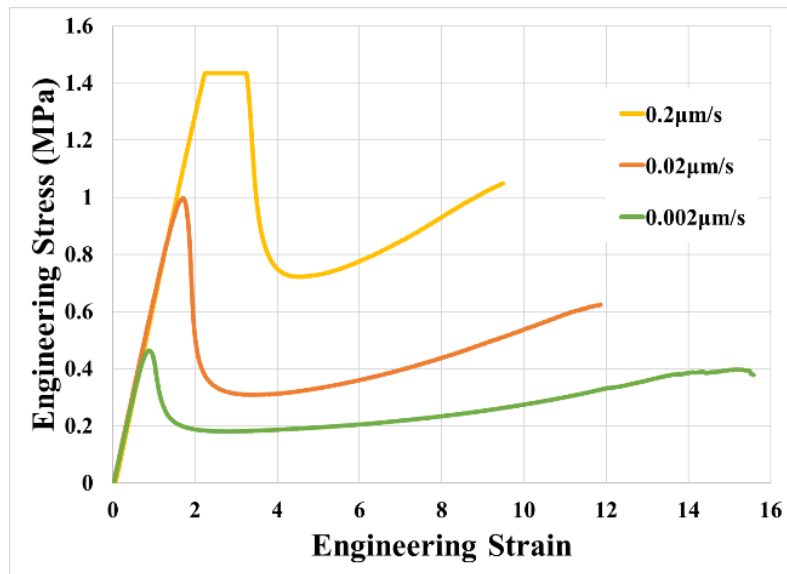


Fig. 30. Loading rate dependent stress-strain behavior of PSA bonded assemblies (missing part of yellow plot is due to the limitation of tester frame).

3.3.3 Effect of bonding conditions:

Because the bond characteristics change with every adhesive and substrate combination, we need a repeatable baseline specimen to compare results in this study. The bonding conditions of the baseline specimen were parametrically studied to establish a bonding process that results in a robust specimen in a reasonable period of bonding time. Fig. 31 shows that post-bonding thermal aging only shows noticeable

effects when proper pressure is applied. This particular PSA and substrate combination are found to achieve its full bonding strength when bonded for 10 s at room temperature under pressure. Higher bonding time or bonding temperature are not found to increase the bonding strength any further, as shown in Fig. 32 and Fig. 33. Bonding contact time and bonding temperature are selected based on guidance from the manufacturer.

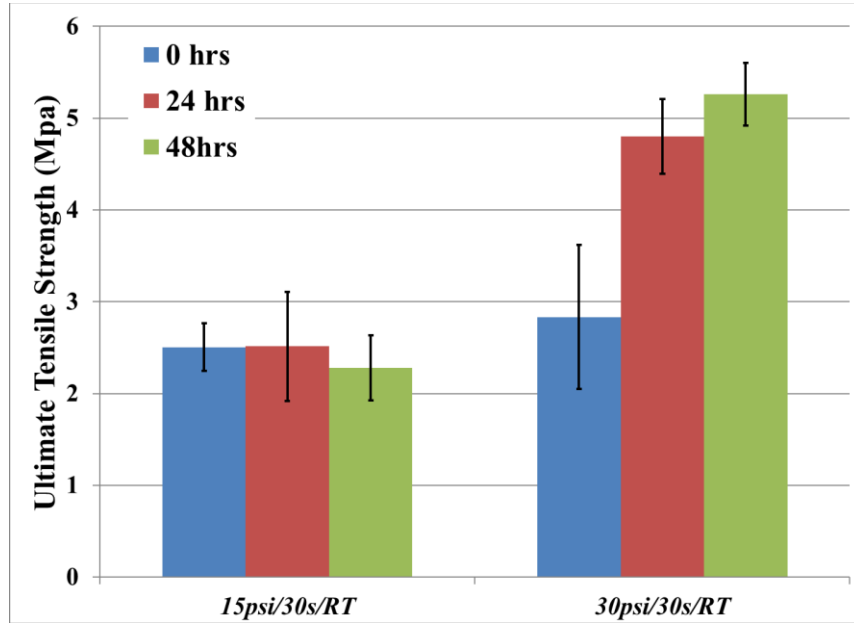


Fig. 31. Effects of bonding pressure and post bonding aging time on the bond strength of PSA bonded assemblies.

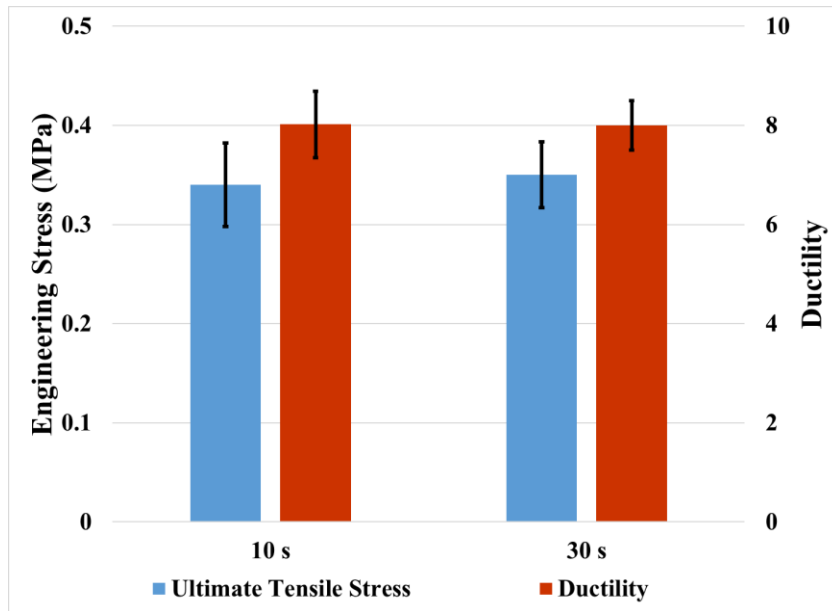


Fig. 32. Effects of bonding time (10s and 30s) on the bond-strength of PSA bonded assemblies (30 psi bonding pressure and 24hrs post bonding age).

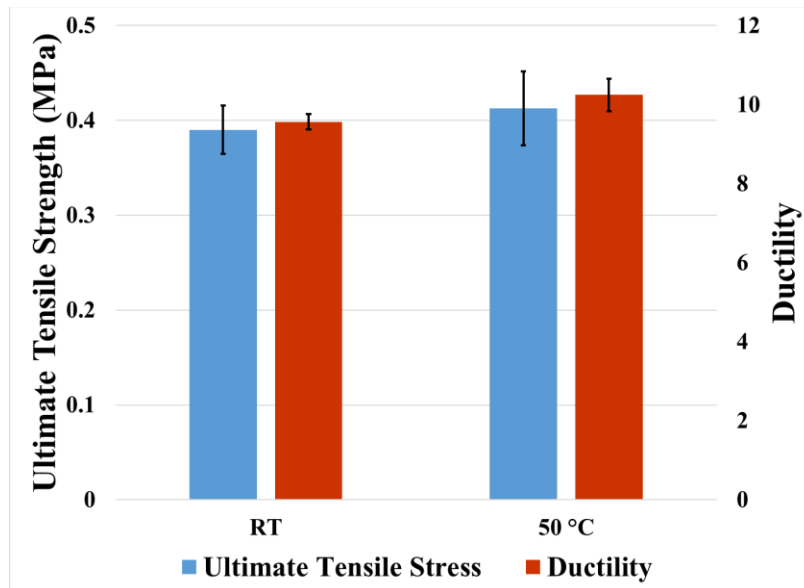


Fig. 33. Effects of bonding temperature (RT and 50°C) on the bond strength of PSA bonded assemblies (30 psi bonding pressure and 24 hrs post bonding age).

The presented results are only valid for this PSA and substrate combination. The bonding and preparation processes described here become the protocol used for the rest

of the study. More details about the optimal bonding conditions are presented in Appendix A1.

3.3.4 Effect of surface roughness:

The surface roughness of the substrate shows complex non-monotonic effects on the stress-strain behavior of PSA bonded assemblies. Fig. 34 shows the test result of PSA bonded to substrates of three different surface roughness values ($R_a=20\text{\AA}$, 400\AA , and 3300\AA). The peak strength for the primary transition does not show any degradation as R_a increases from 20\AA to 400\AA , but then drops 25% as R_a increases to 3300\AA ; suggesting that size distributions of initial interfacial micro-voids (and resulting cavity nucleation rates) are not strongly affected until the R_a becomes significantly large. The strength values beyond the primary transition show strong non-monotonic behavior, strongly increasing as R_a increases from 20\AA to 400\AA , but then dropping back to the original values as R_a increases to 3300\AA . This non-monotonic behavior suggests that there are competing mechanisms: (i) strengthening due to higher effective bonding surface area as surface roughness increases; and (ii) softening due to higher defect size as surface roughness increases. The strengthening effect appears to dominate for $20\text{\AA} < R_a < 400\text{\AA}$, while the softening appears to dominate for $400\text{\AA} < R_a < 3300\text{\AA}$.

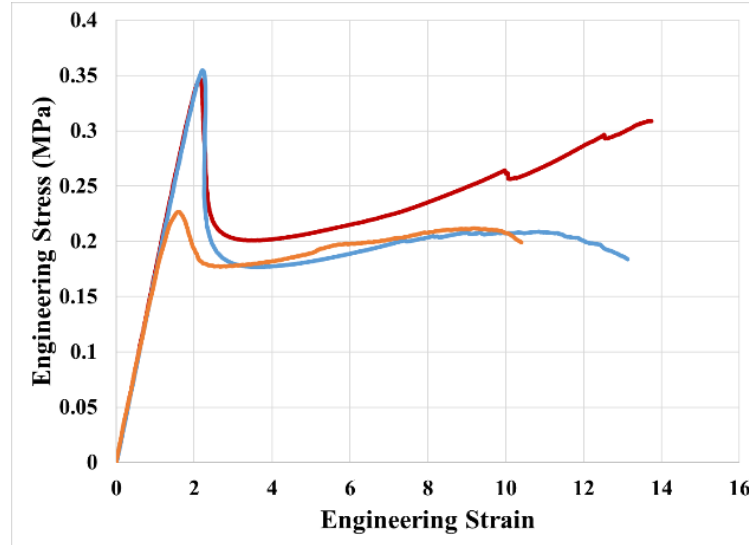


Fig. 34. Stress-strain response of smooth glass (blue, $R_a=20\text{\AA}$), matt glass (red, $R_a=310\text{\AA}$), and rough glass (orange, $R_a=3300\text{\AA}$)

Fig. 35 (a) and (b) shows the surface topography of smooth and matt glass obtained through atomic force microscopy (AFM). Surface topography of very rough glass is not obtained due to the limited range of the AFM approach. As the surface roughness increases, the effective geometric bonding area increases. However, if the substrate is too rough, the pits on the surface can result in initial voids between the adhesive and the substrate as the adhesive is not able to fully penetrate the valleys. The size of the initial defects depends on the surface profile of the bonding substrate, such as wavelength of the roughness and the average height of the profile. These initial defects will decrease the bond-strength, as they require less stress to initiate their growth process (Gay and Leibler, 1999). As discussed above, this conclusion is supported by the non-monotonic test results in Fig. 34. Based on the AFM measurement, Schematic idealization of interfacial bonding condition between PSA and substrate is shown in Fig. 36. The meaning of each symbol will be discussed in the simulation section.

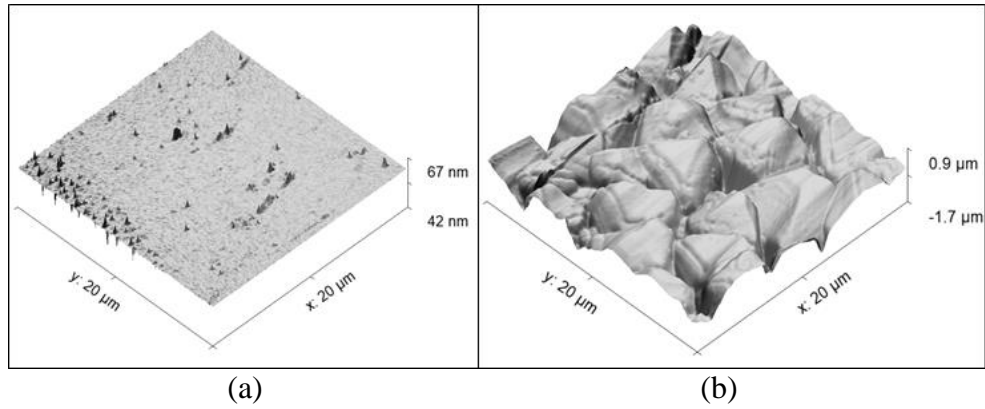


Fig. 35 Surface topography of (a) smooth glass ($R_a=20\text{\AA}$); (b) matt glass ($R_a=400\text{\AA}$);

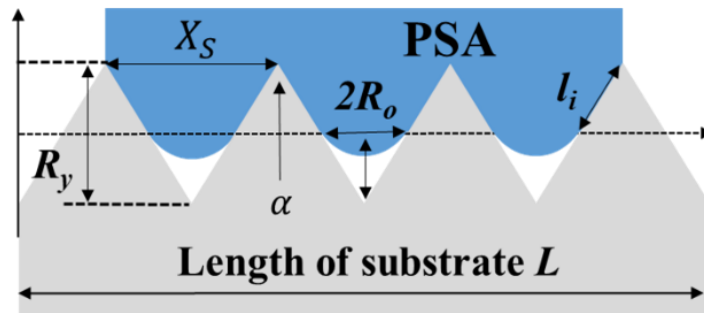


Fig. 36. schematic idealization of interfacial bonding condition between PSA and substrate.

The same test has been repeated with an aluminum substrate but with only three different roughness levels, to understand the negative effects of surface roughness. As shown in Fig. 37, as the average roughness of the bonding substrate increases from 215\AA to 715\AA to 3100\AA , the stress during the deformation process and the degree of strain hardening both decrease dramatically. The initial defects at the bonding interface produced by the rougher substrate are larger than those produced by the smoother substrate. This is verified by the additional graphic evidences of delamination interface (PSA side) shown in Fig. 38. The smoother surface produces smaller and denser initial interfacial defects, while the rougher surface produces larger and sparser initial

interfacial defects. However, under same loading conditions, the number of cavitable defects in the PSA bonded assembly bonded with smoother substrate are less than those in the bonded assembly bonded with rougher substrate, due to the higher stress barrier requires for the smaller defect size. Therefore, on the final delamination interface, the smoother surface produces larger but sparser voids because each cavitable defect in this bonding system has larger mean free path than the system with rougher surface.

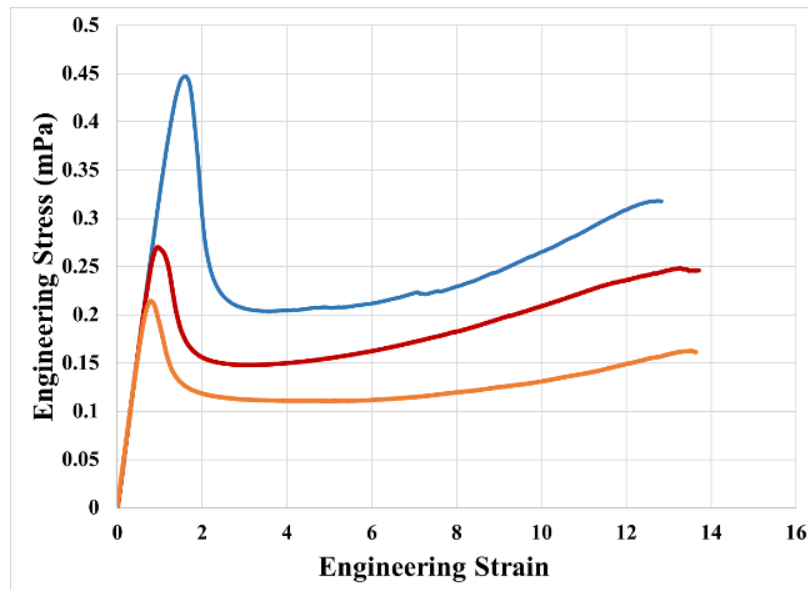


Fig. 37. Effect of roughness on stress-strain behavior of aluminum substrate with three different roughness (blue line, $R_a=270\text{\AA}$; red line, $R_a=715\text{\AA}$; orange line, $R_a=3100\text{\AA}$)

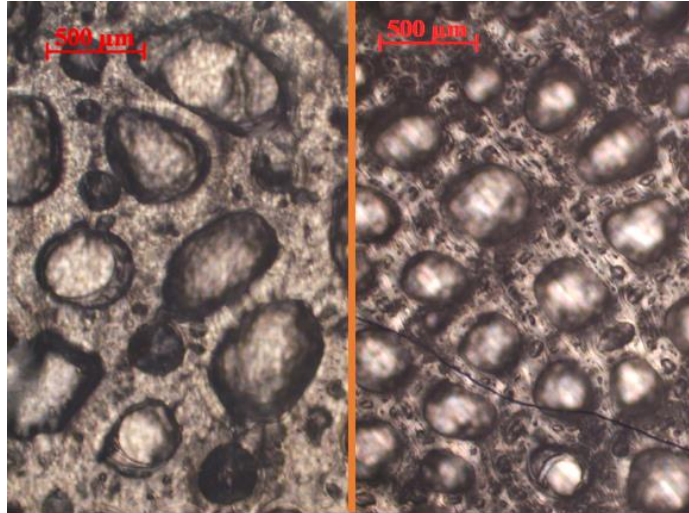


Fig. 38. Delamination interface of PSA bonded (a) with median rough substrate (large mean free path), (b) with rough substrate (small mean free path)

Both tests indicate that surface topography of the substrate plays an important role in the formation and growth of cavities in the PSA bonded assembly during the debonding process. It determines the density, size, and distribution of the initial interfacial defects. It is important to note that R_a is not sufficient for characterizing the effect of surface topography on the adhesion strength. The same average roughness associated with different R_y and characteristic wavelength may give different results due to different pre-existing defect size, as schematically shown in Fig. 39 (a) and (b) (Donoso et al., 2007). The depth of adhesive can penetrate the groove highly depends on the shape of the lump, as pointed by the arrow in Fig. 39, due to the surface tension of the adhesive. When the wavelength is too small, the adhesive material is hard to fully penetrate the groove and results in a larger cavity at the bonding interface and smaller effective bonding area. Therefore, the roughness can have both positive and negative effects on the bond strength. There are currently no empirical results can verify this hypothesis yet, but the simulation comparisons are presented in the simulation section.

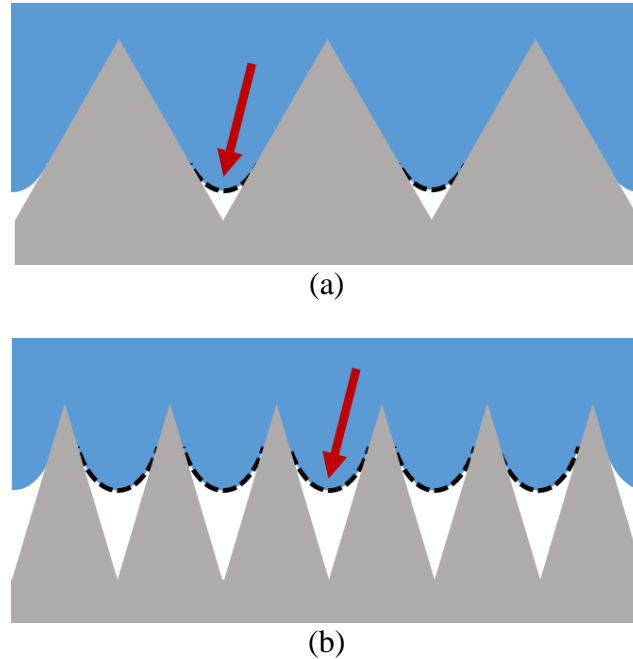


Fig. 39. schematic of effects of wavelength on the size of initial defect

3.3.5 Effect of substrate surface free energy:

In this phase, PSA bonded with different substrate materials are tested. Selected substrates include clear glass, aluminum (with and without adhesion promoting coatings), and coated glass. To isolate the effect of substrate material, the aluminum and coated glass substrates were ground to the same roughness. The clear glass substrate surface was unmodified and remained smooth ($Ra \cong 20 \text{ \AA}$). Fig. 40 clearly shows that even though the roughness of aluminum tab ($Ra \cong 3000 \text{ \AA}$) is much larger than that of the glass tab ($Ra \cong 20 \text{ \AA}$), the debonding stress of PSA-on-aluminum bonded assembly is still higher than that of a PSA-on-glass bonded assembly. Comparing the result of the aluminum tab to the coated glass tab, which have the same roughness, the peak stress differs by about 35%, the final stress differs by about 100%, and the ductility differs by about 35%. Quantitative dependence of PSA bonded assembly

performance on the substrate surface energy is not clearly understood yet, but a comparative study on the roles of surface energy on the tack performance of PSA is reported in literature (Kowalski et al., 2013). According to literature and empirical studies, the effects of substrate surface energy are significant and necessary to be considered in the predictive model.

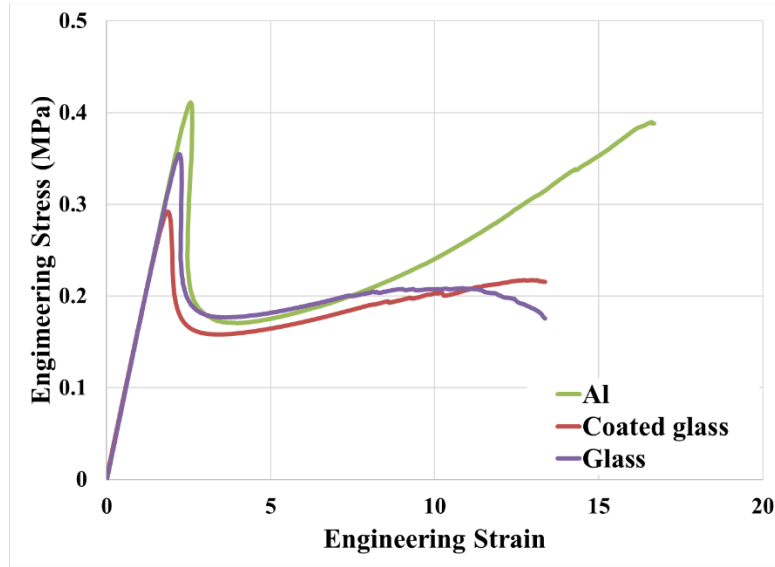


Fig. 40. Effect of bonding substrate material

3.4 Predictive mechanistic model

A 2D coordinate system to describe the main unit block deformation and translational motion is shown in Fig. 41. The deformed geometry of the block during the loading process is assumed to be parabolic, such that the material point (ξ, ζ) moves to the spatial position (x, z) after deformation, as described by the flowing equations

$$x = X_i + \frac{W_0 \xi}{\lambda} + \frac{C_i}{3} (1 - 12\zeta^2) \quad (16)$$

$$z = H_0 \lambda \left(\zeta + \frac{1}{2} \right) \quad (17)$$

where X_i is the location of center of mass of block i , C_i is the maximum deformation of block i at the center of the bonded assembly ($\zeta=0$), W_0 and H_0 are the initial width and height of block and λ is the stretch ratio.

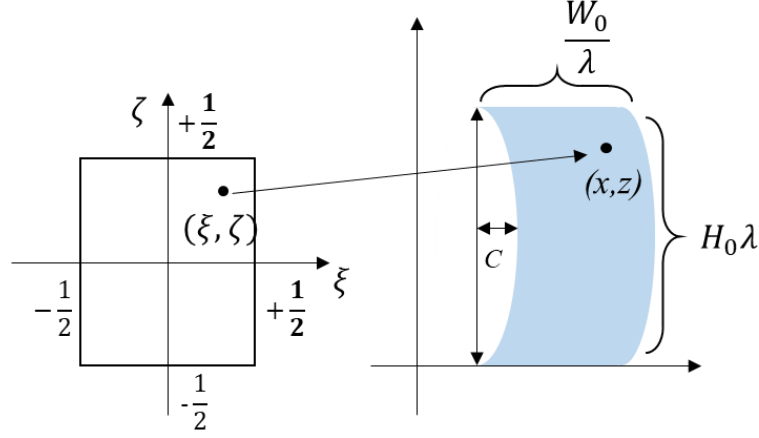


Fig. 41. Coordinate description of block motion and deformation. Coordinate (ξ, ζ) is the material coordinate and coordinate (x, z) is the spatial coordinate

Most of the PSAs that are capable of cavitation and fibrillation can deform more than 1000% of their original shape. Therefore, Green strain is used to account for the large strains. The Green strain tensor for this 2D problem is defined as:

$$E = \begin{bmatrix} \frac{1}{2\lambda^2} - \frac{1}{2} & -\frac{4C}{H^2\lambda}Z \\ -\frac{4C}{H^2\lambda}Z & \frac{32C^2}{H^4}Z^2 + \lambda^2 - 1 \end{bmatrix} \quad (18)$$

where $Z = H_0\zeta$ is the vertical axis in the block. Different Z values are selected for the stress components. $\zeta = -0.5$ or $\zeta = 0.5$ is used for both σ_{zz} (deviatoric stress in Z direction) and σ_{si} (shear stress), since the interest region is at the interface between PSA block and substrate shown in Fig. 42. The velocity gradient, which was defined by Eq. (17) in the classic ‘block’ model, is now defined as:

$$\begin{aligned}
\frac{\partial v_x}{\partial x} &= -\frac{2\dot{\lambda}}{\lambda} \\
\frac{\partial v_x}{\partial z} &= -\frac{8\xi\dot{C}}{\lambda(t)} \\
\frac{\partial v_z}{\partial x} &= -\frac{8\xi\dot{C}}{\lambda(t)} \\
\frac{\partial v_z}{\partial z} &= \frac{2\dot{\lambda}}{\lambda}
\end{aligned} \tag{19}$$

The force balance of the i -th block in the x direction is shown in Fig. 42 and can be written as:

$$(P_{i+1} - P_i)H_0\lambda = 2\sigma_{si}W_0b \tag{20}$$

where b is the ratio of current contact length to the initial contact length. Details of parameter b are discussed in the section of interfacial cavity growth criterion in this paper.

We assume a constitutive relation for the shear stress, in terms of the sliding distance of block i :

$$\sigma_{si} = \mu\dot{X}_{si} \tag{21}$$

where, μ is the friction coefficient at the interface. According to literature (Kowalski et al., 2013) and experimental results, the friction coefficient depends is the function of differences between the substrate surface free energy γ_{Sub} and adhesive surface free energy γ_{PSA} . The interfacial friction coefficient reaches maximum value when $\gamma_{sub} - \gamma_{PSA} \cong 10 \text{ mj/m}^2$

$$\mu \cong f(|\gamma_{PSA} - \gamma_{sub}|) \tag{22}$$

In this study, this classical ‘block model’ is further enhanced by including: strain hardening of bulk PSA material, cavitation initiation criterion in the bulk of the PSA, effects of substrate surface energy on the initiation and growth of interfacial cavities, and effects of surface roughness on pre-existing distributed interfacial micro-voids.

3.4.1 Constitutive equation for bulk PSA:

There is no noticeable strain hardening observed in the stress-strain curves of most tack tests (Tordjeman et al., 2000; Brown et al., 2002; Mohammed et al., 2016; Takahashi et al., 2016) However, significant strain hardening is common in the tensile tests of the PSA bonded assembly. This difference in strain hardening between these two test types depends not only on the adhesive material, but also on the post-bonding aging time and on the selection of bonding substrate surface properties, as shown in Fig. 34 and Fig. 40. The additional aging time in the tensile test (compared to the tack test) seems to help build a better bonding interface between PSA and substrate by allowing additional adhesive flow into the micro-scale pits and valleys on the substrate surface. This increases the effective bonding area and improved interfacial mechanical locking. The stronger bonding interface allows larger stretch in the body of the adhesive fibril before initiating delamination in the foot of the fibril. Large deformation and strong interfacial bonding enable significant strain hardening of the PSA fibril before softening occurs due to the adhesive delaminating from the substrate.

In Yamaguchi’s ‘block’ model (Yamaguchi et al. 2006), linear Maxwell viscoelastic model and hyper-elastic model are applied to the bulk adhesive in the classic ‘block’ model, respectively. This model predicts insignificant hardening after the first transition in the stress-strain curve and is in direct contradiction of the strain-hardening

observed in physical tests. Considering the rate dependent stress-strain response and considerable residual stress after long term relaxation test, a standard linear model, as shown in Fig. 43, with a small elastic element is used as the material constitutive law for the bulk adhesive in the current model.

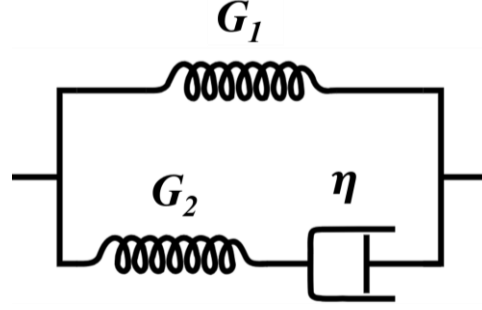


Fig. 43. Schematic of standard linear model

In such a case, now the relevant stress components, σ_{zz} and σ_{si} , are obtained by the following equations:

$$(G_1 + G_2)\sigma_{zz} + \eta\dot{\sigma}_{zz} - \eta\sigma_{zz}\left(\frac{2\dot{\lambda}}{\lambda}\right) = G_1\eta\left(\frac{2\dot{\lambda}}{\lambda}\right) + \frac{1}{2}G_1G_2(\lambda^2 - 1) \quad (24)$$

$$(G_1 + G_2)\sigma_{si} + \eta\dot{\sigma}_{si} - \eta\sigma_{zz}\left(\frac{4\dot{C}}{H_0\lambda}\right) = G_1\eta\left(\frac{4\dot{C}}{H_0\lambda}\right) - G_1G_2\frac{4C}{H^2\lambda} \quad (25)$$

where G_1 is the shear modulus of the individual spring, G_2 is the shear modulus of the spring and η is the viscosity of the dashpot in the Maxwell element in the standard linear model, $\dot{\lambda}$ is the loading strain rate (engineering strain rate) of the PSA block, and \dot{C} is the rate of change of the parabolic measurement of each adhesive block. Viscosity η is related to shear modulus G_2 by $\eta = G_2\tau$, where τ is the relaxation time. Both modulus G_1 and G_2 are strain dependent, as shown in Eq. (26) (Maeda et al., 2011).

$$G_t = G_0 \exp(h\epsilon_t) \quad (26)$$

where G_0 is the initial modulus, G_t is the modulus in the current time step, h is the strain hardening coefficient, and ϵ_t is the true strain of PSA fibril.

3.4.2 Cavitation criterion:

As shown in Fig. 34, Fig. 37, and Fig. 40, strain values of the primary peak are not identical. Prior studies agreed that the primary instability in stress-strain curve is due to the rapid release of hydrostatic stress caused by the cavity initiation and expansion processes, which are directly related to the surface condition (interfacial energy and surface roughness) of the bonding substrate. The critical stress to initiate the growth of an existing defect has been proposed by Gay (Gay et al., 1999). A simplified version of their critical stress cavitation criterion, Eq. (13), is used for the predictive model proposed in this study.

$$\sigma_c = P_o \left[1 + \left(\frac{E}{P_o} \right)^{1/2} \left(\frac{g_c^{3/2}}{P_o^{3/2} \zeta^2 \xi} \right)^{1/2} \right] \quad (27)$$

As shown in the Eq. (27), the critical energy release rate, initial cavity width, and initial cavity depth play important roles in the critical cavitation stress. In order to quantitatively capture the effect of substrate surface roughness, we reduced the complexity of the substrate surface topography by assuming the shape of grooves are uniform on the substrate surface as shown in the schematic in Fig. 35 (c). Now the equation for initial cavity size, R_o , is defined by:

$$R_o = X_s \frac{\sqrt{\frac{X_s^2}{4} + R_y^2} - l_i}{\sqrt{\frac{X_s^2}{4} + R_y^2}} \quad (28)$$

Where, as shown in Fig. 44, R_y is the mean roughness depth, X_s is the characteristic wavelength, and l_i - which is a function of R_z and X_s - is the characteristic depth of the PSA that penetrates into the groove under the given bonding condition. The depth, l_i , that the PSA can penetrate the groove under applied bonding pressure is a function of

peak to peak value R_y and the wavelength X_S . In this study, for simplification, l_i is linearly dependent on arctangent α , as shown in Eq. (29). When the estimated l_i is larger than half of the wavelength X_S , l_i is equal to half of X_S . A detailed study on the dependence of l_i on the topology of the substrate surface will be discussed in a separate paper.

$$l_i \cong \frac{L}{m} \arctan(\alpha) \quad (29)$$

where m is a constant model parameter. When the calculated interfacial cavitation stress is higher than the bulk cavitation stress, then the cavitation initiates in the bulk adhesive. In that case, the initial cavity size, R_o , is simply the initial bulk defect size used in the predictive model.

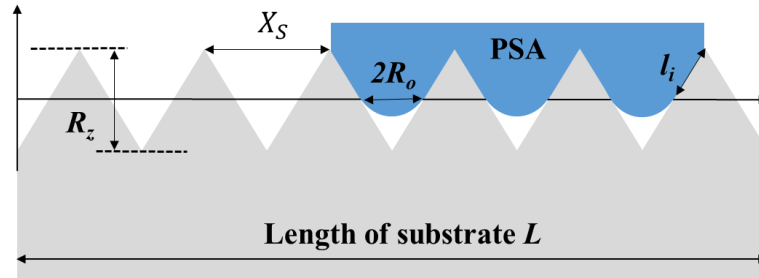


Fig. 44. Schematic idealization of interfacial bonding condition between PSA and substrate.

In Yamaguchi’s conventional ‘block’ model, there is no provision for an energy barrier for the cavity to grow when a displacement load is applied (Yamaguchi et al., 2006). In other words, the cavity starts growing the moment any displacement is applied, regardless of the magnitude of the displacement. Therefore, there is no parameter in the model to control the strain value at which the primary peak occurs. This is an inadequacy of the model since experimental results do show differences in the strain at the primary peak, depending on bonded assembly architecture and bonding

conditions. In the current proposed predictive model, this limitation is mitigated by the use of a threshold stress limit to initiate the growth of preexisting micro-voids at the interface or in the bulk. The instantaneous stress level around each cavity is evaluated at each iteration, and the voids in each block are allowed to grow when the instantaneous stress exceeds the critical stress.

3.4.3 Interfacial cavity growth criterion:

Another limitation of the traditional ‘block’ model is that it does not have adequate direct control over the growth of cavities at bonding interface between PSA and substrate. The only relevant parameter in the ‘block’ model is the interfacial frictional coefficient μ of Eq. (21), which provides indirect and approximate control over this interfacial cavity growth mechanism. While the literature provides some guidance over how this surrogate parameter should explicitly depend on the substrate surface energy, as shown in Eq. (22) (Kowalski et al., 2013), its dependence on other important surface parameters, such as surface roughness, remains unaddressed. Furthermore, parametric exploration reveals that this friction parameter has very limited tuning range over the stress-strain response of PSA bonded assembly. As shown in Fig. 45, even when μ is varied by two orders of magnitude, there is a small inadequate effect on the predicted stress-strain curve. This does not agree with the experiments, shown in Fig. 40, in terms of either the position, magnitude and span of primary transition; or the strain hardening observed after the primary transition.

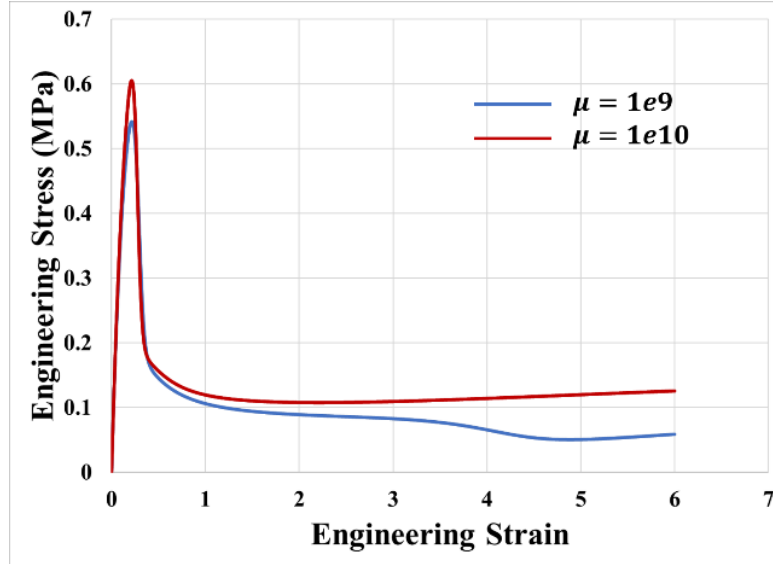


Fig. 45. Effects of interfacial friction coefficient μ on the stress-strain prediction of Yamaguchi's 'block' model

The reason, in part, is because the traditional 'block' model oversimplifies the deformation of each block, as given in Eqs. (16) and (17) (and repeated below in Eqs (30) and (31)). Due to volume conservation, the width W and the height H of the PSA block are defined as:

$$W = W_0/\lambda \quad (30)$$

$$H = H_0\lambda \quad (31)$$

where W_0 and H_0 are the initial width and height of the adhesive block. This simplified deformation field fails to capture the hour-glassing of the fibrils that is usually observed during fibrillation in experiments.

In the proposed improvement to the 'block' model, the non-uniform cross-section of the block is captured by letting the width of the fibril foot vary independently from the width of the fibril neck at the center, as shown in Fig. 42. A similar technique has been reported in the literature before (Toyama et al., 1973). As the fibril deforms,

width W still follows the rule of volume conservation, but the fibril foot length evolves separately due to the interfacial constraint from the bonding substrate. The status of fibril foot length directly affects the stress status in the bulk PSA and the ductility of the PSA bonded assembly. Compared to the traditional ‘block’ model, the current model allows much lower interfacial frictional stress at comparable stretch, because of smaller interfacial delamination at the bonding interface. This can be seen by comparing the governing equations of the classic ‘block’ model, Eq. (32) with that of the current proposed model, Eq. (20).

$$(P_{i+1} - P_i)H_0\lambda = -2\sigma_{si} \frac{W_0}{\lambda} \quad (32)$$

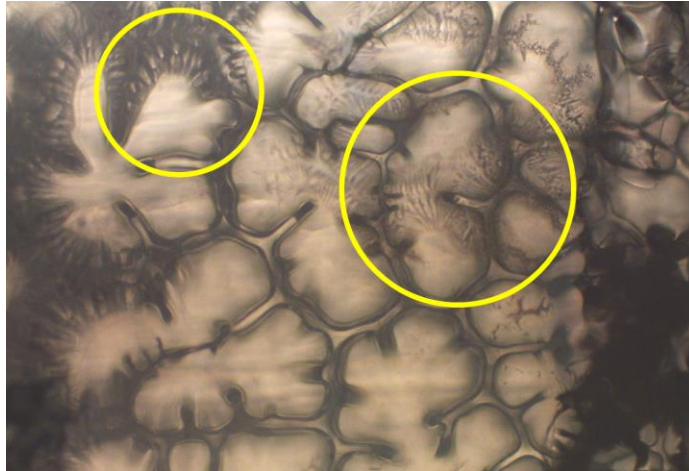


Fig. 46. Footprint of PSA fibril on glass substrate

Evolution of the fibril foot length follows the detachment criterion proposed by Glassmaker and his coworkers. As shown in Fig. 47, the horizontal force to shorten the fibril foot can be related to the vertical force in the fibril body by the conservation of energy in the debonding system (Glassmaker et al., 2008).

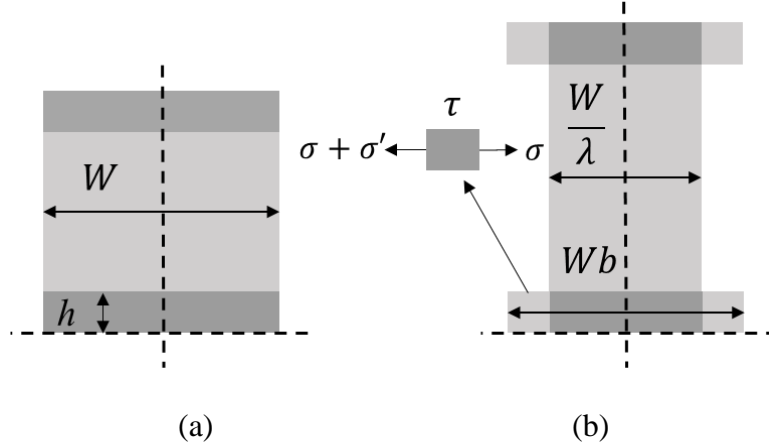


Fig. 47. 2D schematic of PSA fibril during debonding. σ_{vert} is the deviatoric stress along vertical (loading) direction in the fibril, σ is the converted stress along the fibril foot in horizontal direction.

Parameter b is the ratio of current contact length to the initial contact length and can be estimated by applying finite-difference method in the fibril foot, as shown in Eq. (33) (Tayama et al., 1973).

$$b = \frac{(W_0 - 2u)}{W_0} \quad (33)$$

where u is the displacement of the edge of fibril foot, and can be calculated by

$$u_{j,n+1} = u_{j,n} + \frac{\Delta t}{du^2} \left(\frac{2E\lambda}{\alpha\mu W_0} \right) (u_{j-1,n} - 2u_{j,n} + u_{j+1,n}) \quad (34)$$

where E is the modulus of bulk PSA, $u_{(j,n)}$ is the displacement of the fibril foot in node j in the n^{th} step, α is the ratio of original fibril height to fibril width, du is the length of each element in fibril foot, E is the modulus of bulk adhesive, μ is the interfacial friction coefficient, and Δt is the time increment for each step. This equation is under the assumption of rigid body motion of the fibril foot, which means that the displacement of the fibril foot is independent of the position along the horizontal axis. If the bonding interface is in perfect condition, then $b=1$; if the adhesive is fully

delaminated then the width of fibril foot is equal to that of the fibril body (Glassmaker et al., 2008). The initial value of parameter b can be slightly larger than 1 if the substrate has a slightly rough surface.

The parameter b provides an additional degree of freedom to improve the interfacial interaction between PSA and substrate. Deformation is now mainly reflected in the elongation of the fibril and the shrinkage of the fibril foot length (contact length), which is controlled by the applied stress and apparent substrate surface free energy. The apparent surface free energy is the measured surface energy, which already includes the effects of surface roughness and is written as:

$$\gamma_{sv} = \gamma_{sl} + \gamma_{lv} \cos \theta_m \quad (35)$$

where γ_{sv} , γ_{sl} and γ_{lv} are interfacial tension in well-known Young equation. θ_m is the apparent contact angle described by $\cos \theta_m = b \cos \theta_Y$ (θ_Y is the Young's contact angle).

3.4.4 Total debonding force:

Because the actual contact area between the PSA fibril and substrate is now identified by dimensionless ratio b , the debonding force, F_z can be calculated by

$$F_z - P_0 S = \frac{bS}{N} \sum_{i=1}^N \left(\sigma_{zz} - \frac{P_i + P_{i+1}}{2} \right) = bS(\sigma_{zz} - \bar{P}) \quad (36)$$

where b is the actual contact ratio, S is the nominal area, and \bar{P} stands for the average value of all blocks. The debonding stress is then calculated by

$$\sigma_{tot,z} = \frac{F_z}{S} = b(\sigma_{zz} - \bar{P}) + P_0 \quad (37)$$

The total stress (along loading direction) and its corresponding deviatoric component and hydrostatic component are shown in the stress-strain curve in Fig. 48.

3.4.5 Simulation results:

Fig. 48 shows the stress-strain curve predicted for the parameter set from Table 1. Parameters with subscript * are used as reference metric for the rest of parametric studies. As seen, the initial state of the debonding stress is dominated by its hydrostatic part (internal pressure in the adhesive before cavitation). As the cavitation initiates, the hydrostatic stress is released due to the loss of geometric confinement, while the deviatoric stress increases due to the strain hardening caused by the fibrillation process. The total debonding stress in the final debonding state is dominated by the deviatoric part (accumulated by elongation of fibril). The decrement of total stress in the final stage is due to the foot delamination of PSA fibril foot. MATLAB code for single-layered PSA bonded assembly is presented in Appendix A5.

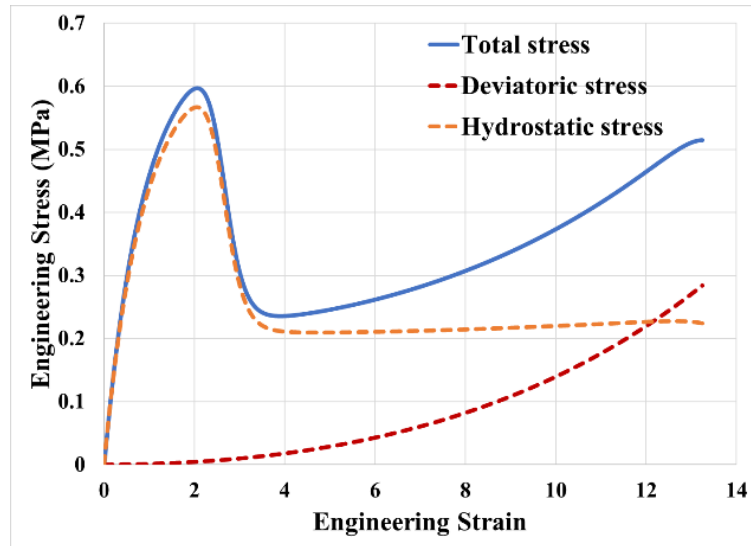


Fig. 48. Simulation result of total debonding stress and its deviatoric (loading direction) and hydrostatic stress component.

Table 1: Simulation parameters for single-layered PSA model

Parameter (unit)	Value
PSA thickness H_0 (m)	1.3×10^{-4}
PSA width W_0 (m)	7×10^{-3}
Separation strain rate	0.02
Relaxation time (s)	3500
Elastic modulus G_1, G_2 (Pa)	40, 200
Strain hardening coefficient	2.2
PSA surface energy γ_p (mJ/m ²)	30
Substrate surface energy γ_p^* (mJ/m ²)	80
Initial cavity R_z^* (m)	5×10^{-8}
Roughness wave length X_s (m)	3×10^{-7}
PSA penetration parameter m	60
Number of blocks	30
Time step (s)	1×10^{-1}

Fig. 49. indicates that the current model has much more versatile control over the initiation of the primary transition. The non-monotonic effects of substrate surface roughness on the stress-strain response is also captured in the current predictive model.

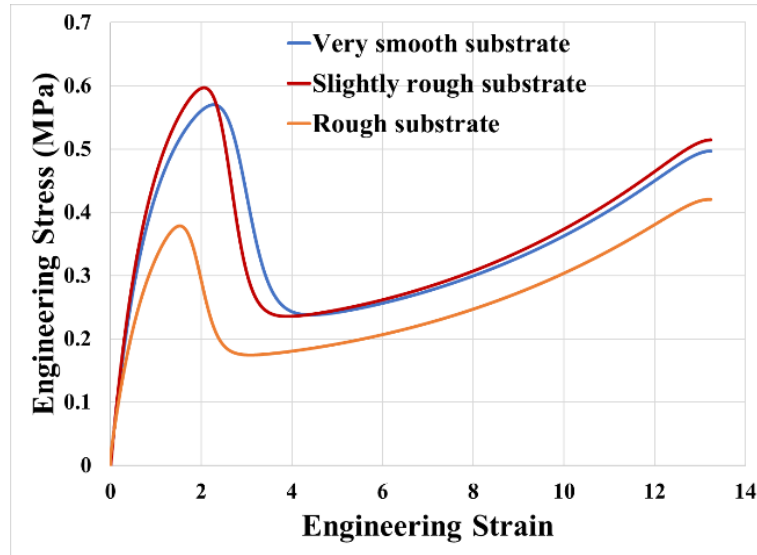


Fig. 49. Effect of substrate surface roughness, red line is the reference modeling prediction, R_z of blue line is $0.5R_z^*$; R_z of blue line is R_z ; R_z of orange line is $2R_z^*$.

Fig. 50 shows the sensitivity of current model to the substrate surface free energy. Increasing the surface energy of substrate leads to an increase in (a) the peak stress, (b) ultimate tensile strength and (c) ductility. The current model predictions are much more sensitive than the existing ‘block’ model (Yamaguchi et al., 2006) to the surface free energy of bonding substrate.

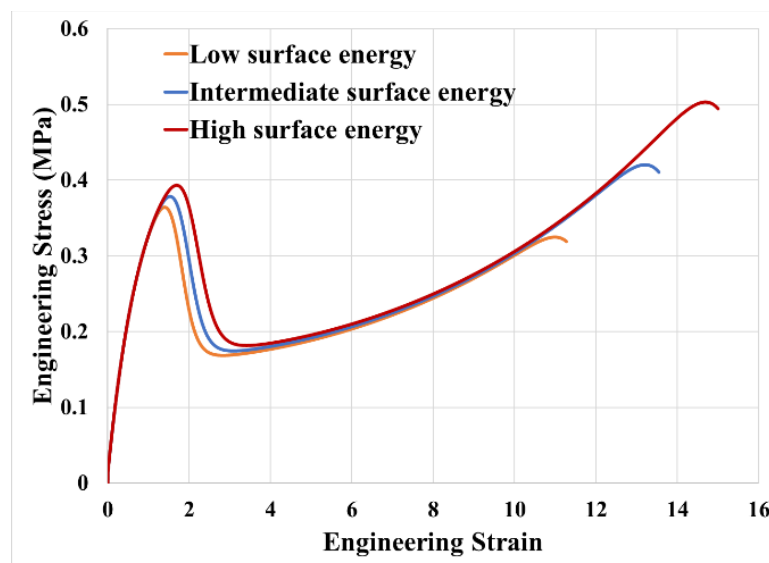


Fig. 50. Effects surface free energy (SFE) on the stress strain curve. SFE of red line is $2\gamma^*$; SFE of blue line is $2\gamma^*$; SFE of orange line is $0.5\gamma^*$.

3.5 Conclusion

In this first chapter of the two-part series, the physics behind the unique multi-phase stress-strain response of PSA bonded assemblies have been presented. The mechanical behavior of PSA bonded assemblies always depends on the combination of the PSA material and the bonding substrate. Substrate surface properties, such as surface roughness and surface energy have significant effects on the mechanisms of interfacial cavitation and interfacial slippage of PSA bonded assembly, and therefore, on the apparent stress-strain curve. Up to certain roughness, bond-strength increases due to increase of effective bonding area and interfacial mechanical locking. Beyond this threshold roughness, the bonding performance reduces because of large initial defects and smaller effective projected bonding area produced by the rough profile of the substrate surface. The bond-strength and ductility of a PSA bonded assembly show strong dependence on the substrate surface free energy.

A predictive mechanistic model is presented to capture the stress-strain responses of single-layered PSA bonded assemblies. The predictive model is based on the ‘block’ model and has been improved by: (i) adding cavitation and cavity growth criteria for interfacial defects; (ii) applying suitable constitutive law for bulk PSA; and (iii) modifying the adhesive fibril foot configuration for interfacial cavity growth. The current model includes the effects of substrate surface roughness, effects of substrate surface energy, and effects of PSA configuration (aspect ratio of adhesive layer). A parametric exploration of the predictive model indicates that it can be tuned to fit

different stress-strain responses, especially the strain and stress value of the primary peak, caused by varied combinations of single-layered PSA and bonding substrate. The model results can be used as stress-strain constitutive model for single-layered PSA bonded assembly for commercial FEA tools (detailed approaches discussed in Appendix A8)

Chapter 4. Creep Response of Assemblies Bonded with Single-Layered PSA

4.1 Abstract

This is Part II of a two-part series on the mechanical response of single-layered pressure sensitive adhesive (PSA) bonded assemblies. Part I had presented the uniaxial tensile stress-strain response while this chapter explores the uniaxial tensile creep response of a single-layered pressure sensitive adhesive (PSA) bonded assembly. This material system exhibits a unique multi-phase creep response that does not have the classical steady-state region due to its multiple transitions caused by the competition of several mechanisms: (i) cavity nucleation and growth in bulk adhesive material of the PSA system as well as at the interfaces between the PSA and the substrate; (ii) fibrillation of the bulk adhesive and (iii) interfacial mechanical locking between the adhesive and the bonding substrate. The result is multiple strain hardening and softening regions evidenced by multiple regions of steady-state creep, separated by strong transitions in the creep rates, this complex, multi-phase, nonlinear creep response cannot be described by conventional creep constitutive models commonly used for polymers in commercial finite element codes.

First, empirical uniaxial tensile creep response curves of single-layered PSA bonded assemblies on different substrates are presented under different stress levels and different temperatures. Investigations in this section focus on the effects of loading stress and substrate surface properties (roughness and material), at different temperatures. Mechanisms behind the multi-phase creep response (cavitation,

fibrillation, and mechanical locking between adhesive and bonding substrate) are also discussed at the end of this section. In the second part of this chapter, a mechanistic model, which is based on the mechanisms listed above for creep response, is presented. This model is capable of capturing the characteristic features of the multiphase creep response of single-layered PSA bonds and produces a quantitative estimate of the creep response of such PSA bonded assemblies, as a function of adhesive material viscoelastic properties, free surface energy in the adhesive material, interfacial surface energy between the adhesive and substrate, and substrate surface roughness.

4.2 Introduction

PSA bonding layer shows superior resistance to loading in shear direction (loading on the xy -plane as shown in Fig. 51. This adhesive system has been widely used in different applications due to their: ease of design; clean and environmentally friendly bonding and rework procedures; as well as uniform thickness and gap filling properties. Many scholars have studied the tack, peel, shear, and shear creep properties of PSA bonded assemblies for the past decades. Fujita et al. studied the effects of miscibility and viscosity on the shear creep resistance of natural-rubber-based PSA. They concluded that the holding time, which is the required time for the PSA tape under shear load to completely debond from the adherend, tended to decrease as the tackifier content increased (Fujita et al., 2000). Sosson et al. investigated the shear failure mechanisms of PSA and found that for a weak cross-linked adhesive, failure occurs by creep rupture while for a highly cross-linked adhesive, failure is caused by fracture (Sosson et al., 2005). Kim et al. tested hot melt PSAs with different viscosities and found that the shear creep resistance increased as the PSA viscosity increased (Kim et

al., 2006). Hait and Barthel proposed a model for evaluating the effect of surface roughness on adhesive bonding. Their model provides approximate analytical expressions for the asperity response and exhibits the full viscoelastic adhesive contact phenomenology such as stress relaxation inside the contact zone and creep at the contact edge (Hait et al., 2007). Poh and Kwo investigated the effects of adhesive (coating) thickness on shear performance of Standard Malaysian Rubber (SMR)-based PSA. They concluded that the shear strength increased as the adhesive thickness increased (Poh et al., 2007). Zosel studied the correlation between the shear strength and the mechanical properties of PSA by measuring the deformation behavior in a static and dynamic shear test. He concluded that the static shear strength and holding time (time to failure) of the sample can be calculated from the master curve of dynamic shear test, but the method cannot be applied to highly viscous polymer (Zosel, 1994). Yamaguchi proposed a simple 'block' model that can capture the major characteristic feature of a tack test curve (Yamaguchi et al., 2006). However, their model does not have enough control over the cavitation or interfacial cavity growth and can only be applied for the stress-strain response. The literature focuses mostly on the understanding of shear creep performance. In contrast, the creep resistance to loading in the out of plane loading direction (peel or z direction), as shown in Fig. 51, does not get enough attention. Compared to the in-plane direction, xx , yy , and xy , loading along the peel direction (zz) shows the most damage for this kind of adhesive bonded assembly structure. In application, this kind of loading can be caused by external multiaxial loading and initial curvature mismatch of bonding substrate. Even the residual stress from a small geometric mismatch can pose a hazard for the performance

of the PSA layer in a long-term application. In summary, highly ductile lightly-crosslinked PSAs show unique multi-phase tensile creep response, which is uncommon in other polymeric (Zheng et al., 2002, Colak et al., 2005) and metallic materials (Mukherjee et al., 2011, Mukherjee et al., 2016, Mukherjee et al. 2016). However, the literature on the long-term tensile (peel) creep performance of PSA bonded assembly is limited.

The primary motive of this chapter of study is to develop a virtual testing capability for the creep response of the PSA bonded assembly. More importantly, this virtual testing model has the potential to be for real-time prognostic health management (PHM). By continuously re-calibrate this model by using the real time in-situ data, such as strain, loading stress and temperature, the tune 'digital twin' can provide updated of the residual life of such adhesive bonded assembly in real time. In current phase, we have empirically investigated the uniaxial creep performance of PSA bonded assembly consisting of two rigid substrates bonded with a single-layered PSA material, under different loading conditions. The bonded assembly variables include the substrate surface material and surface roughness. Based on the empirical observations and measurements, we then propose a mechanistic model that can not only capture the unique multi-phase tensile creep curve but can also predict the change in creep response due to changes in adhesive properties, such as modulus and viscosity; as well as changes in the substrate properties, such as surface free energy and surface roughness.

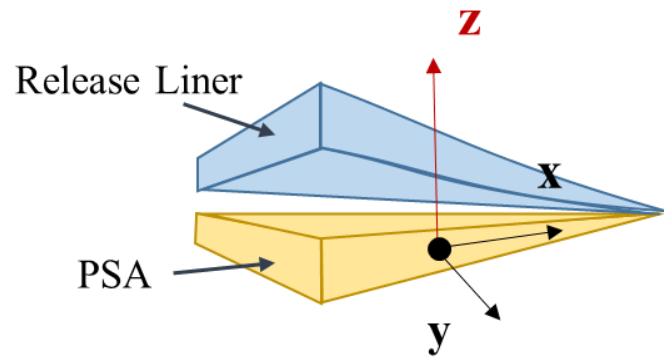


Fig. 51. Schematic of single-layered PSA and loading direction

4.3 Uniaxial creep experiment

The test sample for this study is a uniaxial tensile test coupon to permit loading in the peel (zz direction in Fig. 51). This specimen consists of two rigid T-shaped substrates bonded with a single-layered PSA, as shown in Fig. 13. Both substrates are mounted between tensile loading grips of a Dynamic Mechanical Analysis (DMA) machine for constant stress uniaxial creep test. The size of the PSA bond line is 7×7 mm² with a thickness of 0.05 mm and 0.1 mm. To understand the effect of the loading condition, different stress level, 50 and 70 KPa, are used, and the testing temperature is 70 °C. For simplification, engineering stress and engineering strain are used for the creep plots.

4.3.1 Unique creep response:

A creep result, which consists of a short primary creep region, final tertiary creep region, and long intervening region, under test condition of 50 KPa and 70 °C is shown in Fig. 52. Unlike in metals and traditional polymers, this creep response does not demonstrate a single steady state (secondary) region. Instead, there appear to be

multiple steady-state (secondary creep) regions, separated by sharp peaks and transitions in the creep rates. Over 80% of the observed creep is dominated by the intervening multi-phase secondary creep region. The peak rates during the transitions in this multi-phase secondary region may have more than 6000% change. At the applied loading condition, the transitions lasted for less than 1-hour duration (~10% of total creep time) and accounted for more than 600% strain (about 70% of total creep strain) accumulation in the creep curve. Because the creep test results are sensitive to the interfacial bonding quality and the hard-to-control volumes of air pockets trapped at the bonding interface, the test results presented in this paper are the median values of three replicates.

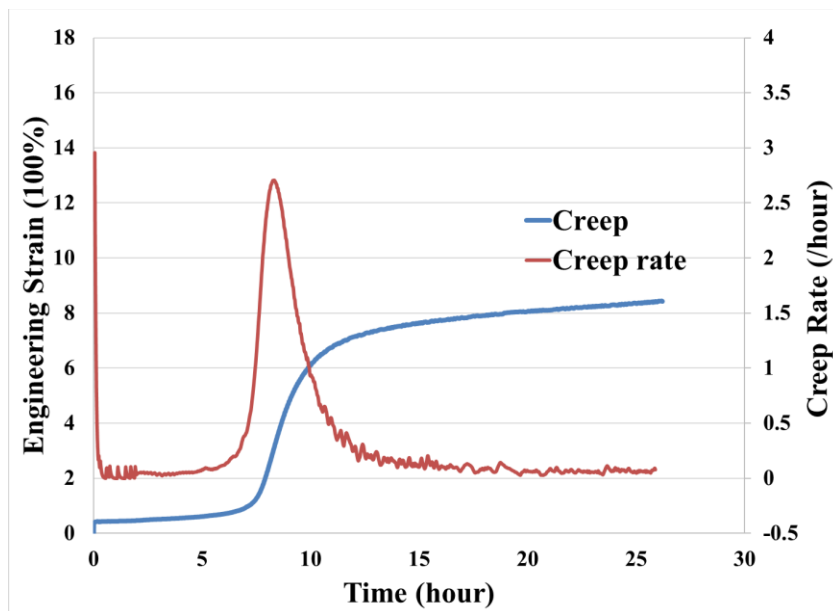


Fig. 52. Creep test result of single-layered PSA under 50 kPa and 70 °C

These transitions in the creep curve are believed to be a result of the same underlying physics that produced the transitions reported elsewhere in the tensile stress-strain tests in Chapter 3, but under different loading conditions. The multiple phases are the result

of competition between the mechanisms of cavitation and fibrillation of the bulk adhesive. The significant difference between the stress-strain test and the creep test is the critical stress needed for initiating the transition. Usually, the initiation of cavity growth in stress-strain tests are associated with high stress level, which is much higher than the creep stress used in this study. The apparent stress level in a creep test can usually not be as high as the required threshold critical stress predicted by Gay and Leibler's model for cavity nucleation (Gay and Leibler's, 1999). Cavity initiation under such low stress level during creep tests is speculated to be due to stress-assisted acceleration of the diffusion process. The initial cavity growth is slow at the initial stages of creep. As the size of initial defects reaches a threshold value, the force balance around the cavity exceeds the threshold levels and the system becomes unstable. Then the cavity starts growing rapidly, resulting in the rapid increase in creep rates seen during the sharp transitions.

Fig. 53 shows the top view of the bonding interface between PSA and the transparent substrate, illustrating the cavitation and fibrillation. In later stages of the debonding process, a majority of the interface is filled by the interfacial cavities (air voids), which are separated by thin webs (adhesive walls which are the ends of the fibrils). The cavitation and cavity growth process lead to a decrease in the geometric confinement of the adhesive layer and therefore decreases the stiffness of the PSA layer. In contrast, the fibrillation process, as shown in Fig. 54, leads to increase the stiffness of the PSA layer because of nonlinear viscoelastic hardening of the fibril material along the loading direction, because of the re-orientation of long-chain molecules along the loading direction. Filaments around the foot of the circular boundary indicates that the cross-

section of the adhesive wall near the bonding interface is larger than the cross-section of the wall in the body of the fibril. The microstructural evolution in the adhesive layer (material softening and stiffening) results in complicated constitutive models for such structural interconnection.

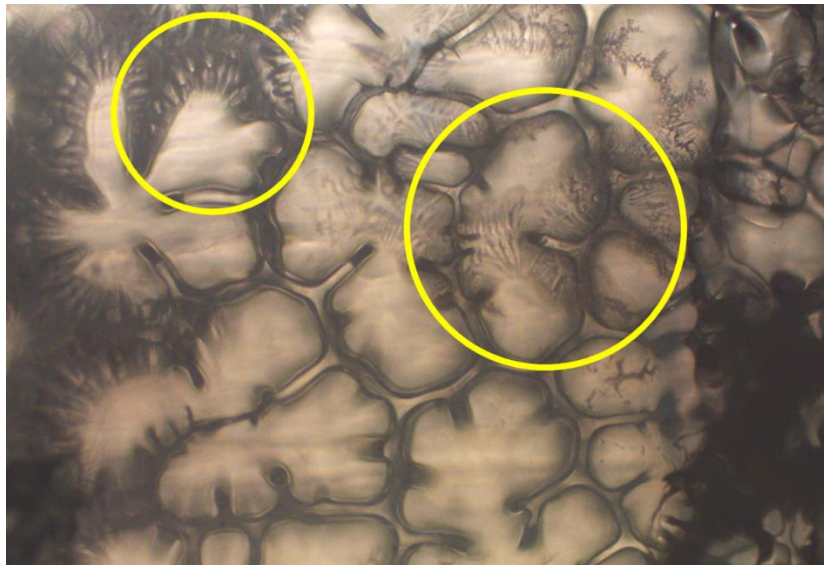


Fig. 53. Top view of the PSA/glass substrate bonding interface (from the real time observation of stress-strain test). Filaments in the fibril foot area are highlighted by circle.

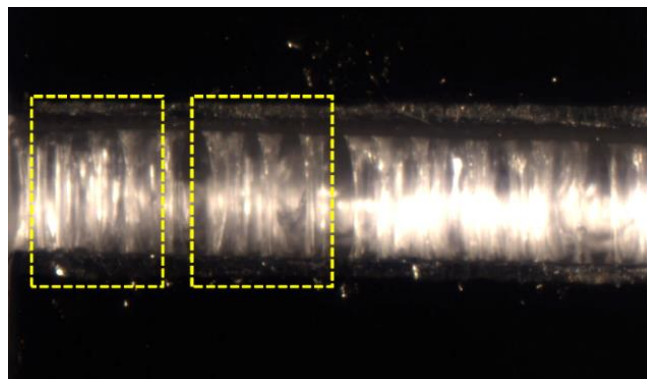


Fig. 54. highly fibrillated adhesive layer during debonding process (from the real time observation of stress-strain test).

Cavitation as well as growth of bulk and interfacial cavities results in thin fibrils that can decrease the confinement, leading to a release of hydrostatic stress stored in the adhesive layer. Since the creep deformation is a stress-controlled process and the total stress is equal to the summation of deviatoric stress and hydrostatic stress, decreasing hydrostatic stress leads to an increase in the deviatoric stress inside the bulk PSA, as shown in Fig. 55. This results in a change in the creep rate during the creep debonding process. The higher the relative growth rate of the cavities, the faster the loss of geometric confinement, the quicker the release of hydrostatic stress and the more dramatic the change in the creep rate.

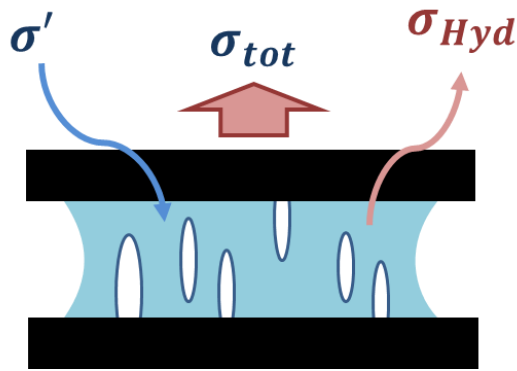


Fig. 55. Schematic of change in hydrostatic σ_H and deviatoric σ' stress due to the mechanism of cavitation, cavity growth and fibrillation. Cavity initiation and growth decreases the geometric confinement of the adhesive layer, thus decreasing σ_H and increasing σ' .

4.3.2 Effect of loading stress level:

Fig. 57 shows the effect of loading stress level on the creep response of single-layered PSA. The higher stress level (blue line, 70 KPa) reduces the time for cavitation but decreases the significance of the transition, as shown in Fig. 57. The drop in the

severity of the transition is speculated to be because of quicker release of hydrostatic stress after cavitation (higher hydrostatic stress, higher cavity growth rate). Therefore, the average creep rate in high-stress condition is twice as much as the low-stress condition. Higher stress around the cavities increases the expansion rate of the cavity but decreases the duration of the transition process.

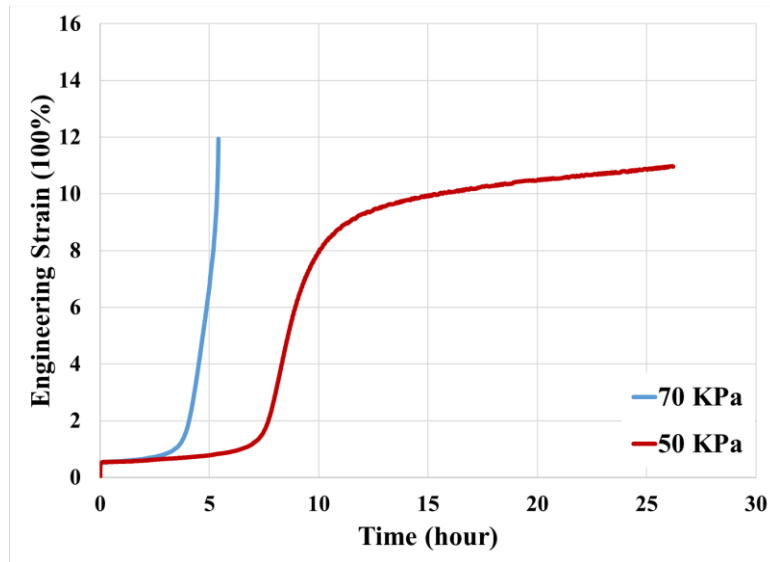


Fig. 56. Effects of stress-level on creep response of single-layered PSA bonded assembly at 70 °C

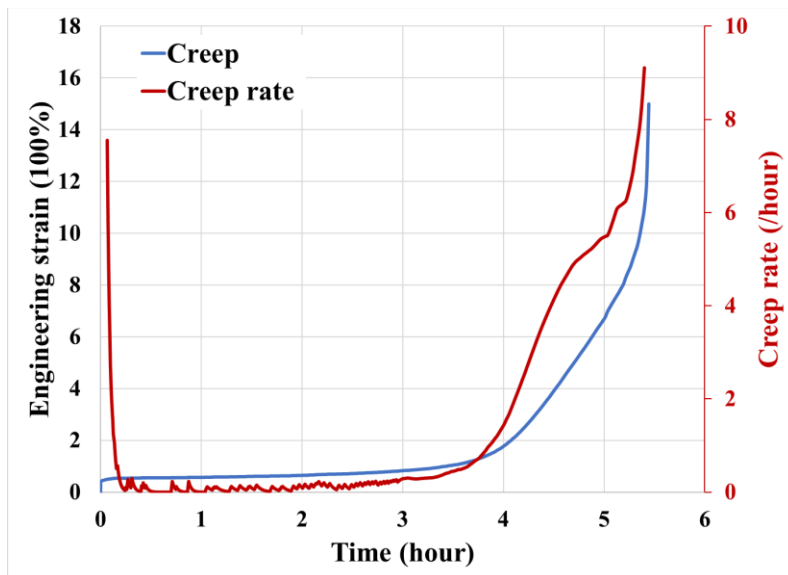


Fig. 57. Creep test result of single-layered PSA under 70 KPa and 70 °C

4.3.3 Effect of bonded assembly geometry:

The creep performance is not only influenced by the loading conditions but also affected by the geometry of the bonded assembly. For example, the creep resistance of the bonded assembly increases as the PSA layer thickness decreases (PSA footprint is controlled). Blue line Fig. 58 is the creep curve of 50 μm thick PSA, which is about 40% of the thickness of the specimen shown in the red line. Compared to the thick sample, it takes much less time (about 30%) to initiate the cavitation in a thinner sample. Under the same footprint, confinement of thinner PSA is higher than thicker PSA. Therefore, the accumulation of hydrostatic stress is much easier in a thin sample than in a thick sample due to the Poisson's contraction (same amount of hydrostatic stress level requires less deformation due to the higher aspect ratio). The higher hydrostatic stress causes earlier cavitation in thin PSA than in the thick PSA. After cavitation, the higher hydrostatic stress can drive the cavities expand faster. Hence, the time span for the transition in the creep curve of thin PSA is shorter than the thick one.

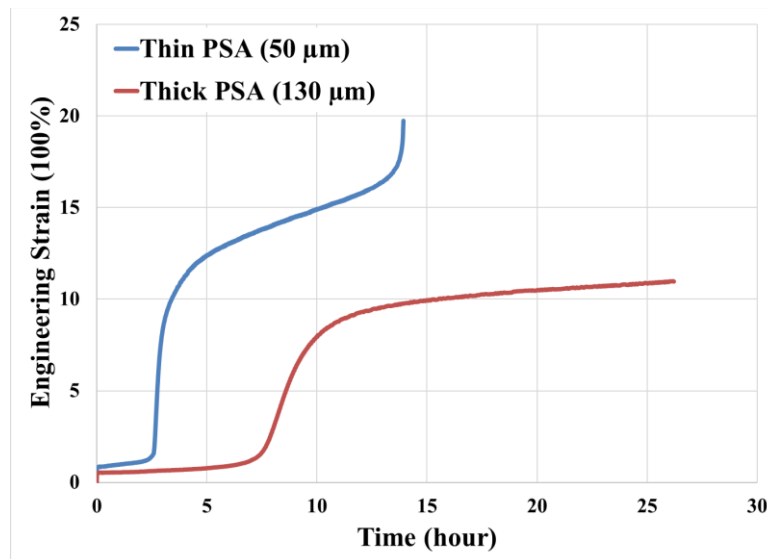


Fig. 58. Creep response of Thin PSA (50 μm) vs. Thick PSA (130 μm) PSA under loading conditions of 50 KPa and 70 $^{\circ}\text{C}$

4.3.4 Effect of substrate surface condition:

The choice of substrate affects the cavitation process and hence affects the creep response. The key features of the substrate are the interfacial wetting (characterized by the interfacial surface energy); and surface roughness. As an example, Fig. 59 shows the effects of surface roughness on the creep of PSA bonded assemblies. In this result, the overall creep resistance decreases by about 65% as the surface roughness increases. The PSA bonded with a higher surface roughness substrate reaches the primary transition in a very short time. This is due to the highly rough surface resulting in more initial defects and less effective bonding area. Surface roughness shown non-monotonic effect on the stress-strain behavior in the Part I of this series study. The results present in the current study are not enough to support the same surface roughness effects on the creep behavior as it on the stress-strain behavior. However, our predictive model, presents in the next section, still indicates the creep response has non-monotonic dependent on the surface roughness of bonding substrate. A more detailed empirical investigation on the relation between the substrate surface roughness and creep response of PSA bonded assembly will be conducted in the future work.

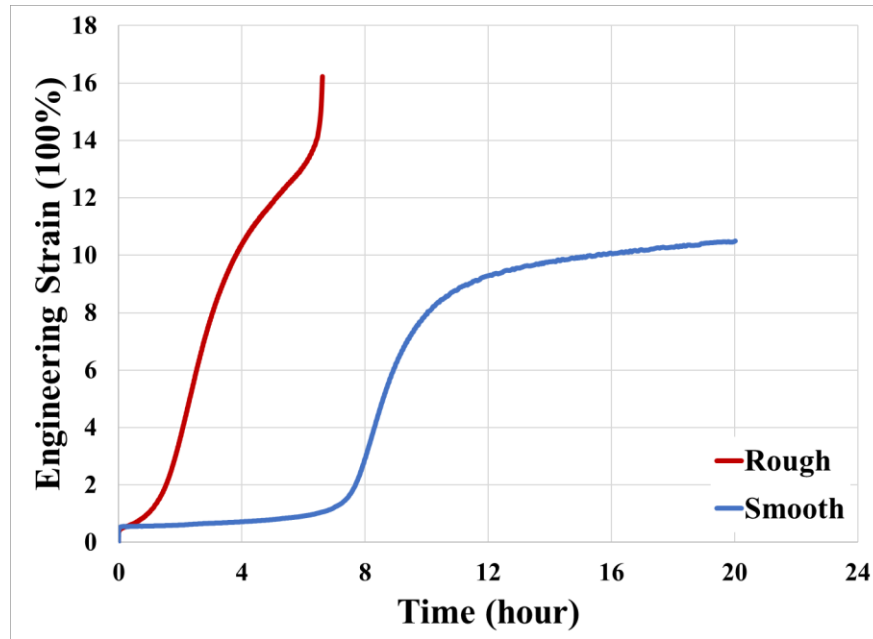


Fig. 59. Effect of surface roughness on the creep responses of PSA bonded with Aluminum substrate with different roughness (blue line, $R_a=715\text{\AA}$; red line, $R_a=3100\text{\AA}$)

Compared to stress-strain response (Huang et al., 2015; Huang et al., 2016; Huang et al., 2017 and Chapter 3), the creep test is more sensitive to the interfacial bonding quality. When PSA is bonded with two rigid substrates, a random amount of air pockets can be trapped at the bonding interface. The trapped air at the bonding interface reduces the effective bonding area, as shown in Fig. 60, and therefore can affect the bonding quality. The actual local stress acting at the interface depends both on the load level and the effective bonding area. Such air pockets can lead to up to 30% variance in the actual stress level acting at the interface of the adhesive bonded assembly.

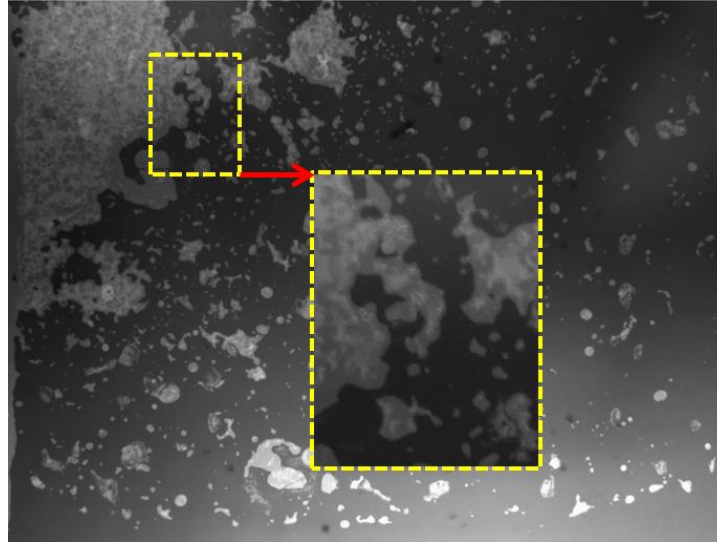


Fig. 60. Marco-voids (air trapped) at the bonding interface during the bonding process when PSA bonded with glass substrates. The dark region is the good bonding region, where adhesive wets well to the substrate; the grey region is the poor bonding region, where the adhesive does not wet the substrate, potentially due to trapped air.

4.4 Creep predictive mechanistic model

Creep deformation can be based on the ‘block’ model with the similar debonding mechanisms, which are cavitation, cavity growth, fibrillation, and interfacial slippage between adhesive and substrate. Competition between these mechanisms results in different rates of released hydrostatic stress stored in the bulk PSA and change of bonded assembly structural stiffness, therefore resulting in a change in creep resistance. The results of the creep tests will be simulated here, using this virtual testing model, to verify the ability of this model to reproduce the test results observed behavior.

The model deformation is adopted from Yamaguchi’s ‘block’ model (Yamaguchi et al., 2006). Yamaguchi presented his ‘block’ model for stress-strain behavior of single-

layered PSA, and we have further developed their model in the Part I of this series study and will modify it in this chapter for creep response.

The elongation deformation is defined by the stretch ratio λ and the global transverse deformation caused by Poisson's effect is described by parameter C , as shown in Fig. 61. Some of the details of this modeling approach are presented in Chapter 2 and Chapter 3 of this study and are repeated here for completeness. Deformation of the block during the loading process is assumed to be parabolic. The material point (ξ, ζ) moves to the spatial position (x, z) , as described by the equations below.

$$x = X_i + \frac{W_0 \xi}{\lambda} + \frac{C_i}{3} (1 - 12\zeta^2) \quad (38)$$

$$z = H_0 \lambda \left(\zeta + \frac{1}{2} \right) \quad (39)$$

where X_i is the location of center of mass of block i , C_i is the parabolic value of block i , W_0 and H_0 are the initial width and height of block and λ is the stretch ratio.

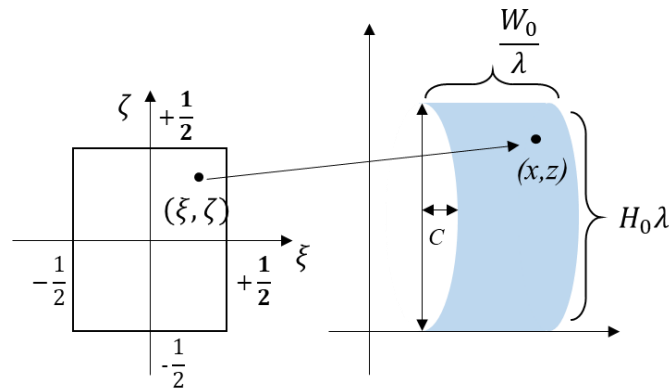


Fig. 61. Material coordinate and spatial coordination to describe the block motion and deformation

Most of the PSAs of interest in this study are highly ductile and capable of cavitation and fibrillation and can deform by more than 1000% of their original shape. Therefore, Green's strain is used to describe the stretched PSA as it is accurate over large strains.

The Green strain tensor for the 2D problem is defined as:

$$E = \begin{bmatrix} \frac{1}{2\lambda^2} - \frac{1}{2} & -\frac{4C}{H^2\lambda}Z \\ -\frac{4C}{H^2\lambda}Z & \frac{32C^2}{H^4}Z^2 + \lambda^2 - 1 \end{bmatrix} \quad (40)$$

where Z is the vertical axis in the block. Since we focus on the stress status near the bonding interface. $\zeta = 0.5$ or $\zeta = -0.5$ is used for evaluating both σ_{zz} (zz -component of deviatoric stress) and σ_{si} (shear stress) at the interface between PSA block and substrate, as shown in Fig. 62. The velocity gradient under thin film assumption is now defined as:

$$\begin{aligned} \frac{\partial v_x}{\partial x} &= -\frac{2\dot{\lambda}}{\lambda} \\ \frac{\partial v_x}{\partial z} &= -\frac{8\xi\dot{C}}{\lambda(t)} \\ \frac{\partial v_z}{\partial x} &= -\frac{8\xi\dot{C}}{\lambda(t)} \\ \frac{\partial v_z}{\partial z} &= \frac{2\dot{\lambda}}{\lambda} \end{aligned} \quad (41)$$

In the current model (as in the literature (Huang et al., 2015; Huang et al., 2016; Huang et al., 2017; Huang et al., 2018)), the width of the fibril is no longer the same as the width of the fibril foot, due to the interfacial mechanical locking. The width of the fibril body follows the volume conservation of an incompressible material (the bulk

PSA is modeled as an incompressible material) while the evolution of the contact length between the fibril foot and substrate follows the detachment model for stretched viscoelastic fibril proposed by Glassmaker (Glassmaker et al., 2008). Details of Glassmaker model were discussed in Chapter 3.

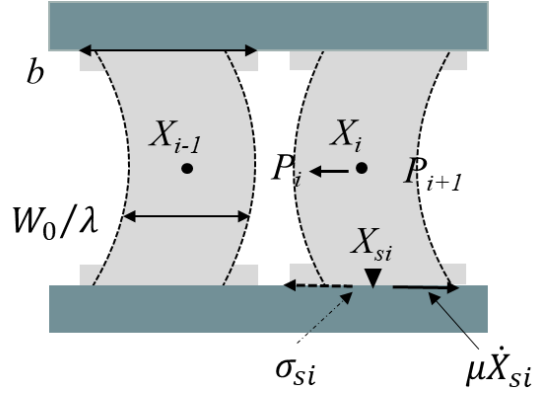


Fig. 62. Force balance of *i*-th block. P_i is the pressure in the region between block *i-1* and *i*. b is the parameter to identify the actual contact length between the fibril foot and bonding substrate

4.4.1 PSA material constitutive model for creep:

The PSA is light cross-linked and can be model by stand linear model. By combining the standard linear model and Green Strain. The constitutive law for bulk PSA is written as:

$$(G_1 + G_2)\sigma_{zz} + \eta\dot{\sigma}_{zz} - \eta\sigma_{zz}\left(\frac{2\dot{\lambda}}{\lambda}\right) = G_1\eta\left(\frac{2\dot{\lambda}}{\lambda}\right) + \frac{1}{2}G_1G_2(\lambda^2 - 1) \quad (42)$$

$$(G_1 + G_2)\sigma_{si} + \eta\dot{\sigma}_{si} - \eta\sigma_{zz}\left(\frac{4\dot{C}}{H_0\lambda}\right) = G_1\eta\left(\frac{4\dot{C}}{H_0\lambda}\right) - G_1G_2\frac{4C}{H^2\lambda} \quad (43)$$

Since the classic ‘block’ model was originally proposed for modeling stress-strain behavior of PSA bonded assemblies, the formulation needs some modification for capturing the creep response, due to the different loading histories of stress-strain and

creep tests. The evolution of creep deformation is highly dependent on the history of the stress components. Therefore, to obtain the full history of the deformation process, the initial stress ramp-up process, shown in Fig. 63, must be included in the creep model. In Phase I, the total stress of the entire PSA bonded assembly is ramped-up to the desired stress level for creep testing. The stress ramp-up phase is a strain-controlled process and is finished within a very short time. Then, in Phase II (constant-stress creep phase), the total stress accumulated at the last step of Phase I is maintained constant. Unlike the stress-strain process, creep deformation is a stress-controlled process. The numerical algorithm of the creep model is shown in Fig. 64.

The same standard linear constitutive model is used for the bulk PSA, both during the initial ramp-up phase and also during the subsequent constant stress creep phase. The constitutive equations for each phase (displacement-controlled and stress-controlled processes) are shown in Eqs. (44) and (33), respectively. Equations of stress and strain components along zz direction are shown.

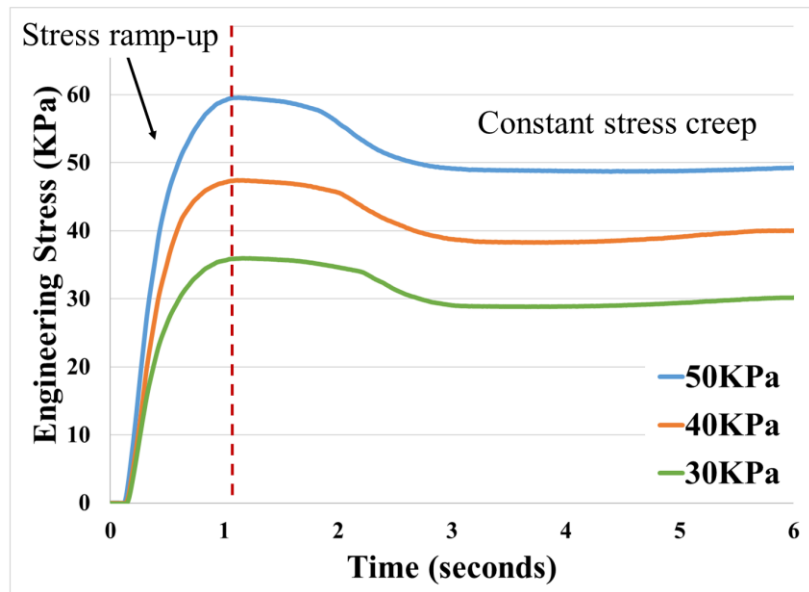


Fig. 63. Initial stress ramp-up in creep test under different preset loading stress level. Targeted stress level is expected to apply on the test coupon within the first 3 seconds of the test.

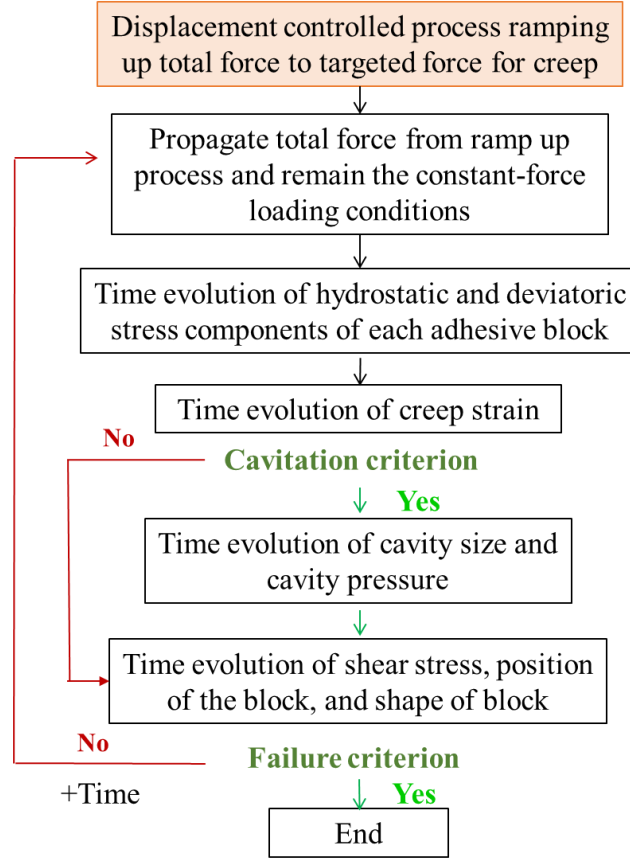


Fig. 64. Modeling algorithm of single-layered creep model

$$\dot{\sigma}_{zz} = \frac{1}{\eta} \left(\frac{1}{2} G_1 G_2 (\lambda^2 - 1) + (G_1 + G_2) \eta \left(\frac{2\dot{\lambda}}{\lambda} \right) + \eta \sigma_{zz} \left(\frac{2\dot{\lambda}}{\lambda} \right) - G_1 \sigma_{zz} \right) \quad (44)$$

$$\dot{\lambda} = \frac{\lambda}{2\eta(G_1 + G_2 + \sigma_{zz})} \left[G_1 \sigma_{zz} + \eta \dot{\sigma}_{zz} - \frac{1}{2} G_1 G_2 (\lambda^2 - 1) \right] \quad (45)$$

Cavitation criterion

The stress level in creep testing is lower than in stress-strain testing under specific range of strain rate. However, plenty of cavities are still observed during the long-term creep deformation process. Therefore, in the creep model, the critical stress criterion is

no longer suitable for cavity initiation, because of the dominance of diffusion-induced cavitation. To account for this difference in Chapter 3, a strain-based cavitation criterion is used for the creep model. The threshold value of the strain for creep cavitation is deduced from the experimental results.

Cavity growth criterion

In creep deformation, there are two deformation regions. One is the far-field slow deformation region, which is in the bulk adhesive, far from the cavity, and the other is the near-field rapid deformation region, which is in the region near the cavity, especially when the cavity is in the initial rapid growth stage. Therefore, we assign different relaxation time, τ^0 and τ^∞ , for these two fields where superscript 0 represents relaxation time under low strain rate and superscript ∞ represents relaxation time in the rapid deformation region. Therefore, when the deformation rate of bulk adhesive in the near-field of the expanding cavities is larger than deformation rate of the bulk adhesive in the far-field of the cavities, the expansion of cavities in a standard linear viscoelastic medium is modified from the original form Eq. (13) and written by:

$$\dot{R} = \frac{R}{4\eta^\infty} \left(-P_i - \frac{2\gamma}{R_i} - \frac{G}{2} \left\{ 5 - \left(\frac{R_{0i}}{R_i} \right)^4 - 4 \frac{R_{0i}}{R_i} \right\} \right) \quad (46)$$

where γ is the surface tension of the adhesive, R_{0i} and R_i are the initial and the current cavity radius, respectively, and G is the modulus of the standard linear solid.

When the cavity size is large enough, the growth rate of the cavity decreases. The deformation rate of the bulk adhesive in the near-field of the cavities become similar to bulk adhesive in the far-field, the expansion of cavities is defined by:

$$\dot{R} = \frac{R}{4\eta^0} \left(-P_i - \frac{2\gamma}{R_i} - \frac{G}{2} \left\{ 5 - \left(\frac{R_{0i}}{R_i} \right)^4 - 4 \frac{R_{0i}}{R_i} \right\} \right), \quad (47)$$

Stress component in creep model

The total stress during the stress ramping up process is

$$\sigma_{tot,z}^i = P_0 + (\sigma_{zz}^i - \bar{P}^i) b^i \quad (48)$$

where $\bar{\dots}$ stands for the average over all blocks, b represents the ratio of actual bonding area to the area of a substrate.

In the constant stress creep process. The total stress is held constant from the last step of stress ramp up. The deviatoric stress component σ_{zz} at the bonding interface evolves as follows:

$$\sigma_{zz}^i = \frac{(\sigma_{tot,z}^m - P_0)}{b^i} + \bar{P}^i \quad (49)$$

where superscript m represents the last step of initial stress ramps up. Total stress remains constant during the creep process. However, the partitioning between the hydrostatic stress and the deviatoric stress continuously evolves, leading to the change in the creep rate.

4.4.2 Creep response of single-layered PSA bonded assembly:

Fig. 65 shows the creep curve predicted by this model, for the parameter set from Table 1 with the constant loading stress of 50 KPa. Parameters with subscript * are used as reference metrics for the rest of the parametric studies. As seen, during the initial stages of deformation, there is a steady creep rate. As the cavitation initiates (approximately at a strain of 180%), we see a transient phase where the creep strain rate increases dramatically and reaches its peak within a very short period and then

decreases significantly and quickly stabilizes at a lower value close to that in the initial stage. The duration for this transient phase is about 10% of the total creep debonding process, while the corresponding creep strain accumulation during this transient phase is more than 70% of the total creep deformation. These values are consistent with the empirical results used for model calibration. MATLAB code for the single-layered creep model presents on Appendix A6.

Table 2: Simulation parameters

Parameter (unit)	Value
PSA thickness H_0 (m)	1.3×10^{-4}
PSA width W_0 (m)	7×10^{-3}
Stress level (Pa)	50000
Relaxation time (s)	3000
Elastic modulus G_1, G_2 (Pa)	35, 250
Strain hardening coefficient	1.2
PSA surface energy γ_p (mJ/m ²)	0.03
Substrate surface energy γ_p (mJ/m ²)	0.06
Initial cavity R_z^* (m)	4.3×10^{-7}
Roughness wavelength X_s (m)	5×10^{-6}
PSA penetration parameter m	80
Number of blocks	30
Time step (s)	0.1

Fig. 65 shows the prediction of creep response of single-layered PSA bonded assembly under a loading stress of 50 KPa. In this model, due to the use of rate-

dependent viscosity, the viscosity around the cavities is 100 times lower than the viscosity in the rest of the bulk area.

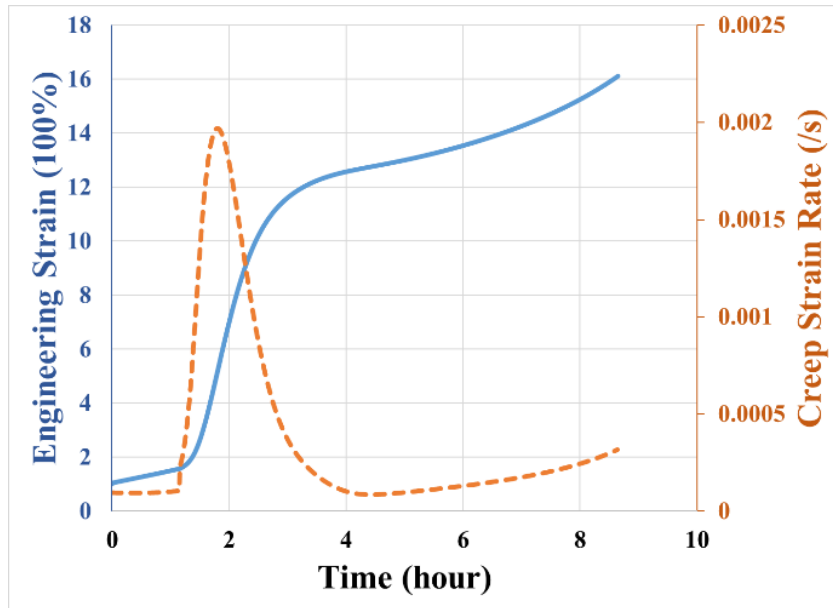


Fig. 65. Model prediction of creep response of PSA bonded assembly based on the parameter on Table 2

4.4.3 Deformation and history of stress component:

The corresponding history of relevant stress components is shown in Fig. 66. The loading force is the average far-field force applied on the bonding substrate and is maintained constant during the entire creep deformation. The hydrostatic part of the stress field dominates over the deviatoric part during the initial stage of the creep deformation due to the high geometric confinement. However, it starts decreasing as the stresses start relaxing due to cavitation initiation. By the end of the transition phase, more than 90% of the hydrostatic stress has been released. In contrast, the z -component of deviatoric stress starts to increase as the cavitation initiates and the rate of increase slows down towards the end of the transition phase (shown by the shaded region in Fig.

66). There is a noticeable increase in the z -component of deviatoric stress in the final stage of the creep response. The increment in the z -component of deviatoric part is due to the initiation of partial delamination between PSA fibril and bonding substrate. The delamination process decreases the actual length of the PSA fibril foot, thus increasing the actual stress acting in the adhesive fibril.

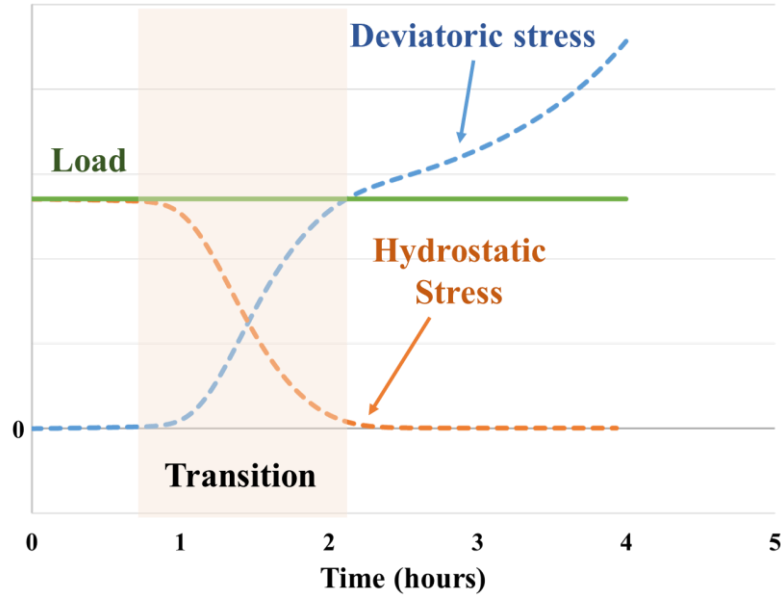


Fig. 66. History plot of z -component of the deviatoric stress tensor and hydrostatic stress in the foot area of PSA fibril

4.4.4 Effects of loading stress level:

The creep stress is introduced by the rate-controlled stress-strain process. The stress ramp-up process is automatically terminated by the algorithm as the total force reaches the preset level for each creep test. This process is shown in Fig. 65, and affects the methods that are used to apply the external load or boundary condition. Fig. 67 shows the effects of loading stress level on creep model prediction. The transition under the high-stress level shifts to the end of the creep deformation. Which means that the

plateau region between the primary transition and the tertiary creep reduces as the stress level increases.

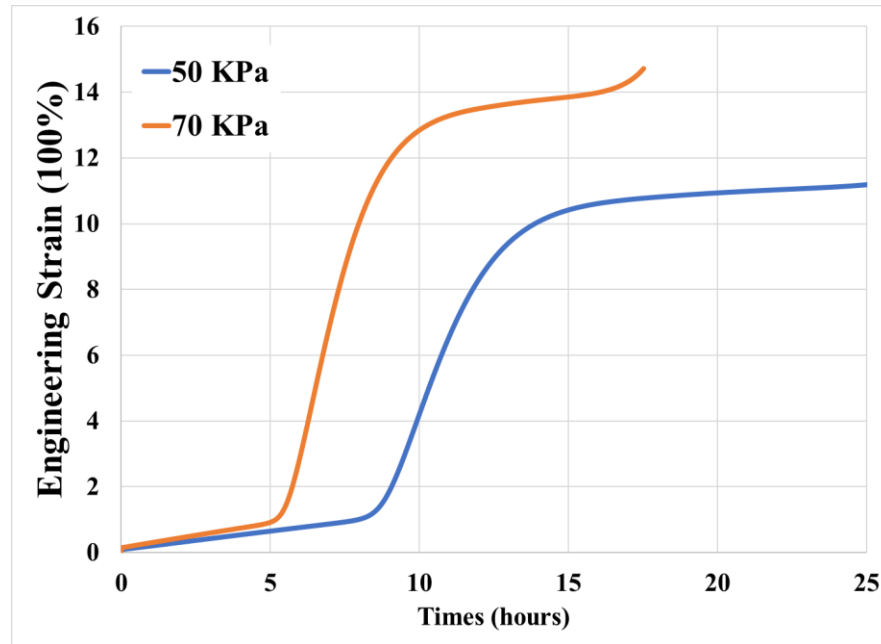


Fig. 67. Effects of loading stress level on creep model prediction

4.4.5 Effect of adhesive modulus and viscosity:

Different PSA materials have different modulus and viscosities. The mechanistic model is sensitive to both sets of adhesive material properties. Fig. 68 clearly indicates that the creep curves for different viscosities of the adhesive exhibit different degrees of transition and different total creep strain histories for a given stress. Increases in the shear modulus of the adhesive leads to decreases the deformation during the transition process in the creep response. The lower the modulus, the softer the material, the more significant the strain you are expecting within the transition.

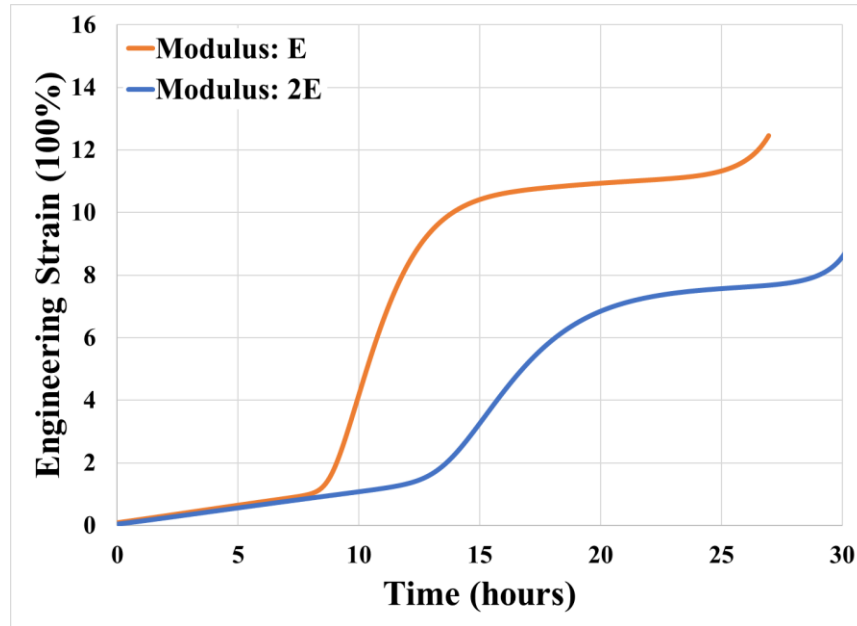


Fig. 68. Effects of adhesive modulus on creep model prediction

Fig. 69 shows how the creep curve depends on the stress relaxation time τ (or viscosity, η) of the adhesive material. The time span for the primary transition decreases and the peak value of the creep rate during the primary transition increases with the increase of τ (or increase of η , when modulus E is controlled). The decrease in the time span is because the cavities in media with low relaxation time (low viscosity) expands faster than the cavities in media with high relaxation time (high viscosity). Thus, the transition can finish within a shorter period.

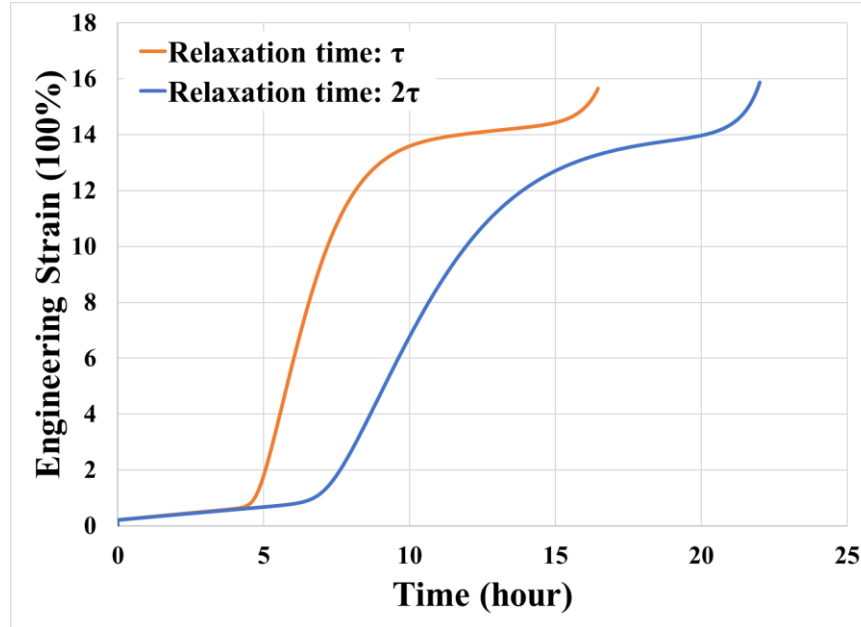


Fig. 69. Effects of PSA stress relaxation time on creep model prediction

4.4.6 Effect of substrate surface roughness:

In Chapter 3, non-monotonic dependent of stress-strain response on the bonding substrate surface roughness is discussed and included in the mechanistic model with simplified model for capturing the effects of surface topology on the effective bonding area and initial defect size. Up to a moderate level of roughness, surface roughness helps to increase the effective bonding area. Beyond a critical level of roughness, surface roughness can affect the size of initial interfacial defects (micro-voids) (Huang et al. 2018). Simulation results, Fig. 70, show that creep resistance of PSA bonded assemblies has a non-monotonic effect on the substrate surface roughness. Up to a moderate level of roughness, surface roughness helps to increase the creep resistance. The non-monotonic effect is due to larger effective bonding area and better interfacial mechanical locking. However, beyond a critical value, interfacial roughness can reduce the creep resistance by affecting the size of initial micro-voids at the bonding interface.

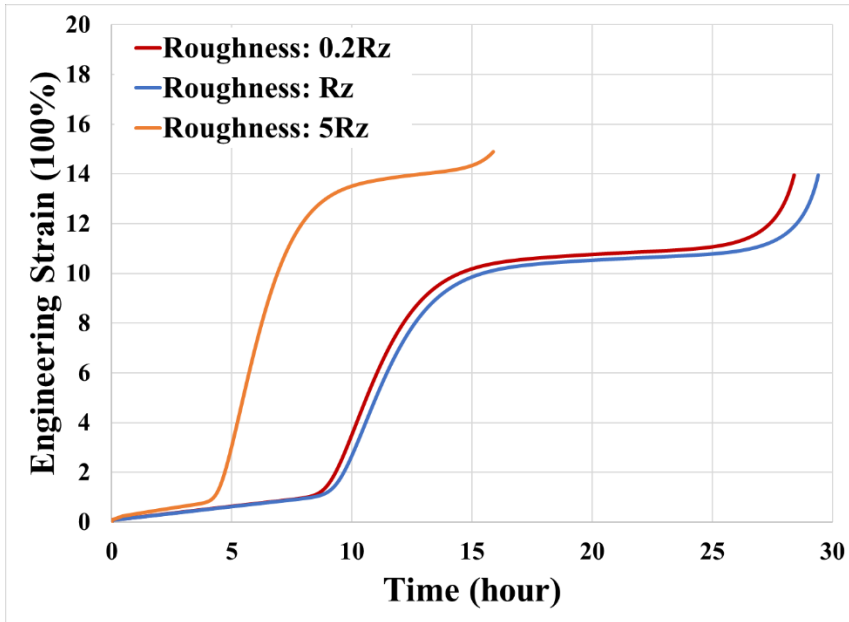


Fig. 70. Effect of substrate surface roughness on creep model prediction

4.4.7 Effect of substrate surface free energy:

Simulation results, as shown in Fig. 71, indicate that substrate surface free energy shows positive effects on the creep resistance. The adhesive wets better on the surface of substrates with higher surface energy, therefore increasing the adhesion strength and interfacial mechanical locking and decreasing the chance of premature fibril foot delamination during the deformation process.

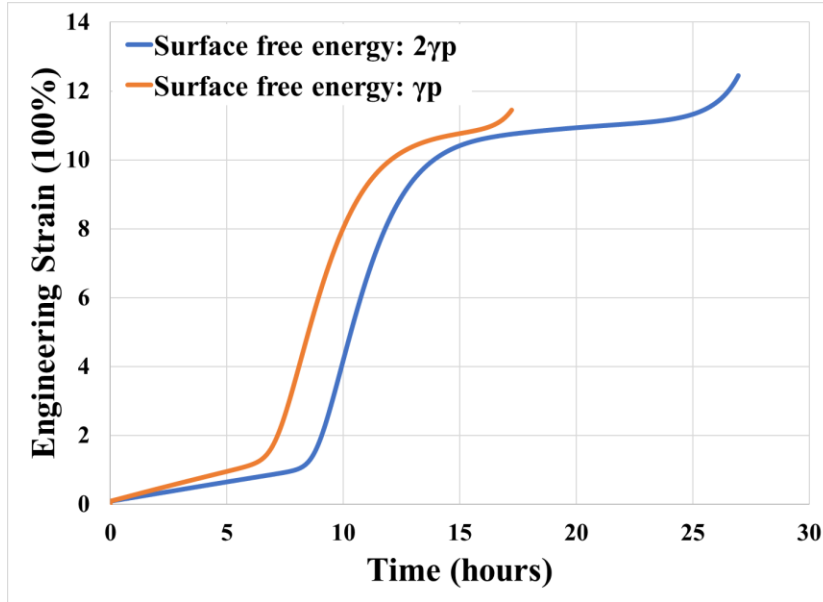


Fig. 71. Effect of substrate surface free energy on creep model prediction

4.5 Conclusion

Multiphase creep response is observed when rigid substrates are bonded with highly ductile single-layered PSA. The transitions in the creep curve are the result of competition between mechanisms of softening due to cavitation and stiffening due to fibrillation during the debonding process. The interplay of these mechanisms is highly dependent on the adhesive properties and surface properties of the bonding substrate.

A predictive mechanistic model, which is based on mechanisms of cavitation, the growth of cavities, fibrillation and interfacial mechanical locking, is presented to capture the tensile creep response of single-layered PSA/substrate bonded assemblies. The predictive model shares a similar modeling technique with the stress-strain model presented in Chapter 3 but uses a different algorithm due to the differences in the loading history. The proposed creep model is capable of reproducing the unique response of uniaxial creep of single-layered PSA bonded with rigid substrates.

Moreover, it is able to provide insights about the effects of PSA properties (modulus and viscosity) and substrate surface properties (surface free energy and roughness), on the creep response of PSA/substrate bonded assembly. Parametric studies using the predictive model are carried out to demonstrate the tunability and sensitivity of the creep model to different material and model parameters and the loading stress level as well. The model results can be used as creep constitutive model for single-layered PSA bonded assembly for commercial FEA tools (detailed approaches discussed in Appendix A8)

Chapter 5. Stress-Strain and Creep Response of Assemblies Bonded with Double-Layered PSA

5.1 Abstract

The mechanical behavior, i.e. stress-strain and creep response, of adhesive bonded assemblies containing double-layered pressure sensitive adhesive (PSA) is investigated in this chapter, using a combination of experiments and mechanistic modeling. PSAs usually come in two laminated configurations: single-layered PSA (only a layer of adhesive) and double-layered (two adhesive layers on both sides of a thin carrier layer). Both configurations are widely used for packaging consumer electronic products because permanent bonds can be easily formed at room temperature, thereby avoiding thermal damage to the electronics during assembly. These devices are expected to experience complex hygro-thermo-mechanical loading conditions during their life cycle, so a thorough understanding of the mechanical behavior of PSA is necessary. In this study we focus on the response to external mechanical loading only. Mechanical behavior of single-layered PSA bonded assemblies has been presented by the Chapter 3 and Chapter 4 and authors elsewhere in the literature (presents in in Chapter 1). This chapter focuses on the mechanical behavior of adhesive bonded assemblies using double-layered PSA.

Compared to the single-layered PSA bonded assembly, double-layered PSA bonded assemblies show more complex mechanical behavior, such as multiple transitions in their stress-strain and creep curves. The severity of the secondary transition can increase with the thickness of the carrier layer. The reason for these secondary transitions is hypothesized to be due to nonuniform sequential cavitation of the

adhesive at each interface (interfaces with substrates and with carrier layer). This nonuniformity may be influenced by (i) anomalies in the local surface wettability of the bonding substrate and carrier layer; (ii) variations in the flexural rigidity of the carrier layer due to variations in the thickness; and (iii) variations in the transverse constraint on the adhesive layer caused by variations in the in-plane stiffness of the carrier layer. The effect of flexural rigidity of the carrier layer is experimentally investigated, and a simplified mechanistic model based on the out-of-plane constraint from the carrier layer is developed. The resulting displacement histories exhibited multiple transitions, which resulted in the transitions in the stress-strain and creep behavior.

5.2 Introduction

Double-layered PSA systems, as shown in Fig. 72, are used as widely as single-layered PSA systems. In particular, the consumer micro-electronics industry uses a large number of PSA bonded assemblies for the construction of components. due to the ease of design, affordability, low processing temperature, and additional structural support from carrier layer. The presence of carrier layers can provide additional structural support or can act as a cushion for the assembly depending on what kind of carrier layer is used.

PSAs are usually very soft, compliant, highly dissipative polymers, such as acrylics, butyl rubber, natural rubber, nitriles, etc. The carrier layer usually consists of a relatively stiff polyethylene terephthalate (PET) sheet or a relatively compliant polyurethane (PU) foam. Normally the PSA bonded assemblies show superior strength in shear direction but are more vulnerable to loading along the tensile (peel) direction.

In field applications, multiaxial stress states in the adhesive layer due to mechanical and thermal loading can result in critical deformation along its tensile direction. This study focuses on the mechanical response (short term stress-strain response and long-term creep response) to uniaxial tensile stresses along the peel direction.

Experiments (uniaxial tensile tests) of PSA bonded assemblies show significant differences in the stress-strain and creep behaviors between single-layered and double-layered PSA systems. The main difference is that additional transitions in the stress-strain and creep response are observed in double-layered PSA bonded assemblies. The additional transitions are believed to be due to staggered bimodal interfacial cavitation of the PSA adhesive at different interfaces (interfaces with the substrate layers and interfaces with the carrier layer). However, there is very limited literature on this unique multi-phase mechanical response of double-layered PSA bonded assemblies, i.e. multiple transitions in stress-strain and creep curves. Yamaguchi et al. indicated that the additional transition in the force-displacement curve during a tack test is caused by the bimodal force-displacement curves of the two adhesive layers and the bending of the inner film (Yamaguchi et al., 2008). They reported that this multi-modal force-displacement behavior segments the PSA system into multiple asymmetric domains and that this phenomenon is very sensitive to the flexural rigidity of the carrier layer. Yamaguchi et al. have also proposed a simple ‘block’ model for single-layered PSA system, but do not attempt the modeling of double layered PSA bonded assemblies. Furthermore, their single-layered PSA model lacks some of the detailed physics needed to explain the full non-linear force-displacement curve of a PSA bonded assembly, as we have discussed elsewhere in Chapter 3.

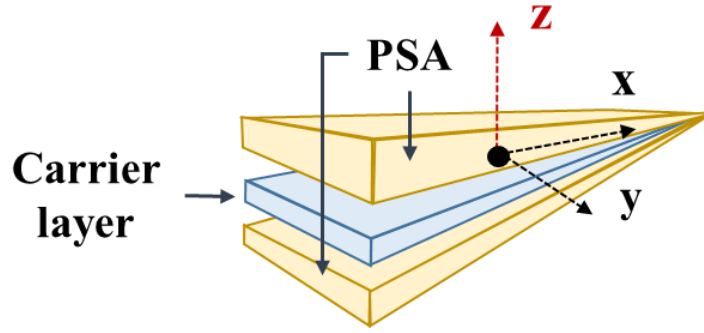


Fig. 72. Schematic of double-layered PSA system and interested loading direction

The previous chapters present how the bonding conditions, substrate surface properties, and adhesive material properties can affect the stress-strain and creep behaviors of single-layered PSA bonded assemblies. We also presented an advanced version of the single-layered ‘block’ model that is able to capture the unique characteristic features in the corresponding PSA/substrate assemblies.

The purpose of this paper is first to extend the study to double-layered PSA bonded assemblies, by investigating the underlying physics of the debonding process of double-layered PSA bonded assemblies. We experimentally investigate the effects of carrier layer thickness and discuss the different failure sites. Then, the underlying physics is incorporated into the advanced ‘block’ model (proposed by us for the single-layered PSA system) such that it captures the empirically observed additional transitions in the stress-strain and creep response of double-layered PSA bonded assemblies. As discussed above, this unique multi-phase stress-strain behavior is hypothesized to be due to nonuniform sequential cavitation in the bulk adhesive and at each interface (with substrates or with carrier layer). This nonuniformity may be influenced by: (i) anomalies in the local surface wettability of the bonding substrate and carrier layer; (ii) variations in the flexural rigidity of the carrier layer due to

different thickness of carrier layer; and (iii) variations in the lateral constraint on the adhesive layer caused by the different in-plane stiffness of the carrier layer. The proposed double-layered ‘block’ model is able to mechanistically capture some characteristic features of the stress-strain and creep curves of double-layered PSA bonded assemblies, including a primary transition, a secondary transition, and strain hardening before and after the secondary transition. The modeled PSA behavior is based on the out-of-plane constraint provided by the carrier layer and nonuniform interfacial bonding strength at the interfaces with the carrier layer and substrate. The effect of the in-plane constraints (caused by the carrier layer) on the PSA stress field and on the resulting cavitation is deferred to future work.

5.3 Experiment

In this study, the configuration of the tensile test coupon is two aluminum substrates bonded together with a double-layered PSA system, as shown in Fig. 73. Three different carrier layer thicknesses are tested, 30, 80 and 130 μm , with a constant PSA thickness of 50 μm on both sides of carrier layer. Therefore, the total thickness of the double-layered PSA systems used in this study are 130, 180 and 230 μm , respectively. The bonded assembly has a square footprint of 7 mm x 7 mm. The adhesive material and substrate material are controlled parameters in this chapter of study.

Uniaxial tensile tests are conducted on a commercial Dynamic Mechanical Analyzer (DMA). The loading rate in the displacement-controlled stress-strain test is 0.02 mm/s at room temperature. The loading condition of the stress-controlled creep test is 50 KPa at 70 °C. Such debonding conditions were proved to show the most pronounced effects of cavitation and fibrillation on the stress-strain and creep responses of selected single-

layered PSA systems with the same adhesive material in the investigations in Chapter 3 and Chapter 4. The controlled lamination conditions for preparing the test samples is room temperature, 45 psi bonding pressure, 45 s bonding time, and 72 hrs post-bonding aging at room temperature. The bonding conditions are determined by followed the protocol proposed in Appendix A1. A commercial adhesion promoter is used to improve the wettability of the bonding surfaces of the aluminum substrates. For the stress-strain test, five replicates are used; for creep test, three replicates are used.

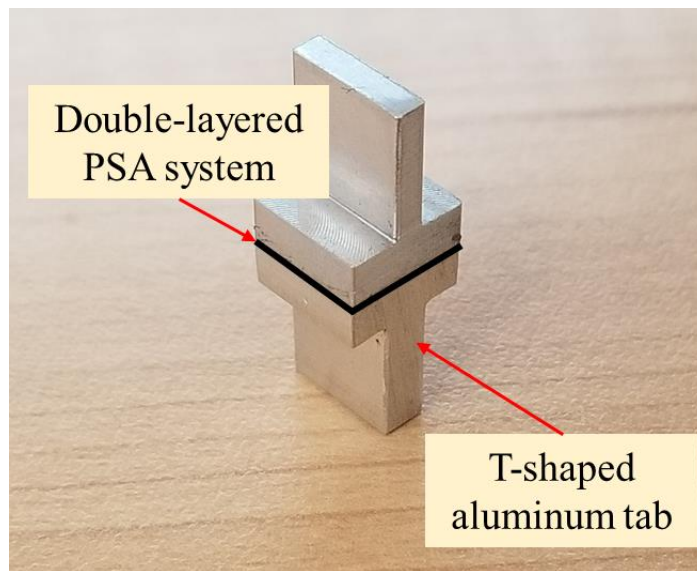


Fig. 73. Double-layered PSA system bonded with aluminum tabs

Previous studies in this dissertation and literature (discussed in literature review in Chapter 2) indicated that there are more transitions in the stress-strain curves of double-layered PSA bonded assemblies than of single-layered PSA bonded assemblies. Preliminary experiments in the present study also indicated the same for creep response. The additional transition (sequential cavitation and fibrillation) is due to the additional bonding interface and mechanical constraints introduced by the carrier layer.

In this study, we focus on varying the flexural rigidity of carrier layer and thickness of the PSA layers to understand the effect on the stress-strain and creep response of PSA bonded assemblies. The flexural rigidity of the carrier layer increases nonlinearly with its thickness when the material properties are held constant. The effects of carrier layer surface properties, e.g. surface free energy and surface roughness will be addressed in the future work.

5.3.1 Stress-strain behavior of double-layered PSA:

Fig. 74 shows an average stress-strain curve with standard deviation, for the peak stresses during the primary and secondary transitions. The blue line is for PSA system with 130 μm carrier layer and the amber line is for PSA system with 30 μm carrier layer. The engineering strain value is estimated based on the PSA thickness, excluding carrier layer thickness. In other words, the assumption here is that the extension of the carrier layer in the loading direction is insignificant, compared to that in the PSA layers. As the carrier layer's thickness increases, the variation of the stress-strain response increases, which is clearly shown by the standard deviation.

Fig. 75 shows the variability of the secondary transition of the PSA bonded assembly with the thick carrier layer (130 μm). At the loading rate investigated here, the stress drops during the transition ranges from a nearly unobservable drop (red line) to about a 40% drop (green line). In contrast, the variability of the secondary transition of the PSA with the thin carrier layer (30 μm) is much smaller. This difference is caused by the lower flexural rigidity of the thinner carrier layer, which helps the carrier layer to deform and buckle locally, this reducing the effect of the global asymmetric deformation field seen for the thick carrier layer due to both the non-uniform initial

defects (micro-void) distribution and the non-uniform non-wetted area (macro-void) distribution at the bonding interface between PSA and substrate, as shown in Fig. 76, when PSA bonded to transparent glass substrate. In practice, macro-voids are formed during the bonding process due to random amounts of air trapped at the interface. This is very common when a thin layer of PSA is bonded with two rigid substrates. Besides that, the roughness pattern (which influences the initial defect distribution) of the two bonding substrates will not be identical and the adhesion strength of PSA/carrier interface could be different as well. Thus, the stress distribution in the two adhesive layers will not be the same and also the stress distribution will be non-uniform even within each adhesive layer.

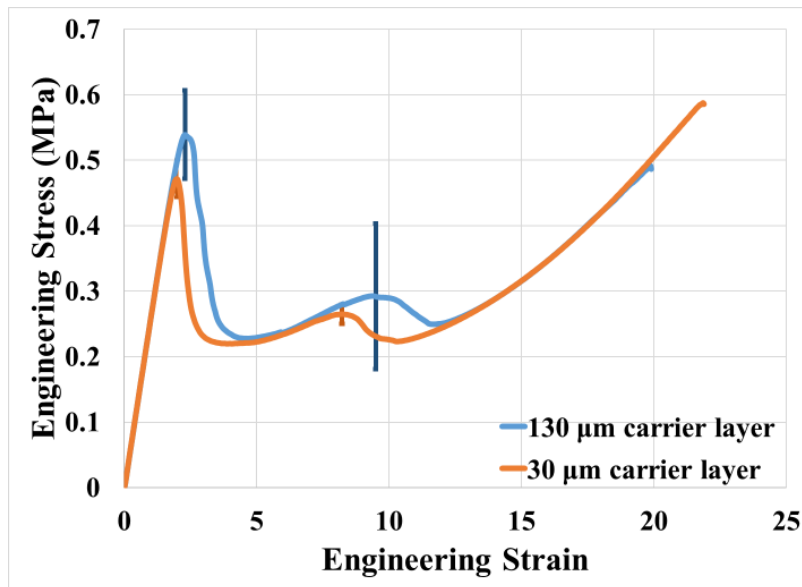


Fig. 74. Effect of carrier layer thicknesses on the stress-strain performance of PSA bonded assembly (carrier thickness: 30 vs.130 μm)

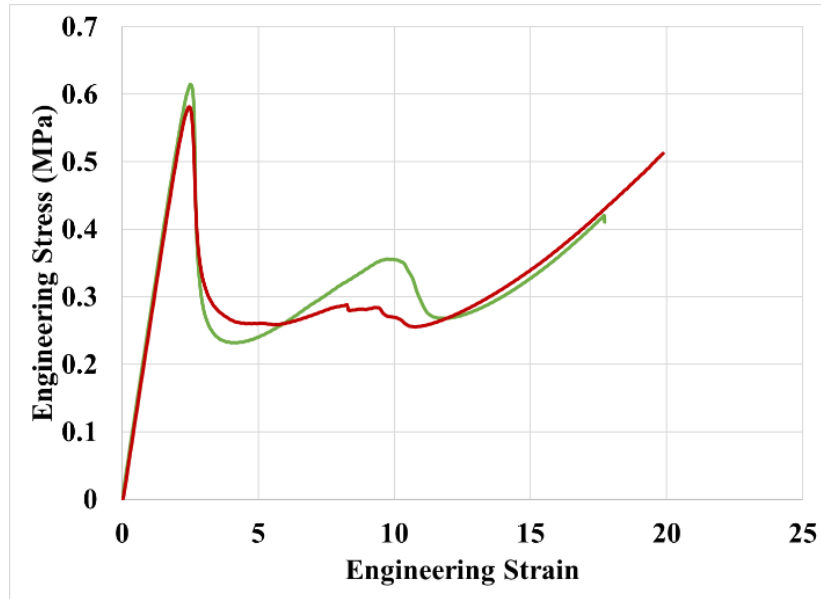
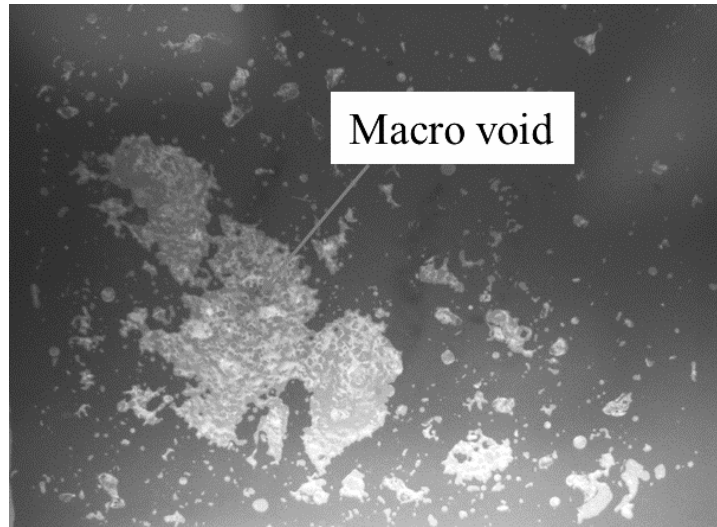


Fig. 75. Different response of secondary transition when PSA on thick carrier layer



(a)



(b)

Fig. 76. Initial macro void at the bonding interface between PSA and glass substrate:

(a) at the corner region; (b) at the center region

A thick carrier layer is not be able to flex sufficiently to accommodate the nonuniform stress distribution caused by the nonuniform cavitation rates in the two adhesive layers on either side of the carrier layer. When testing double-layered PSA with different carrier layer thickness, three cases are observed.

Case I: When the carrier layer is thick and the initial voids are uniformly distributed over the bonded assembly footprint, cavitation occurs simultaneously over the entire footprint sequentially on both sides of the carrier layer, as shown in Fig. 77.

Case II: When the carrier layer is thick, but the initial void distributions are nonuniform (for example, with macro-void at one side of the bonding interface, as shown in Fig. 76 (a)) the resulting nonuniformity in the stress and deformation distribution could tilt the thick carrier layer, as shown in Fig. 78. In this example, the cavitation process initiates at one end of the bonding interface and propagates to the other.

Case III: When the carrier layer is thin, it can flex enough to wrinkle due to transverse Poisson shrinkage of the PSA. This generates local variations in the stress field that dilutes the effect of any global asymmetries in the stress fields, that may be caused by nonuniform cavitation rates. As shown in Fig. 79, significant wrinkling of carrier layer, highlighted by dotted line, is caused by the non-identical stress in the upper and bottom layer of PSA. These local variations in the stress field obscure the effects of global asymmetry, if any.

The first case results in the most severe secondary transition in the stress-strain curve (green line in Fig. 75) because each layer of adhesive cavitates sequentially; the second case results in a less noticeable or non-noticeable secondary transition (red line in Fig. 75). The third case generates more consistent stress-strain curve with mild secondary transition, as shown in orange line in Fig. 74, because the thinner carrier layer shows weaker effects on the stress-strain response of double-layered PSA bonded assembly. Besides, the initial defect distribution is hard to control, since it can be caused by both the roughness pattern of the bonding substrate and the size and location of the macrovoid at the interface between PSA and rigid substrate produced during the lamination process. Therefore, the magnitude of the secondary transition in stress-strain curves is influenced by both the initial defect distribution and the flexural rigidity of the carrier layer.

The first case results in the most severe secondary transition in the stress-strain curve (green line in Fig. 75) because each layer of adhesive cavitates sequentially; the second case results in a less noticeable secondary transition (red line in Fig. 75). The third case generates more consistent stress-strain curve with mild secondary transition, as shown

in amber line in Fig. 74, because the thinner carrier layer shows weaker secondary transition on the stress-strain response of double-layered PSA bonded assembly. Besides, the initial defect distribution is hard to control, since it can be caused by both the roughness pattern (micro-void) of the bonding substrate and the size and location of the macro-void at the interface between PSA and rigid substrate produced during the lamination process. Therefore, the magnitude of the secondary transition in stress-strain curves is influenced by both the initial defect distribution and the flexural rigidity of the carrier layer.

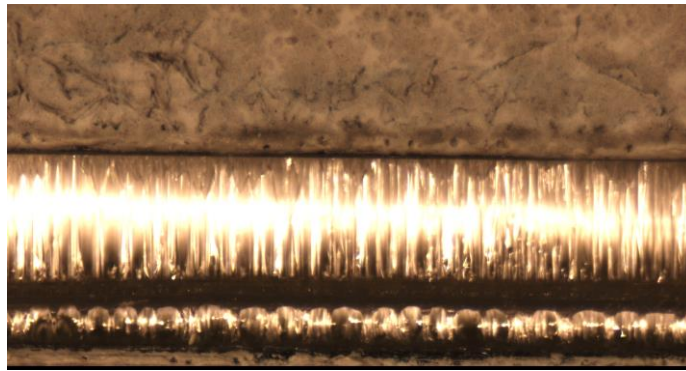


Fig. 77. Flat of thick carrier layer due to force balance by high flexible rigidity of thick carrier layer

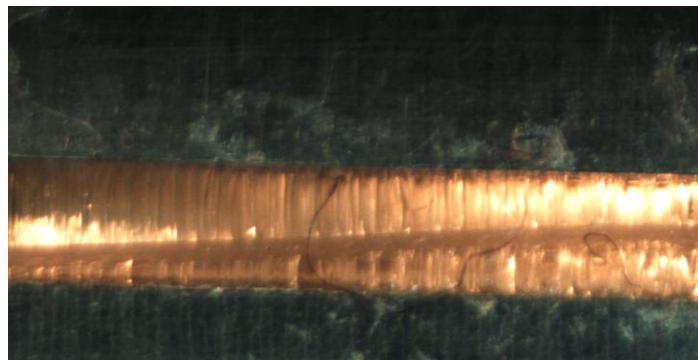


Fig. 78. Global tilted of thick carrier layer due to asymmetric stress distribution

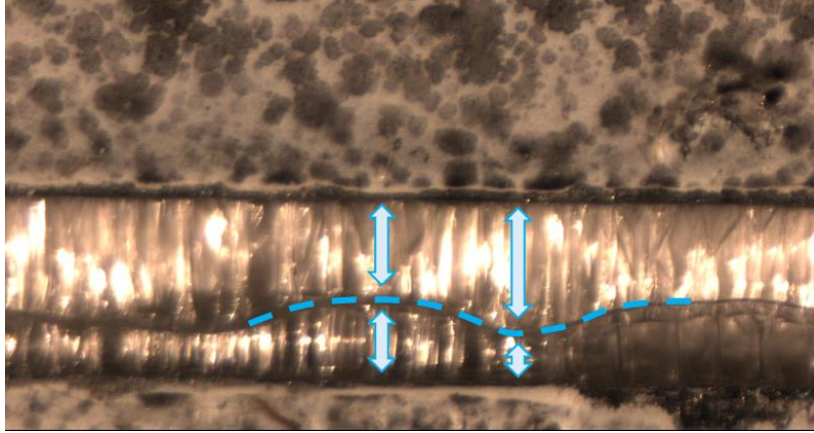


Fig. 79. Wrinkling of thin carrier layered due to transverse Poisson contraction

5.3.2 Creep of double-layered PSA:

Fig. 80 shows the creep response of a select double-layered PSA system. Multiple transitions have divided the creep curve into several phases (as shown in the colored regions). The presence of carrier layer allows the subsequent hydrostatic stress release in the different adhesive layer. Therefore, compared to the creep curve of single-layered PSA, as shown in Fig. 81, additional transitions are shown in the creep curve of double-layered PSA bonded assemblies. Similar to the stress-strain curve, the first transition, region II, in the creep curve is more pronounced with a more significant change in the slope, and the second transition, Region IV, is shallower. The creep rates in the different constant creep phase, Region I and III are also different. In Region V, the fibril foot starts to delaminate from the bonding substrate and loss adhesion. The adhesive bonded assembly will fail when the effective fibril foot area cannot sustain the pulling stress.

Fig. 80 shows the creep response of a select double-layered PSA system. Multiple transitions have divided the creep curve into several phases (as shown in the colored regions). The amber regions are the transitions, the green regions are the intervening

steady-state regions. The presence of the carrier layer allows the sequential cavitation and fibrillation the different adhesive layer on either side of carrier layer. Therefore, compared to the creep curve of a single-layered PSA bonded assembly, as shown in Fig. 81, additional transitions are shown in the creep curve of double-layered PSA bonded assemblies. As seen before in the stress-strain curve, the primary transition in the creep curve (Region II in Fig. 80) is more pronounced than the secondary transition (Region IV in Fig. 80), with a more significant change in the slope, and a more significant peak. The creep rates in the different constant creep phases (Regions I and III in Fig. 80) are also different. In region V, the fibril foot starts to delaminate from the bonding substrate and lose adhesion. The adhesive bonded assembly will fail when the effective fibril foot area cannot sustain the pulling stress.

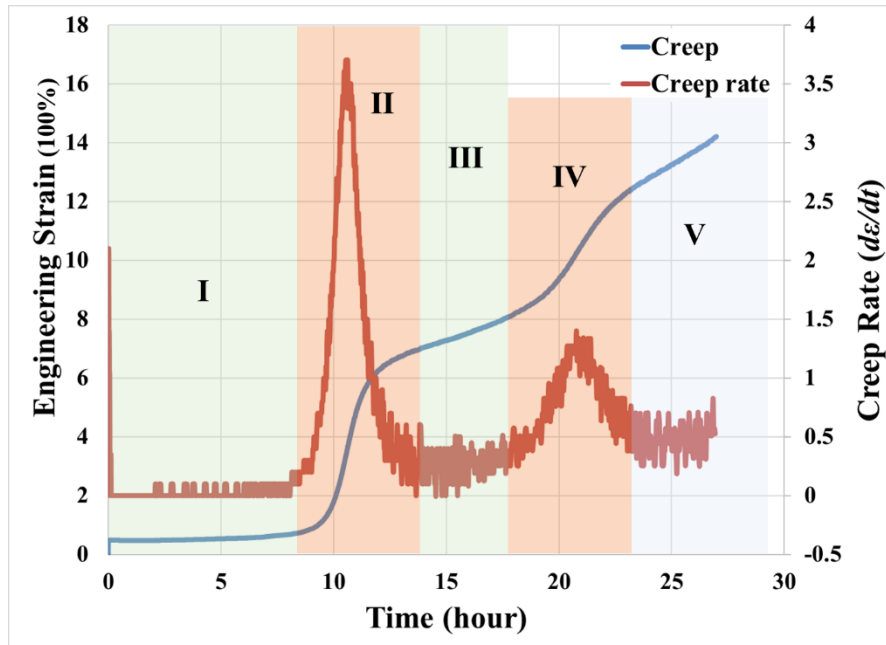


Fig. 80 Creep response of double-layered PSA bonded assembly

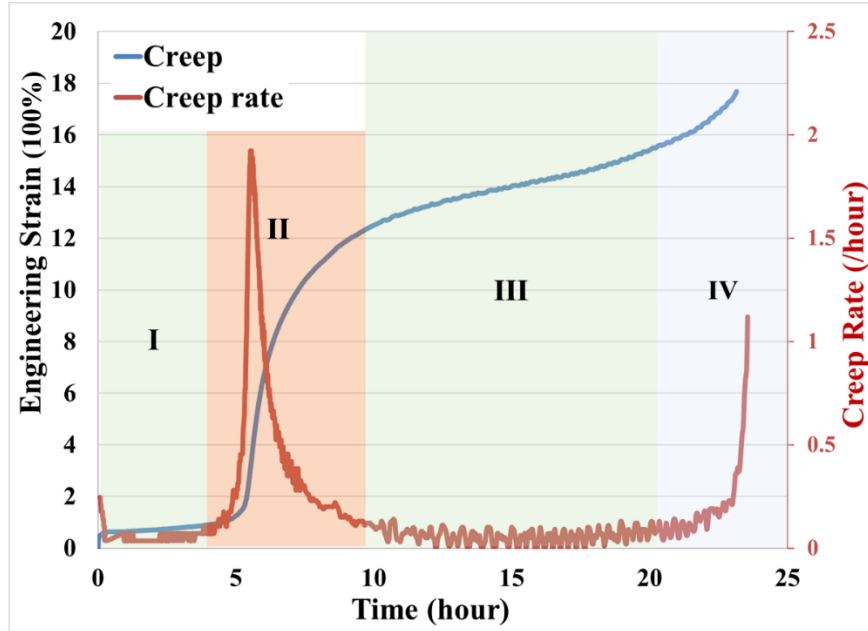


Fig. 81. Creep response of single-layered PSA bonded assembly

Fig. 82 shows the effects of carrier layer thickness on the creep response of double-layered PSA bonded assemblies. The overall creep resistance of the PSA system decreases as the carrier layer thickness increases. The reasons behind that are suspected to be due to the higher cavitation rate due to higher hydrostatic stress in the PSA system with the thicker carrier layer, caused by higher transverse resistance to Poisson deformation. The most significant feature of the better performance of PSA with the thin carrier is the extended Phase I, which lasts about twice as long as the PSA with the thick carrier layer, for the tested configuration. The higher hydrostatic stress causes earlier cavitation in PSA with thick carrier layer than in the PSA with the thin carrier layer. After cavitation, the rest of the phases in these two curves look similar.

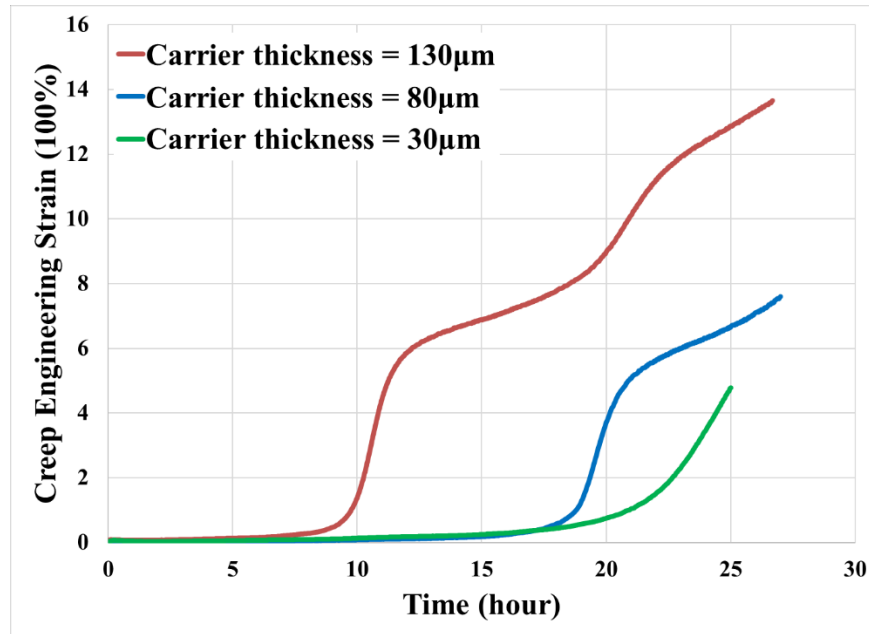
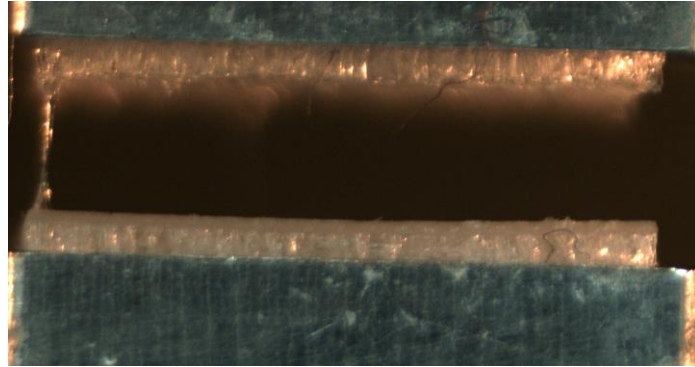


Fig. 82. Effects of carrier layer thickness on creep response of double-layered PSA bonded assembly

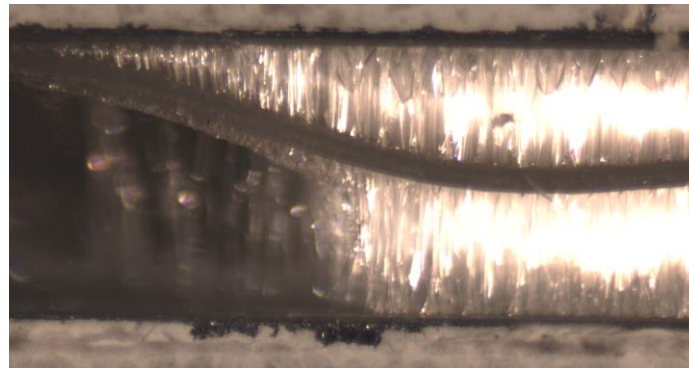
5.3.3 Delamination of PSA bonded assembly:

Theoretically, there are three potential failure modes for adhesive bonding system: adhesive, cohesive, and mixed-mode. For this double-layered PSA system, the adhesive failure mode can be found both at the interface of PSA/substrate and the interface of PSA/carrier. Different failure modes are shown in Fig. 83, and all three potential failure modes are captured in such bonded assembly design. These failure modes indicate that the adhesive strength (for both PSA/substrate and PSA/carrier interfaces) and cohesive strength of the bonding system are comparable. Therefore, the final failure mode is hypothesized to be determined by the initial defect distribution at each bonding interface. For substrates with poorer surface conditions, adhesive failure at PSA/substrate interface is more prevalent due to the weaker adhesion strength. Studies of the failure mode of the double-layered PSA bonded assemblies indicate that

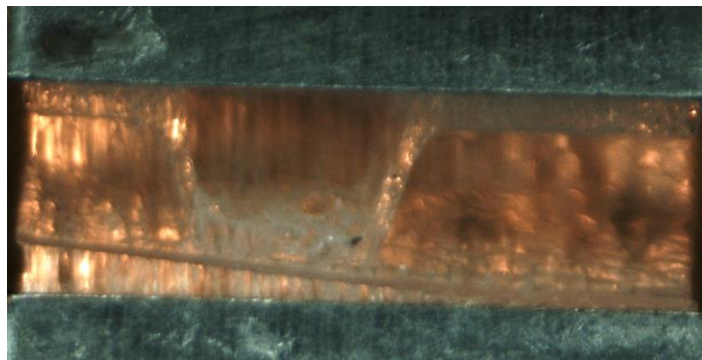
both interfacial (PSA/substrate and PSA/carrier) and bulk properties play a significant role throughout the debonding process of double-layered PSA bonded assemblies.



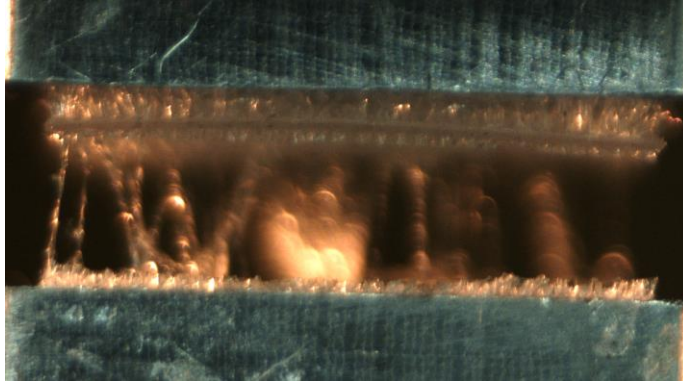
(a)



(b)



(c)



(d)

Fig. 83. Different failure modes of double-layered PSA bonded with aluminum substrate due to the variation of adhesion strength: (a) adhesive failure at PSA/carrier interface; (b) adhesive failure at PSA/substrate interface; (c) mixed mode failure; (d) cohesive failure

5.4 Mechanistic model

For single-layered PSA, the total elongation of the bonded assembly under tensile loading is almost the same as the elongation of the adhesive layer (stiffness of substrate is much larger than the stiffness of PSA). For double-layered PSAs, the total elongation of the bonded assembly is equal to the summation of the deformation in the two adhesive layers. The corresponding elongation of the substrate and carrier layer are negligible in comparison. If the elongation of the adhesive layer has local nonuniformities (accommodate and enabled by wrinkling, flexure and tilting of the carrier layer), the deformation field, initiation of cavitation and fibrillation in the two adhesive layers are different. The elongation of the adhesive layer can, therefore, become non-uniform if the carrier layer is able to accommodate and compensate for this non-uniformity, as shown in Fig. 79. The light amber dotted line in Fig. 79 is the carrier layer.

5.4.1 Stress-strain response of double-layered PSA bonded assembly:

To model the additional physics introduced by the carrier layer, the earlier ‘block’ model proposed by Yamaguchi (Yamaguchi et al., 2006) and then improved by Chapter 3 and Chapter 4 of this dissertation is further modified. The carrier layer and two adhesive layers are considered with a segmental model configuration as shown in Fig. 84. Each segment in this partitioned ‘block’ model uses a combination of bulk cavitation and interfacial cavitation. In order to be consistent with the single-layered ‘block’ model formulation, any nonuniform movement of the carrier layer along the loading direction has been simplified into piece-wise uniform movement of connected segments that are each capable of different movement in the loading (out-of-plane) direction. This model approximately captures (in a piece-wise linear sense) the deformation field in the loading direction due to global tilt (Case I) or global flexing (Case II) of the carrier layer caused by asymmetric cavitation rates discussed earlier. However, in thin carrier layers we also reported wrinkling deformation (Case III) caused by compressive Poisson stresses in the transverse (in-plane) direction. This transverse Poisson compression mode is not included in the current version of the segmental block model, Thus this model is more accurate for thick carrier layers and gradually loses accuracy as the carrier layer becomes thinner and more flexurally compliant.

The constraint provided by the flexural rigidity of the carrier layer, for Cases I and II listed above is approximated with a piece-wise rigid carrier layer where, neighboring segments are now interconnected with out-of-plane linear springs of stiffness K , as shown in Fig. 84. The stiffness K is estimated from the flexural rigidity of the carrier layer. The displacement field of the spring (including the relative displacement of the

carrier segments) is now controlled both by the instantaneous force F_s and F_c of the adhesive layers and the stiffness K . In the schematic, subscript s stands for stiff segments of the adhesive that have not yet cavitated, while subscript c stands for the compliant segments of the adhesive after it has cavitated. The carrier layer is treated as a piecewise rigid sheet in the current simplified segmented model because the modulus of the PET carrier layer is much larger than the modulus of the adhesive layer.

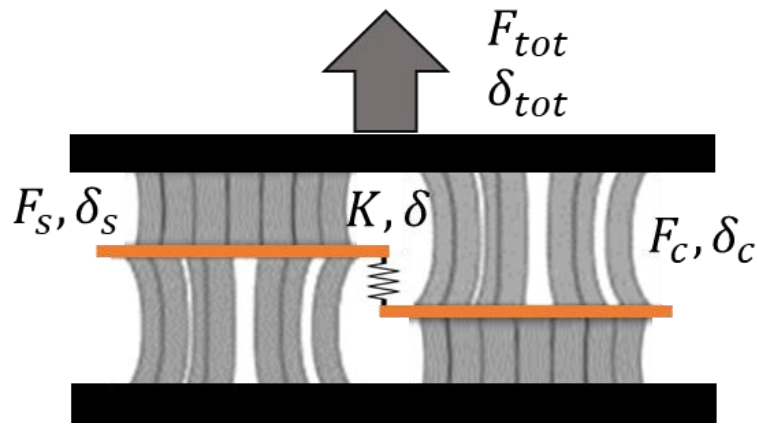


Fig. 84. Schematic of model configuration for double-layered PSA showing segmented carrier layer

The ‘compliant’ segments are the ones that cavitate first. Hence these segments have larger initial interfacial defects with higher inter-defect spacing, at the bonding interface between PSA and substrate (lower cavitation energy used in the cavitation criterion). Conversely, the ‘stiff’ region (before cavitation) has a smaller but denser distribution of initial interfacial defects (higher cavitation energy used in the cavitation criterion and better geometric constraint). Thus, during the debonding process, the compliant regions cavitate first, resulting in a lowering of the stiffness of this region (between primary and secondary transition). This sequential (as opposed to

simultaneous) cavitation in the different segments of the adhesive layers is the key reason for the multiple transitions. The current double-layered model cannot handle the effects of interfacial conditions between the adhesive layer and the carrier layer, such as surface roughness and surface free energy of carrier layer. This limitations will be addressed in the future work. To satisfy displacement continuity, the deformation of the linear spring K is equal to the displacement difference between the stiff and compliant adhesive layers. Therefore, the parameters required for this simplified double-layered model are listed in Table 3. Similar to the interface between the adhesive layer and the substrate (in the single-layered model), the interaction at the interface between PSA and carrier layer is controlled by the detachment of viscoelastic fibrils proposed by Glassmaker and his coworkers (Glassmaker et al., 2008). To verify the feasibility of this simplified approach, a coarse model, using only two segments, as shown in Fig. 84, is used to model the carrier layer in this paper. A generalized version with finer modeling methodology (using more segments for the carrier layer and control on the width of the segment due to the transvers Poisson's shrinkage) would be able to improve the model accuracy by capturing more effects of the waviness of the carrier layer on the double-layered PSA bonded assembly. This will be discussed in future publications.

Table 3: Simulation parameters for simplified double-layered model

Parameters	Unit
PSA thickness	m
PSA width	m
Separation speed (stress-strain)	m/s

Preset stress level (creep)	Pa
Relaxation time	s
Elastic modulus	Pa
PSA surface free energy	mJ/m ²
Friction coefficient	Pa s/m
Initial cavity size (segment I)	m
Initial cavity size (segment II)	m
Initial length (segment I)	m
Initial length (segment II)	m
Block density (segment I)	number/m
Block density (segment II)	number/m
Stiffness of linear spring	N/m
Time step	s

The stress-strain and creep model for each adhesive region are presented in Chapter 3 and Chapter 4. Geometric and meachnically constraints for double-layered model is defined by the equations as followed:

$$\dot{\delta}_c + \dot{\delta}_s = \dot{\delta}_{tot} \quad \text{Eq. (50)}$$

$$\delta_c - \delta_s = \delta \quad \text{Eq. (51)}$$

$$F_s = F_c + K\delta \quad \text{Eq. (52)}$$

$$F_{tot} = F_s + F_c \quad \text{Eq. (53)}$$

The summation of the deformation of each adhesive layer should be the same as the total deformation of the entire PSA system, as indicated by Eq. (50). The length of the connected spring (to mimic the flexural rigidity of carrier layer) is governed by the difference in elongation between the ‘compliant’ region and the ‘stiff’ region, as

indicated by Eq. (51). The ‘compliant’ region and the ‘stiff’ region differed by the initial defect density at each bonding interface. Eq. (52) indicates the equilibrium force status of the two individual segments: the force in ‘stiff’ region is equal to the summation of the force in ‘compliant’ region and the linear spring. Also, the total force applied on the PSA system is equal to the total force of the ‘stiff’ region and ‘compliant’ region. For modeling algorithm of the stress-strain model, the displacement rate is the input and total deformation of the adhesive system will be updated in the first step of each iteration. Based on the Eq. (50), the model will assigned a different value for $\dot{\delta}_c$ and $\dot{\delta}_s$ for the compliant and stiff region respectively. Each region iterates separately (iteration for each segment will follow the single-layered model) and generate the stress output F_c and F_s for the corresponding displacement input. Then the stress equilibrium in the system is evaluated. If the value F_s in the current step is the same or very close to the value $F_c + K\delta$, then the current iteration is determined to have converged and the model advances to the next iteration step. However, if the difference between F_s and $F_c + K\delta$ is more than 0.2%, then the model has not yet converged and a new set of δ_c and δ_s is assigned for the next trial. If $F_s > F_c + K\delta$, $\delta_c^{i+1} = \delta_c^i + 0.5^i \dot{\delta}_{tot}$; conversely if $F_s < F_c + K\delta$, $\delta_c^{i+1} = \delta_c^i - 0.5^i \dot{\delta}_{tot}$, where i representd the i^{th} trial in current iteration step. The detailed algorithm for the double-layered model is shown in Fig. 85. This section only talks about the mechanics introduced be the spring. The basic ‘block’ model mechanics and equations are discussed in approaches in the Chapter 2.

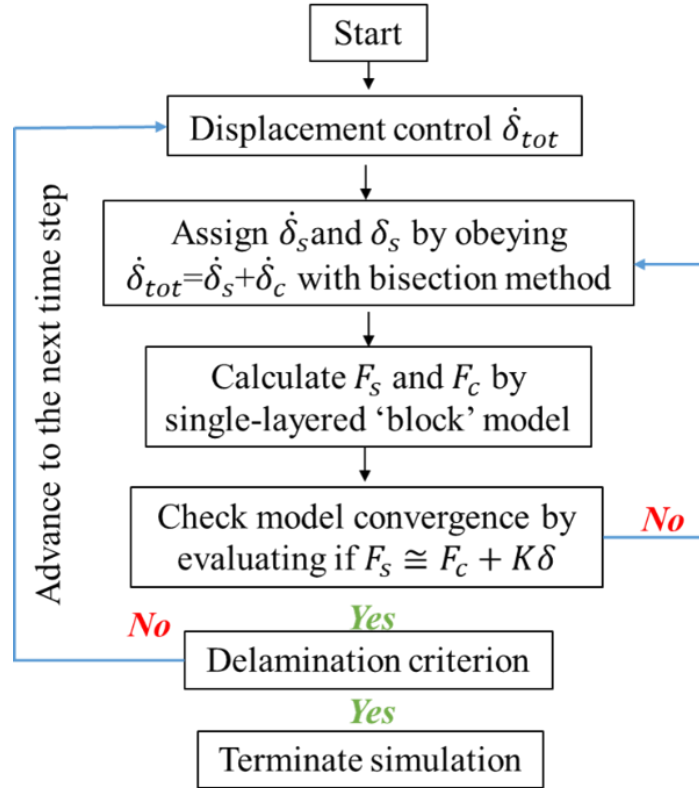


Fig. 85. Modeling algorithm of double-layered stress-strain model

Fig. 86 shows the model prediction of the simplified double-layered PSA bonded assembly stress-strain model. Multiple transitions are predicted in the stress-strain model throughout the entire debonding process, which corresponds to the empirical observation in Fig. 74. The stress increases rapidly in the initial stages due to the hydrostatic stress accumulated in the highly confined geometry due to the high aspect ratio (thickness versus length/width) of the PSA layer. The first drop of the stress value is due to the release of hydrostatic stress caused by cavitation initiation in the ‘compliant’ region, which requires lower energy to initiate the cavitation process. After the primary transition, the stress starts to increase again due to the hardening from fibrillation and due to the vertical constraint provided by the spring connector. As the hydrostatic stress accumulates and exceeds the cavitation criterion in the ‘stiff’ region,

the cavitation process initiates in the ‘stiff’(noncavitated) region and results in the secondary transition of the stress-strain curve. Fibrillation process in the adhesive layer on both sides of the carrier layer results in the strain hardening in the late debonding region of the stress strain curve.

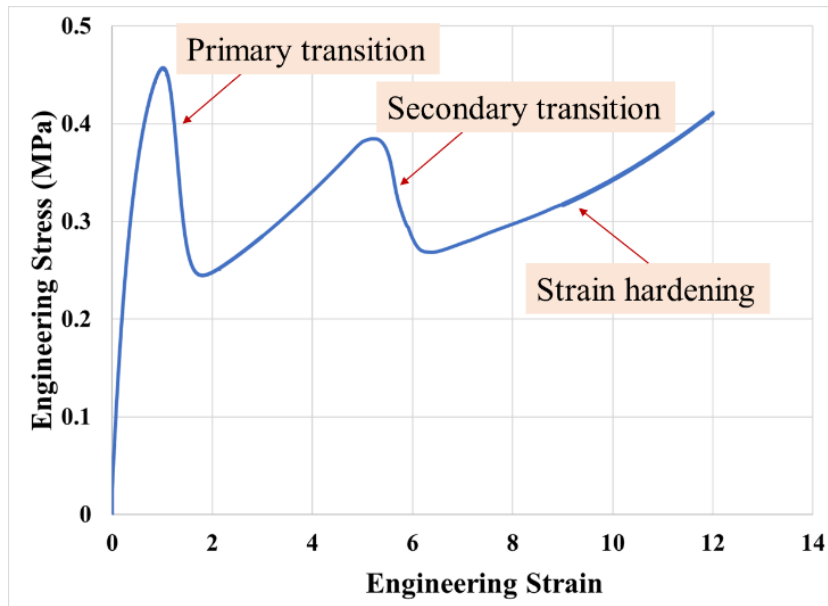


Fig. 86. Sample of model prediction of the simplified double-layered stress-strain model

The stress-strain response of each segment is shown in Fig. 87. At the initial debonding stage, stress in all adhesive regions increases monotonically as the strain increases. Deformation of the PSA system is schematically shown in Fig. 88 (a). The ‘compliant’ region will first reach the cavitation criterion and release stress due to larger initial defects. This also decreases the stiffness of the entire double-layered PSA system and results in the primary transition in the stress-strain curve, as shown in Fig. 86. After the primary transition, the displacement difference between the ‘stiff’ and ‘compliant’ regions starts increasing, which is embodied by the stretch of the spring in Fig. 88 (b). Then due to the fibrillation process and out-of-plane constraint provided by

the spring, the PSA system starts gaining stiffness again and picks up stress in both adhesive layers as the deformation continues. The stretch of the spring reaches the maximum in this phase and it is shown in Fig. 88 (c). Then, the ‘stiff’ region reaches its cavitation stress and starts to cavitate and releases stress. This stress release causes the secondary transition in the stress-strain curve. After the secondary transition, the stiffness of the ‘stiff’ region decreases and the displacement difference between the ‘stiff’ and ‘compliant’ regions starts decreasing, as shown in Fig. 88 (d). In the late debonding phase, both adhesive layers experience fibrillation process and result in strain hardening in the entire system. In this phase, the displacement difference between the ‘stiff’ and ‘compliant’ regions is back to a closed level, as shown in Fig. 88 (e).

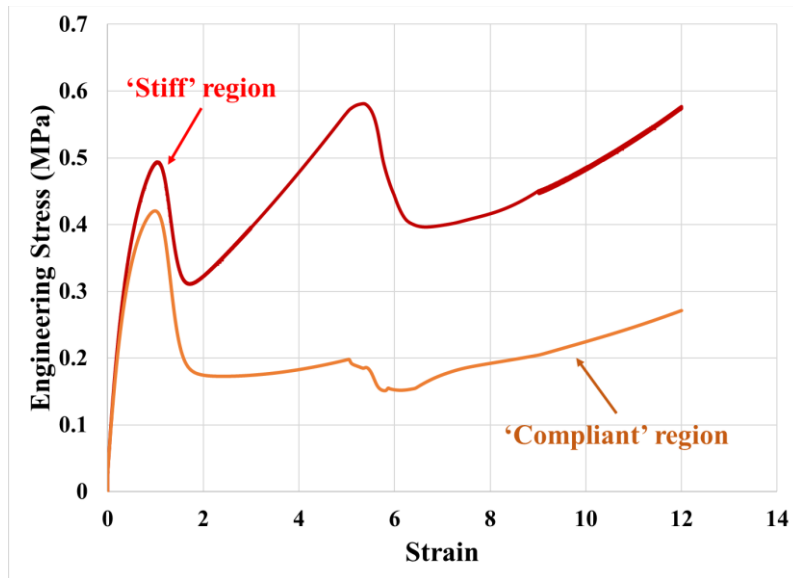


Fig. 87. Stress-strain response of ‘compliant’ region (amber line) and ‘stiff’ region (red line) during the debonding process of double-layered PSA systems

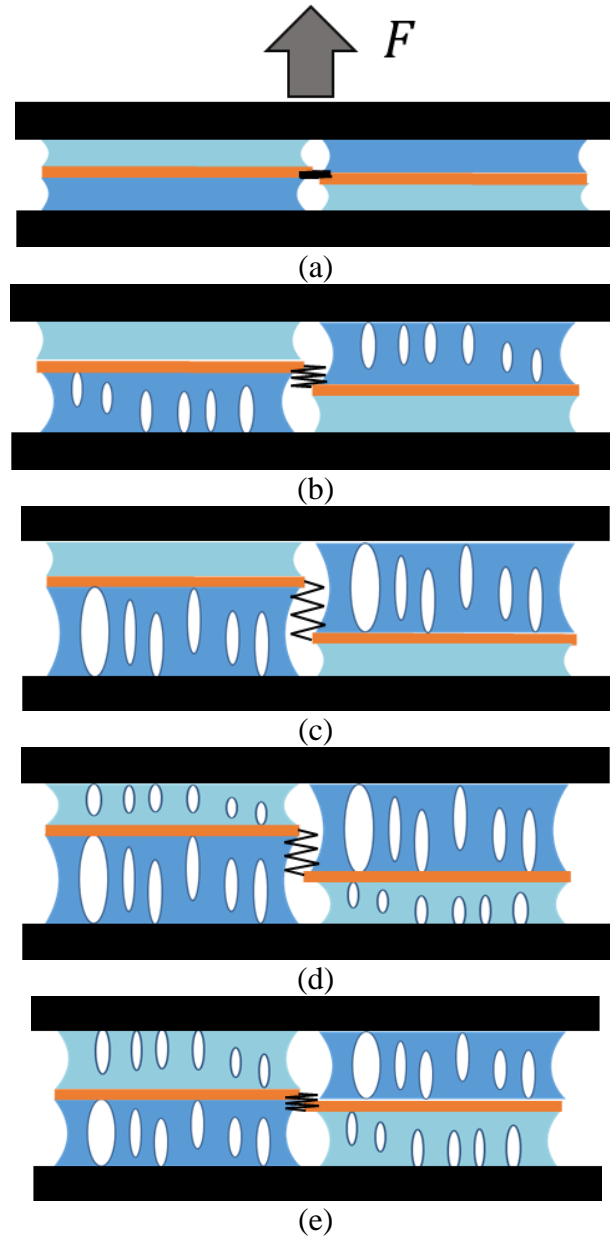


Fig. 88. Schematic of simulation result of five deformation stages of double-layered PSA bonded assembly (for stress-strain deformation the dark blue represents the ‘compliant’ region and the light blue represents the ‘stiff’ region; for creep deformation dark blue represents the ‘stiff’ region and the light blue represents the ‘compliant’ region) at (a) small deformation $\epsilon=0.2$ (Region I in Fig. 80); (b) during primary transition $\epsilon=2$ (cavitation in ‘compliant’ region); (c) spring reaches

maximum deformation; (d) during secondary transition (cavitation in ‘stiff’ region and fibrillation in ‘compliant’ region); (e) $\varepsilon=8$ (fibrillation in both regions)

5.4.2 Creep response of double-layered PSA bonded assembly:

The detailed algorithm for creep deformation under constant stress for a double-layered PSA bonded assembly is shown in Fig. 89. It is similar to the algorithm for the stress-strain behavior but with different loading history. The creep model includes the loading history from stress ramp-up (displacement-controlled) to creep (stress-controlled). Since the creep phase is controlled by stress and the stress level for the entire system is constant, based on Eq. (53), the model assigns different stress values to the ‘stiff’ and the ‘compliant’ regions, and then check if the assigned values fulfill the relationship of Eq. (51). This results in the values of F_s and F_c being controlled by the elongation of the linear spring. For each step, there is one specific deflection of the spring, δ , between zero and the total displacement of the PSA system of the current step, that ensures the system satisfies all four equations. The strain equilibrium status in the system is evaluated. If the difference between δ_c and $\delta_s + \delta$ in the current step is less than 1%, then the current step is determined to have converged and the model advances to the next iteration. However, if the difference between δ_c and $\delta_s + \delta$ is greater than 0.2%, the model is determined as failed to converge. Then a new value is assigned to δ for the next trial. The detailed algorithm for the double-layered PSA bonded assembly creep model is shown in Fig. 89.

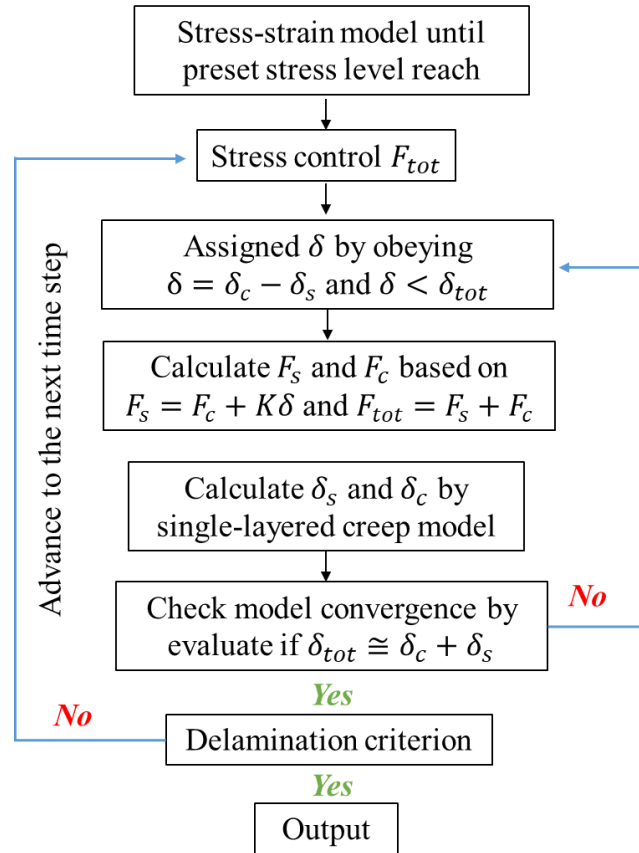


Fig. 89. Modeling algorithm of double-layered creep model

Fig. 90 shows the model prediction of creep response of double-layered PSA system and corresponding creep rate. The double-layered model can reproduce the multiphase creep response that has been observed in the empirical measurement, as shown in Fig. 80. The first increase of the creep rate is due to the stress migration from the hydrostatic part to the deviatoric part caused by cavity initiation and growth in the ‘compliant’ region. The second increase of the creep rate is due to the stress migration in the ‘stiff’ region. Due to the reduced portion of ‘stiff’, non-cavitated regions, the secondary transition is not as significant as the primary transition.

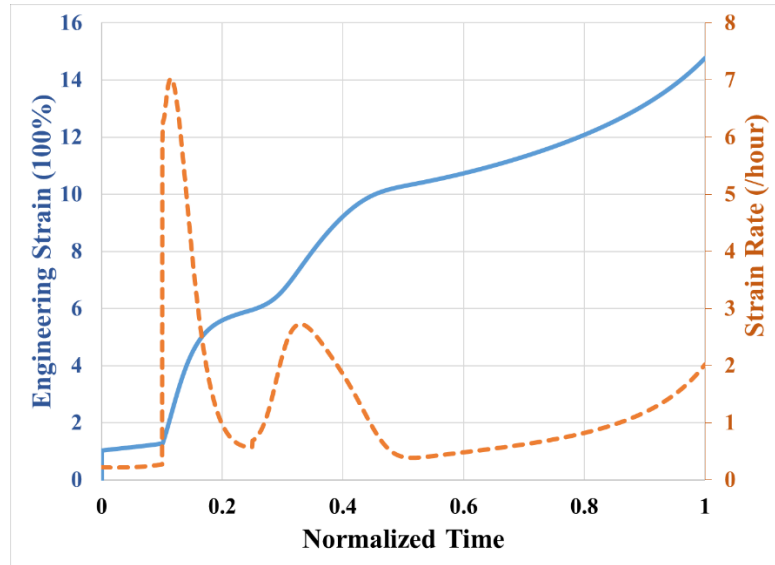


Fig. 90. Predictive model prediction of double-layered PSA bonded assembly creep response

The corresponding history of deviatoric stress in the ‘stiff’ and ‘compliant’ segments is shown in Fig. 91. Before primary transition (cavitation), deviatoric stresses in all adhesive regions increase monotonically as the creep strain increases, shown in stage (a) in Fig. 88. However, after the primary transition (early cavitation in the ‘stiff’ region due to higher hydrostatic stress), the deviatoric stress in the ‘stiff’ region increases dramatically due to the constant force loading condition and the release of hydrostatic stress caused by the cavitation process. The instantaneous stiffness of the ‘stiff’ region decreases and thus accumulates more creep deformation than the ‘compliant’ (non-cavitated) region, shown as Fig. 88(b). Therefore, the deviatoric stress increases dramatically in this phase, as shown in the red block in Fig. 91. Meanwhile, the strain of ‘compliant’ region decreases slightly due to the imbalance of stiffness of the two regions in caused by the softening of the ‘stiff’ region after cavitation. The unbalanced stiffness in two regions leads to an increasing displacement difference between the

‘stiff’ and ‘compliant’ regions. As the fibrillation process in the ‘stiff’ region begins, the ‘stiff’ region starts gaining stiffness again (strain hardening). Then the deviatoric stress of the ‘compliant’ region slowly increases due to the fibrillation process in the ‘stiff’ region and out-of-plane constraint provided by the spring connector. The difference in the creep deformation between the two segments reaches the maximum in this phase, as shown in Fig. 88(c). When the ‘compliant’ region reaches the cavitation criterion, the same procedure that happened in ‘stiff’ region now happens in the ‘compliant’ region. The displacement difference between the ‘stiff’ and ‘compliant’ regions, Fig. 88(d), starts decreasing as the stiffness of ‘compliant’ region decreases due to the cavitation process. Then, in Fig. 88(e), the difference in deformation between the two segments decreases to a minimum, and the increment of deviatoric stress in the late debonding stage is due to fibrillation in both adhesive layers.

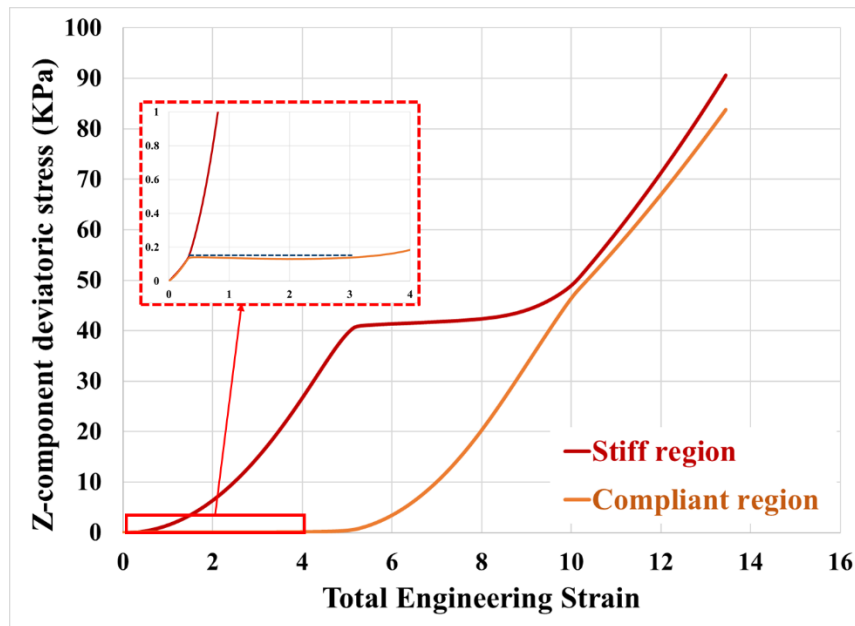


Fig. 91. History of zz -component deviatoric stress (true stress) in bulk adhesive of ‘stiff’ and ‘compliant’ regions during debonding process.

5.5 Conclusion

This chapter has focused on the complex stress-strain and creep response of multi-layered sandwich systems, specifically double-layered PSA systems bonded with two rigid substrates (substrate/PSA/carrier/PSA/substrate). During experiments, we have observed multiple transitions in both stress-strain and creep curves. These transitions are due to the competition between the mechanisms of cavitation, fibrillation, and interfacial mechanical locking in the PSAs on both sides of the carrier layer. Experimental results indicate that the thickness of carrier layer has a significant effect on both stress-strain and creep responses by affecting the geometric confinement of the adhesive system. The PSA system with a thin carrier layer has enough flexibility to accommodate the stress distribution in the adhesive due to uneven defects at the bonding interface. However, the PSA system with thick carrier layer has less flexibility and can better retain the geometric confinement during the debonding process. Therefore, a more wavy pattern is observed in the PSA system with the thin carrier layer, but the local pattern disappears as the thickness of carrier layer is increased. A predictive mechanistic model, based on simplified debonding mechanisms of double-layered PSA bonded assembly, is developed. The modeling algorithm assumes the geometric constraint provided by the carrier layer can balance the stress difference between the regions with different initial defect distributions. The model is able to capture the secondary transition in the stress-strain and creep curve by balancing the force between the ‘stiff’ and ‘compliant’ segments of PSA bonded assembly through a linear spring connector, which represents the out-of-plane, flexural rigidity of the carrier layer.

Chapter 6. Discussion and Summary

The major objective of this dissertation study was to gain insights into the mechanical behavior of pressure sensitive adhesives (PSAs), using a combination of parametric experimentation and mechanistic modeling. The first step was to develop a methodology for identifying preferred bonding conditions for selected combinations of PSA/substrate, which could then be used as a guideline to prepare the samples for experimentation. Tensile tests were conducted on selected PSA bonded assemblies to gain in-depth understanding of the physics of the complex multi-phase mechanical behavior of PSA materials with and without carrier layers. A predictive mechanistic model (enhanced ‘block’ model) was developed, based on the observed physics, to enable mechanistic prediction of the stress-strain and creep behaviors of PSA bonded assemblies. This model proved to be capable of providing reasonable predictions of the tensile stress-strain behavior and creep behavior of bonded assemblies consisting of substrates bonded with single-layered PSA materials. An overall discussion about the conclusions and outcomes of this dissertation is provided in Section 6.1. In Section 6.2, the contributions of the dissertation are highlighted. Finally, the limitations of the current study and recommendation for future work are discussed in Section 6.3.

6.1 Conclusions

Empirical investigations of the tensile mechanical behavior of selected single and double-layered bonded assembly reveal that:

1. Different PSA/substrate combinations require different bonding combinations (bonding stress, bonding time, bonding temperature and post bonding aging time) to obtain desired bonded assembly performance.
2. As the operating temperature increases, the bonding strength, creep resistance, and delamination strain decrease, and the variability of the stress-strain and creep performance of PSA bonded assembly increases.
3. Debonding mechanisms of stress-strain and creep behavior of single and double-layered PSA bonded assemblies:
 - 3.1. Primary transitions in stress-strain and creep responses are due to cavitation and fibrillation.
 - 3.2. Secondary transition due to sequential cavitation and fibrillation in double-layered PSA bonded assembly; degree of secondary transition is dependent on the global and local flex of carrier layer.
 - 3.3. Interfacial delamination due to receding of fibril foot; receding rate is dependent on the surface properties of bonding substrate.
4. Effects of PSA configuration on mechanical performance of PSA bonded assembly:
 - 4.1. Presence of carrier layer results in additional transitions in the stress-strain and creep curve of PSA bonded assemblies, resulting in a primary transition and a secondary transition.

- 4.2. An increase in PSA thickness leads to increase in primary peak and ultimate bond strength but decreases in ductility.
- 4.3. A double-layered PSA bonded assembly shows lower ductility than single-layered PSA bonded assemblies.
- 4.4. Buckling of thin carrier layers due to transverse Poisson's shrinkage results in non-identical stress distribution in the adhesive layers on both sides of the carrier layer.
- 4.5. An increase in thickness of PSA carrier layer leads to a decrease in severity of the secondary transitions in the stress-strain curve.
- 4.6. An increase in thickness of PSA carrier layer leads to a decrease in creep resistance.
5. Effects of surface condition (surface roughness and surface free energy) of the substrate on mechanical tensile performance of PSA bonded assembly:
 - 5.1. Increase in surface roughness results in a decrease in the peak strength, plateau strength, ultimate strength, and therefore decreased work of adhesion, in tensile stress-strain tests
 - 5.2. Tensile stress-strain response shows non-monotonic dependence on the surface roughness of bonding substrate. The bonding strength, peak strength and ultimate strength, has a non-monotonic dependence on the surface roughness of the substrate, slowly increasing to a maximum value at a critical roughness and dropping again as the surface roughness is further increased. The critical roughness value and the maximum bonding strength both depend on the combination of PSA and substrate.

5.3. Tensile stress-strain response shows non-monotonic dependence on the surface free energy of the bonding substrate. PSA bonded assembly achieves optimal interfacial bonding energy and bonding performance when substrate surface free energy is slightly higher than the adhesive surface free energy.

The mechanistic modeling approaches developed for the mechanical tensile response (stress-strain behavior and creep behavior) of a single-layered PSA-bonded assembly are now able to:

1. Capture the major characteristic features including the primary transition and strain hardening in the stress-strain and creep behavior of single-layered PSA bonded assembly
2. Quantitatively evaluate the non-monotonic dependence of tensile stress-strain and creep response of PSA bonded assemblies on the substrate surface roughness
3. Quantitatively evaluate the non-monotonic dependence of tensile stress-strain and creep response of PSA bonded assemblies on the substrate surface free energy
4. Predict the delamination strength and strain observed in tensile stress-strain tests
5. Predict the delamination rupture strain and rupture time observed in tensile creep tests

The mechanistic modeling approach developed for the tensile mechanical response of double-layered PSA-bonded assemblies is now able to:

1. Capture the primary and secondary transitions, and strain hardening in the stress-strain and creep behavior of double-layered PSA bonded assemblies

2. Partially capture the effect of carrier layer flexural rigidity (out-of-plane constraint) on the stress-strain and creep response of double-layered PSA bonded assemblies
3. Evaluate the effects of loading rate and temperature on the stress-strain curves of double-layered PSA bonded assemblies
4. Evaluate the effects of loading stress level and temperature on the creep curves of double-layered PSA bonded assemblies

6.2 Contributions

1. A comprehensive study has been conducted to understand the uniaxial stress-strain behavior of single and double-layered PSA bonded assemblies with extended post-bonding aging time
 - 1.1. Comprehensive understanding on the effects of post-bonding aging time on the interfacial adhesion of PSA bonded assemblies.
 - 1.2. Optical observation to understand the effects of post-bonding aging time on the size of macro-voids.
 - 1.3. Numerical method to investigate the effects of macro-voids on the bonding strength of adhesive bonded assemblies.
 - 1.4. Method to rank the stress-strain performance of PSA bonded assembly with extended post-bonding aging time based on the peak strength, ultimate strength, toughness, and creep resistance.
 - 1.5. First study to investigate the potential failure modes of double-layered PSA bonded assemblies.
2. First detailed study to provide a fundamental understanding of uniaxial creep response of single and double-layered PSA bonded flat rigid substrates
 - 2.1. Most comprehensive experimental results to date, on the unique multi-phase creep response of single and double-layered PSA bonding assemblies under various conditions
 - Effects of loading stress level and temperature
 - Effects of PSA system's configuration
 - Effects of bonding substrate surface roughness and surface free energy

- 2.2. Explicit demonstration and understanding of the mechanism of sequential cavitation and fibrillation behind the multi-phase and multi-transition creep curve, that was not available in the literature before this study.
3. Comprehensive experimental and numerical studies to investigate the role of carrier layer on the stress-strain and creep behavior of double-layered PSA bonded assembly.
 - 3.1. Influence of carrier layer flexural rigidity on the stress-strain and creep response of double-layered PSA bonded assembly
 - 3.1.1. Primary and secondary transition in the stress-strain and creep curve
 - 3.1.2. Overall creep resistance
 - 3.2. *In-situ* real-time observation discloses the combine of local and global flex of carrier layer in the debonding process of a double-layered PSA bonded assembly.
4. Improved tensile stress-strain model of single-layered PSA bonded assembly
 - 4.1. Quantitatively estimates the effect of substrate surface roughness and surface free energy on the stress-strain response in single-layered PSA bonded assembly.
 - 4.2. Includes cavitation criterion to control the initiation/nucleation and growth of interfacial defects and initiation/nucleation of bulk cavities.
 - 4.3. Provides quantitative estimate of the delamination strain and strength.
5. First mechanism-based modeling approach for tensile creep response of single-layered PSA bonded assemblies
 - 5.1. Quantitatively captures the transition caused by the cavitation and fibrillation.

- 5.2. Quantitatively estimates the creep rupture time.
- 5.3. Quantitatively evaluates the effect of substrate surface free energy and substrate surface roughness on the creep response of single-layered PSA bonded assembly.
- 6. First mechanism-based modeling approach for tensile stress-strain and tensile creep response of double-layered PSA bonded assemblies
 - 6.1. Major characteristic features show reasonable agreement to the empirical observation.
 - 6.2. Qualitatively reproduces the additional phases and transition in the stress-strain and creep curve.
 - 6.3. Approximately captures the dependence of tensile mechanical response on the flexural rigidity of the carrier layer.

In summary, the contributions of this dissertation are new and more comprehensive understanding of the mechanical stress-strain and creep response of single and double-layered PSA bonding assemblies, based on experimental observations and mechanistic modeling. The model has the benefits of providing: (i) parametric insights into the mechanical behavior of PSA-bonded assemblies as a function of various bonded assembly features and loading conditions; (ii) a virtual testing capability to supplement expensive and time-consuming physical testing; and (iii) the potential to be utilized for real-time prognostics and health management, based on continuous real-time calibration and updates in functional joints, to estimate the residual life of mechanically loaded bonded assemblies that are bonded with PSA material systems.

6.3 Limitations & future work

Experimental limitations and future work

1. Macro-voids at the bonding interface: macro-voids in the current study are only considered as a factor that causes variation in the stress-strain and creep response.
 - 1.1. Empirical investigation will help to reveal the effects of Macro-voids (size and location) on the geometric confinement of single and double-layered PSA bonded assembly
 - 1.2. Finite element method to understand the effects of location and size of macro-voids on the hydrostatic stress status in the adhesive layer
2. Effects of loading conditions on the stress-strain and creep performance of PSA bonded assemblies are not fully understood.
 - 2.1. Additional mechanical test under different temperature to understand the temperature dependent material property and debonding mechanism.
 - 2.2. Additional mechanical test under different loading rate to understand the loading rate dependent material property and debonding mechanism.
3. Effects of carrier layer on stress-strain and creep performance of PSA bonded assemblies: Empirical investigation focus only on the out-of-plane constraint provided by the carrier layer along the loading direction
 - 3.1. Different in-plane constraint due to the flexural rigidity of carrier layer
 - 3.2. Interfacial interaction between PSA and carrier layer

Modeling limitations and future work

1. Material property: some model parameters used in the simulation are assumed to be linearly rate-dependent and temperature-dependent; they should be modeled in

stress-strain and creep simulation with more accurate nonlinear temperature and rate dependence instead of linearized dependence.

2. Control of the number of cavities: a cavity starts forming within the adhesive layer or the interface between adhesive and substrate when the hydrostatic stress exceeds the threshold value. In this dissertation study, the number of cavities is pre-set.

2.1. Detailed study of the influence of the density of blocks on model outputs will improve the completeness of the stress-strain and creep models.

2.2. Defining the number of cavities by the current stress state and defect distribution will help in forming a more comprehensive mechanistic model.

3. Degradation of PSA material properties: products which contain PSA bonded assemblies in field applications are expected to have a long-life cycle. Including the degradation history of material properties, such as modulus and viscosity, will help the mechanistic model in estimating the residual life of the PSA bonded assemblies.

4. Cavitation and cavity growth criteria can be enhanced in the mechanistic creep model

4.1. A stress-dependent, diffusion-driven cavitation criterion will improve the accuracy of the creep model

4.2. Rate dependent material properties of adhesive in the near-field of the cavity will help to better capture the cavity growth during the creep deformation process.

5. Application of the stress-strain and creep mechanistic model is limited to the tensile loading not for shear loading.
6. Interfacial friction between the adhesive and the substrate is suggested to be improved by
 - 6.1. non-linear dependence on the substrate surface free energy
 - 6.2. non-linear dependence on the substrate roughness
7. Effects of carrier layer properties: the double-layered model focuses only on the out-of-plane constraint provided by the carrier layer along the loading direction.
 - 7.1. Including the in-plane constraint of the carrier layer in the simulation will help better estimate the transverse Poisson deformation in the PSA materials and also the degree of flexural deformation of the carrier layer due to buckling effects.
 - 7.2. Including the in-plane constraint of the carrier layer in the simulation would help better estimate the accumulation of hydrostatic stress in the adhesive layer, thus improving the evaluation of the cavitation initiation of double-layered PSA bonded assembly.
 - 7.3. Detailed empirical study of the interfacial slippage between PSA and carrier layer will further improve the understanding on the effects of carrier layer on the mechanical performance of the double-layered PSA bonded assemblies.

Appendices

A1: Identification of Preferred Bonding Conditions

PSA bonded assembly performance is affected by how it has been fabricated. The objective of this step is to understand the effects of different bonding conditions on the selected PSA system and determining a set of acceptable bonding parameters for fabricating PSA bonding assemblies for mechanical characterization. The acceptable bonding combination is not the optimal bonding combination for the PSA material. It is a set of selected bonding parameters after balancing the sample fabrication duration and cost for this study. This exclusive fabrication combination will be applied to bond PSA bonded assemblies through this study.

Effects of bonding parameters

The mechanical performance of PSA bonded assemblies highly depends on their fabrication conditions, including bonding temperature, bonding time, bonding pressure, and post bonding aging time. The purpose of this phrase study is to carry out a methodology for identifying the desired fabrication conditions.

As shown in the Fig. 92, two aluminum T-shape tab are gripped in the upper and lower arm of DMA. The PSA sheet will first be mounted on one side of tab. Then DMA will apply the preset bonding condition, known as bonding time, pressure and temperature, to form a permanent bond between PSA and two aluminum tab. The after-bonding specimens will be aged at room temperature for selected duration, known as post bonding aging time, before the sample is ready for the tensile test. In this study, five samples are tested for each combination of bonding parameters. The tensile test

for studying the effects of fabrication conditions are also conducted by DMA with constant loading rate $2 \mu\text{m/s}$ at room temperature. An acceptable combination of bonding parameters will be screened out based on the tensile test result. The acceptable bonding combination should be able to fabricate the specimen with maximum tensile strength and toughness within acceptable operational time. The acceptable bonding combination will be used to bond all the samples with this specific PSA system through this dissertation study. Test matrix for this study is shown in Table 4. The combination of bonding parameters will be chosen from this table. For example, one candidate bonding combination is bonding pressure 15 Psi, bonding duration 10 second, post bonding aging time 0 hours, at room temperature. Theoretically, to find out the acceptable bonding parameter within those combinations, there are total 36 different combinations will be evaluated. To reduce the amount of test, an arrangement of parametric study was being used. Details will be discussed in next.

In this phase, a methodology of determining the desirable fabrication conditions for the PSA bonded assemblies is developed based on the parametric studies of the effects of different bonding conditions on the PSA bonded assemblies' mechanical performance, particularly refers to the stress-strain behavior in this part's study.

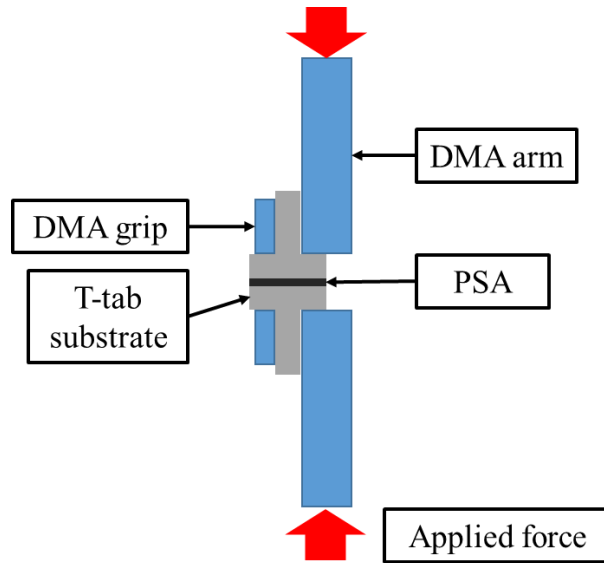


Fig. 92 Schematic of PSA bonded assembly in tester

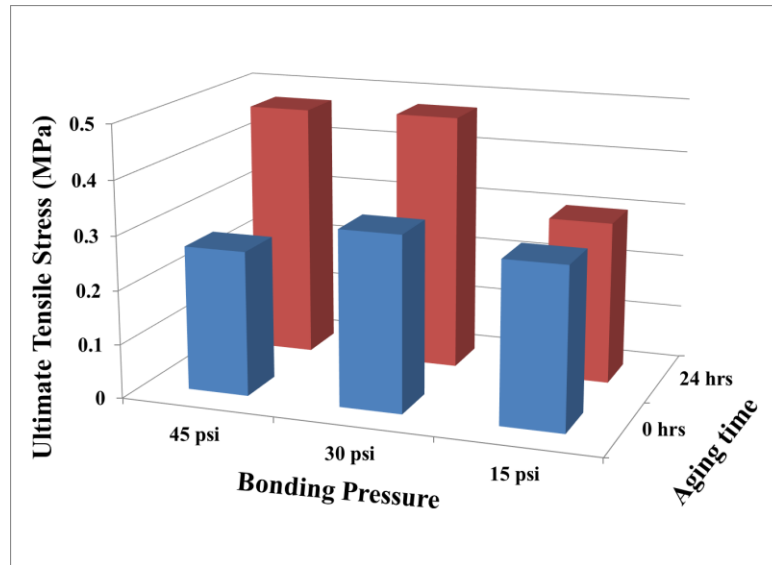
Table 4: Test matrix for desired fabrication conditions identification

Bonding Pressure		
15 Psi	30 Psi	45 Psi
Bonding Time		
10 second	30 second	60 second
Post Bonding Aging Time		
0 hours	24 hours	
Bonding Temperature		
Room Temperature	50 °C	

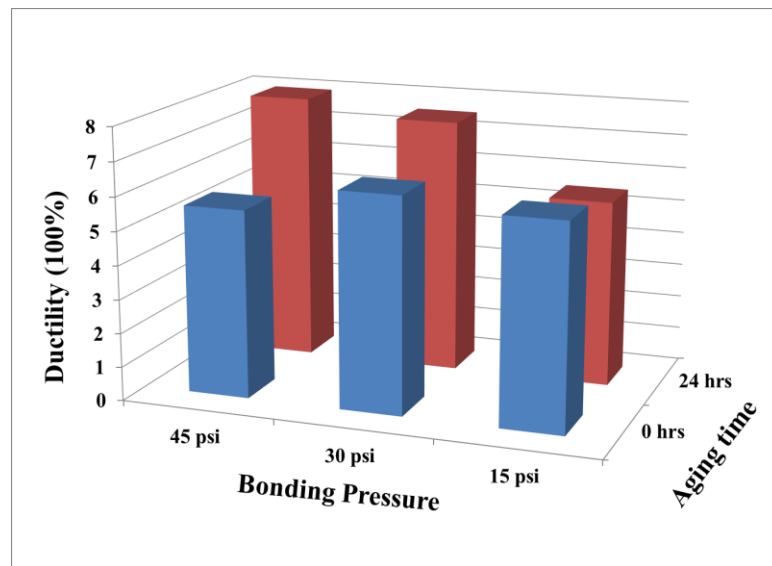
Effects of bonding pressure and post bonding aging time

There are many different bonding conditions that can affect the mechanical performance of PSA bonded assemblies. In this phase of study, the effects of the bonding pressure and post bonding aging time will first be investigated. There are two reasons for selecting these two parameters to study firstly. First, as the way that PSA

been named, it is very sensitive to the applied pressure. Thus, study the effects bonding pressure will become a priority for any kinds of PSA system; second, in order to distinguish with the probe tack test, a very popular standard test method for analyzing the tack performance of the PSA bonded assemblies, the effects of the post-bonding aging time have been proposed. Because the longer the post-bonding aging time, the better adhesive can wet on the bonding substrate, and therefore, to form a stronger bond. The result of the parametric studies of different combinations of bonding pressure and aging time on strength and ductility is shown in Fig. 93 (a) and (b). In general, increasing the aging time is found to increase the strength and ductility. However, the ultimate tensile strength and ductility seem to be saturated after the aging time exceeds 24 hours. Generally, the PSA bonded assemblies that have longer post bonding aging time has the better mechanical performance than those do not have. However, to keep the aging time within practical limit, all the test specimens are selected to be aged for 24 hours. At this aging period, the ultimate strength and ductility reached a saturation limit at about 30 Psi and further increase in the bonding pressure provided negligible effects on the sample's strength and ductility. Based on these parametric insights, the bonding pressure was selected to be 30 psi. The bonding pressure and post-bonding aging time determined in this section are used for fabricating all PSA bonded assemblies with this selected PSA.



(a)



(b)

Fig. 93 Effect of bonding pressure and post aging time on PSA bonded assemblies:

(a) ultimate tensile stress (b) ductility

Effects of bonding temperature

Effects of bonding temperature has been studied after the bonding pressure and post bonding aging time were determined. The selected bonding temperatures are room

temperature (25 °C) and 50 °C. The test results are shown as Fig. 94. A statistically significant test has been conducted based on the experimental data to evaluate the significant of difference between two test groups. It shows that the significant of the difference of the ultimate tensile stress due to the different bonding temperature is less than 95% (detail for determining the significance see Appendix II). Therefore, the ultimate tensile stress is considered as not sensitive to the bonding temperature. However, the significant of difference of ductility between two bonding temperature is over 95%, but the value of difference is very small. Therefore, the ductility is considered slightly dependent on the bonding temperature.

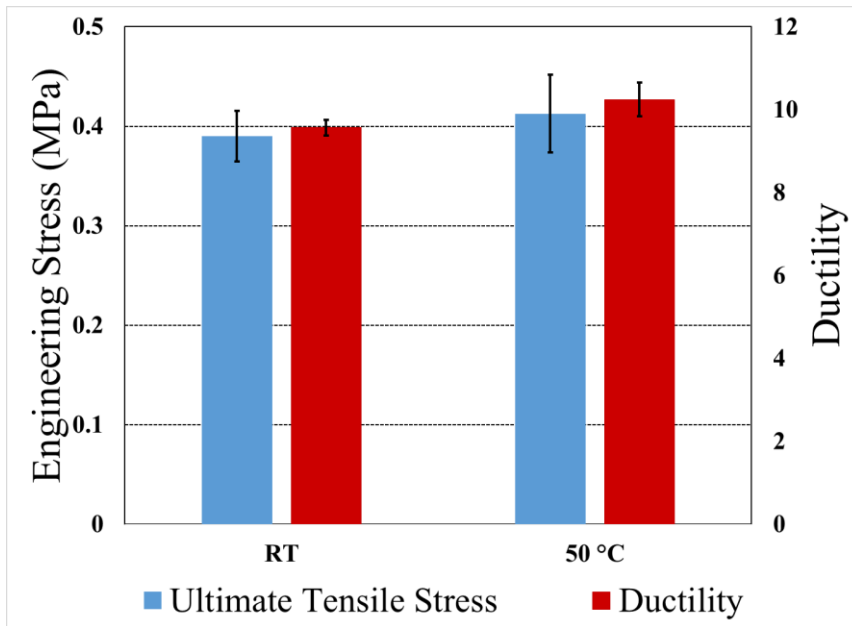


Fig. 94 Effects of bonding temperature on the PSA bonded assembly strength and ductility

Effects of contact duration

Similar to the bonding time investigation. The effects of bonding temperature has also been studied with the pre-determined bonding pressure and post-bonding aging

time. The candidate bonding time are 10 s and 30 s. According to the experimental result, shown in Fig. 95, and statistical significance test (details in Appendix II) indicates that the , the selected bonding time has insignificant effects on the performance of PSA bonded assemblies when the sample bonded at 30 Psi and aged for 24 hours. Therefore, in interests of reliability, 30 s bonding time is selected as an acceptable bonding time for this kind of PSA.

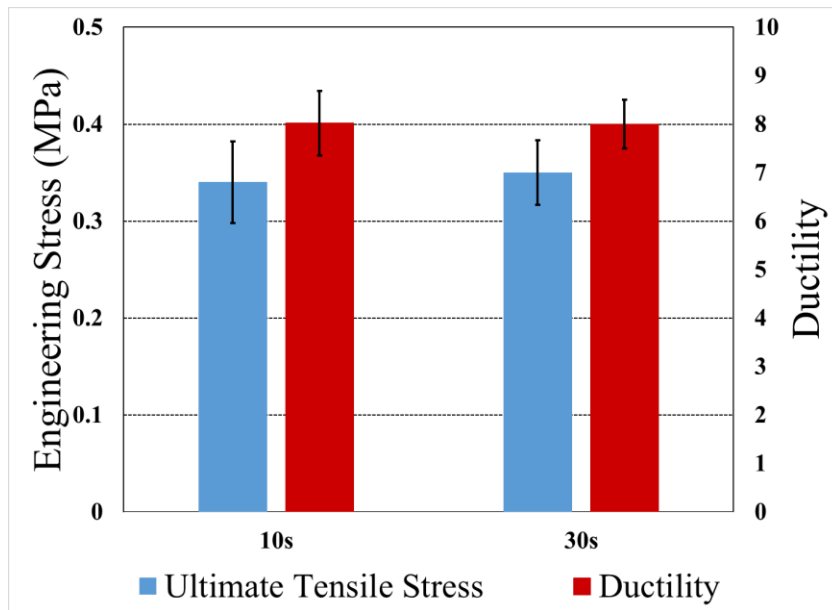


Fig. 95 Effects of contact time on the PSA bonded assembly strength and ductility

Based on the methodology discussed above, the acceptable fabrication conditions for this specific PSA system are: bonding pressure: 30 Psi, bonding time: 30 s, bonding temperature: room temperature (~25 °C) and post-bonding aging time: 24 hours. The acceptable fabrication conditions determined in this phase is only applicable for the selected PSA systems used for the experiment. For other kinds of PSA materials or PSA systems, the desired fabrication conditions maybe vary, but can also be determined by follow the same routine.

A2: Finite Element Modeling the Effect of Carrier Layer Thickness on Deformation of Double-Layered PSA Bonded Assemblies

The variations of the stress-strain response between PSA systems show noticeable dependence on the thickness of carrier layer. Deformation of carrier layer during the debonding process will give important information about the physics behind the difference in the stress-strain response. Figure 5 and 6 are the real time side view of the PSA with thin carrier layer and thick carrier layer under tension and before secondary drop in their stress-strain curves. Clearly, through the comparison between the thin and the thick layer sample, the thinner one has more server deformation of the carrier layer and formed waviness pattern while the thicker one remains flat. The waviness of the thin carrier layer enables local flex to accommodate the non-uniform stress distribution in top and bottom adhesive layers caused by non-identical initial interfacial defects distribution. Thus, allowing the cavitation initial non-simultaneously at different region of the interface. Therefore, minimize the release rate of the hydrostatic stress in unit area and decrease the severity of secondary transition in stress-strain response.

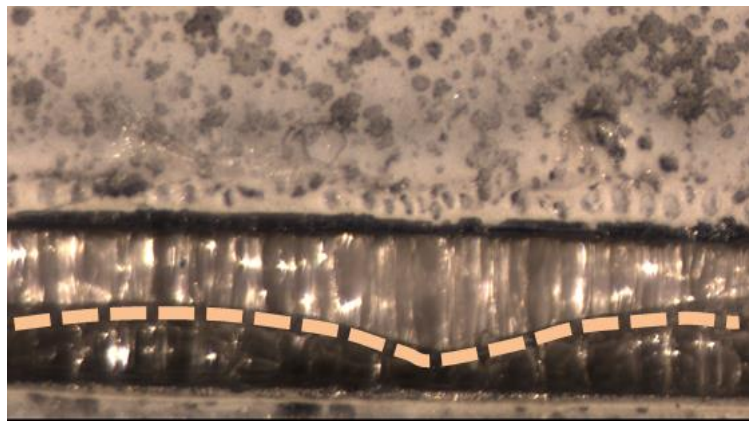


Fig. 96 Wavy carrier layer during debonding process (thin carrier)

Higher stiffness of the thicker carrier layer decreases its deformity and remains the carrier layer in flat during the debonding process. The flatness of carrier layer can average the stress distribution in the adhesive layer (not able to accommodate the non-uniform distribution) and offer higher in-plane constraint on the adhesive layer (no wrinkled carrier observed). Therefore, it allows the cavitation occurs over the entire footprint on both side of adhesive layer. However, if the roughness distribution in substrate is much higher on one side than the other side. The stress distribution could tilt the carrier layer, as shown in Fig. 98, and result in the least sever secondary transition. In this particular sample, the cavitation initiated at one end of the bonding interface and propagated to the other end.

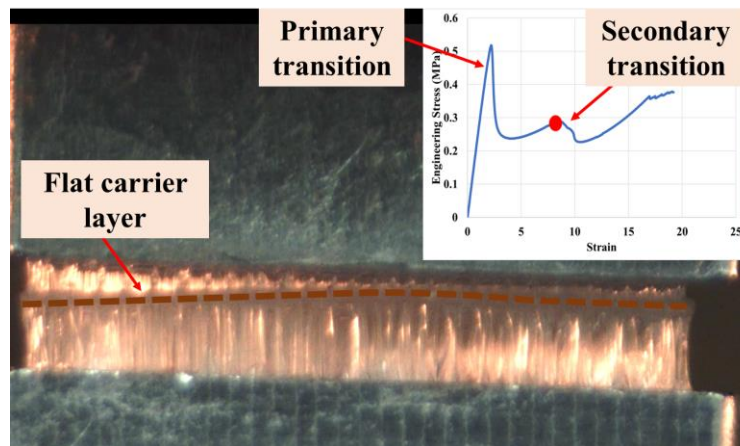


Fig. 97 Flat carrier layer during debonding (thick carrier)

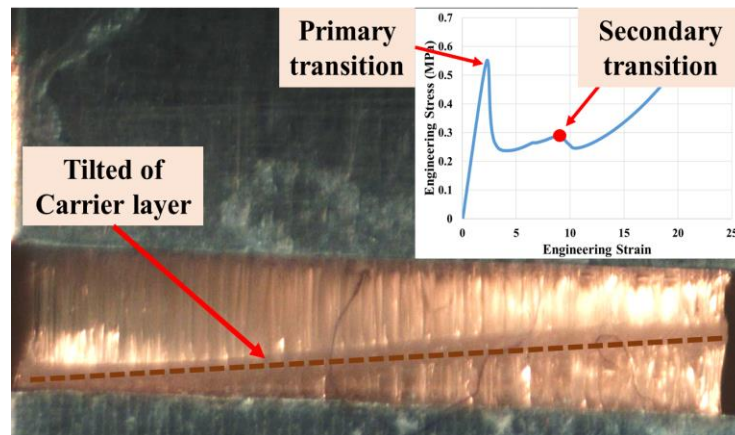


Fig. 98 Tilted carrier layer during debonding (thick carrier)

Empirical results show that the stress-strain responses are highly depends on the thickness of carrier layer. In order to understand the role of carrier on the PSA system, we developed a FEA model based on the configuration of our test samples to understand the influence different amount of constraint offered by carrier layer. As shown in Figure 8, we made a half model for PSA bonded assembly, since it is a symmetric system. Material property of adhesive layer is the empirical stress-strain test result of single-layered PSA system. Different properties assign in the partition depends on the interest of study. PET's properties are used for the carrier layer. Interaction between PSA/substrate and PSA/carrier layer are ignored in the current model. The bottom boundary of the PSA system is encastred and the top boundary PSA only allows to move in vertical direction. Displacement boundary condition with strain rate of 0.02 is applied on the top boundary of upper adhesive layer. Parametric study on the thickness of the carrier layer to evaluate the effects of carrier layer flexural rigidity on the deformation and stress distribution of PSA system during debonding.

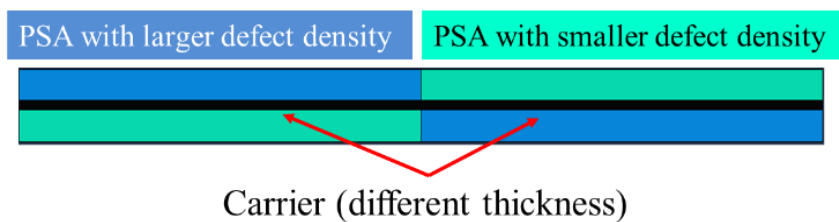
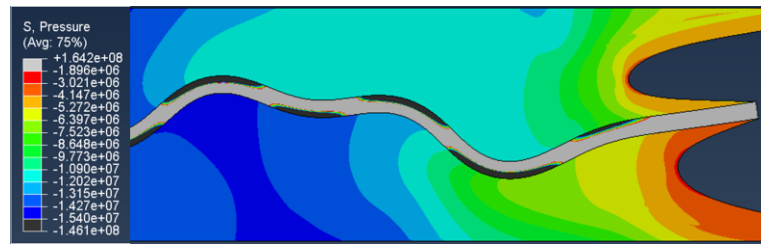


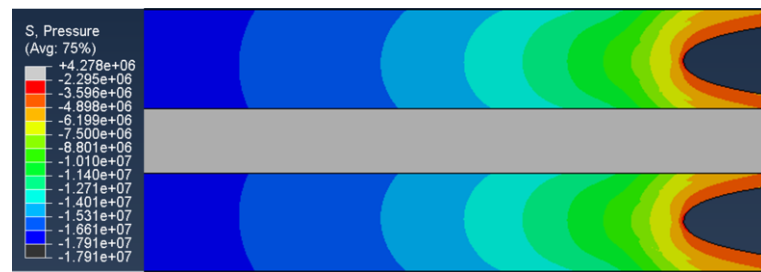
Fig. 99 Schematic of carrier layer pattern: (A) tilted (flat) carrier layer; (B) wavy carrier layer

Modeling results of PSA with thin (thick ratio of carrier to adhesive layer is 3:10) and thick (thick ratio of carrier to adhesive layer is 13:10) carrier layer are shown in Fig. 100 (a) and (b). The ratio of carrier to adhesive layer are consistent to the test

samples. What is the most noticeable that is the waviness of the carrier layer between the thin and thick model. In the thin model, the carrier layer shows short wave length, high amplitude wavy pattern at the stretched ratio of 2 (the stretched ratio of the PSA system is equal to the ratio of total displacement to the thickness of adhesive layer, since the thickness change in the stiff carrier can be ignored when compare to the thickness change in very soft adhesive at the same deformation). The modeling results match the empirical results that show in Figure 5 and 6. The range of stress contour has been narrowed for better showing the distribution of hydrostatic stress (negative of pressure) after wrinkling initiation.



(a)



(b)

Fig. 100 FEA result of PSA system with (a) pressure status of adhesive on thin carrier layer; (b) pressure status of adhesive on thick carrier layer

In order to verify the tilt of thick carrier layer as shown in Fig. 98, we assigned different constitutive properties from tests of single-layered PSA bonded with substrate with different roughness pattern for the partition part of adhesive and made the model

configuration antisymmetric. Although some wavy patterns are noticeable in the deformed carrier, the carrier layer is dominated by tilted pattern in the FEM results in Fig. 101. This matches the empirical observation in Fig. 98.

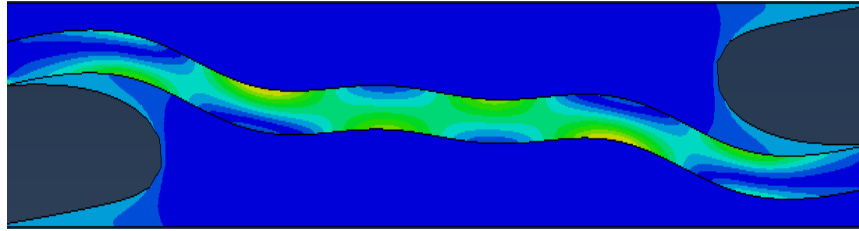


Fig. 101 FEA result of tilted carrier layer

Waviness of carrier layer, if presents, plays very important role in the stress distribution in the adhesive layer. Fig. 102 shows the history plot of hydrostatic stress of two elements on middle plane of top and bottom adhesive with thin (a) and thick (b) carrier layer, which corresponding to the modeling results in Fig. 100. In thin carrier model, stress history of two selected elements are identical until wrinkling of carrier initiates. After wrinkling initiation, hydrostatic stress in concave side is appearing to be lower than the stress in the convex side, which can also be found in the stress contour in Fig. 100 (a), and the discrepancy of hydrostatic stress between two layers is increased as the stretch ratio of the PSA system increased. Compare to thin carrier layer, the hydrostatic stress history of two selected elements are identical through the entire modeling period. This explains: a) the cavities are mostly initiating in the convex region in the PSA with thin carrier layer; b) more sever secondary drop can be observed in the stress-strain response of PSA with thick carrier layer. Mechanisms of cavitation and cavity growth are driven by the surrounding hydrostatic stress. Therefore, the flexural rigidity of carrier layer is influencing the cavitation and cavity growth process by affecting the hydrostatic stress distribution in the adhesive layer.

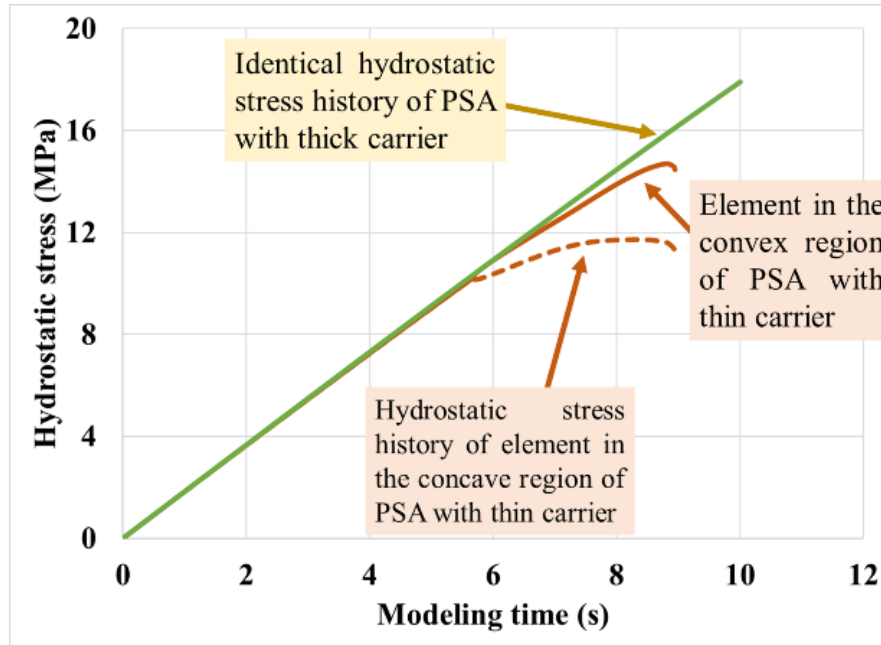


Fig. 102 Hydrostatic stress history of elements on two side of carrier layer (thin and thick carrier)

A3: Statistical Significance

Statistical check conducts on the test results when the differences between two or more groups are not significant.

Test statistic:

$$t = \frac{\bar{Y}_2 - \bar{Y}_1}{\hat{\sigma}_{\bar{Y}_2 - \bar{Y}_1}} \tag{54}$$

To compare the significance of the two tests group on section 6.1.3, we can evaluate t from the known data:

$$t = \frac{(\bar{Y}_1 - \bar{Y}_2) - (\mu_1 - \mu_2)}{\sqrt{\frac{s_1^2}{n_1} + \frac{s_2^2}{n_2}}} \tag{55}$$

where $(\bar{Y}_1 - \bar{Y}_2)$ is the difference of mean value of two test group, $(\mu_1 - \mu_2)$ is the null hypothesis, S_1 and S_2 are the mean value of each test group, and n is the number of test data in each group

Let's set the null hypothesis is $H_0: \mu_1 - \mu_2 = 0$ (not difference between two test groups).

For effects of bonding temperature on PSA bonded assembly strength shown in Fig. **94**.

The t value for the ultimate tensile stress is $t=0.46$ with $d.f. = 8$

The t value for the ductility result is $t=0.045$ with $d.f. = 8$

According to the t-student distribution table with $d.f. = 8$, t must be at least 2.145 to reach $p < .05$. Therefore, the difference of ultimate tensile stress and ductility caused by different bonding temperature is not statistically significant.

For effects of bonding time on PSA bonded assembly strength shown in Fig. **95**.

The t value for the ultimate tensile stress is $t=1.08$ with $d.f. = 8$

The t value for the ductility result is $t=3.38$ with $d.f. = 8$

According to the t-student distribution table with $d.f. = 8$, t must be at least 2.145 to reach $p < .05$, so the difference of ultimate tensile stress caused by different bonding temperature is not statistically significant, but the difference of ductility caused by the different bonding temperature is statistically significant. But the value is very small.

A4: Effects of Macro-Void (Air Trapped) on the Mechanical Response of PSA Bonded assembly

The stress-strain behavior and creep curve of the testing PSA bonded assemblies show relatively large sample to sample variability. Through the study of failure mode

of the debonded samples and the direct observation of the bonding interface between PSA and transparent substrates, a considerable size of non-wetted regions has been found on the interface of the PSA and bonding substrate. As shown in Fig. 103, two different regions can be easily classified on the bonding interface. The darker region is the well bonded region and the light grey region is the non-wetted region. The transition from the well bonded and non-wetting region has less adhesion strength than the well bonded region. This transition region is included in the well bonded region, but it is too weak to maintain two substrate surfaces bonded together during the entire debonding process. The formation of the non-wetted region is due to the air trapped between the PSA and rigid substrate (it is hard to avoid air trapped on both interface when rigid to rigid connection with adhesive). Therefore, random amounts of air might be trapped in the bonding interface between PSA and rigid substrate and result in the non-uniform non-wetted regions. The amount of non-wetted and weak wetted area is hard to control during the bonding process, especially when PSA bonded with two rigid substrates. Therefore, the bond strength is varied between samples. A 2-D simple model is carried out to study the correlation between the bonding strength and the size of non-wetted weak bonding area.

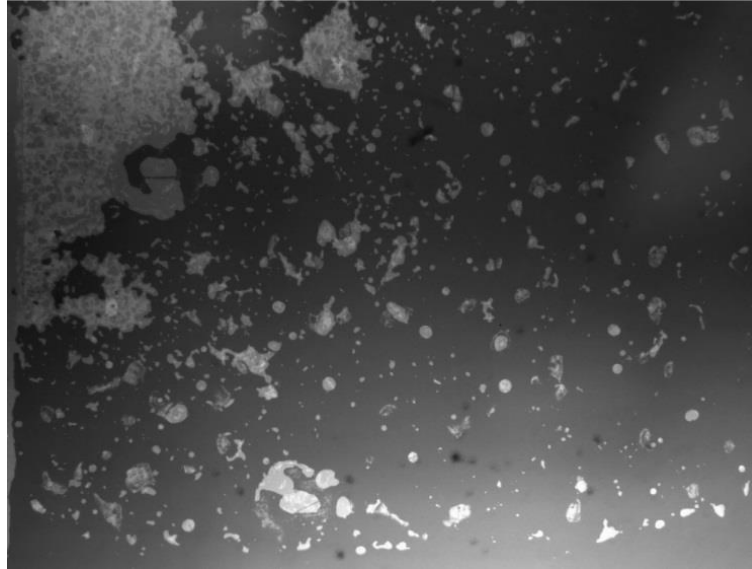


Fig. 103 Bonding interface of PSA and glass substrate

The difference between non-wetted and strong bonding region in the PSA surface delaminated from substrate is shown in Fig. 104. Two different regions are clearly shown at the surface of adhesive after delamination from bonding substrate. The relative flat shining region on the upper half of figure is non-wetted or weak bonding area which is caused by the macro-voids at the bonding interface. Size of the macro-voids is related to the flatness of substrate and adhesive and depends on the alignment of bonding fixture. There is no or very low adhesion between the adhesive and substrate in this area. Therefore, the adhesive delaminates from the substrate before the stress is high enough to initiate a cavitation process in the adhesive layer. Thus, no cavity (permanent deformation) shows in this area. The bottom part of the picture is strong bonding area. Compare it to the weak bonding area, dense cavity shows in this area. This indicates that the adhesion strength in this area is large enough to allow the initiation of cavitation.



Fig. 104. non-wetted and good wetted area of PSA-substrate interface

According to Fig. 105, the bonding interface can be divided into three regions, the well bonded region, the non-wetted area, and the weakly bonded region, which is the interim region between the well bonding and non-wetting region. In Figure 42, the dark region is the well bonded region, where the PSA is perfectly bonded with the substrate. The white region is the non-wetting region, which is due to an air pocket trapped in the bonding interface during the bonding process. The dark gray region is the weakly bonded region, where the PSA is wetted to the substrate, but unlike the well bonded region, the interfacial bonding strength is too weak to maintain the contact between bulk PSA and the bonding substrate. This results in a premature detachment of the bulk PSA from the substrate. The presence of the non-wetted region leads to an underestimation of the actual stress status of the adhesive layer. The variation of the non-wetted region causes scatters in the stress-strain and creep curves. To reduce the errors caused by the non-wetted regions, a stress adjustment Eq. (56) is proposed.

Where σ_m is the modified stress, σ_t is the stress from test data, and $\frac{S_n}{S}$ is the ratio of non-wetted regions to total bonding area. For simplification, the interim region from well bonding region to non-wetted area is ignored. Therefore, the simple 2D model only includes the well bonded region and non-wetted region. In this model, the non-wetted region is defined by pre-seeded initial cracks in the bonding interface of the adhesive and bonding substrate, as shown in Fig. 106 (b). Therefore, the size of the non-wetted region can be adjusted by controlling the size of the cracks. The crack propagation (partial detachment of PSA) is not considered, since it out of scope of this part. A parametric study of PSA bonded samples with 0 (perfect bonding), 5, 10 15, and 20 percent non-wetted regions has been evaluated. The model geometry and mesh are shown in Fig. 106. The parametric study result is reported in Fig. 107. As expected, the FEA model predictions fits the theoretical result very well.

$$\sigma_m = \frac{\sigma_t}{1 - \left(\frac{S_n}{S}\right)} \quad (56)$$

In the current stage, the effects of the non-wetted region will not be included in the predictive model. The purpose of this sub-section is to demonstrate that the non-wetted regions is one of the major reasons for the large piece to piece variability seen in the stress-strain and creep curves. Therefore, it is reasonable that the scatters of stress-strain and creep curves for PSAs are larger than other materials. Since the size of the non-wetted region is dependent on the amount of air trapped at the interface of PSA/substrate, quantitative effects of the non-wetted region on the bonding performance needs more detailed investigations. If the average value of weakly bonded and non-wetting regions can be quantitated from empirical investigation, this value will

be very useful in evaluating the differences between model estimations and empirical measurements.

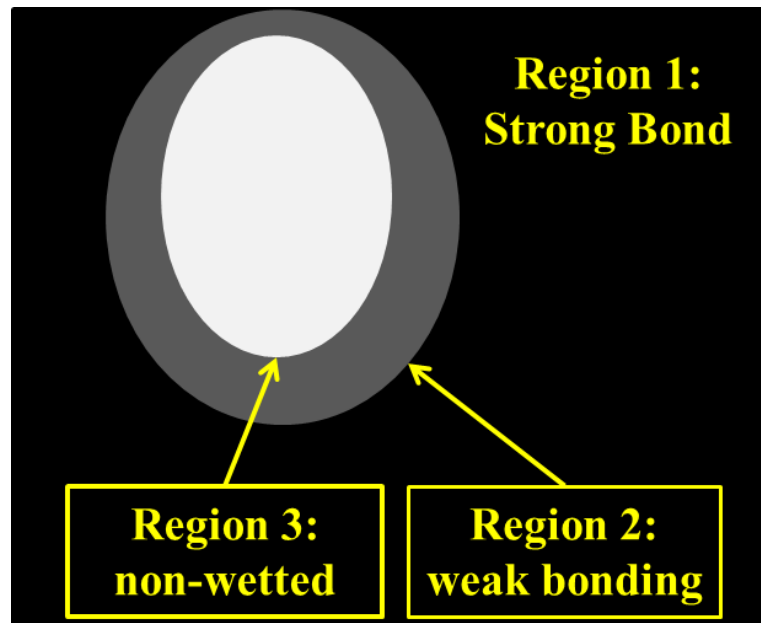


Fig. 105. Schematic of macro-voids at the bonding interface

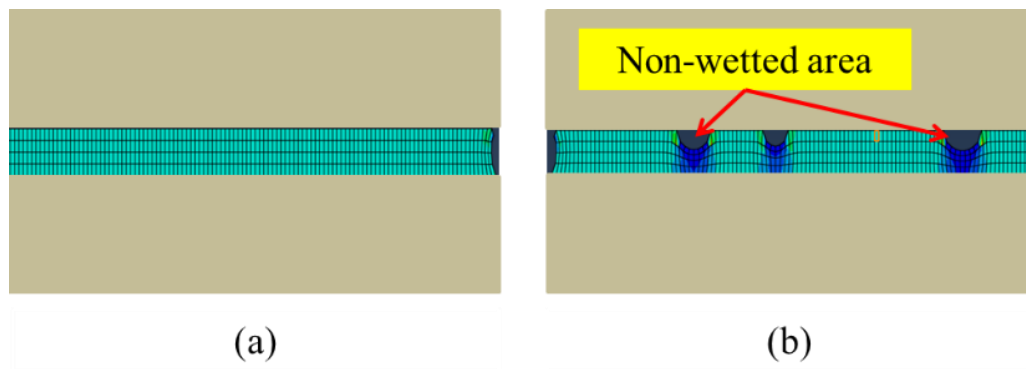


Fig. 106. (a) Perfect bonding model; (b) Bonding interface with macro-voids

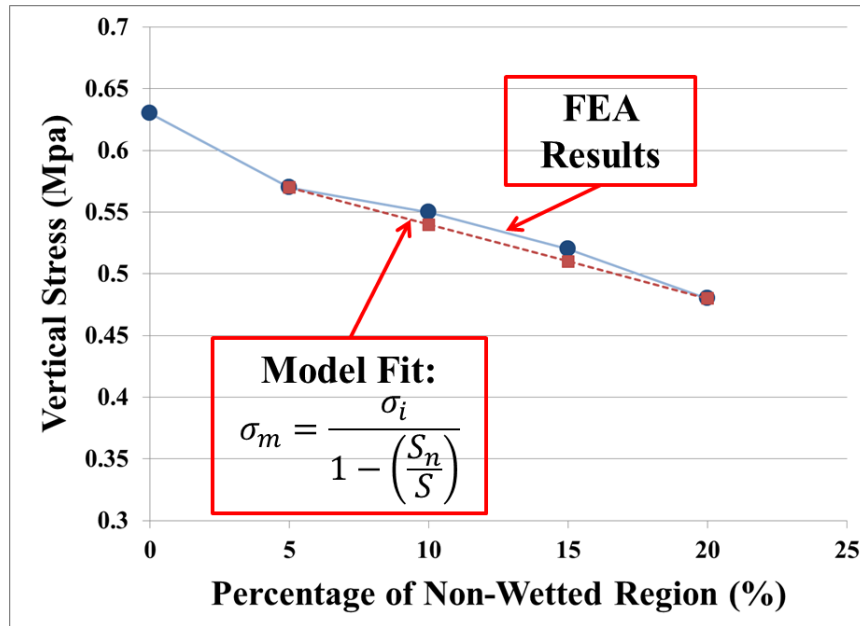


Fig. 107. FEA results with 0, 5, 10, 15, and 20 % non-wetted region and the theoretical prediction

A5: MATLAB Code: Stress-Strain Response of Single-Layered PSA

```

z=10001;
k=20
for a=2:2
    Lam=zeros(1,z);
    DC=zeros(k,z);
    R=zeros(k,z);
    Ry=zeros(k,1);
    DR=zeros(k,z);
    li=zeros(k,1);
    Alpha=zeros(k,1);
    zeta=zeros(k,1);
    xi=zeros(k,1);
    DR1=zeros(k,z);
    C=zeros(k,z);
    Pcav=zeros(k,z);
    P=zeros(k+1,z);
    Pn=zeros(1,z);
    Sigzz=zeros(1,z);
    Sigs=zeros(k,z);
    DSigs=zeros(k,z);
    x1=zeros(k,z);

```

```

x2=zeros(k,z);
x3=zeros(k,z);
x4=zeros(k,z);
x5=zeros(k,z);
x6=zeros(k,z);
epsilon=zeros(1,z);
Tepsilon=zeros(1,z);
eta1=zeros(1,z);
eta2=zeros(1,z);
b=zeros(1,z);
bc=zeros(1,z);
TOT=zeros(1,z);
Dlam=zeros(1,z);
DSigzz=zeros(1,z);
G1=zeros(1,z);
G2=zeros(1,z);
t=zeros(1,z);
th=zeros(1,z);
Dt1=zeros(1,z);
P1=zeros(k+1,z);
A11=zeros(k-1,k-1);
B11=zeros(k-1,1);

for i= 1:k-2
    A11(i,i+1)=1;
    A11(i+1,i)=1;
end
Temp =60;
ct = 95250*Temp^(-2.8);
E1=70*(2^(-2+2))*ct; E2=340*(2^(-2+2))*ct;
h=0.80*(2^(-2+2));
Gc=0.5;
tau=6000*(1.6^(-2+2))*ct;
gamma=0.02*ct;
gammaS = 60*(2^(-2+3))*ct;
mu1=(7*10^(8)*gammaS^2.5+1.3*10^(10))*(0.5^(-2+2));
mu2=(1.1*10^(2)*gammaS^2.5+5*10^(5))*(0.5^(-2+2));
Po=00000;
Arat = 20;
Ho=0.00006;
Lo=0.07;
cb = 1.8e3*(2^(-2+2));
cc = 40;
Dlam(1:600) = 0.10;
Dt1 = 0.02;
Dt2 = 20;

```

```

Wo=Lo/k;
P(:,z)=Po;
P1(:,1)=Po;
G1(1)= E1;
G2(1)= E2;
Pn(1,:)=Po;
Pcav(:,1)=100000;
xp = 21+(1-1)*10;
dx = zeros (1,10); dt = zeros (1,10);
x = zeros (xp,10);
utemp = zeros(xp,z);
u = zeros (xp,z);
gridL = [1, 0.6, 0.36, 0.216, 0.1296, 0.07776, 0.046656, 0.0279936, 0.01679676,
0.010077696];

```

```

for g = 1:10
    dx(1,g)=gridL(1,g)/(xp-1);
    dt(1,g) = 0.9*dx(1,g)^2/2;
    for j = 1:21
        x(j,g)=1-gridL(g)+(j-1)* dx(1,g);
    end
end
g = 1;
eta1(1)=tau*G2(1);

```

```

for i=1:k
    Ry(i)=(0.00000044*(5^(a-2)));
    WL=0.000005;
    Alpha(i)=atand(WL/(2*Ry(i)));
    L(i) = (WL^2/4+Ry(i)^2)^0.5;
    li(i) = L(i)*(Alpha(i)/80)^1.5;
    if li(i)>L(i)
        li(i)=L(i);
    else li(i)=li(i);
    end

    Ro(i) = (L(i)-li(i));
    if Ro(i) < 0.0000003
        R(i,:) = 0.0000003;
    else R(i,:) = Ro(i);
    end
    zeta(i)=WL*(L(i)-li(i))/(L(i));
    xi(i)=((L(i)-li(i))^2-(zeta(i)/2)^2)^0.5;
end

```



```

b(:)= sum(2*li(:)/WL)/k;

for m= 1:1000;
    Lam(1)=1;
    m
    t(m+1)=t(m)+Dt1;
    th(m+1)=t(m+1)/3600;
    Lam(m+1)=Lam(m)+Dlam(m)*Dt1;
    sh = exp(h*log(Lam(m)));
    G1(m+1)=sh*E1;
    G2(m+1)=sh*E2;
    epsilon(m+1)=Lam(m+1)-1;
    eta1(m+1)=tau*G2(m+1);

    DSigzz(m)=(0.5*G1(m)*G2(m)*(Lam(m+1))^2-
1)+(G1(m)+G2(m)+Sigzz(m))*eta1(m+1)*2*Dlam(m)/Lam(m)-
G2(m)*Sigzz(m))/eta1(m+1);
    Sigzz(m+1) = Sigzz(m)+DSigzz(m)*Dt1;
    Pcav(:,m+1)=(Pcav(:,1).*((R(:,1)/R(:,m+1)).^2));

    for i=2:k
        x2(i,m+1) = 2*(Wo*b(m)/(Ho*Lam(m+1)))*(1-Dt1*(G1(m+1))/eta1(m+1)-
6*Dt1*(Sigzz(m+1)+G1(m+1)+G2(m+1))/(mu1*Ho*Lam(m+1)))*(Sigs(i-1,m)-
Sigs(i,m));
        x6(i,m+1) = -8*(Wo*b(m)/(Ho*Lam(m+1)))*G1(m+1)*G2(m+1)*(C(i,m)-
C(i-1,m))*Dt1/Lam(m+1)/Ho/eta1(m+1);
        end
        x1(:,m+1) =
2*(1+6*pi*Wo*b(m)*Dt1*(Sigzz(m+1)+G1(m+1)+G2(m+1))*(R(:,m+1).^2)/(eta1(
m+1)*(Ho^3)*(Lam(m+1)^3)));
        x3(:,m+1) =
Pcav(:,m+1).*(12*pi*b(m)*Wo*Dt1*(Sigzz(m+1)+G1(m+1)+G2(m+1))*(R(:,m+1).^
2))/(eta1(m+1)*(Ho^3)*(Lam(m+1)^3));
        x4(:,m+1) = -
12*pi*Wo*b(m)*gamma*Dt1*(Sigzz(m+1)+G1(m+1)+G2(m+1))*R(:,m+1)/(eta1(m
+1)*(Ho^3)*(Lam(m+1)^3));
        x5(:,m+1) = -
12*(Wo^2)*b(m)*Dlam(m)*Dt1*(Sigzz(m+1)+G1(m+1)+G2(m+1))*(1+pi*(R(:,m+
1).^2)/(Ho*Wo))/((Ho^2)*(Lam(m+1)^4));

    for i=1:k-1
        A11(i,i) = -x1(i+1,m+1);
        B11(i) = x2(i+1,m+1)+x3(i+1,m+1)-x4(i+1,m+1)-x5(i+1,m+1)-
x6(i+1,m+1);
        end
        B11(1)=B11(1)-Po;

```

```

B11(k-1)=B11(k-1)-Po;
P = A11\B11;

P1(1,m+1)=Po;
P1(k+1,m+1)=Po;

for i=2:k
    P1(i,m+1)=P(i-1);
end

Pn(m+1)=mean(P1(1:k+1,m+1));
for i=1:k;
    Sigs(i,m+1)=(-Ho*(Lam(m+1)^1)/(2*Wo*b(m)))*(P1(i+1,m+1)-P1(i,m+1));
end
DSigs(:,m)=(Sigs(:,m+1)-Sigs(:,m))/Dt1;

DC(:,m)=Ho*Lam(m+1)*(DSigs(:,m)*eta1(m)+(G1(m+1)+G2(m+1))*Sigs(:,m+1)+
G1(m+1)*G2(m+1)*2*C(:,m)/Ho^2/Lam(m+1))/(Sigzz(m+1)*eta1(m+1)+G1(m+1)*
eta1(m+1))/4;
C(:,m+1)=C(:,m)+DC(:,m)*Dt1;
TOT(m+1)=Po+(Sigzz(m+1)-Pn(m+1))*b(m);
if TOT(m+1)> (69000/1)*(1.5^(-2+2))
    break
end
end
eta1(m+1)=tau*G2(m+1)*cb;
Dlam(m+1:z)=0;

for n=m+1:z-1
    n
    t(n+1)=t(n)+Dt2;
    th(n+1)=t(n+1)/3600;
    sh= exp(h*log(Lam(n)));
    G1(n+1)=sh*E1;
    G2(n+1)=sh*E2;
    eta2(n)=tau*G2(n+1)*cb;
    for i=2:k
        x2(i,n+1) = 2*(Wo*b(n-1)/(Ho*Lam(n)))*(1-Dt2*(G1(n))/eta2(n)-
6*Dt2*(Sigzz(n)+G1(n)+G2(n))/(mu1*Ho*Lam(n)))*(Sigs(i-1,n)-Sigs(i,n));
        x6(i,n+1) = -8*(Wo*b(n-1)/(Ho*Lam(n)))*G1(n)*G2(n)*(C(i,n)-C(i-
1,n))*Dt2/Lam(n)/Ho/eta2(n);
    end
    x1(:,n+1) = 2*(1+6*pi*Wo*b(n-
1)*Dt2*(Sigzz(n)+G1(n)+G2(n))*(R(:,n).^2)/(eta1(n)*(Ho^3)*(Lam(n)^3)));
    x3(:,n+1) = Pcav(:,n+1).*(12*pi*b(n-
1)*Wo*Dt2*(Sigzz(n)+G1(n)+G2(n))*(R(:,n).^2)/(eta1(n)*(Ho^3)*(Lam(n)^3)));

```

```

x4(:,n+1) = -12*pi*Wo*b(n-
1)*gamma*Dt2*(Sigzz(n)+G1(n)+G2(n))*R(:,n)/(eta1(n)*(Ho^3)*(Lam(n)^3));
x5(:,n+1) = -12*(Wo^2)*b(n-
1)*Dlam(n)*Dt2*(Sigzz(n)+G1(n)+G2(n))*(1+pi*(R(:,n).^2)/(Ho*Wo))/((Ho^2)*(La
m(n)^4));

```

```

for i=1:k-1
    A11(i,i) = -x1(i+1,n+1);
    B11(i) = x2(i+1,n+1)+x3(i+1,n+1)-x4(i+1,n+1)-x5(i+1,n+1)-x6(i+1,n+1);
end
B11(1)=B11(1)-Po;
B11(k-1)=B11(k-1)-Po;
P = A11\B11;
P1(1,n+1)=Po;
P1(k+1,n+1)=Po;

```

```

for i=2:k
    P1(i,n+1)=P(i-1);
end
Pn(n+1)=mean(P1(1:k+1,n+1));
Sigzz(n+1) = (TOT(m+1)-Po)/b(n-1)+Pn(n+1);
DSigzz(n) = (Sigzz(n+1)-Sigzz(n))/Dt2;
Dlam(n) =

```

```

(Lam(n)/2/eta2(n)/(G1(n)+G2(n)+Sigzz(n)))*(G2(n)*Sigzz(n)+DSigzz(n)*eta2(n)-
G1(n)*G2(n)*(Lam(n)^2-1)/2);
Lam(n+1)=Lam(n)+Dlam(n)*Dt2;
epsilon(n+1)=Lam(n+1)-1;

```

```

E=sh*(E1);

```

```

for j=2:xp-1
    u(j,n) = u(j,n-1)+(u(j-1,n-1)-2*u(j,n-1)+u(j+1,n-
1))*(Dt2*(E/mu2)/(Arat*Lam(n+1)))/(dx(1,g)^2);
end

```

```

bc(n) = E*Sigzz(n+1)*(Arat*Lam(n+1));
u(1,n) = u(3,n)-bc(n)*2*dx(1,g);
u(xp,n) = u(xp-2,n);
b(1,n) = b(1) - abs(u(xp,n));

```

```

if Lam(n+1) > 1.3

```

```

    for j=2:k
        if Pcav(j,n)-P1(j,n)-gamma/R(j,n) > 0
            eta1(n+1)=tau*G2(n+1)*cc;
            DR(j,n+1)=(R(j,n)/(2*eta1(n+1)))*(Pcav(j,n)-P1(j,n)-gamma/R(j,n));
            R(j,n+1)=R(j,n)+DR(j,n+1)*Dt2;
        else if DR(j,n) ~= 0
            eta1(n+1)=tau*G2(n+1)*cb;
        end
    end
end

```

```

        DR(j,n+1)=(R(j,n)/(2*eta1(n+1)))*(Pcav(j,n)-P1(j,n)-gamma/R(j,n));
    else DR(j,n+1) = 0;
    end
end
end
eta1(n+1)=tau*G2(n+1)*cb;
else
for j=2:k
    eta1(n+1)=tau*G2(n+1)*cb;
    R(j,n+1)=R(j,n)+DR(j,n+1)*Dt2;
end
end
for i=1:20;
    Sigs(i,n+1)=-Ho*(Lam(n+1))/(2*Wo*b(n))*(P1(i+1,n+1)-P1(i,n+1));
end
DSigs(:,n)=(Sigs(:,n+1)-Sigs(:,n))/Dt2;
DC(:,n)=Ho*Lam(n)*(DSigs(:,n)*eta2(n)+(G1(n)+G2(n))*Sigs(:,n)+G1(n)*G2(n)*2*
C(:,n)/Ho^2/Lam(n+1))/(Sigzz(n)+G1(n))/4/eta2(n);
C(:,n+1)=C(:,n)+DC(:,n)*Dt2;

for j=2:k
    Pcav(j,n+1)=Pcav(j,1)*((R(j,1)/R(j,n+1))^2);
end
if Lam(n+1)>13
    break
end
end

cb=a;
S(1:n-1,cb)=epsilon(1:n-1);
O(1:n-1,cb)=Pn(1:n-1);
T(1:n-1,cb)=th(1:n-1);
filename = [ 'a' num2str(a), '.mat' ]
save(filename);
end

plot(T(:,,:),S(:,,:));
hold on

```

A6: MATLAB Code: Creep Model of Single-Layered PSA

```

z=7001;
k=20
for a=2:2
    % variables
    Lam=zeros(1,z);

```

```

DC=zeros(k,z); %time increment of C
R=zeros(k,z);
Ry=zeros(k,1);
DR=zeros(k,z);
li=zeros(k,1);
Alpha=zeros(k,1);
zeta=zeros(k,1);
xi=zeros(k,1);
DR1=zeros(k,z);
C=zeros(k,z);
Pcav=zeros(k,z);
P=zeros(k+1,z);
Pn=zeros(1,z);
Sigzz=zeros(1,z);
Sigs=zeros(k,z);
DSigs=zeros(k,z);
x1=zeros(k,z);
x2=zeros(k,z);
x3=zeros(k,z);
x4=zeros(k,z);
x5=zeros(k,z);
x6=zeros(k,z);
epsilon=zeros(1,z);
Tepsilon=zeros(1,z);
eta1=zeros(1,z);
eta2=zeros(1,z);
b=zeros(1,z);
bc=zeros(1,z);
TOT=zeros(1,z);
Dlam=zeros(1,z);
G=zeros(1,z);
DSigzz=zeros(1,z);
G1=zeros(1,z);
G2=zeros(1,z);
t=zeros(1,z);
th=zeros(1,z);
Dt1=zeros(1,z);
P1=zeros(k+1,z);
A11=zeros(k-1,k-1);
B11=zeros(k-1,1);

for i= 1:k-2
    A11(i,i+1)=1;
    A11(i+1,i)=1;
end

```

```

ct = 1;

%initial value
E1=70*(2^(-2+2))*ct; E2=340*(2^(-2+2))*ct;
%strain hardening coefficient
h=0.80*(2^(-2+2));
%critical energy release rate
Gc=0.5;
%relaxation time
tau=6000*(1.6^(-2+2))*ct;
%PSA surface free energy
gamma=0.02*ct;
%Substrate surface free energy
gammaS = 40*(2^(-2+3))*ct;%40*(2^(-2+2));
%friction coefficient for fibril movement
mu1=(gammaS*8*10^(11)+1.3*10^(10))*(0.5^(-2+2));
mu2=(gammaS*5*10^(5)+5*10^(5))*(0.5^(-2+2));
%relative pressure
Po=00000;
%initial ratio of foot to fibril
Arat = 20*(2^(-2+2));
%thickness of PSA
Ho=0.00012;
%length of PSA
Lo=0.007;
%viscosity parameter for bulk PSA
cb = 1.8e3*(2^(-2+2))*ct;
%viscosity parameter for cavity
cc = 60*ct;
%loading strain rate
Dlam(1:600) = 0.10;
%step time
Dt1 = 0.02; %ramp up
Dt2 = 20; %creep

Wo=Lo/k; %Block length
% Ro=0.0000003;
% R(:,:)=Ro; %Initial value of R
P(:,z)=Po;
P1(:,1)=Po;
G1(1)= E1;
G2(1)= E2;
G(1) = G1(1)+G2(1);
Pn(1,:)=Po;
Pcav(:,1)=0000000;
xp = 21+(1-1)*10;

```

```

dx = zeros (1,10); dt = zeros (1,10);
x = zeros (xp,10);
utemp = zeros(xp,z);
u = zeros (xp,z);
gridL = [1, 0.6, 0.36, 0.216, 0.1296, 0.07776, 0.046656, 0.0279936, 0.01679676,
0.010077696];

for g = 1:10
    dx(1,g)=gridL(1,g)/(xp-1);
    dt(1,g) = 0.9*dx(1,g)^2/2;
    for j = 1:21
        x(j,g)=1-gridL(g)+(j-1)* dx(1,g);
    end
end
g = 1;
eta1(1)=tau*G2(1);

for i=1:k
    Ry(i)=(0.00000044*(5^(a-2)));
    WL=0.000005;
    Alpha(i)=atand(WL/(2*Ry(i)));
    L(i) = (WL^2/4+Ry(i)^2)^0.5;
    li(i) = L(i)*(Alpha(i)/80)^1.5;
    if li(i)>L(i)
        li(i)=L(i);
    else li(i)=li(i);
    end

    Ro(i) = (L(i)-li(i));% WL*(L(i)-li(i))/(L(i));
    if Ro(i) < 0.0000003
        R(i,:) = 0.0000003;
    else R(i,:) = Ro(i);
    end
    zeta(i)=WL*(L(i)-li(i))/(L(i));
    xi(i)=((L(i)-li(i))^2-(zeta(i)/2)^2)^0.5;

%     if L(i)-li(i)== 0
%         cavP2(i)= -500000;
%     else cavP2(i)= -min(Po*(1+(20000/Po)^0.5*((Gc*(1+0.2*(m-
2))))^(3/2)./(Po^(3/2)*(zeta(i)^0.5).*xi(i))).^0.5,500000);
%     end

end
b(:)= sum(2*li(:)/WL)/k;

for m= 1:1000;

```

```

Lam(1)=1;
m
t(m+1)=t(m)+Dt1;
th(m+1)=t(m+1)/3600;
Lam(m+1)=Lam(m)+Dlam(m)*Dt1; %time evolution of Lam
sh = exp(h*log(Lam(m)));
G1(m+1)=sh*E1;
G2(m+1)=sh*E2;
G(m+1) = G1(m+1)+G2(m+1);
epsilon(m+1)=Lam(m+1)-1;
eta1(m+1)=tau*G2(m+1);

%Dsigzz(n)=(tau*(G1(n)+G2(n))*2*Dlam(n)/Lam(n)+(G1(n)*epsilon(n+1)-
Sigzz(n)))/(tau+Dt);
DSigzz(m)=(0.5*G1(m)*G2(m)*(Lam(m+1)^2-
1)+(G1(m)+G2(m)+Sigzz(m))*eta1(m+1)*2*Dlam(m)/Lam(m)-
G2(m)*Sigzz(m))/eta1(m+1);
Sigzz(m+1) = Sigzz(m)+DSigzz(m)*Dt1;

%time evolution of Pcav
Pcav(:,m+1)=(Pcav(:,1).*((R(:,1)./R(:,m+1)).^2));

for i=2:k
    x2(i,m+1) = 2*(Wo*b(m)/(Ho*Lam(m+1)))*(1-Dt1*(G1(m+1))/eta1(m+1)-
6*Dt1*(Sigzz(m+1)+G1(m+1)+G2(m+1))/(mu1*Ho*Lam(m+1)))*(Sigs(i-1,m)-
Sigs(i,m));
    x6(i,m+1) = -8*(Wo*b(m)/(Ho*Lam(m+1)))*G1(m+1)*G2(m+1)*(C(i,m)-
C(i-1,m))*Dt1/Lam(m+1)/Ho/eta1(m+1);
end
x1(:,m+1) =
2*(1+6*pi*Wo*b(m)*Dt1*(Sigzz(m+1)+G1(m+1)+G2(m+1))*(R(:,m+1).^2)/(eta1(
m+1)*(Ho^3)*(Lam(m+1)^3)));
x3(:,m+1) =
Pcav(:,m+1).*(12*pi*b(m)*Wo*Dt1*(Sigzz(m+1)+G1(m+1)+G2(m+1))*(R(:,m+1).^
2))/(eta1(m+1)*(Ho^3)*(Lam(m+1)^3));
x4(:,m+1) = -
12*pi*Wo*b(m)*gamma*Dt1*(Sigzz(m+1)+G1(m+1)+G2(m+1))*R(:,m+1)/(eta1(m
+1)*(Ho^3)*(Lam(m+1)^3));
x5(:,m+1) = -
12*(Wo^2)*b(m)*Dlam(m)*Dt1*(Sigzz(m+1)+G1(m+1)+G2(m+1))*(1+pi*(R(:,m+
1).^2)/(Ho*Wo))/((Ho^2)*(Lam(m+1)^4));

for i=1:k-1
    A11(i,i) = -x1(i+1,m+1);
    B11(i) = x2(i+1,m+1)+x3(i+1,m+1)-x4(i+1,m+1)-x5(i+1,m+1)-
x6(i+1,m+1);

```



```

end
B11(1)=B11(1)-Po;
B11(k-1)=B11(k-1)-Po;
P = A11\B11;

P1(1,m+1)=Po;
P1(k+1,m+1)=Po;

for i=2:k
    P1(i,m+1)=P(i-1);
end

Pn(m+1)=mean(P1(1:k+1,m+1));
%time evolution of Sigs
for i=1:k;
    Sigs(i,m+1)=(-Ho*(Lam(m+1)^1)/(2*Wo*b(m)))*(P1(i+1,m+1)-P1(i,m+1));
%(16)
end
DSigs(:,m)=(Sigs(:,m+1)-Sigs(:,m))/Dt1;

%time evolution of DC

DC(:,m)=Ho*Lam(m+1)*(DSigs(:,m)*eta1(m)+(G1(m+1)+G2(m+1))*Sigs(:,m+1)+
G1(m+1)*G2(m+1)*2*C(:,m)/Ho^2/Lam(m+1))/(Sigzz(m+1)*eta1(m+1)+G1(m+1)*
eta1(m+1))/4;
C(:,m+1)=C(:,m)+DC(:,m)*Dt1;

TOT(m+1)=Po+(Sigzz(m+1)-Pn(m+1))*b(m);
if TOT(m+1)> (50000/1)*(1.5^(-2+2)) %expected creep stress
    break
end
end

eta1(m+1)=tau*G2(m+1)*cb;
Dlam(m+1:z)=0;

for n=m+1:z-1
    n
    t(n+1)=t(n)+Dt2;
    th(n+1)=t(n+1)/3600;
    sh= exp(h*log(Lam(n)));
    G1(n+1)=sh*E1;
    G2(n+1)=sh*E2;

    eta2(n)=tau*G2(n+1)*cb;

```

```

for i=2:k
    x2(i,n+1) = 2*(Wo*b(n-1)/(Ho*Lam(n)))*(1-Dt2*(G1(n))/eta2(n)-
6*Dt2*(Sigzz(n)+G1(n)+G2(n))/(mu1*Ho*Lam(n)))*(Sigs(i-1,n)-Sigs(i,n));
    x6(i,n+1) = -8*(Wo*b(n-1)/(Ho*Lam(n)))*G1(n)*G2(n)*(C(i,n)-C(i-
1,n))*Dt2/Lam(n)/Ho/eta2(n);
end
x1(:,n+1) = 2*(1+6*pi*Wo*b(n-
1)*Dt2*(Sigzz(n)+G1(n)+G2(n))*(R(:,n).^2)/(eta1(n)*(Ho^3)*(Lam(n)^3)));
x3(:,n+1) = Pcav(:,n+1).*(12*pi*b(n-
1)*Wo*Dt2*(Sigzz(n)+G1(n)+G2(n))*(R(:,n).^2)/(eta1(n)*(Ho^3)*(Lam(n)^3)));
x4(:,n+1) = -12*pi*Wo*b(n-
1)*gamma*Dt2*(Sigzz(n)+G1(n)+G2(n))*R(:,n)/(eta1(n)*(Ho^3)*(Lam(n)^3));
x5(:,n+1) = -12*(Wo^2)*b(n-
1)*Dlam(n)*Dt2*(Sigzz(n)+G1(n)+G2(n))*(1+pi*(R(:,n).^2)/(Ho*Wo))/((Ho^2)*(La
m(n)^4));

for i=1:k-1
    A11(i,i) = -x1(i+1,n+1);
    B11(i) = x2(i+1,n+1)+x3(i+1,n+1)-x4(i+1,n+1)-x5(i+1,n+1)-x6(i+1,n+1);
end
B11(1)=B11(1)-Po;
B11(k-1)=B11(k-1)-Po;
P = A11\B11;
P1(1,n+1)=Po;
P1(k+1,n+1)=Po;

for i=2:k
    P1(i,n+1)=P(i-1);
end
%time evolution of total stress
Pn(n+1)=mean(P1(1:k+1,n+1));
Sigzz(n+1) = (TOT(m+1)-Po)/b(n-1)+Pn(n+1); %TOT(m+1)=Po+(Sigzz(m+1)-
Pn(m+1))*b(m)-(100000*(1/Lam1(n+1)^2)-100000)*(1-b1(m));
DSigzz(n) = (Sigzz(n+1)-Sigzz(n))/Dt2;
%Dlam(n) = (Sigzz(n)+DSigzz(n)*tau-G1(n)*epsilon(n))/((G1(n)+G2(n))*tau);
Dlam(n) =
(Lam(n)/2/eta2(n)/(G1(n)+G2(n)+Sigzz(n)))*(G2(n)*Sigzz(n)+DSigzz(n)*eta2(n)-
G1(n)*G2(n)*(Lam(n)^2-1)/2);
Lam(n+1)=Lam(n)+Dlam(n)*Dt2;
G(n+1) = G1(n+1)+G2(n+1);
epsilon(n+1)=Lam(n+1)-1;

E=sh*(E1);
for j=2:xp-1

```

```

    u(j,n) = u(j,n-1)+(u(j-1,n-1)-2*u(j,n-1)+u(j+1,n-
1))*(Dt2*(E/mu2)/(Arat*Lam(n+1)))/(dx(1,g)^2);
    end
    %boundary condition
    bc(n) = E*Sigzz(n+1)*(Arat*Lam(n+1));
    u(1,n) = u(3,n)-bc(n)*2*dx(1,g); % left B.C.
    u(xp,n) = u(xp-2,n); % left B.C.
    b(1,n) = b(1) - abs(u(xp,n));

    if Lam(n+1) > 1.3
        for j=2:k
            if Pcav(j,n)-P1(j,n)-gamma/R(j,n) > 0
                eta1(n+1)=tau*G2(n+1)*cc;
                DR(j,n+1)=(R(j,n)/(2*eta1(n+1)))*(Pcav(j,n)-P1(j,n)-gamma/R(j,n));
% (20)
                R(j,n+1)=R(j,n)+DR(j,n+1)*Dt2;
            else if DR(j,n) ~= 0
                eta1(n+1)=tau*G2(n+1)*cb;
                DR(j,n+1)=(R(j,n)/(2*eta1(n+1)))*(Pcav(j,n)-P1(j,n)-gamma/R(j,n));
            else DR(j,n+1) = 0;
            end
        end
    end
    eta1(n+1)=tau*G2(n+1)*cb;
else
    for j=2:k
        eta1(n+1)=tau*G2(n+1)*cb;
        R(j,n+1)=R(j,n)+DR(j,n+1)*Dt2;
    end
end

%time evolution of Sigs
for i=1:20;
    Sigs(i,n+1)=-Ho*(Lam(n+1))/(2*Wo*b(n))*(P1(i+1,n+1)-P1(i,n+1));
% (16)
end
DSigs(:,n)=(Sigs(:,n+1)-Sigs(:,n))/Dt2;

%time evolution of DC

DC(:,n)=Ho*Lam(n)*(DSigs(:,n)*eta2(n)+(G1(n)+G2(n))*Sigs(:,n)+G1(n)*G2(n)*2*
C(:,n)/Ho^2/Lam(n+1))/(Sigzz(n)+G1(n))/4/eta2(n); % (24)
C(:,n+1)=C(:,n)+DC(:,n)*Dt2;

%time evolution of Pcav
for j=2:k

```

```

        Pcav(j,n+1)=Pcav(j,1)*((R(j,1)/R(j,n+1))^2);
    end

%    if b(n) < 9/Lam(n) && Lam(n) > 10
%        break
%    end
    if Lam(n+1)>9 %&& Dlam(n)>0.0003
        break
    end
%    if b(n+1)<1 && b(n+1) < (7)/Lam(n+1)
%        break
%    end
end

cb=a;
S(1:n-1,cb)=epsilon(1:n-1);
O(1:n-1,cb)=Pn(1:n-1);
T(1:n-1,cb)=th(1:n-1);
filename = [ 'a' num2str(a), '.mat' ]
save(filename);
end

% for i=1:2
%    plot(T(:,i),L(:,i));
%    hold on
% end
%plot(th(1:n-1),L(1:n-1));
%    % c=m;
%    % T(:,c)=Lam;
%    % DT(:,c)=Dlam;
%    % filename = [ 'mu2' num2str(m), '.mat' ]
%    % save(filename);

plot(T(:,:),S(:,:));
hold on
%plot(T(:,2),L(:,2),'b');

```

A7: MATLAB code: Stress-Strain and Creep Model of Double-Layered PSA

```

z = 23000;
k= 21;

for m=2:2
K3 =3000000*(1.3-0.2*m)^3;

```

```

TOT=zeros(1,z-1);
Lam1=zeros(1,z);
LS=zeros(1,z);
Dlam1=zeros(1,z);
C1=zeros(k,z);
DC1=zeros(k,z);
Ry1=zeros(k,1);
Ro1=zeros(k,1);
R1=zeros(k,z);
L1=zeros(k,1);
li1=zeros(k,1);
Alpha1=zeros(k,1);
zeta1=zeros(k,1);
xi1=zeros(k,1);
DR1=zeros(k,z);
Pcav1=zeros(k,z);
P1=zeros(k+1,z);
Pn1=zeros(1,z);
TOT1=zeros(1,z);
Sigzz1=zeros(1,z);
Sigs1=zeros(k,z);
DSigs1=zeros(k,z);
X1=zeros(k,z);
Xs1=zeros(k,z);
DX1=zeros(k,z);
x11=zeros(k,z);
x12=zeros(k,z);
x13=zeros(k,z);
x14=zeros(k,z);
x15=zeros(k,z);
x16=zeros(k,z);
bc1=zeros(1,z);
b1=zeros(1,z);
eta1=zeros(1,z);
e1=zeros(1,z);
e2=zeros(1,z);
tau=zeros(1,z);
G1=zeros(1,z);
G2=zeros(1,z);
A11=zeros(k-1,k-1);
B11=zeros(k-1,1);
for i= 1:k-2
    A11(i,i+1)=1;
    A11(i+1,i)=1;
end
h=1.4;

```

```

gammaS = 160 + 60*(3-3);
a=60;
Gc = 0.3;
E1=50; E2=4*E1;
G1(1)=E1;
G2(1)=E2;
Ho = 0.00006*(0.9+0.1*2);
RHo= 0.00006;
Lo=0.007;
Wo1=Lo*b1(1)/k;
nu=0.49;
mu=1*10^(12);
mu2=1.5*10^(8);
gammaP=0.04;
Po=100000;

for i=1:k
    Ry1(i)=(0.00000014+0.00000003*(1-1))*(1+randn/300);
    WL1=0.0000003;
    Alpha1(i)=atand(WL1/(2*Ry1(i)));
    L1(i) = (WL1^2/4+Ry1(i)^2)^0.5;
    li1(i) = L1(i)*(Alpha1(i)/a)^1.5;
    if li1(i)>L1(i)
        li1(i)=L1(i);
    else li1(i)=li1(i);
    end

    Ro1(i) = (L1(i)-li1(i));
    if Ro1(i) < 0.00000005
        R1(i,1) = 0.00000005;
    else R1(i,1) = Ro1(i);
    end
    zeta1(i)=WL1*(L1(i)-li1(i))/(L1(i));
    xi1(i)=((L1(i)-li1(i))^2-(zeta1(i)/2)^2)^0.5;

    if L1(i)-li1(i)== 0
        cavP1(i)= -gammaP/0.00000005;
    else cavP1(i)= -
min(100000*(1+(20000/100000)^0.5*(Gc^(3/2))./(100000^(3/2)*(zeta1(i)^0.5).*xi1(i)
)).^0.5,gammaP/0.00000005);
    end
end
b1(1)= sum(2*li1(:)/WL1)/k;
Wo1=Lo*b1(1)/k;

tau=3500;

```

```

eta1(1)=tau*G1(1);
P1(:,1)=Po;
Lam1(1)=1;
Pcav1(:,1)=0;
Pn1(:,1)=Po;
Dlam1(:) = 0.02;
Dlam1(:) = 0.02;
A12=zeros(k-1,k-1);
B12=zeros(k-1,1);
for i= 1:k-2
    A12(i,i+1)=1;
    A12(i+1,i)=1;
end
xp = 21;
dx = zeros (1,10); dt = zeros (1,10);
x = zeros (xp,10);
u1 = zeros (xp,z);
u2 = zeros (xp,z);
Arat = 3;
gridL = [1, 0.6, 0.36, 0.216, 0.1296, 0.07776, 0.046656, 0.0279936, 0.01679676,
0.010077696];
for g = 1:10
    dx(1,g)=gridL(1,g)/(xp-1);
    dt(1,g) = 0.9*dx(1,g)^2/2;
    for j = 1:21
        x(j,g)=1-gridL(g)+(j-1)* dx(1,g);
    end
end
g = 1
Lam2=zeros(1,z);
Dlam2=zeros(1,z);
C2=zeros(k,z);
DC2=zeros(k,z);
R2=zeros(k,z);
Ry2=zeros(k,1);
Ro2=zeros(k,1);
L2=zeros(k,1);
li2=zeros(k,1);
Alpha2=zeros(k,1);
zeta2=zeros(k,1);
xi2=zeros(k,1);
DR2=zeros(k,z);
Pcav2=zeros(k,z);
P2=zeros(k+1,z);
Pn2=zeros(1,z);
TOT2=zeros(1,z);

```

```

Sigzz2=zeros(1,z);
Sigs2=zeros(k,z);
DSigs2=zeros(k,z);
X2=zeros(k,z);
Xs2=zeros(k,z);
DX2=zeros(k,z);
x21=zeros(k,z);
x22=zeros(k,z);
x23=zeros(k,z);
x24=zeros(k,z);
x25=zeros(k,z);
x26=zeros(k,z);
bc2=zeros(1,z);
b2=zeros(1,z);
eta2=zeros(1,z);
TOT1(:)=1;
Wo2=Lo*b2(1)/k;

for i=1:k
    Ry2(i)=(0.00000028)*(1+randn/300);
    WL2=0.0000003;
    Alpha2(i)=atand(WL2/(2*Ry2(i)));
    L2(i) = (WL2^2/4+Ry2(i)^2)^0.5;
    li2(i) = L2(i)*(Alpha2(i)/a)^1.5;
    if li2(i)>L2(i)
        li2(i)=L2(i);
    else li2(i)=li2(i);
    end

    Ro2(i) = (L2(i)-li2(i));
    if Ro2(i) < 0.00000005
        R2(i,1) = 0.00000005;
    else R2(i,1) = Ro2(i);
    end
    zeta2(i)=WL2*(L2(i)-li2(i))/(L2(i));
    xi2(i)=((L2(i)-li2(i))^2-(zeta2(i)/2)^2)^0.5;

    if L2(i)-li2(i)== 0
        cavP2(i)= -gammaP/0.00000005;
    else cavP2(i)= -
min(100000*(1+(20000/100000)^0.5*(Gc^(3/2))./(100000^(3/2)*(zeta2(i)^0.5).*xi2(i)
)).^0.5),gammaP/0.00000005);
    end

end
b2(1)= sum(2*li2(:)/WL2)/k;

```


Wo2=Lo*b2(1)/k;

eta2(1)=tau*G2(1);

P2(:,1)=Po;

Lam2(1)=1;

Pcav2(:,1)=0;

Pn2(:,1)=Po;

Dlam2(:) = 0.02;

Dlam2(:) = 0.02;

g=1;

Dt = 0.03;

for n= 1:z-1

 n

 N = 0;

 e1(n) = abs(TOT1(n+1)*Lo/2 - TOT2(n+1)*Lo/2-K3*LS(n+1));

 e2(n) = 0.005*abs(TOT1(n+1)*Lo/2);

 while e1(n) > e2(n) && N < 2000

 Lam1(n+1)=Lam1(n)+Dlam1(n)*Dt;

 sh1=exp(h*log(Lam1(1,n+1)));

 G1(n+1)=sh1*E1;

 G2(n+1)=sh1*E2;

 eta1(n+1)=tau*G2(n+1);

 DSigzz1(n)=(0.5*G1(n)*G2(n)*(Lam1(n+1)^2-
1)+2*(G1(n)+G2(n)+Sigzz1(n))*eta1(n+1)*Dlam1(n)/Lam1(n)-
G1(n)*Sigzz1(n))/eta1(n+1);

 Sigzz1(n+1) = Sigzz1(n)+DSigzz1(n)*Dt;

 for j = 2:k

 if P1(j,n) > cavP1(j) && R1(j,n)== R1(j,1) && DR1(j,n) == 0;

 DR1(j,n+1)=0;

 R1(j,n+1) = R1(j,n);

 else

 DR1(j,n+1)=(R1(j,n)/(2*eta1(n+1)))*(Pcav1(j,n)-P1(j,n)-
2*gammaP/R1(j,n));

 R1(j,n+1)=R1(j,n)+DR1(j,n+1)*Dt;

 end

 Pcav1(j,n+1)=Pcav1(j,1)*((R1(j,1)/R1(j,n+1))^2);

 end

for i=2:k

 x12(i,n+1) = 2*(Wo1*b1(n)/(RHo*Lam1(n+1)))*(1-Dt*(G1(n+1))/eta1(n+1)-
6*Dt*(Sigzz1(n+1)+G1(n+1)+G2(n+1))/(mu*Ho*Lam1(n+1)))*(Sigs1(i-1,n)-
Sigs1(i,n));

```

        x16(i,n+1) = -
8*(Wo1*b1(n)/(RHo*Lam1(n+1)))*G1(n+1)*G2(n+1)*(C1(i,n)-C1(i-
1,n))*Dt/Lam1(n+1)/RHo/eta1(n+1);
end
        x11(:,n+1) =
2*(1+6*pi*Wo1*b1(n)*Dt*(Sigzz1(n+1)+G1(n+1)+G2(n+1))*(R1(:,n+1).^2)/(eta1(n
+1)*(RHo^2*Ho)*(Lam1(n+1)^3)));
        x13(:,n+1) =
Pcav1(:,n+1).*(12*pi*b1(n)*Wo1*Dt*(Sigzz1(n+1)+G1(n+1)+G2(n+1)).*(R1(:,n+1)
.^2))/(eta1(n+1)*(RHo^2*Ho)*(Lam1(n+1)^3));
        x14(:,n+1) = -
12*pi*Wo1*b1(n)*gammaP*Dt*(Sigzz1(n+1)+G1(n+1)+G2(n+1))*R1(:,n+1)/(eta1(
n+1)*(RHo^2*Ho)*(Lam1(n+1)^3));
        x15(:,n+1) = -
12*(Wo1^2)*b1(n)*Dlam1(n)*Dt*(Sigzz1(n+1)+G1(n+1)+G2(n+1))*(1+pi*(R1(:,n+
1).^2)/(RHo*Wo1))/((RHo^1*Ho)*(Lam1(n+1)^4));

        for i=1:k-1
            A11(i,i) = -x11(i+1,n+1);
            B11(i) = x12(i+1,n+1)+x13(i+1,n+1)-x14(i+1,n+1)-x15(i+1,n+1)-
x16(i,n+1);
        end
        B11(1)=B11(1)-Po;
        B11(k-1)=B11(k-1)-Po*((1/Lam1(n+1))^2);
        P = inv(A11)*B11;

        P1(1,n+1)=Po;
        P1(k+1,n+1)=Po*((1/Lam1(n+1))^2);
        for i=2:k
            P1(i,n+1)=P(i-1);
        end

        for i=1:k;
            Sigs1(i,n+1)=(-RHo*(Lam1(n+1))/(2*Wo1*b1(1,n)))*(P1(i+1,n+1)-
P1(i,n+1));
            DSigs1(i,n+1)=(Sigs1(i,n+1)-Sigs1(i,n))/Dt;
        end

        for i=1:k

DC1(i,n+1)=Ho*Lam1(n+1)*(DSigs1(i,n+1)*eta1(n+1)+Sigs1(i,n+1)*(G1(n+1)+G2(
n+1))+G1(n+1)*G2(n+1)*4*C1(i,n)/RHo/Lam1(n+1))/(4*(Sigzz1(n+1)*eta1(n+1)+G
1(n+1)));
            C1(i,n+1)=C1(i,n)+DC1(i,n+1)*Dt;
        end
end

```

```

for i=1:k
    DX1(i,n+1)=Sigs1(i,n+1)/mu+2*DC1(i,n+1)/3;
    X1(i,n+1)=X1(i,n)+DX1(i,n+1)*Dt;
    Xs1(i,n+1)=X1(i,n+1)-(2/3)*C1(i,n+1);
end

Pn1(n+1)=mean(P1(1:k+1,n+1));
TOT1(n+1)=Po+(Sigzz1(n+1)-Pn1(n+1))*b1(n);

for j= 2:20
    u1(j,n+1) = u1(j,n)+(u1(j-1,n)-
2*u1(j,n)+u1(j+1,n))*(Dt*(10/Lam1(n))*G1(n)/mu2)/(dx(1,g)^2);
end

bc1(n) = Sigzz1(1,n+1)*Arat/(3*G1(n));
u1(1,n+1) = u1(3,n+1)-bc1(n)*2*dx(1,g);
u1(xp,n+1) = u1(xp-3,n+1);

b1(1,n+1) = b1(1) - abs(u1(xp,n+1));

if b1(1,n+1) < 0.1
    break
end
if (Dt*3*G1(n)/mu2) >= dt(1,g)
    break
end

Lam2(n+1)=Lam2(n)+Dlam2(n)*Dt;
LS(n+1)= (-Lam1(n+1)+Lam2(n+1))*RHo;
sh2=exp(h*log(Lam2(1,n+1)));
G1(n+1)=sh2*E1;
G2(n+1)=sh2*E2;
eta2(n+1)=tau*G2(n+1);
DSigzz2(n)=(0.5*G1(n)*G2(n)*(Lam2(n+1)^2-
1)+2*(G1(n)+G2(n)+Sigzz2(n))*eta2(n+1)*Dlam2(n)/Lam2(n)-
G1(n)*Sigzz2(n))/eta2(n+1);
Sigzz2(n+1) = Sigzz2(n)+DSigzz2(n)*Dt;

for j=2:k
    if P2(j,n) > cavP2(j) && R2(j,n)== R2(j,1) && DR2(j,n) == 0;
        DR2(j,n+1)=0;
        R2(j,n+1) = R2(j,n);
    else
        DR2(j,n+1)=(R2(j,n)/(2*eta2(n+1)))*(Pcav2(j,n)-P2(j,n)-
2*gammaP/R2(j,n));
    end
end

```

```

R2(j,n+1)=R2(j,n)+DR2(j,n+1)*Dt;

end
end
for j=2:k
    Pcav2(j,n+1)=Pcav2(j,1)*((R2(j,1)/R2(j,n+1))^2);
end

for i=2:k
    x22(i,n+1) = 2*(Wo2*b2(n)/(RHo*Lam2(n+1)))*(1-Dt*(G1(n+1))/eta2(n+1)-
6*Dt*(Sigzz2(n+1)+G1(n+1)+G2(n+1))/(mu*Ho*Lam2(n+1)))*(Sigs2(i-1,n)-
Sigs2(i,n));
    x26(i,n+1) = -
8*(Wo2*b2(n)/(RHo*Lam2(n+1)))*G1(n+1)*G2(n+1)*(C2(i,n)-C2(i-
1,n))*Dt/Lam2(n+1)/RHo/eta2(n+1);
end
    x21(:,n+1) =
2*(1+6*pi*Wo2*b2(n)*Dt*(Sigzz2(n+1)+G1(n+1)+G2(n+1))*(R2(:,n+1).^2)/(eta2(n
+1)*(RHo^2*Ho)*(Lam2(n+1)^3)));
    x23(:,n+1) =
Pcav2(:,n+1).*(12*pi*b2(n)*Wo2*Dt*(Sigzz2(n+1)+G1(n+1)+G2(n+1))*(R2(:,n+1).
^2)/(eta2(n+1)*(RHo^2*Ho)*(Lam2(n+1)^3)));
    x24(:,n+1) = -
12*pi*Wo2*b2(n)*gammaP*Dt*(Sigzz2(n+1)+G1(n+1)+G2(n+1))*R2(:,n+1)/(eta2(
n+1)*(RHo^2*Ho)*(Lam2(n+1)^3));
    x25(:,n+1) = -
12*(Wo2^2)*b2(n)*Dlam2(n)*Dt*(Sigzz2(n+1)+G1(n+1)+G2(n+1))*(1+pi*(R2(:,n+
1).^2)/(RHo*Wo2))/((RHo^1*Ho)*(Lam2(n+1)^4));

for i=1:k-1
    A12(i,i) = -x21(i+1,n+1);
    B12(i) = x22(i+1,n+1)+x23(i+1,n+1)-x24(i+1,n+1)-x25(i+1,n+1)-
x26(i,n+1);
end
    B12(1)=B12(1)-Po*((1/Lam2(n+1))^2);
    B12(k-1)=B12(k-1)-Po;
    P = inv(A12)*B12;

    P2(1,n+1)=Po*((1/Lam2(n+1))^2);
    P2(k+1,n+1)=Po;
for i=2:k
    P2(i,n+1)=P(i-1);
end

for i=1:k;

```

```

    Sigs2(i,n+1)=(-RHo*(Lam2(n+1))/(2*Wo2*b2(1,n)))*(P2(i+1,n+1)-
P2(i,n+1));
    DSigs2(i,n+1)=(Sigs2(i,n+1)-Sigs2(i,n))/Dt;
end

for i=1:k

DC2(i,n+1)=Ho*Lam2(n+1)*(DSigs2(i,n+1)*eta2(n+1)+Sigs2(i,n+1)*(G1(n+1)+G2(
n+1))+G1(n+1)*G2(n+1)*4*C2(i,n)/RHo/Lam2(n+1))/(4*(Sigzz2(n+1)*eta2(n+1)+G
2(n+1)));
    C2(i,n+1)=C2(i,n)+DC2(i,n+1)*Dt;
end

for i=1:k
    DX2(i,n+1)=Sigs2(i,n+1)/mu+2*DC2(i,n+1)/3;
    X2(i,n+1)=X2(i,n)+DX2(i,n+1)*Dt;
    Xs2(i,n+1)=X2(i,n+1)-(2/3)*C2(i,n+1);
end

Pn2(n+1)=mean(P2(1:k+1,n+1));
TOT2(n+1)=Po+(Sigzz2(n+1)-Pn2(n+1))*b2(n)
for j= 2:20
    u2(j,n+1) = u2(j,n)+(u2(j-1,n)-
2*u2(j,n)+u2(j+1,n))*(Dt*(10/Lam2(n))*G2(n)/mu2)/(dx(1,g)^2);
end
bc2(n) = Sigzz2(1,n+1)*Arat/(3*G2(n));
u2(1,n+1) = u2(3,n+1)-bc2(n)*2*dx(1,g);
u2(xp,n+1) = u2(xp-2,n+1);
b2(1,n+1) = b2(1) - abs(u2(xp,n+1));
if b2(1,n+1) < 0.1
    break
end
if (Dt*3*G2(n)/mu2) >= dt(1,g)
    break
end

if TOT1(n+1)*Lo/2 > TOT2(n+1)*Lo/2+K3*LS(n+1)
    Dlam1(n)= Dlam1(n)-0.03*(0.9)^(N); Dlam2(n)=Dlam2(n)+0.03*(0.9)^(N);
else
    Dlam1(n)= Dlam1(n)+0.03*(0.9)^(N); Dlam2(n)=Dlam2(n)-0.03*(0.9)^(N);
end
e1(n) = abs(TOT1(n+1)*Lo/2 - TOT2(n+1)*Lo/2-K3*LS(n+1));
e2(n) = 0.03*abs(TOT1(n+1)*Lo/2);
N = N+1;
if N == 1999
    N

```

```

    end
end
TOT(n)=(TOT1(n)+TOT2(n))/2;
Lam(n,m)=0.5*(Lam1(n)+Lam2(n));
epsilon(n,m)=Lam(n,m)-1;
end
c=m;
T(:,c)=TOT;
filename = [ 'a' num2str(m), '.mat' ]
save(filename);
end
plot(epsilon(:,:),T(:,:))
hold on

```

A8: Phenomenological Series Model for Creep Deformation of PSA Bonded with PSA

Systems

PSAs with carrier layers have unique nonlinear and non-monotonic mechanical behavior, as shown in Fig. 108. These unique behaviors cannot be adequately described by conventional constitutive models (eg. Norton Law) currently available in commercial FEA tools. Therefore, if engineers want to do a computational estimation (compared to physical testing methods) on a product that contain PSA bonded assemblies by some commercial FEA tools, a suitable constitutive model is required to describe the unique mechanical performances of PSA bonded assemblies. Based on the trend of the creep curve, a piece-wise visco-plastic model incorporating strain hardening (red solid lines) is fitted to the creep curve. Since these models do not exist in the commonly used commercial FEA tools, a user-defined subroutine is required and used in order to implement these material models into the FEA tools as constitutive equations for the PSA bonded assembly.

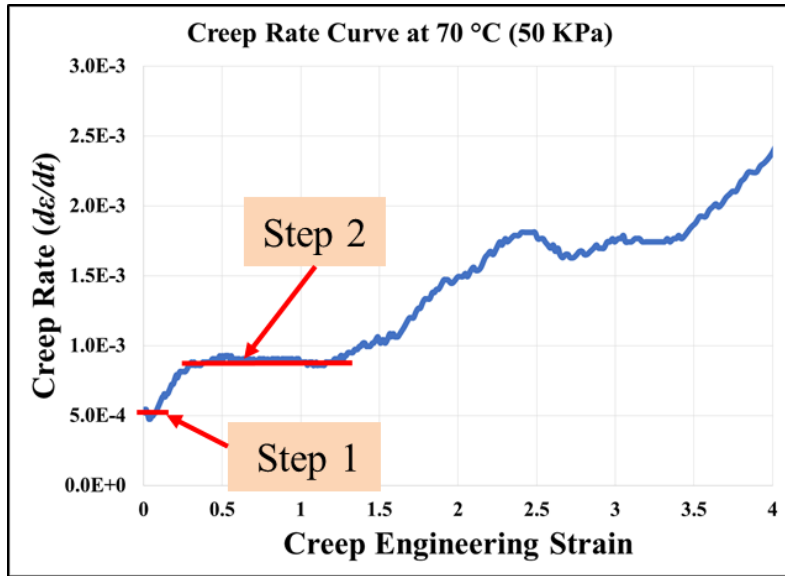


Fig. 108 segmental model for creep deformation

The multi-stage creep curves of PSAs with carrier layers, as shown in Fig. 109, require new multi-stage models. In the current stage, the methodologies used to define the model constants and FEA implementation have been generated for the 1st and 2nd stages of the secondary creep curve.

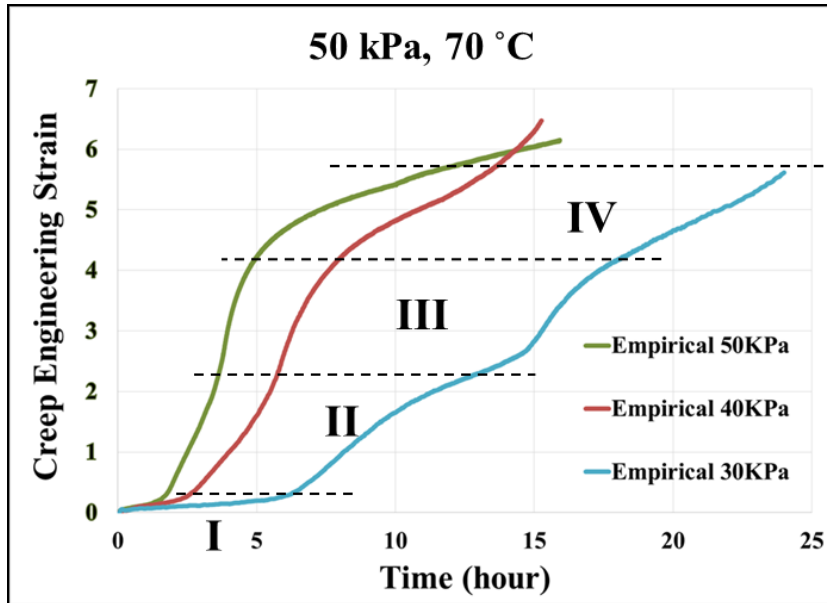


Fig. 109 Multi-stage creep curves at different stress level

Fig. 110 (a) shows a symmetric half of the test coupon configuration. It is two T-shaped aluminum tabs with the PSA bond line in between. Fig. 110 (b) is the zoom-in of the finite element model that models this configuration. In the FEA model, the bond line is modeled with one continuous finite element layer of equivalent homogeneous material. In reality, the PSA system has double sided PSA on the either side of the carrier layer, but the system is not broken down into separate carrier and adhesive layers in the FEA model. The model treats that region as an equivalent homogeneous material with material properties equivalent to reference material that captures the overall deformation of the entire PSA system (the entire system consisting of all the adhesive and carrier layers for double sided PSAs). In other words, this equivalent homogenous material will match the physically measured experimental results.

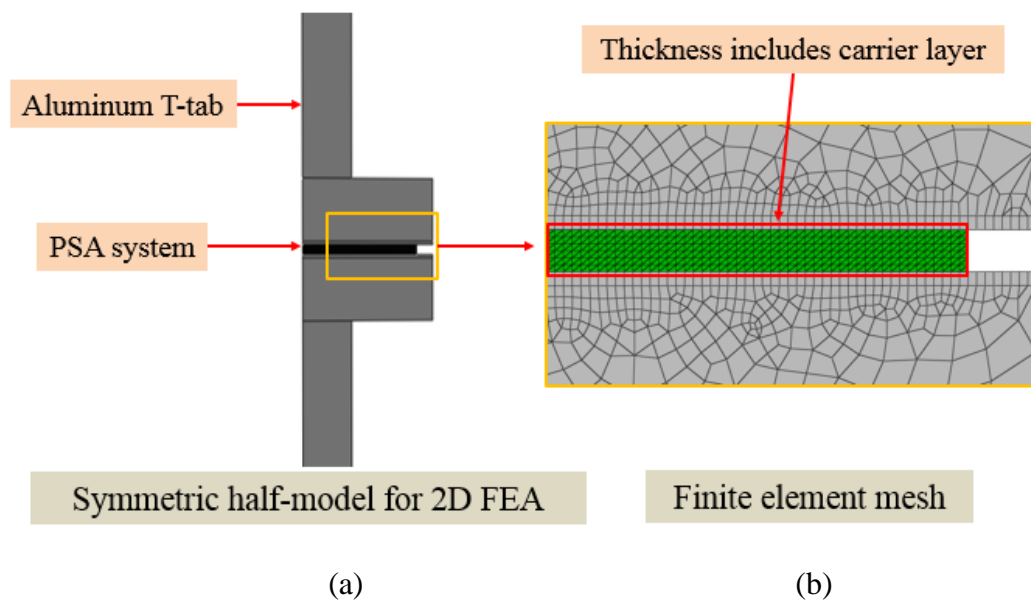


Fig. 110 (a) Schematic of symmetric half of test coupon; (b) FEA model and mesh

Compared to the secondary creep, the primary creep of PSA is very short and contributes little strain to the overall creep strain. Therefore, the FEA model is based

on steady-state creep (primary creep is ignored). The piece-wise creep constitutive model is:

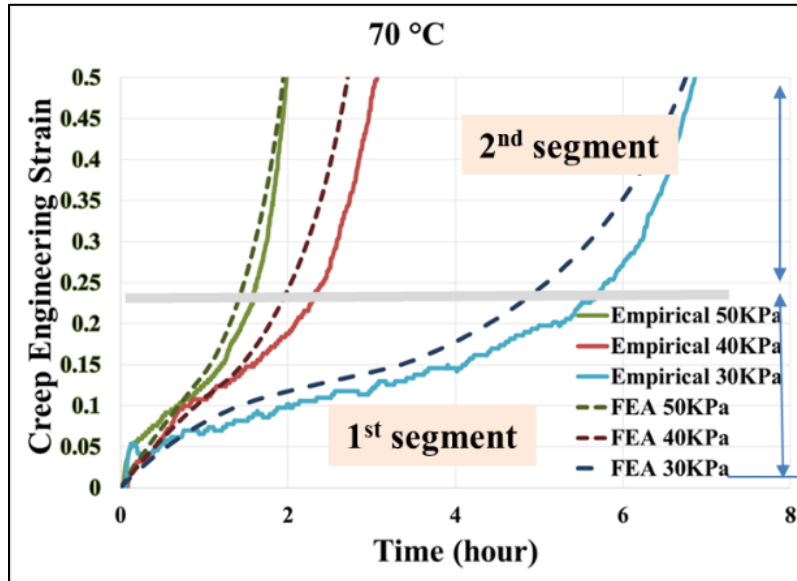
$$\dot{\epsilon}_{cr_i} = A_i \sigma^n \exp\left(-\frac{Q}{RT}\right) \quad \text{Eq. (57)}$$

where A is the proportionality constant, n is the stress exponent constant, Q is activation energy, R is gas constant, T is temperature, and i is the step identify.

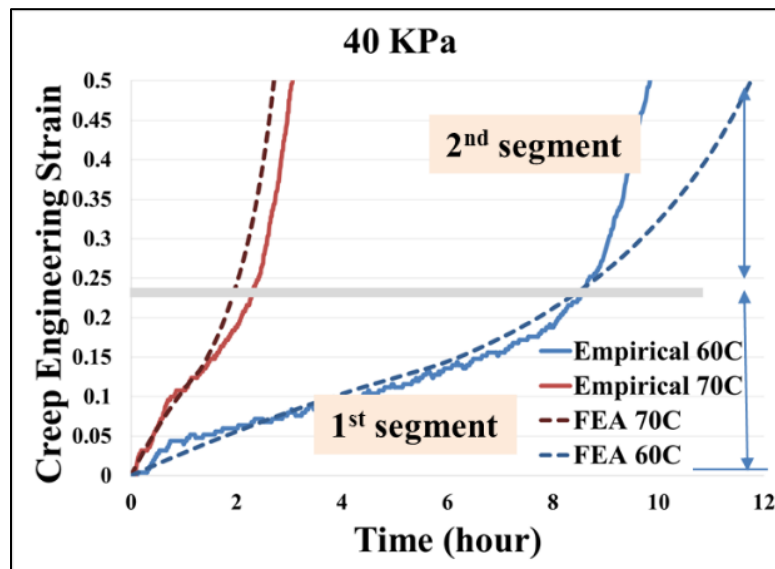
As discussed before, the transition of the creep rate relates to the degree of PSA deformation, which is a function of stretch ratio. Therefore, the equivalent creep strain is selected as the parameter to control when to change the constants. For simplification, in the preliminary study, the difference between strain rate of each stage is described by the difference of the proportionality constant A . This piece-wise model is not available in commercial FEA tools, such as ABAQUS and ANSYS. In order to apply the model into the commercial FEA tools as a creep constitutive equation for PSA materials, a special user-defined subroutine is required. In this study, a user defined subroutine, attached in Appendix III, is developed for defining the creep constitutive law of PSAs in ABAQUS. As an example, the FEA model fit to one PSA/substrate combination is shown in Fig. 111 (a) (creep at different stress level) and Fig. 111 (b) (creep at different temperature) with the model constants listed in Table 5. Considering the reality of applications and complexity of the mechanical modeling, in this stage, the total creep deformation is designed to capture the creep behavior of PSA bonded assemblies up to 50% engineering creep tensile strain (approx. 80 to 100% total engineering tensile strain, depending on stress level).

Table 5: Sample model constant of double-stage model

Segment	Activation Energy Q_i (J/mol)	Proportionality constant A_i	Stress hardening exponent sm_i	Gas constant R_i (JK ⁻¹ mol ⁻¹)	Creep strain at the beginning of i th transition CS_i
1	140000	2.03E+15	0.45	8.315	0.95, 0.45, 0.4 for case 30, 40, 50 KPa
2	140000	3.00E+16	0.45	8.315	



(a)



(b)

Fig. 111 FEA model fit to creep curves at (a) different stress levels; (b) different loading temperature

The Fortran code below shows the user defined subroutine for define the PSA constitutive model for the example above.

```

0  SUBROUTINE CREEP(DECRA,DESWA,STATEV,SERD,EC,ESW,P,QTILD,
+TEMP,DTEMP,PREDEF,DPRED,TIME,DTIME,CMNAME,LEXIMP,LEND,
+COORDS,NSTATV,NOEL,NPT,LAYER,KSPT,KSTEP,KINC,NTENS)
  INCLUDE 'ABA_PARAM.INC'
  CHARACTER*80 CMNAME
  DIMENSION DECRA(5),DESWA(5),STATEV(*),PREDEF(*),DPRED(*),
+TIME(3),COORDS(*),EC(2),ESW(2)

C  ***Piece-wise linear strain softening/hardening creep model***
C  QTILD: Equivalent stress
C  EC(1) : Creep at the start of increment
C  DECRA(1) : Equivalent Creep strain increment
C  DECRA(5) : Partial derivative of DECRA(1) respect to change
C             of equivalent stress
C  LEXIMP : Explicit/implicit flag
C
C  ***DEFINE CONSTANTS***
C  CSi: Creep strain at the beginning of ith transition
C  sm: Stress hardening exponent for ith segment of creep law
C  Ai: Proportionality constant for ith segment of creep law
C  Q: Activation energy of creep law
C  R: Gas constant
C
C  *** APPLIED CONSTANTS***
  REAL A1 A2 sm CS1 Q R T
  A1 = 2.03E+15
  A2 = 3.E+16
  sm = 0.45
  CS1 = case dependent
  Q = 140000
  R = 8.31446
  T = case dependent
C
C  ***DEFINE STRAIN RATE FOR EACH PHASE***
  IF(EC(1) .LT. CS1) THEN
    DECRA(1) = A1*(QTILD**(sm))*EXP(-Q/(R*TEMP))*DTIME
  ELSE
    DECRA(1) = A2*(QTILD**(sm))*EXP(-Q/(R*TEMP))*DTIME
  
```

```
END IF
C
IF(LEXIMP .EQ. 1) THEN
DECRA(5) = sm1*(QTILD**(sm-1))*EXP(-Q/(R*T))*DTIME
END IF
C
RETURN
END
```

Bibliography

- Bergström, J. S., and M. C. Boyce, (1998). "Constitutive modeling of the large strain time-dependent behavior of elastomers." *Journal of the Mechanics and Physics of Solids* 46.5: 931-954.
- Brennen, C.E., 1995. *Cavitation and bubble dynamics* (Oxford University Press, New York, 1995)
- Brown, K., Hooker, J. C., & Creton, C. (2002). Micromechanisms of tack of soft adhesives based on styrenic block copolymers. *Macromolecular Materials and Engineering*, 287(3), 163-179.
- Chiche, A., Pareige, P., and Creton, C., (2000). Role of surface roughness in controlling the adhesion of a soft adhesive on a hard surface, *Comptes Rendus de l'Academie des Science – Series IV- Physics*, Vol. 1, Issue 9, pp. 1197-1204 (2000)
- Chikina, I., & Gay, C. (2000). Cavitation in adhesives. *Physical review letters*, 85(21), 4546.
- Chun, H., Kim, H. A., Kim, G., Kim, J., and Lim, K. Y., (2007). Effect of the stress relaxation property of acrylic pressure sensitive adhesive on light-leakage phenomenon of polarizer in liquid crystal display, *Journal of Applied Polymer Science*, Vol. 106, 2746-2752 (2007)
- Colak, O. U. (2005). Modeling deformation behavior of polymers with viscoplasticity theory based on overstress. *International Journal of Plasticity*, 21(1), 145-160.
- Creton, C., Hooker, J., & Shull, K. R. (2001). *Bulk and interfacial contributions to the debonding mechanisms of soft adhesives: extension to large strains*. *Langmuir*, 17(16), 4948-4954.
- Creton, C., Leibler, L., 1996. How does tack depend on contact time and contact pressure, *Journal of Polymer Science: Part B: Polymer Physics*, Vol 34, 545-554 (1996)
- Creton, C., Lakrout, H., 2000. Micromechanics of flat-probe adhesion tests of soft viscoelastic polymer films. *Journal of Polymer Science: Part B: Polymer Physics*, Vol. 38, 965-979 (2000)
- Creton, C., 2003. Pressure-sensitive adhesives: an introductory courses, *MRS Bulletin*, June 2003
- Creton, C., Hooker, J., and Shull, K. R., 2011. *Langmuir* (2011) 17, 4948-4954
- Crosby, A.J., and Shull, K.R., 1999. Adhesive failure analysis of pressure-sensitive adhesives, *Journal of Polymer Science B: Polymer Physics* 37: 3455-3472, 1999
- Deplace, F., Carelli, C., Mariot, S., Retsos, H., Chateauminois, A., Ouzineb, K., & Creton, C. (2009). Fine tuning the adhesive properties of a soft nanostructured adhesive with rheological measurements. *The Journal of Adhesion*, 85(1), 18-54.
- Donoso, M. G., Méndez-Vilas, A., Bruque, J. M., & González-Martin, M. L. (2007). On the relationship between common amplitude surface roughness parameters and surface area: Implications for the study of cell–material

- interactions. *International Biodeterioration & Biodegradation*, 59(3), 245-251.
- Eveloy, V., Rodgers, P., & Pecht, M. G. (2004). Reliability of pressure-sensitive adhesive tapes for heat sink attachment in air-cooled electronic assemblies. *IEEE Transactions on Device and Materials Reliability*, 4(4), 650-657.
- Everitt, S.L., Harlen, O.G. Wilson, H.J. and Read, D.J., 2003. Bubble dynamics in viscoelastic fluids with application to reacting and non-reacting polymer foams, *Journal of Non-Newtonian Fluid Mechanics*, Vol. 114, Issues 2-3, pp. 83-107
- Fujita, M., Kajiyama, M., Takemura, A., Ono, H., Mizumachi, H., and Hayashi, S., 1998. Effects of miscibility on peel strength of natural-rubber based pressure-sensitive adhesives, *Journal of Applied Polymer Science*, Vol. 70, Issue 4, pp. 777-784, 1998
- Fujita, M., Takemura, A., Ono, H., Kajiyama, M., Hayashi, S., & Mizumachi, H. (2000). Effects of miscibility and viscoelasticity on shear creep resistance of natural-rubber-based pressure-sensitive adhesives. *Journal of applied polymer science*, 75(12), 1535-1545.
- Gay, C., and Leibler, L., (1999). Theory of Tackiness, *Physical Review Letters*, Vol. 82, Number 5, pp. 936-939
- Gay, C. (2002). Stickiness—some fundamentals of adhesion. *Integrative and comparative biology*, 42(6), 1123-1126.
- Gent, A.N., and Lindley, P.B., 1959. Internal rupture of bonded rubber cylinders in tension, *The Royal Society*, Vol. 249, No. 1257 (Jan. 1, 1959), pp. 195-205
- Glassmaker, N.J., Hui, C.Y., Yamaguchi, T., and Creton, C., Detachment of stretched viscoelastic fibrils, *Eur. Phys. J. E*. 25, 253-266 (2008)
- Haiat, G., & Barthel, E. (2007). An approximate model for the adhesive contact of rough viscoelastic surfaces. *Langmuir*, 23(23), 11643-11650.
- Huang, H., Dasgupta, A., & Mirbagheri, E. (2016, April). Mechanistic model for the mechanical behavior of assemblies bonded with pressure-sensitive adhesives. In *Thermal, Mechanical and Multi-Physics Simulation and Experiments in Microelectronics and Microsystems (EuroSimE), 2016 17th International Conference on (pp. 1-4)*. IEEE.
- Huang, H., Dasgupta, A., & Mirbagheri, E. (2017, May). Mechanical behavior of pressure-sensitive adhesives (PSAs). In *Thermal and Thermomechanical Phenomena in Electronic Systems (ITherm), 2017 16th IEEE Intersociety Conference on (pp. 1393-1397)*. IEEE.
- Huang, H., Dasgupta, A., Mirbagheri, E., & Darbha, K. (2018, May). Mechanical Response of Assemblies Bonded with Double-Layered Pressure-Sensitive Adhesives (PSAs). In *2018 17th IEEE Intersociety Conference on Thermal and Thermomechanical Phenomena in Electronic Systems (ITherm) (pp. 1128-1132)*. IEEE.
- Huang, H., Jiang, Q., Dasgupta, A., Mirbagheri, E., & Darbha, K. (2018, August). Creep Response of Assemblies Bonded With Pressure Sensitive Adhesive (PSA). In *ASME 2018 International Technical Conference and Exhibition on Packaging and Integration of Electronic and Photonic Microsystems (pp. V001T01A008-V001T01A008)*. American Society of Mechanical Engineers.

- Hui, C.Y. and Baney, J.M., 1998. Contact mechanics and adhesion of viscoelastic spheres, *Langmuir* 1998, 14, 6570-6578
- Johnson, K.L., Kemdall, K., and Roberts, A.D., 1971. Surface energy and the contact of elastic solids, *Proceedings of the Royal Society of London. Series A, Mathematical and Physical Sciences*, Vol. 324, No. 1558 (Sep. 8, 1971), pp. 301-313
- Kaelble, D.H., 1964. Theory and analysis of peel adhesion: rate-temperature dependence of viscoelastic interlayers. *Journal of Colloid Science*, Vol. 19. 413-424 (1964)
- Kaelble, D. H. (1992). Theory and analysis of peel adhesion: adhesive thickness effects. *The Journal of Adhesion*, 37(1-3), 205-214.
- Katerina, F., Mavrantzas, V.G., Dimakopoulos, Y., and Tsamopoulos, J., 2006. Numerical simulation of multiple bubbles growing in a Newtonian liquid filament undergoing stretching, *Physics of Fluids* 18, 042106 (2006)
- Khan, I., Poh, B. T., 2010. Effect of molecular weight and testing rate on peel and shear strength of epoxidized natural rubber (ENR 50)-based adhesive. *Journal of Applied Polymer Science*, Vol. 120, 2641-2647 (2011)
- Kim, D. J., Kim, H. J., & Yoon, G. H. (2006). Shear creep resistance of styrene-isoprene-styrene (SIS)-based hot-melt pressure-sensitive adhesives. *Journal of applied polymer science*, 100(1), 825-831.
- Kowalski, A. and Czech, Z., 2015. The effects of substrate surface properties on tack performance of acrylic Pressure-Sensitive Adhesive (PSAs), *International Journal of Adhesion & Adhesive*, 60 (2015) 9-15
- Lamanna, G., Basile, A., 2013. Mechanics of soft PSAs, *The Open Material Science Journal*, 2013, 7, 23-28
- Lakrout, H., Sergot, P., Creton, C., 1999. Direct observation of cavitation and fibrillation in a probe tack experiment on model acrylic pressure-sensitive-adhesives. *Journal of adhesion*. 1999, Vol. 69, pp. 307-359
- Lai, J.H., Knudson, C., Hallgren, L., Douglas, R.B., and Griffin R.B., 1985. Effect of humidity and temperature on the adhesive strength of pressure sensitive adhesives. Vol. 25, Issue 12, pp. 778-781, 1985
- Lin, Y.Y., and Hui, C.Y., 2004. Cavity growth from crack-like defects in soft materials, *International Journal of Fracture*, 2004, Vol. 126, Issue 3, pp 205-221,
- Lin, T. I., Chen, A., Chen, S. I., and Leu, J., 2015. Effects of thermomechanical properties of polarizer components on light leakage in thin-film transistor liquid-crystal displays, *Japanese Journal of Applied Physics* 54, 076701 (2015)
- Li, L., Tirrell, M., Korba, G. A., and Pocius, A. V., 2001. Surface energy and adhesion studies on acrylic pressure sensitive adhesives, *The Journal of Adhesion*, 2001, 76: 307-34
- Maeda, K., Okazawa, S., and Nishiguchi, K., 2011. New material model for describing large deformation of Pressure Sensitive Adhesive. In: Ao S.I., Castillo O., Huang X. (eds) *Intelligent Control and Computer Engineering. Lecture Notes in Electrical Engineering*, vol 70. Springer, Dordrecht

- Mohammed, I. K., Charalambides, M. N., & Kinloch, A. J. (2016). Modeling the effect of rate and geometry on peeling and tack of pressure-sensitive adhesives. *Journal of Non-Newtonian Fluid Mechanics*, 233, 85-94.
- Mukherjee, S., & Dasgupta, A. (2010, January). An evaluation of a modified iosipescu specimen for measurement of elastic-plastic properties of solder materials. *In ASME 2010 International Mechanical Engineering Congress and Exposition (pp. 351-356)*. American Society of Mechanical Engineers.
- Mukherjee, S., Nuhi, M., Dasgupta, A., & Modarres, M. (2016). Creep constitutive models suitable for solder alloys in electronic assemblies. *Journal of Electronic Packaging*, 138(3), 030801.
- Mukherjee, S., Zhou, B., Dasgupta, A., & Bieler, T. R. (2016). Multiscale modeling of the anisotropic transient creep response of heterogeneous single crystal SnAgCu solder. *International Journal of Plasticity*, 78, 1-25.
- Nam, I., Ha, K., Lee, K., Kim, L. J., Kim, M., Seong, I., and Chang, T., 2011. Novel versatile pressure sensitive adhesive for polarizing film of TFT-LCDs: viscoelastic characteristics and light leakage performance, *International Journal of Adhesion & Adhesives*, 31 (2011) 708-714
- Nakamura, Y., Imamura, K., Ito, K., Nakano, S., Sueoka, A., Fuji, S., Sasaki, M., and Urahama, Y., 2012. Contact time and temperature dependencies of tack in polyacrylic block copolymer pressure-sensitive adhesives measured by the probe tack test, *Journal of Adhesion Science and Technology*, 26 (2012) 231-249
- Newby, B.M.Z, Chaudhury, M.K., 1997. Effect of interfacial slippage on viscoelastic adhesion, *Languir* 1997, 13, 2805-1809
- Sun, C., Zhang, D., and Wadsworth L. C., 1999. Corona treatment of polyolefin films - a review, *Advances in Polymer Technology*, Vol. 18, No. 2, 171-180, 1999
- Shon, S., 2003. Various ways to control the bulk properties of pressure sensitive adhesives, *Journal of Adhesion Science Technology*, Vol. 17, No.5, pp. 703-723 (2003)
- Shon, S., Yang, S., 2003. On the work of adhesion and peel strength between pressure sensitive adhesives and the polymeric films used in LCD devices, *Journal of Adhesion Science Technology*, Vol. 17, No. 7, pp. 903-915 (2003)
- Sosson, F., Chateauminois, A., & Creton, C. (2005). Investigation of shear failure mechanisms of pressure-sensitive adhesives. *Journal of Polymer Science Part B: Polymer Physics*, 43(22), 3316-3330.
- Steven-Fountain, A. J., Atkins, A. G., Jeronimidis, G., Vincent, J. F. V., Farrar, D. F., & Chivers, R. A. (2002). The effect of flexible substrates on pressure-sensitive adhesive performance. *International journal of adhesion and adhesives*, 22(6), 423-430.
- Street, J. R., 1968. The rheology of phase growth in elastic liquids, *Transaction of the Society of Rheology*, 12:1, 103-131(1968)
- Sun. S., Li, M., and Liu, A., 2013. A review on mechanical properties of pressure sensitives, *International Journal of Adhesion and Adhesives* 41 (2013) 98-106

- Temiz, Ş., Özel, A., & Aydin, M. D. (2004). A study on durability of bonded assemblies bonded with pressure-sensitive adhesives. *Journal of Adhesion Science and Technology*, 18(10), 1187-1198.
- Tierney, H. J., 1956. Pressure sensitive adhesive strapping tape, *U.S. Patent US2750315 A*, June 12, 1956
- Takahashi, K., Yamagata, Y., Inaba, K., Kishimoto, K., Tomioka, S., & Sugizaki, T. (2016). Characterization of Tack Strength Based on Cavity-Growth Criterion. *Langmuir*, 32(14), 3525-3531.
- Toyama M, Ito T, Nukatsuka H, Ikeda M. Studies on tack of pressure-sensitive adhesive tapes: On the relationship between pressure-sensitive adhesion and surface energy of adherends. *Journal of Applied Polymer Science*. 1973 Nov;17(11):3495-502.
- Vakula, V. L., and Pritykin, L. M., 1992. Polymer adhesion: basic physico-chemical principles, *Polymer International*, Vol. 28, Issue 1, pp. 96 (1992)
- Williams, M. L., Landel, R. F., and Ferry, J. D., 1955. Temperature dependence of relaxation mechanism in amorphous polymers and other glass-forming liquids, *Journal of the American Chemical Society*, 1955; 77: 3701-6
- Williams, M. L., and Schapery, R. A., 1965. Spherical flaw instability in hydrostatic tension, *International Journal of Fracture Mechanics*, Vol. 1, Issue 1, pp 64-72, 1965
- Ozel, A., Temiz, S., and Aydin, M. D., 2005. Effect of overlap length on durability of bonded assemblies bonded with a pressure-sensitive adhesive, *Journal of Adhesion Science Technology*, Vol. 19, No.1, pp. 57-71 (2005)
- Ozel, A., Temiz, S., and Aydin, M. D., 2005. Effect of overlap length on durability of bonded assemblies bonded with a pressure sensitive adhesive, *Journal of Adhesion Science Technology*, Vol. 19, No. 1, pp. 57-71 (2005)
- Peykova, Y., Guriyanova, S., Lebedeva, O. V., Diethert, A., Müller-Buschbaum, P., & Willenbacher, N. (2010). The effect of surface roughness on adhesive properties of acrylate copolymers. *International Journal of Adhesion and Adhesives*, 30(4), 245-254.
- Pho, B.T., and Khan, I., 2012. Effect of test rate on adhesion properties of SMRL, ENR-25 and ENR-50-based pressure-sensitive adhesive, *Journal of Adhesion Science and Technology*, Vol. 26, Issue 6, 2012
- Poh, B. T., & Kwo, H. K. (2007). Shear strength of SMR—based pressure-sensitive adhesives. *Polymer-Plastics Technology and Engineering*, 46(10), 1021-1024.
- Villey, R., Creton, C., Cortet, P. P., Dalbe, M. J., Jet, T., Saintyves, B., ... & Ciccotti, M. (2015). Rate-dependent elastic hysteresis during the peeling of pressure sensitive adhesives. *Soft Matter*, 11(17), 3480-3491.
- Yamaguchi T, Creton C, Doi M. Simple model on debonding of soft adhesives. *Soft matter*. 2018.
- Yamaguchi, T., Creton, C., & Doi, M. (2018). Simple model on debonding of soft adhesives. *Soft matter*.
- Yamaguchi, T., and Doi, M., 2006. Debonding dynamics of pressure sensitive adhesives: 3D block model, *European Physical Journal E* 21, 331-339

- Yamaguchi, T., Morita, H., and Doi, M., 2006. Modeling on debonding dynamics of pressure-sensitive adhesives, *European Physical Journal E* 20, 7-17 (2006)
- Yamaguchi, T., Muroo, H., Sumino, Y., Doi, M., 2012. Asymmetry-symmetry transition of double-sided adhesive tapes. *Physical Review E* 85, 061802 (2012)
- Yao, M.W., McKinley, G.H., and Debbaut, B., 1998, Extensional deformation, stress relaxation and necking failure of viscoelastic filaments, *Journal of Non-Newtonian Fluid Mechanics*. 79 (1998) 469-501
- Zheng, S. F., & Weng, G. J. (2002). A new constitutive equation for the long-term creep of polymers based on physical aging. *European Journal of Mechanics-A/Solids*, 21(3), 411-421.
- Zosel, A. (1985). Adhesion and tack of polymers: Influence of mechanical properties and surface tension. *Colloid & Polymer Science* 263:541-553 (1985)
- Zosel, A. (1989). Adhesive failure and deformation behavior of polymers, *The Journal of Adhesion*, Vol. 30, Issue 1-4, pp. 135-149
- Zosel, A. (1991). Effect of cross-linking on tack and peel strength of polymers, *The Journal of Adhesion*, Vol. 34, Issue 1-4, pp. 201-209
- Zosel, A. (1998). The effect of fibrillation on the tack of pressure sensitive adhesives, *International Journal of Adhesion and Adhesive*. 18, 265
- Zosel, A. (1994). Shear strength of pressure sensitive adhesives and its correlation to mechanical properties. *The Journal of Adhesion*, 44(1-2), 1-16.